

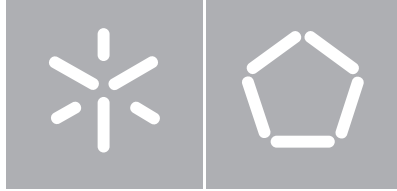


Universidade do Minho
Escola de Engenharia

Joel Oliveira Correia Vasco

**A study on the performance of microinjection
moulds obtained using additive manufacturing**

December 2010



Universidade do Minho
Escola de Engenharia

Joel Oliveira Correia Vasco

**A study on the performance of microinjection
moulds obtained using additive manufacturing**

Tese de Doutoramento
Ciência e Engenharia de Polímeros

Trabalho efectuado sob a orientação do
Professor António Sérgio Pouzada

Acknowledgements

To my Ph.D. Advisor, Professor António Sérgio Pouzada, from the Department of Polymer Engineering at the University of Minho, for his wise supervision, guidance, great wisdom, extensive knowledge and experience. Thanks to him, this research work was kept on track, properly focused on the good results obtained. It was a privilege to share these few years of research work with Professor Pouzada, following his lead on projects, publications and international presentations. This research work showed us that many problems are still unsolved and many questions are unanswered. Some solutions are still under development in order to obtain answers and therefore, many topics are still open to further discussion. It will be a privilege to have Professor Pouzada's contributions in the future, both as researcher and... if I may, as a friend.

To Professor João Maia from the University of Minho and the Case Western Reserve University, Cleveland, (United States of America), for his knowledge and cooperation on rheometry and the microrheometry evaluation carried out in this research work. Since common areas of interest are open for research, future projects may appear that could produce profitable results.

To the Portuguese Foundation for Science and Technology, for supporting this research work and the result dissemination activities under the grant SFRH/BD/36982/2007.

To the University of Minho and to the Polytechnic Institute of Leiria, for the cooperation protocol established between both institutions under which this research work was developed. The University of Minho provided all the necessary conditions to develop the experimental trials carried out, including the existent equipment, the acquired equipment as well as the specific components required for accomplishing the goals of this research. The Polytechnic Institute of Leiria provided the necessary conditions for the preliminary characterization of the moulding blocks through optical microscopy and roughness contact measurement.

To Doctor António Pontes, Eng^r João Ferro and Mr. Arlindo Sampaio from the Department of Polymer Engineering at the University of Minho, for their support on handling the microinjection equipment and the data acquisition system, necessary to develop all the research activities here included.

To Eng^r Teresa Neves from Simulflow, Lda., for her constant cooperation, expertise and support on Moldex 3D throughout this research work. As local reseller of Moldex 3D and considering the interest of this research, future cooperation is expected, both on research and training on microinjection moulding simulation. Core-Tech Systems (Taiwan) provided the 9.1 release of Moldex 3D for research purposes and supported this work during the experimental phase, concerning the model meshing for microinjection simulation. The University of Minho, Simulflow, Lda. and Core-Tech Systems established the cooperation protocol concerning research on microinjection.

To Doctor Ludwig Cardon from the CPMT – Centre for Polymer and Moulds Technology, Hogeschool Ghent (Belgium) and his crew, Kim Ragaert, Arne Dekeyser and Sven Vernailen for their friendship and support along this work. The cooperation with CPMT provided the cooperation with SIRRIS where the BA00SLA moulding blocks were produced.

To Eng^{rs} André Voets and Bruno Guerra from SIRRIS (Belgium), for accepting the challenge of producing the high precision stereolithography BA00SLA moulding blocks with their 3D Systems Viper Si², which were used afterwards for the microinjection tests.

To Doctor Edith Ariza Avila, from the SEMAT at the University of Minho, for performing the SEM and elemental analysis required for a proper characterization of the moulding blocks produced by high-precision stereolithography after use.

To Professor Arlindo Ramalho and Eng^r Luis Figueiredo from the Mechanical Engineering Department at the University of Coimbra for the profilemetry evaluations performed with the laser perthometer Rodenstock RM600-3D.

To Eng^f Hugo Brito from Equipack, Lda., for all his support on the installation and setup of the Priamus pressure sensors and data acquisition system.

To Priamus Technologies (Switzerland), in particular, to Mr. Christopherus Bader, for his cooperation, support and interest in this research work. Such cooperation supplied the two miniaturized pressure sensors 6006B at symbolic costs, enabling the gathering of valuable data to describe polymer flow at high shear rates.

To Mr. Joaquim Martins and Eng^f Pedro Oliveira from Famolde S. A., for their interest, expertise and support to this work on the manufacture of the micromould and moulding blocks. Without their full cooperation, it would not be possible to perform the research work within the experimental period defined on the planning.

To Eng^f Jose Cortes from Fundación Prodimtec (Spain), for his cooperation and support to this research work. This cooperation enabled the manufacture of the BA00SLM moulding blocks at symbolic costs, using their EOSINT M270 equipment.

To Mr. Terry Wohlers from Wohlers Associates, Inc. (United States of America), for his cooperation on providing a copy of the Wohlers Report 2009, which enabled an important update on the rapid manufacturing equipments' state-of-the-art.

To the Head of the Mechanical Engineering Department at the Polytechnic Institute of Leiria, Doctor Fátima Barreiros for her constant support and encouragement throughout this research work

To my good friend and department colleague, Rui Rúben, for his precious help and expertise on the preparation and analysis of the heat transfer simulations carried out on Abaqus software.

To my Ph.D. colleagues and friends from the Polytechnic Institute of Leiria for their companionship and mutual support throughout this period, António Selada, Irene Ferreira, João Matias, Mário Correia, Mário Pereira, Nuno André, Pedro Martinho and Rui Carvalho.

To all my good and trustful friends, here and abroad, who have always supported me and encouraged me to proceed! Hopefully, the future will bring us new prospects for collaboration.

To my girl, Gorete, my better half. She supported all my bad moods and disappointments with patience and perseverance. She was the one who stood by me, the one who gave me strength to carry on ... in fact, she is the one... the one I love! And that's why I want to share this achievement with her.

Finally, but not for last... I wish to thank to my parents. This research work and the degree itself are entirely dedicated to them. These words are for them even if they are written in English. However, I'm sure they are proud of me for achieving this goal as much as I am very proud of them. Throughout the years, they have made efforts and sacrifices to give the best to their sons. Furthermore, they gave us all the proper values and teachings by which we rule our lives and our conducts, both personally and professionally. I am what I am today thanks to them.

*Obrigado Mãe, obrigado Pai!
É a vocês que dedico este trabalho.*

Abstract

The development of smaller and more effective microsystems for medical, electronic and automotive applications is driving the industry and research institutions to the development of new manufacturing processes. In the last two decades several techniques were developed complying with the requirements of micromanufacturing. Considering their specific nature and purpose, microreplication processes such as microinjection are the most suitable for high production levels. Nevertheless, microinjection moulding is still a relatively unknown process considering polymer flow behaviour at the microscale. Therefore, experimental studies and numerical analyses were required to enable process optimization. Microscale effects such as wall-slip and heat transfer can have a significant influence on microinjection processing conditions as well as on the quality of the moulded parts. Therefore, these effects must be accounted for a numerical simulation with accurate results. For that purpose, tests on an instrumented micromould were carried out to obtain suitable data to be compared with filling and packing simulation results. Furthermore, when considering the use of moulding blocks manufactured by additive technologies such as stereolithography (SLA) and selective laser melting (SLM), it is important to evaluate their mechanical behaviour after the experimental tests have been performed. The use of this type moulding blocks decisively contributes for the time-to-market decrease of plastic micro-components obtained through microinjection moulding.

Resumo

O desenvolvimento de microsistemas cada vez mais pequenos e eficazes para aplicações médicas, electrónica e automóvel está a conduzir a indústria e centros de investigação para o desenvolvimento de novos processos de fabrico. Foram desenvolvidas diversas técnicas nas últimas duas décadas orientadas para o cumprimento dos requisitos da microfabricação. Considerando a sua natureza específica e objectivos, os processos de microreplicação como a microinjecção revelam-se como os mais adequados para elevados níveis de produção. Contudo, a moldação por microinjecção é ainda um processo relativamente pouco dominado considerando o comportamento do escoamento de polímero à microescala. Assim sendo, é fundamental a realização de estudos experimentais e de simulações numéricas para otimizar o processo. Efeitos de escoamento à microescala, tais como o escorregamento e a transferência de calor podem ter uma influência significativa nas condições de processamento da microinjecção assim como na qualidade das peças moldadas. Estes efeitos devem assim ser contabilizados para que se possa realizar uma simulação numérica que produza resultados precisos. Para esse efeito, foram realizados testes de microinjecção num micromolde instrumentado com o objectivo de retirar dados comparáveis com os resultados numéricos do enchimento e da compactação. Adicionalmente, considerando a utilização de blocos moldantes fabricados por tecnologias aditivas tais como a estereolitografia (SLA) e a fusão selectiva por laser (SLM), revela-se importante a avaliação do seu comportamento mecânico após a realização dos testes experimentais. A utilização deste tipo de blocos moldantes contribui decisivamente para o decréscimo do time-to-market para microcomponentes plásticos obtidos por micromoldação por injecção.

List of Publications from this work

Thermo-rheological behaviour of polymer melts in microinjection moulding, J. C. Vasco, J. M. Maia and A. S. Pouzada, *Journal of Micromechanics and Microengineering*, ISSN 0960-1317, 19, 105012, pages 1-8, 2009

Microinjection Moulding – Wall-Slip Evaluation of POM Flow in Microchannels, J. C. Vasco, J. M. Maia and A. S. Pouzada, *Proceedings of PPS-26, The 26th Annual Meeting of the Polymer Processing Society*, 6th July 2010, Banff, Canada

A study on the mouldability of POM microdetails in moulding blocks using micromanufacturing technologies”, J. C. Vasco, A. Selada, T. Neves and A. S. Pouzada, *Proceedings of PMI 2010, Polymer and Moulds Innovation*, 17th September 2010, Ghent, Belgium

Index

Acknowledgements	i
Abstract	v
Resumo	vii
List of Publications from this work	ix
List of Acronyms	xvii
Chapter 1 – Introduction	1
1.1. The context of the research work.....	1
1.2. Description of the thesis content.....	2
Chapter 2 – State of the art	5
2.1. Mass production <i>versus</i> short/medium-run techniques	5
2.2. Microfabrication technologies	6
2.3. Additive microfabrication technologies	8
2.3.1. Photocuring-based processes.....	8
2.3.2. Metal sintering/fusing-based processes.....	10
2.3.3. Additive processes classification.....	13
2.4. Subtractive microfabrication technologies	14
2.4.1. Chemical etching	14
2.4.2. Breaking of molecular chains	15
2.4.3. Sublimation	16
2.4.4. Cutting.....	16

2.4.5.	Subtractive processes classification	18
2.5.	Hybrid microfabrication technologies	18
2.6.	Microreplication technologies	20
2.6.1.	Injection moulding processes	20
2.6.2.	Embossing-based processes	21
2.7.	Microinjection moulding	21
2.8.	Flow phenomena at the microscale	24
2.8.1.	Conventional mathematical models for cavity filling	26
2.9.	Detailed objectives	27
Chapter 3 – Flow in microinjection moulding		29
3.1.	Flow models	29
3.1.1.	Capillary and slit flow models.....	29
3.1.2.	Wall slip effect	31
3.2.	Experimental methods	32
3.2.1.	Concept	32
3.2.2.	Methodology	34
3.2.3.	Moulding blocks for microchannels	38
3.2.4.	Instrumentation.....	39
3.2.5.	Materials.....	40
3.2.6.	Microinjection moulding.....	40
3.3.	Results and discussion	42
3.3.1.	Conventional rheometry.....	42
3.3.2.	Flow in microchannels	44
3.3.3.	Plug flow transition.....	45
3.3.4.	Interpreting the plug flow transition	46

Chapter 4 – Design of the Micromould	51
4.1. Design constraints.....	51
4.2. The mould.....	52
4.3. Moulding blocks	54
4.4. Feed system	55
4.5. Temperature control	56
4.6. Ejection system.....	57
4.7. Venting	58
4.8. Pressure and temperature monitoring	58
4.9. The microinjection moulding cell.....	62
4.10. Process control data sheet.....	65
4.11. Microinjection moulding cell operation procedures.....	66
Chapter 5 – Experimental techniques and methods.....	67
5.1. Tooling.....	67
5.1.1. Subtractive technologies	67
5.2. Additive technologies.....	71
5.3. Materials	74
5.3.1. Subtractive technologies	74
5.3.2. Additive technologies	74
Stereolithography	74
Selective Laser Melting	75
5.3. Polymers for microinjection moulding.....	76
5.4. Rapid prototyping	77
5.4.1. High-resolution stereolithography	77
5.4.2. Selective laser melting	78

5.5.	Capillary rheometry	81
5.6.	Microinjection moulding	81
5.6.1.	Injection moulding program	81
5.7.	Characterization	83
5.7.1.	Microscopy	83
5.7.2.	Roughness evaluation	85
5.7.3.	SEM and X-ray spectroscopy	85
5.8.	Numerical simulation	87
5.8.1.	Heat transfer simulations.....	87
	Simulation model.....	87
	Loads and boundary conditions	88
	Heat transfer simulation planning.....	89
5.8.2.	Filling simulations	89
	Simulation models	89
	Filling simulations planning	91
Chapter 6 – Results and discussion		93
6.1.	Moulding blocks	93
6.1.1.	Cavity geometries	94
6.1.2.	Steel moulding blocks	96
6.1.3.	RPT moulding blocks	97
	SLA moulding blocks	97
	SLM moulding blocks	100
6.1.4.	Moulding block assessment.....	100
6.2.	Microinjection moulding	104
6.2.1.	Polymer characterization.....	104
6.2.2.	Instrumentation.....	106

6.2.3.	Mouldability	108
	Steel moulding blocks	108
	SLA moulding blocks	111
	SLM moulding blocks	115
6.2.4.	Moulding repeatability	118
6.3.	Moulding surface replication	120
6.4.	Surface wear	123
6.5.	Structural integrity	124
6.6.	Numerical simulation	135
6.6.1.	Injection moulding simulation	135
	Moulding cycle	135
	Filling	138
	Temperature	140
	Pressure	143
6.6.2.	Heat transfer simulation	148
	Heat transfer on elements of the moulding blocks	148
	Heat transfer on nodes of the moulding blocks	149
	Conclusions	155
	Future work	161
	References	163

List of Acronyms

2PP – Two-Photon Polymerization
3DP – Three Dimensional Printing
BLM – Boundary Layer Mesh
CAD – Computer Aided Design
CCD – Charge-Coupled Device
DIN – Deutsches Institut für Normung
DLP – Digital Light Processing
DMD – Digital Micromirror Device
DMLS – Direct Metal Laser Sintering
EBM – Electron Beam Melting
ECM – Electro Chemical Machining
EDM/WEDM/ μ EDM – Electric Discharge Machining/Wire EDM/MicroEDM
EFAB – EFAB Technology, patented by Microfabrica (2005)
EN – European Norm
FEP – FluorEthylkene Polymer
HPEA – Hyperbranched PolyEster Acrylate
ISO – International Standards Organization
LBM – Laser Beam Machning
LENS – Laser Engineered Net Shape
LIGA – Litographie Galvanik Abforming
MEMS – MicroElectrico Mechanical Systems
Nd:YAG – Neodymium-doped Ytrium Aluminum Garnet
ORMOCER – ORganic MODified CERamic
PFA – PerFluorAlkoxy
POM - PolyOxyMethilene
PP – PolyPropylene
PS – PolyStyrene
PTFE – PolyTetraFluorEthylene
Ra – Average Roughness

RbPD – Roll-based Powder Deposition

Re – Reynolds number

Rmax – Maximum peak-to-valley height

RMPD – Rapid Micro Product Development

RPT – Rapid Prototyping and Tooling

Rz – Mean peak-to-valley height

SDM – Shape Deposition Manufacturing

SEM – Scanning Electron Microscopy

SL/ μ SL – StereoLithography/MicroStereoLithography

SLA – StereoLithography Apparatus

SLM – Selective Laser Melting

SLS – Selective Laser Sintering

SRE – Synchrotron Radiation Etching

STL – StereoLithography format

Tg – Glass transition temperature

TTS – Time-Temperature Superposition principle

UPSAMS – UltraPrecision Manufacturing of Self Assembled Micro Systems

μ SRD – Micro System Rapid Development

Chapter 1 – Introduction

1.1. The context of the research work

The development of smaller and more effective microsystems for medical, electronic and automotive applications is driving the industry and research institutions to the development of new manufacturing processes, suitable to produce components and systems at the microscale. In the last three decades several techniques were developed complying with the requirements of microfabrication. These developments are supported by expensive technologies, highly complex equipments or even the use of exotic materials which make microfabrication techniques less affordable. Therefore, microfabrication needs the ability of mass production to become economically feasible and popular. One of the processes that possess mass production capacity at the microscale concerning flexibility and repeatability is microinjection moulding.

During the last decades injection moulding of thermoplastics was responsible for the mass production of components and systems such as cell phones or home appliances. The shapes and size of plastics parts vary illustrating the versatility of the process. On microinjection, the same principles are applicable. Products, as small as hearing aids or micro gearwheels, are being produced for specific customer demands. However, the success of the process at the microscale is not just a question of downsizing. The injection equipment design, mould design, part design and process parameters must be also considered [1]. Furthermore, the flow at the microscale exhibits differences from the conventional [2]. The governing equations that are used for modelling the polymer flow may require additional terms to include microscale effects and to enable their use on microinjection numerical modelling [3].

The more recent challenge is to perform microinjection on moulding blocks manufactured by additive technologies. The use of this type of moulding blocks contributes decisively for the time-to-market decrease of plastic microcomponents as they can be produced faster and without tooling problems. Additive technologies are quite flexible concerning tridimensionality and multimaterial layering which opens an all new world of possibilities to micromoulding.

The additive technologies have gained relevancy on this domain since they can process materials that withstand mechanical efforts and temperature variations without significant degradation [4]. Their use at the conventional scale is limited to particular cases due to the costs involved. In fact,

the cost of a normal-sized part manufactured by an additive technology is dependent on height and construction volume [5]. However, at the micrometric domain, even if the materials are rather expensive, the height and construction volume are quite small. The cost/size ratio at the microscale can be feasible, providing that conventional micromoulding blocks and micromould design are optimized to incorporate inserts produced by additive technologies. Allied to this economic advantage, the capacity of building freeform geometries or the use of multiple materials gives microinjection extended capabilities such as the use of conformal cooling channels or localized material thermal characteristics to enhance plastic part cooling. Nevertheless, not all additive microfabrication technologies are suitable for building the micromoulding blocks, as degradation and surface finishing problems may arise. Such problems can only be assessed experimentally.

In this scenario this research work has three main goals: 1) to develop rheometry studies on microchannel flow to determine the effects of wall-slip and heat transfer; these results will be considered on subsequent studies and the resulting data considered for use with commercial software to ascertain their value on predicting actual moulding, 2) to generate data for modelling the polymer flow at microscale, these data being for use with simulation software to fill in the mathematical gap on the governing equations created by microinjection, and 3) assess the capability of additive technologies for use in precision microinjection moulding.

1.2. Description of the thesis content

The state-of-the-art of microtechnologies is made on Chapter 2. Notions such as – what a microcomponent is, what dimensions, tolerances, weight or features should be considered on the microscale – are required to understand the classification made afterwards. These notions are included on the subtopic ‘Preliminary definitions’. Regarding microfabrication processes, two techniques – material addition and material removal – have significant differences and different capacities concerning the geometries produced and the processed materials. The difference between a microfabrication and microreplication processes is pointed out in terms of the economic feasibility of microcomponents and microsystems. The ‘Microfabrication technologies’ are analysed in two subtopics concerning additive and subtractive technologies. Current microreplication technologies are grouped and their classification made according to the technologies used. Equipment features for microinjection, micromould design and manufacturing are also described.

Despite its resemblance with conventional injection, the phenomena at the microscale make this process mathematically less predictable with the current governing equations. Heat transfer, wall-slip and surface tension are effects not accounted for in current mathematical models, making numerical simulation not entirely reliable at this scale. The mathematical models used in commercial simulation tools are analysed and its discrepancies with microinjection highlighted. The Chapter 2 closes with the fully detailed objectives of this research work.

On Chapter 3 the engineering solution design for the microrheometry studies is described. A mould was designed for this purpose, comprehending the required functional systems and data acquisition system for pressure monitoring. Standard and commercial microinjection equipments were used to perform the injection trials required. The results obtained on this setup are compared with the results from traditional rheometry and from numerical simulations using Moldex 3D. The injection tests performed with the moulding blocks manufactured by subtractive techniques are summarized in the subtopic 'Microinjection moulding'. Three geometries with different aspect-ratios are tested. A fourth geometry with a through hole was used to evaluate weld-line formation. The use of moulding blocks manufactured by additive technologies is reported on the subtopic 'Additive technologies in microinjection moulding'.

The comparison between conventional and microscale rheometry is also made in Chapter 3. Mathematical models are discussed pointing out polymer flow phenomena on microfeatures such as ultrathin walls, high aspect-ratio features and capillary flow. Methods for data retrieval and treatment are also discussed considering the required comparison of experimental results and numerical modelling results. The microrheometry results are compared with conventional capillary rheometry establishing a reference on polymer flow at this scale. The microrheometry test data are compared with numerical solutions using Moldex 3D to assess the effect of the non-accounted for variables on current mathematical models.

Chapter 4 contains a full description of the mould design, concerning design options, functional systems, monitoring devices and the optimization of the mould-injection machine interface.

The experimental results obtained with the tools described in Chapter 5 and are reviewed in Chapter 6, which includes a detailed discussion of the main features studied in the selected

micromoulding parts. Microinjection results on moulding blocks obtained by subtractive technologies and additive technologies are analysed and compared to Moldex 3D results.

The conclusions of the research work highlight the contribution of the work to the academic and industrial communities.

This work, despite its contribution to microinjection research, suggests further research, especially considering the current evolution on nano-filled materials. Possible activities are suggested in the final 'Future work' section.

Chapter 2 – State of the art

Microtechnologies have been widely employed in microcomponents and microsystems for many types of applications over the last two decades. Most applications are quite complex, thus, their microsystems are developed combining subsystems for key tasks like fluid analysis, microsensing or microactuators. Today, emerging areas of application of microtechnologies include microoptics, microfluidics, microelectronics and micromechanics [6, 7].

The concept of microcomponent has been associated to high surface-to-volume ratio [7], small lateral dimensions and high aspect-ratios [8], weight of the part [9], or the detail of microstructured regions and features with micrometric dimensions [10]. The most commonly accepted definition of microcomponents or microstructures refers to objects with sub-millimetre dimensions and tolerances of few micrometers [11]. The aspect-ratio of microfeatures is a main issue on microfabrication. The capacity of a process is recognized by the aspect-ratio of the components it can produce. The aspect-ratio is given by the feature's maximum height divided by the smallest dimension of feature's base [12] as exemplified in Figure 2.1.

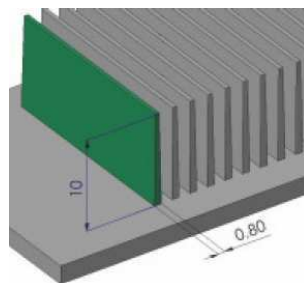


Figure 2.1. Aspect-ratio of microfeatures

2.1. Mass production *versus* short/medium-run techniques

The continuous development of microcomponents and microsystems is supported by the success of mass production techniques. Technologies such as microinjection or micro hot-embossing are commonly used for large series. However, initial developments for components or systems, no matter which scale they belong to, still rely on experimental trials in real working conditions. For

such experiments prototype parts that can represent the final parts are required, concerning material and manufacturing method. Considering the particular case of microinjection, an alternative approach can be done by using hybrid moulds [13]. This concept enables the use of alternative materials as well as the combination of manufacturing techniques. The moulding blocks for this approach can be manufactured by additive technologies, enabling time-to-market reduction for the microsystem or microcomponent. Some additive technologies such as stereolithography can process materials that guarantee dimensional precision at the micrometer domain. Other additive technologies such as selective laser melting produce fully dense metallic moulding blocks. Using current technologies, the process can produce tools for large series but for the micrometer domain, further finishing operations are required. On the other hand, stereolithography products can only withstand the mechanical efforts imposed by the injection process for a short period of time, making these materials suitable for small run series. These materials exhibit physical, mechanical and thermal properties rather different from conventional materials, introducing a new challenge, concerning the prediction of its behaviour, using numerical simulation [14]. Furthermore, these differences on properties also affect the moulded parts since the thermal behaviour of the moulding blocks has great influence on polymer flow.

2.2. Microfabrication technologies

The mouldmaking industry has already adopted subtractive methods in microinjection moulding, mainly because of their similarity to the conventional processes used. In the micrometric domain, laser technologies have been extensively used both on top-to-bottom (subtractive) and bottom-to-top (additive) processes. Both techniques need improvement for their use on micromanufacturing and this can be achieved by new developments on laser features and material characteristics [15]. Considering the methodology used, top-to-bottom processes show significant technological developments regarding accuracy and surface finishing improvements. On the other hand, bottom-

to-top processes benefit from advances on chemical technologies, enabling better process control at a similar dimension level as top-to-bottom technologies. The developments verified on both approaches enable their integration into new manufacturing methods [6].

The microfabrication processes, concerning the direct application of their products as a mass production tool can be classified as hard and soft tooling processes. All manufacturing processes described here are suitable for microfabrication, however, some cannot produce parts capable of supporting the mechanical efforts required by a replication process like microinjection on a long run series (Figure 2.2).

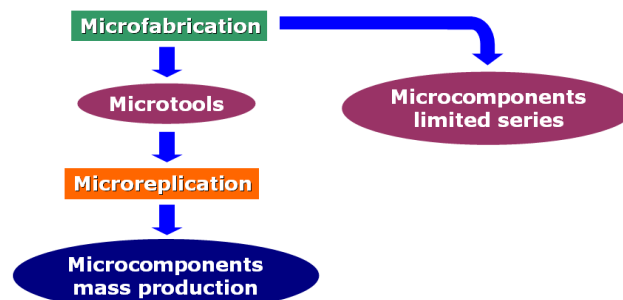


Figure 2.2. Microtechnologies: hard tooling *versus* soft tooling

Additive manufacturing processes, that build the part bottom-to-top, usually have no problems in generating undercuts and other details like holes or cavities beneath the part surface, impossible to obtain on a top-to-bottom strategy; geometry is in fact free for such processes [16]. The capacity of working with metal and ceramics as well as photopolymerising polymers gave these processes the possibility of entering both the rapid tooling domain and the rapid manufacturing world where their products, can also be used mould tooling, and end-use functional parts, besides prototyping [17].

On the other hand, subtractive manufacturing processes still possess relevant features despite the fact that these processes consist on a top-to-bottom strategy for generating geometry [6]. Features such as achievable aspect-ratio and surface finishing still provide to this type of processes significant advantages concerning some domains of application [18, 19].

2.3. Additive microfabrication technologies

The additive manufacturing technologies rely basically on the phase transformation of a specific material to form a tridimensional object [15]. Whether it is a photo polymeric liquid or a micro-sized powder, additive techniques comprehend energy sources that can supply a light beam for a curing process or a heat source for a sintering process [20].

2.3.1. Photocuring-based processes

The photocuring processes are based on the polymerization of a photosensitive medium such as liquid monomer by the absorption of a given amount of photons per volume unit of medium. The absorbed light generates reactive species that induce crosslinking of monomer chains. The three dimensional object is generated layer wise [21].

The microstereolithography process was first developed at the Department of Microsystem Engineering of the Nagoya University in 1992. The process is under continuous development; layer thickness has been lowered to 200 nm by processing the resin below a glass slide to prevent resin agitation. Laser spot size has also been reduced, shorter focal length and higher pulse frequency, increasing process microfabrication capacities [20]. An important development such as the integral exposure for each layer instead of laser beam scanning across the resin surface is shown in Figure 2.3 [22].

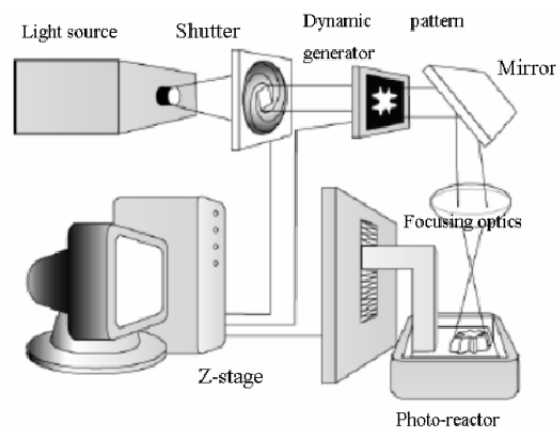


Figure 2.3. Integral exposure of a single layer (Bertsch *et al.* 2003)

The MicroTec Corporation (Germany) patented the Rapid Micro Product Development (RMPD). RMPD process is based on microstereolithography; however, the laser beam is split by optical means into several beams, enabling several parts to be created at the same time, greatly increasing productivity. The process shows high precision and layer thickness is as small as $1\mu\text{m}$. By splitting the laser beam, RMPD process can produce up to 150 000 parts per machine and hour [15].

The μSRD process was developed at the Lazer Zentrum Hannover (Germany). The process is an evolution of stereolithography but includes special key features that make this process suitable for microfabrication. Working area is limited to $40\times 40\text{ mm}$ and its movements are precisely controlled by piezoelectric actuators. Vertical steps below $10\mu\text{m}$ enable good lateral surface finishing and the fabrication of high aspect-ratio microcomponents [23].

Envisiontec GmbH (Germany) commercializes the Perfactory equipment using the DLP[®] technology based on the DMD (Digital Micromirror Device) chip developed by Texas Instruments (Figure 2.4). The insertion of this technology does not change the manufacturing process but it can speed it up by accelerating the most time consuming phase – the mask generation [24]. The CAD model is initially converted to STL format and the DLP[®] technology can now output the generated pattern to cure each resin layer [25].

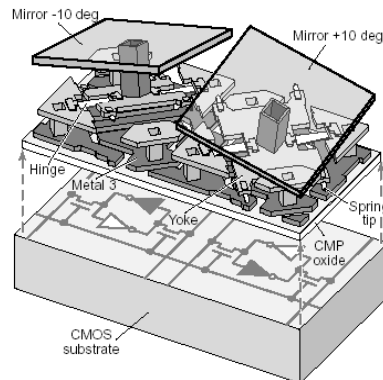


Figure 2.4. DMD chip developed by Texas Instruments (Hornbeck 1998)

The Two-Photon Polymerization (2PP) process was developed at the Lazer Zentrum Hannover (Germany). This process, unlike the previous ones which are based on layer-by-layer processing, allows the generation of fully freeform geometry. The use of hybrid polymers like ORMOCER[®] - ORganic MOdified CERamic [26] or HPEA - Hyperbranched PolyEster Acrylate [27] enables the laser beam to emit two photons to a tightly focused voxel of resin, allowing localized cure due to

the quadratic dependence of the two-photon absorption rate on the laser intensity. Both materials show important features for this process, high optical transparency, excellent thermal and mechanical properties and high chemical resistance due to the absence of porosities [28].

In this research work high precision stereolithography was used for the production of moulding blocks for microinjection and the process will be detailed later on Chapter 5.

2.3.2. Metal sintering/fusing-based processes

Selective Laser Sintering (SLS) has been used since the late 80s in several applications on the rapid prototyping and rapid manufacturing domains, due to its ability to produce both prototypes and fully functional components, in polymer or metal. Object consolidation is achieved by scanning the processing areas with a focused laser beam over the powder layer wise, supplying the thermal energy required for binding the powder particles [29].

Selective Laser Sintering suffered significant developments, especially concerning to the binding mechanisms used to consolidate the powder. One of the most recent advances is Selective Laser Melting (SLM). Both processes are layer-wise material addition techniques, but, different binding mechanisms are responsible for building the object. The SLS process exhibits molten and non-molten material areas after fusing the powder mixture and therefore, its consolidating method is Partial Melting. On the other hand, the SLM process exhibits near full density, since the laser beam completely melts the powder – Full Melting [30].

The SLM process is currently available in industrial equipments from several companies which use proprietary materials and their own specifications for the process. EOS GmbH (Germany) uses Direct Metal Laser-Sintering (DMLS) on its EOSINT M 270 model. Concept-Laser GmbH (Germany) developed the LaserCUSING process in 2000 and incorporates it used on their equipments [31]. MTT Technologies (United Kingdom) also use SLM on their Realizer II and SLM100 models [32]. The scheme for the SLM process is shown in Figure 2.5.

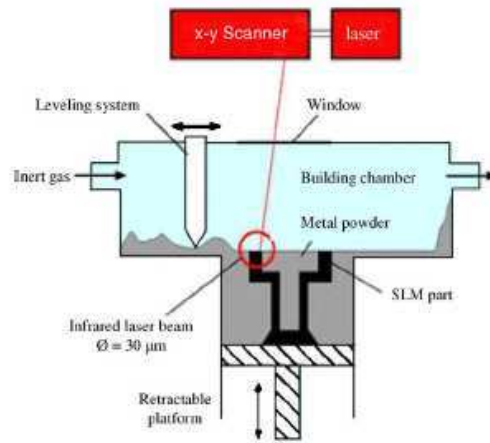


Figure 2.5. Scheme of Selective Laser Melting technology (Santos *et al.* 2006)

The MicroSINTERING[®] process was developed at the Laserinstitut Mittelsachsen and patented in 2003 [20]. The continuous development verified both on laser characteristics and material grain size enabled a performance increase on the process. Currently, it is possible to have material grain sizes in the 5 µm range. Solid state lasers have also evolved, from spot sizes of few hundreds of micrometers to a few tens of micrometers, enabling higher resolution on part building [16]. The process takes place inside a working chamber with controlled temperature, pressure and atmosphere environment. Similarly to conventional SLS process, undercuts are supported by unprocessed powder, therefore, enabling a clean part at the end of processing.

The LENS process produces structures using a Nd:YAG laser beam to form a molten pool of material on a substrate. Powder particles are blown into this molten pool and fused to add new material. The process occurs on a controlled atmosphere work chamber, where the part is built on a 3D positioning system under powder delivery units [33]. Laser scanning over the substrate or previously deposited material enable the addition of a new layer of material by repeating this sequence [34]. The LENS process was developed by Sandia National Laboratories (United States) and implemented by several North-american companies, such as Optomec, MTS Systems and AeroMet [35]. In Figure 2.6 it is shown the path of a single powder particle. The particle is directed to the beam axis at the beam's waist.

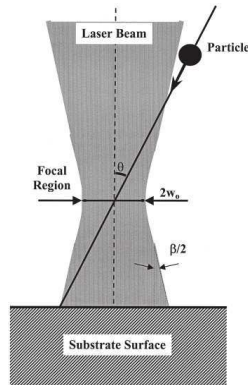


Figure 2.6. Powder interaction with laser beam (Grujicic *et al.* 2001)

The Micro Spark Coating process was co-developed by the Japanese companies Ishikawajima-Harima Heavy Industries Co. and Mitsubishi Electric. This technology is meant for surface coating and cladding by small electric discharge pulses. The tool is an electrode made of semi-sintered powder. The microelectric discharge pulses generated between the electrode and the work piece surface, submerged in dielectric fluid, melts the electrode and part of the work piece surface. The melted powder moves toward the work piece surface (Figure 2.7). Repeated discharges form strong bonds between the coated layer and the surface [15, 36].

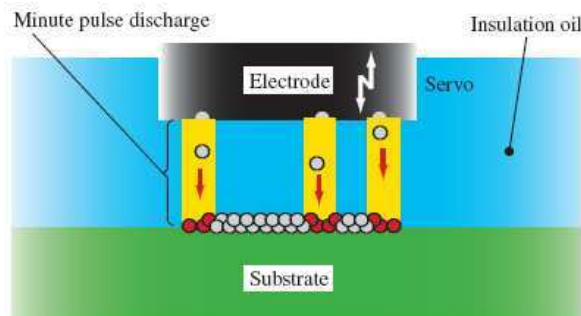


Figure 2.7. MSCoating process schematics (Ochiai *et al.* 2006)

The Electron Beam Melting[®] (EBM) is a process patented by Arcam AB (Sweden). The process is based on FIB technology, on its deposition capacity. The material, typically titanium, on powder form is melted by the electron beam and deposited over the substrate. After melting and solidifying one layer of titanium powder, the process is repeated for the subsequent layers. The parts are built in a vacuum chamber which provides a clean environment, resulting in good material characteristics, quite suitable for processing reactive metal alloys like titanium. The

vacuum also provides a good thermal environment, giving good thermal stability during the build. Final machining can be done with any conventional method [37].

In this research work SLM was used for the production of moulding blocks for microinjection and the process will be detailed later on Chapter 5.

2.3.3. Additive processes classification

The additive processes that were described here are classified next on Table 2.1 according to their products capacity of being used as replication tools.

Process	Classification	Process features
Microstereolithography (μ SL)	Indirect	Suitable for microfabrication, microreplication possible for small runs
Rapid Micro Product Development (RMPD)	Indirect	Suitable for microfabrication
Two-Photon Polymerisation (2PP)	Indirect	Suitable for microfabrication
MicroSystem Rapid Development (μ SRD)	Indirect	Suitable for microfabrication
Three-D Printing (3DP)	Indirect	Suitable for microfabrication
Digital Light Processing (DLP)	Indirect	Suitable for microfabrication
MicroSINTERING	Direct	Suitable for microfabrication / microreplication
LaserCUSING	Direct	Good potential for microfabrication / microreplication
Roll-based Powder Deposition (RbPD)	Direct	Suitable for microfabrication / microreplication
Laser Engineered Net Shape (LENSTM)	Direct	Good potential for microfabrication / microreplication
Micro Spark Coating (MSC)	Direct	Good potential for microfabrication / microreplication
Electron Beam Machining (EBM)	Direct	Good potential for microfabrication / microreplication

2.4. Subtractive microfabrication technologies

The production of microcomponents and microsystems was initially focused on technologies traditionally used in the world of electronics and semiconductor industries, like etching, lithography and other fabrication techniques [18]. However, an increasing trend towards product miniaturization has arisen along with the rapid development of microengineering technologies based on conventional manufacturing processes such as milling, turning or EDM [38]. The subtractive manufacturing technologies rely on different mechanisms for material removal which make them suitable for specific applications.

2.4.1. Chemical etching

The lithographical processes were the first to show potential for microfabrication. The original LIGA process was developed nearly 20 years ago by the Research Center FZK at Karlsruhe [39]. The acronym LIGA stands for the German designations for all process phases, *L*itographie *G*alvanoformung *A*bformung. The process consists on: a) radiation exposure of material through a mask, d) developing the irradiated material and electrodeposition of metallic material and c) use of the obtained metallic component as an insert for a microreplication process (Figure 2.8).

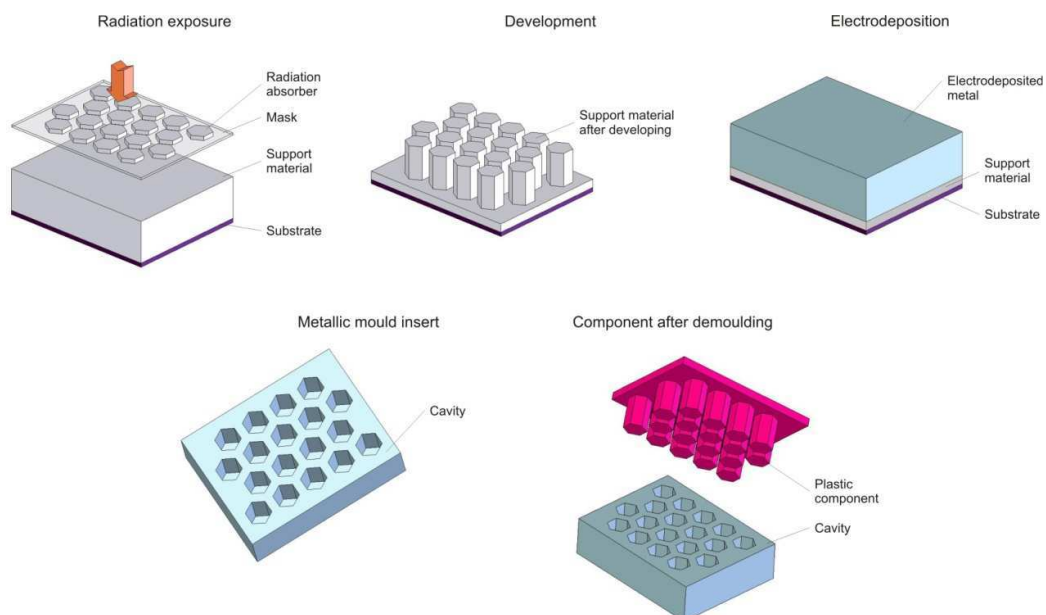


Figure 2.8. LIGA process phases

The original LIGA process uses X-ray radiation from a synchrotron. However, the cost of using this equipment makes this process expensive despite its known capacities. Several researchers have looked for others sources of radiation and they succeeded in creating new variants for the LIGA process. Ultra-violet light [40], ion beam [41] and laser beam [42] have been explored as alternative radiation sources.

The Synchrotron Radiation Etching (SRE) process was developed to overcome processing difficulties on specific materials like polytetrafluorethylene (PTFE), perfluoralkoxy (PFA) or fluorethylene polymer (FEP) that are transparent within the ultraviolet and infrared wavelength, causing difficulties on laser ablation processing [43]. Unlike LIGA, SRE is a maskless process. The etching procedure is carried out inside a heated vacuum chamber. The SRE process uses low intensity X-rays, quite lower than those used on LIGA X-ray processing. Being a maskless process, it enables tilted angle operations to obtain slanted or curved side walls [44].

The ElectroChemical Machining (ECM) shows several advantages, such as the absence of wear on tools, good surface finishing of the processed products. Furthermore, the process possesses the ability to machine complex shapes on electrically conductive materials regardless of their physical properties. ECM is based on an anodic electrochemical dissolution using potential difference and uses ultra short voltage pulses, which guarantee precise micro-machining. For the microECM process, parameters such as machining voltage, electrolyte concentration, pulse on time and frequency of the pulsed power supply have direct influence on the material removal rate and the accuracy at the microscale [45].

2.4.2. Breaking of molecular chains

Ion beam has been extensively used since the early 80s but the first commercial equipments using this technology appeared almost a decade after that. The system consists of an ion column to generate and guide the ion beam, a work chamber, a vacuum system and/or gas injection system. The process consists on the emission of Ga^+ ions, generated on the ion column. The beam is obtained through the application of a high intensity magnetic field on an ion source, causing the emission of positively charged ions in the sample. The process takes place inside a working chamber under vacuum, typically 10^{-6} Pa, the same pressure value used for the ion column. Working tables for sample processing may have up to 5-motion axes, allowing several degrees of freedom and enabling 3D micromachining [46].

Laser ablation is a technique widely used on fields such as microfabrication of medical surgery appliances, mass spectrometry and film synthesis. The process may involve both photothermal and photochemical processes, depending on the type of the processed polymers. The photothermal process involves the absorption of photons, followed by the release of the photons into the polymer matrix through vibrational cooling. This induces a rapid temperature rise in the bulk material leading to the thermal decomposition of the polymer. If the vibrational energy attains a particular fluence threshold, then bonds in the polymer will break. On the other hand, the photochemical process involves the breaking of chemical bonds due to interaction with nanosecond or picosecond highpower ultraviolet (UV) pulses yielding gaseous photoproducts. During this process, thermal and mechanical damage to the surrounding polymer is minimized, therefore achieving more precise control over the ablated region [47].

2.4.3. Sublimation

The use of laser-assisted metal machining by metal sublimation has been around since 1995 [48]. However, the first commercial equipments fully prepared for the process appeared only a few years later. The laser milling process is based on metal sublimation, the material absorbs the heat provided by the laser beam, a melt pool is formed rapidly and due to the intense heat, metal is vaporized causing shock waves to expel out molten metal in the form of re-solidified particles. The types of lasers used for this type of processing equipment are Nd:YAG or excimer lasers due to material's energy absorption, typically up to 80%. Commercial equipments are currently using Nd:YAG lasers due to their reliability, operating at 1064 nm, in pulse or continuous modes. Laser milling has proven its capacities in the mould making industry enabling high savings on processing time for small volume EDM operations, nevertheless, the maximum aspect-ratio this process can obtain is of 10:1 [49].

2.4.4. Cutting

Micromilling and microturning are evolutions to the microscale from their conventional size processes. However, tools and equipments for these processes are not just miniaturized versions, they must comply with the precision and repeatability required at this level. As in conventional size processes, also micromilling and microturning work with cutting tools. This means that tools

are extremely small and fragile. For micromilling process, endmill's diameter can be smaller than a human hair, down to 20 μm [50]. Tool miniaturization, however, brought some benefits. Errors caused by thermal expansion or workpiece deformation are minimized since cutting forces are much smaller. Several field experiments on microturning have achieved excellent surface finishing along with high performance on contouring, grooving and threading operations [51].

Concerning Wire/Electric Discharge Machining (W/EDM), the principle of operation for these microfabrication processes is quite similar to their conventional size versions. Material is eroded through localized electrical discharges. The conductivity of the dielectric fluid is controlled by the distance between material and tool. When the tool approaches the material, the dielectric fluid becomes conductive enabling electrical discharges on the material. The released thermal energy is used to melt and vaporize the material. The tool size is dramatically reduced but the main issue is still the equipment. With conventional mechanisms and actuators it is extremely difficult to control small movements within the sub-micron range due to contact friction. Companies like GF Agie Charmilles (Switzerland) are exploring alternative solutions taking advantage of controlled material deformation and high precision linear motors [52].

Operating parameters for microEDM/WEDM are also very specific. On microEDM, gap size may cause troubles on particle evacuation if smaller than 3 μm . Conditions like these also cause difficulties on dielectric fluid circulation. For microWEDM, commercial equipments are already available on the market. Wire diameters of 25 μm and precise motion control enable positioning precision of $\pm 1,5 \mu\text{m}$ [53]. Some studies have been conducted in order to increase microEDM efficiency using ultrasounds. Applying this type of vibration to the electrode, the flow of dielectric fluid is increased and consequently, surface finishing is clearly better [54].

This research work used micromilling, microEDM and LBM as subtractive processes, mainly related to the mouldmaking industry. Such option is due to the expectable relevance of the use of such processes, many of them are already available, in the production of microcomponents through replication processes that require suitable tools. The processes used for the production of moulding blocks for microinjection will be detailed later on Chapter 5.

2.4.5. Subtractive processes classification

Subtractive processes are described here and classified on Table 2.3 according to the capacity of their products to be used as replication tools.

Process	Classification	Process features
LIGA processes (X-ray, UV, IB and Laser)	Direct	Suitable for microfabrication / microreplication
Synchrotron Radiation Etching (SRE)	Indirect	Suitable for microfabrication
Focused Ion Beam (FIB)	Direct	Suitable for microfabrication / microreplication
Laser Milling	Direct	Suitable for microfabrication / microreplication
Micromilling / turning	Direct	Suitable for microfabrication / microreplication
MicroEDM / WEDM	Direct	Suitable for microfabrication / microreplication

2.5. Hybrid microfabrication technologies

The so called hybrid processes rely on the combination of electrodeposition or welding techniques and machining or other surface regularisation techniques, respectively for the additive and the subtractive components of the process. Therefore, such manufacturing approach can use both structural and sacrificial material enabling the production of self-assembled microsystems. Furthermore, the additive component of the process may comprehend several materials that can be used to optimize the performance of the microcomponent or the microsystem produced [15].

The EFAB process was presented in 1999 and it is actually owned by Microfabrica (USA) The process itself is based on the chemical electro deposition of both structural and sacrificial material on a layer-by-layer fashion, using a proprietary technique known as Instant Masking to define how material is to be deposited, allowing a quick, repetitive and precise deposition of a theoretically unlimited number of layers [55].

Lumex 25C is the commercial name of the hybrid equipment developed by Matsuura Machinery (Japan). It combines freeform manufacturing by a CO₂ laser sintering and high speed milling. The integration of these two technologies eliminates finishing operations [15].

The UPSAMS process was developed at the Department of Manufacturing Engineering and Fraunhofer USA Center for Manufacturing Innovation. The process uses diamond tools to

machine structures with a sub-micrometer resolution and a surface quality in the nanometer range. UPSAMS combines the capacities of material removal processes with the electrodeposition of nickel, aluminium, copper or brass to produce full 3D geometries maintaining tolerances in the nanometer range as well [56].

The Rapid Prototyping Laboratory (RPL) at Stanford University developed the SDM process. SDM builds up a part from material layers; the additive process is accomplished with plasma or laser welding, casting, or UV curing. In the addition phase, the process can add structural material but also sacrificial material to support the component to be generated. The subtractive component of the SDM process is accomplished by grinding, turning, or milling material using CNC machining. In addition, different materials can be deposited during the building cycles to produce multi-material objects with spatially varying material properties [15].

The hybrid microfabrication technologies described here are classified according to their products' capacity to be used as replication tools. However, their combination of both subtractive and additive capacities makes them unique considering the geometries they can produce. Table 2.4 summarizes the hybrid processes described above and its classification.

Table 2.4. Hybrid processes

Process	Classification	Process features
Electrochemical Fabrication (EFAB)	Indirect	Suitable for microfabrication
Lumex	Direct	Good potential for microfabrication and microreplication
UltraPrecision Manufacturing of Self Assembled Micro Systems (UPSAMS)	Direct	Suitable for microfabrication and microreplication
Shape Deposition Manufacturing (SDM)	Direct	Suitable for microfabrication and microreplication

2.6. Microreplication technologies

The market success of microsystems depends on the cost-effective production of microstructures in large scale [8]. This sentence reveals the importance of replication processes on the massification of microtechnology. Manufacturing costs for microtools may still be relevant on the component final cost but after the tool is created, it will be able to produce thousands of microcomponents with no significant cost increase. The costs for raw material are even reduced due to the small amount of material used. Therefore, considering polymers as raw material and the wide range of applications they possess, it is possible to obtain plastic microcomponents for almost every purpose [57].

Two replication processes have succeeded at the microproduct market and commercial equipments are available: microinjection and micro hot-embossing. These techniques may compete on the same market segment depending on the part geometry but, in fact they are complementary processes [58].

Besides microinjection and micro hot-embossing, there are other relevant microreplication processes such as reaction injection moulding, injection compression moulding and thermoforming. However the significant developments on microinjection and micro hot-embossing contributed to the higher popularity of these replication techniques [57].

2.6.1. Injection moulding processes

Injection moulding of polymers is the more widespread technology for large scale fabrication of high precision parts. Microinjection moulding as a downsizing of the existing technology has been successfully applied in large scale series of microparts [8]. The first developments of the microinjection process started in the middle of the 90 decade, aiming at the production of parts weighing around 25 mg and reducing the material residence time in the injection cylinder [59].

Currently, microinjection is specifically designed for the mass production of components weighing less than 1 mg, dimensions smaller than 1mm and the capacity of reproducing details in the nanometer dimension scale. The technology is still under development, the material flow behaviour and the temperature dependence attracting research and experimental work [9].

2.6.2. Embossing-based processes

The hot embossing method was first developed by the Forschungszentrum Karlsruhe (Germany). Besides microinjection, this is one of the established replication processes used for plastic microcomponents and microstructures. Process capacities enable its products to have delicate microstructures with high aspect ratio and low residual stresses [60]. Hot embossing is also a highly productive method for replicating microfeatures onto plastic substrates. The process is very flexible, both stamping tools and plastic type can be easily changed resulting in short setup times [58]. This technique is widely applied on microstructure fabrication for MEMS, optical sensors or bio-chip applications [60, 61].

The hot embossing process consists of three main steps (Figure 2.44): 1) a heated thermoplastic film is inserted into the stamping tools, 2) the microstructured stamping tool is pressed against the film with a pre-determined force inside an evacuated chamber and 3) the setup is cooled and the stamping tool releases the microstructured component [58]. The process takes place inside a vacuum chamber to ensure complete filling of the microstructured part; typically a value of 10^{-1} hPa is used. The plastic film must be heated up to its softening temperature before the stamping tool force is applied. This force must be kept during cooling phase to avoid undesired shrinkage or sink marks on the part [62].

2.7. Microinjection moulding

The microinjection process can be considered as similar to conventional injection moulding except for the equipments used and processing parameters adopted. The microinjection equipments typically have an initial plasticising chamber where the material is heated, mixed and melted. Then, by means of a plasticising screw or a injection piston, the melt is injected into the dosing chamber or directly to the microimpression. The melt volume is metered with precision and then, an injection piston or an injection screw injects it into the closed mould. Each manufacturer has its own approach to what might be considered as the best solution for metering and process control. A detailed overview on commercially available microinjection equipments is included next.

In the last decade several equipments dedicated to microinjection from traditional injection machine manufacturers have arisen. However, the particular specifications required for this replication process have delayed the commercialization of some of these products

The commercial equipment with the most highly recognized capacity for microinjection is the Battenfeld Microsystem 50 (Germany). This equipment contains a unique set of solutions for injection moulding, handling and quality control of the microparts. The most important feature is its minimal and precise dosage capacity. Another important feature is the nozzle design. The mould for this equipment must be designed according to it. By making the machine nozzle reach the mould parting plane, the sprue can be reduced, therefore, increasing material efficiency (Figure 2.9).

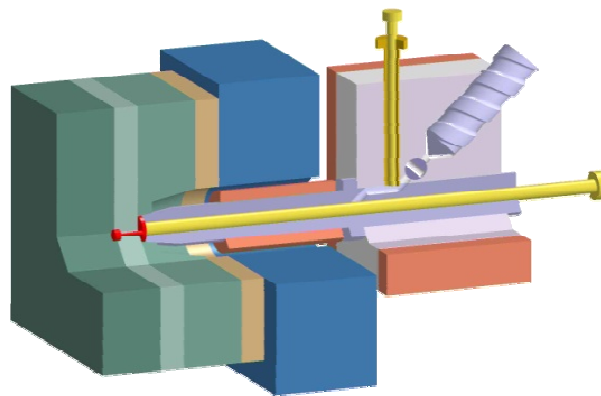


Figure 2.9. Battenfeld Microsystem 50 injection unit

The Sumitomo Plastics Machinery (Japan) has recently released its new SE7M injection machine incorporating the SK-II system to eliminate back flow during screw pull back. Specially developed for microinjection, this equipment improves shot density control by pre-setting a pressure and forward screw speed, automatically compensating for any changes in polymer properties, achieving high precision levels on injection fill (shot weight and density) and peak pressure stability. During plasticizing, the screw rotation allows the check ring and seal to align so the channel is open for melt flow (Figure 2.10 – SK open). On completion of recovery, the screw counter-rotates to block the flow channel and the channel remains blocked during screw pullback and fill (Figure 2.10 – SK close).

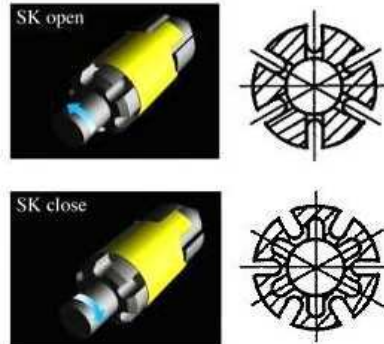


Figure 2.10. Sumitomo's SK-II system

Boy (Germany) has launched the 12 A model on the market in 2004, specially dedicated to microinjection. This equipment is fully hydraulic and is designed for very small moulds and enables high metering precision from 0,0001 to 0,01 mm³. The injection unit supports three plasticising units of 12, 14 and 18 mm of diameter (Figure 2.57). In 2009, the company launched a new and more compact solution, the XS model. Equipment features are not that different from the Boy 12 A since it can operate also with two plasticising units of 12, 14 mm of diameter for thermoplastics and a 16 mm plasticising unit for elastomers.

The former MCP Group, now called MTT Technologies Group (United Kingdom) has presented in 2007 their 12/90 HSP and VSP models, specially developed for microinjection. The equipment is fully electrical which enables high precision and quick movements. It uses a plasticising screw of 16 mm and combines it with a dosing plunger for metering precision (Figure 2.11). A recent development from DESMAtec (Germany) resulted on newly introduced microinjection equipment, the formicaPLAST 1K model. This equipment enables high precision on material dosage due to its two-phase injection units, much alike Battenfeld Microsystem 50. The injection unit consists of two pistons, a Ø6 mm plasticizing piston and a Ø3 mm injection piston, allowing injection pressure up to 300 MPa (Figure 2.12). Besides this model, this manufacturer offers the formicaPLAST 2K, a bimaterial microinjection unit equipped with two similar injection units side-by-side.

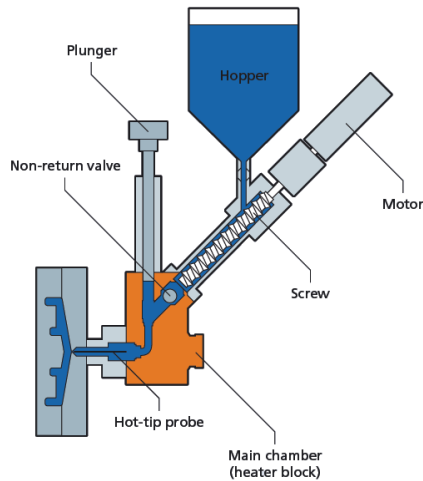


Figure 2.11. MCP 12/90 HSP injection unit detail

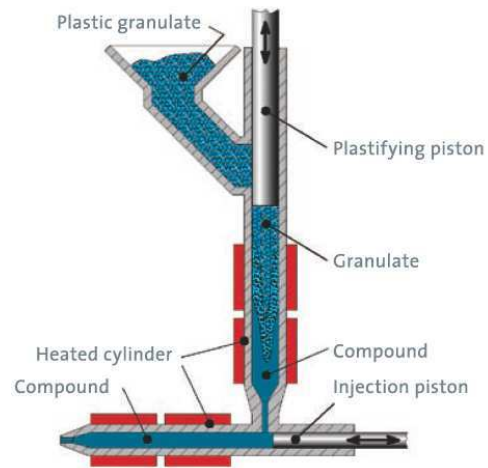


Figure 2.12. DESMAtec formicaPLAST injection unit

The microinjection equipment selected for this research work was the Boy 12A due to its metering precision and availability. Furthermore, the equipment has features suitable for successful microinjection monitoring such as injection speed and pressure [63].

2.8. Flow phenomena at the microscale

Current rheological data used on CAE analysis for flow simulation on microchannels depends on data obtained on macroscale experiments. Actually, there is enough evidence to support the fact that polymeric flows differs significantly from macroscale to microscale channels [64, 65]. As the size of the microchannel decreases, polymer viscosity also decreases due to the wall slip effect. The wall slip effect occurs when the shear stress in the material exceeds a critical value [64] pushed by high injection speed and pressure, causing material to slip on channel walls (Figure 2.13).

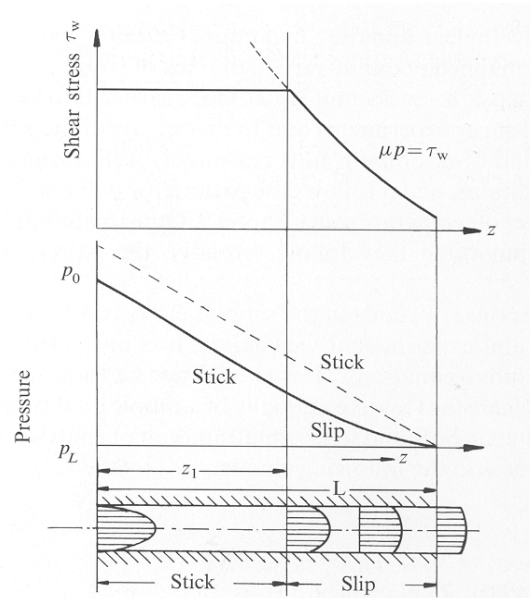


Figure 2.13. Wall slip effect [66]

The evaluation of wall stress in conventional sized channels and microchannels, showed that wall stress increases rapidly with channel size decrease. This also causes average speed to increase as well as the material flow length. The wall slip effect on heat transfer is still under investigation. Heat transfer has a significant influence on the material flow length calculation. To determine this effect, Yu *et al.* introduced code changes on commercial software to help predict the material flow length considering the wall slip and its influence on other variables [67]. These studies reveal that flow in microchannels possesses characteristics not considered on conventional scaled channels flow. Commercial software needs suitable code to predict these effects and thus, perform a realistic simulation for the microinjection process [65].

Other related effects such as polymer surface tension were already successfully modelled and tested [68]. Interfacial effects such as wettability, adhesion and friction between polymer melt and the mould cavity surface are relevant. If the polymer exhibits a good wettability, the attainment of higher aspect-ratios are feasible and an excellent replication of microdetails is expected [69].

Flow length is also an important issue on microinjection. The evaluation of flow length on microchannels is made with the following assumptions: a) injection time is short enough to assume that there's no heat loss in the cavity during injection procedure, b) melt pressure is dependent on the volume filled and c) the melt flow rate is constant. These considerations were established to determine the ability to fill a cylindrical microfeature. The flow length is strongly

dependent on heat transfer phenomena, also related to the thermal behaviour of the mould material [3].

2.8.1. Conventional mathematical models for cavity filling

The equations for modelling the cavity filling are obtained from general equations for common fluids, therefore, several assumptions have to be done to make computing time more reasonable. The conventional injection moulding process modelling lies on transient rheology and heat transfer which already makes this domain rather complex [66, 70]. The fluid flow on injection simulation is modelled considering the constitutive equations for momentum, mass and heat transfer as following [71].

The use of standard commercial software tools to simulate the microinjection process has revealed significant differences between numerical analysis results and real experiments. Typically, default analysis would predict short-shots unless high injection speed and pressure were imposed to the process. This causes the material viscosity to be reduced through shear rate increase. This can also be seen through the use of different flow models used on numerical analysis. Flow models like Hele-Shaw, Stokes and Navier-Stokes have been used, studied and evaluated their suitability for microinjection simulation [65, 72].

Polymer flow behaviour on microchannels causes viscosity to be much higher near the channel walls, 50 to 80% higher than bulk viscosity. For that reason, classical Navier-Stokes equation cannot fully explain polymer flow on these circumstances unless it incorporates molecular orientation effects [65].

The Hele-Shaw flow model provides simplified governing equations for non-isothermal, non-Newtonian and inelastic flows on thin cavities and it is the most common approach to microinjection simulation. However, software simplifications on flow velocity, pressure and temperature can cause errors on predicting the flow, using the Hele-Shaw model [73].

Extensive flow model testing on commercial software tools were performed and compared to field experiments and flow model analysis was carried out [72]. The results are depicted on Figure 2.14.

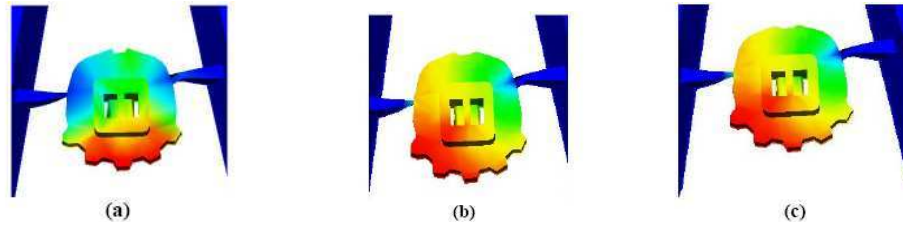


Figure 2.14. Fill simulations using Hele-Shaw (a), Stokes (b) and Navier-Stokes (c) flow models [72]

Figure 2.14 shows differences in temperature distribution for each flow model used. The gates are of equal size but not symmetric, thus, a symmetric temperature like the Hele-Shaw model predicted is not realistic (a). Stokes (b) and Navier-Stokes (c) models were comparable to the parts obtained on microinjection trials, reflecting same weld-line location as in numerical analysis [72].

2.9. Detailed objectives

The development of moulds for microinjection moulding brings about specific aspects that are related to the dimensional scale of the tools used with the process. These aspects include flow behaviour, evaluation of roughness at the microscale, cooling and structure build up or the ejection of the microparts. The current know how on injection mould design needs to accommodate not only the rheological and thermo-mechanical aspects of the microinjection process, but also the capabilities and limitations of new techniques used for manufacturing the micromoulding blocks. Once these aspects are fully understood and integrated, guidelines for development of moulds for microinjection moulding may be envisaged for this new market niche.

For that purpose, rheometry studies on microchannel flow were carried out to determine the effects of wall-slip and heat transfer in microinjection moulding. The results of these preliminary studies will be considered on the subsequent studies and the resulting data considered for use with commercial software to ascertain its value on simulation of the experimental performance. Another challenge is to perform microinjection on moulding blocks manufactured by additive technologies. The use of this type of moulding blocks may contribute to the time-to-market decrease of plastic microcomponents.

The detailed objectives of this research work can then be organized into the following topics:

- i) Assessment of the injection moulding flow at the microscale,
 - Evaluation of flow phenomena at the microscale,

- Effects of processing conditions on flow behaviour;
 - Rheological characterisation of the moulding materials at the processing conditions likely to occur during microinjection moulding,
- ii) Design and manufacturing of the research micromould,
- Design of a flexible mould to be used on a microinjection machine, able to accommodate different sets of moulding blocks,
 - Design of the instrumentation and temperature control setup
 - Manufacturing of the mould structure,
 - Micromanufacturing of the moulding blocks by additive technologies;
- iii) Assessment of additive processes and moulding geometries,
- Assessment of the additive processes for the production of specific geometries,
 - Definition of impression geometries for assessment of the flowability in the mould and the product performance (shrinkage, roughness, weldline strength),
- iv) Rheological characterisation, flow and heat transfer simulation,
- Filling and cooling simulations of the mouldings,
 - Assessment of the flow simulations referring to experimental results;
 - Assessment of the heat transfer on moulding blocks;
- v) Structural integrity of the moulding blocks,
- Microinjection tests using the moulding blocks obtained by subtractive processes,
 - Microinjection tests using the moulding blocks obtained by additive processes,
- vi) Microproduct assessment,
- Metrologic analysis of the mouldings in terms of shrinkage and roughness,
 - Microscopic analysis for replication details evaluation,

Chapter 3 – Flow in microinjection moulding

The content of this chapter is an expanded version of the research paper already published in the Journal of Micromechanics and Microengineering (VASCO, J. C.; MAIA, J. M.; POUZADA, A. S., Thermo-rheological behaviour of polymer melts in microinjection moulding, *J. Micromech Microeng.*, Vol. 19, 10 (2009). A copy of this paper is attached in Annex A3.

This part of the research work aimed at the understanding of the polymer filling behaviour in channels at the microscale, establishing how it differs from the flow in conventional geometries and contributing with flow data that could improve the performance of simulation tools currently available. These softwares do not account for flow effects such as wall slip, surface tension and heat transfer phenomena.

Considering the flow conditions and the dimension range in this research work, capillary rheometry was selected to study the flow behaviour of the melt. The resulting data will be compared with the flow curves obtained from the microchannels, enabling the application of the time-temperature superposition principle (TTS) to determine the real temperature within the microchannel.

3.1. Flow models

3.1.1. Capillary and slit flow models

The polymer flow in microchannels is considered similar to that in capillary rheometry [64, 74-76]. The test data in capillary rheometry are based on the relationships between the pressure drop along the capillary channel and the imposed flow rate [77]. The following assumptions are made:

- the Reynolds number (Re) is smaller than 2000, thus, laminar flow occurs;
- steady state: $\frac{\partial}{\partial t} = 0$;
- fully developed unidirectional flow: $V_r = V_\theta = 0$ and $V_z = V_z(r)$;

- no slip at the capillary walls: $V_z(r = R) = 0$ and $\frac{dV_z}{dr} = \frac{dV_z}{dr}(\sigma_{rz})$;

Considering the microchannel geometry used in this study, the mathematical models used to describe polymer flow are the same as for capillary rheometry (Equation 3.1) and slit flow.

$$\dot{\gamma}_{w(\text{app})} = \frac{4Q}{\pi \cdot R^3} \quad (3.1)$$

After the Rabinowitsch correction for the shear rate at the wall, the following equation for non-Newtonian fluid shear rate results [78]

$$\dot{\gamma}_{w(\text{real})} = \frac{4Q}{\pi \cdot R^3} \left(\frac{3}{4} + \frac{1}{4}n \right) \quad (3.2)$$

where Q - volumetric flow rate,

R - radius of the capillary channel, and

n - slope obtained by the bi-logarithmic correlation between $\log \dot{\gamma}_{w(\text{app})}$ and $\log \tau_w$.

In order to eliminate the viscous and elastic effects at the capillary entrance the application of the Bagley correction to the apparent shear stress, τ_w

$$\tau_{w(\text{app})} = \frac{\Delta P}{2L} R \quad (3.3)$$

leads to the following expression for the shear stress at wall [78]

$$\tau_{w(\text{real})} = \frac{\Delta P}{2 \left(\frac{L}{R} + e \right)} = \frac{\Delta P - P_0}{2L} R \quad (3.4)$$

where ΔP - pressure drop along the capillary,

L and R - length and radius of the capillary,

e - Bagley correction factor, and

P_0 - pressure drop for a capillary with zero length for a given rate of shear.

The model for the flow in a slit also derives from the equations used on the capillary viscometer in a similar way to the previous flow models. The apparent shear rate in a slit is given by

$$\dot{\gamma}_{w(\text{app})} = \frac{6Q}{w \cdot h^2} \quad (3.5)$$

After applying the Walter correction for non-Newtonian fluids [78], it becomes

$$\dot{\gamma}_{w(\text{real})} = \frac{6Q}{w \cdot h^2} \left(\frac{2}{3} + \frac{1}{3}n \right) \quad (3.6)$$

where Q - volumetric flow rate,

w and h - width and height of the rectangular cross-sectioned channel, and

n - slope obtained by the bi-logarithmic correlation between $\log \dot{\gamma}_{w(\text{app})}$ and $\log \tau_w$.

The real shear stress equation for Newtonian fluids is given by

$$\tau_{w(\text{real})} = \frac{h}{2} \left(\frac{-\Delta P_{\text{real}}}{L} \right) \quad (3.7)$$

In the case of the slit, the edge effect on the shear stress must be corrected when the width / thickness ratio is below 10. Thus the Equation 3.8 becomes [78]:

$$\tau_{w(\text{real})} = \frac{w \cdot h}{2(w + h)} \left(\frac{-\Delta P_{\text{real}}}{L} \right) \quad (3.8)$$

After the corrections on the capillary and the slit flow models, the real viscosity can be calculated for each type of flow by dividing the real shear stress by the real shear rate, resulting on [77, 78]:

$$\eta_{(\text{real})} = \frac{\tau_{\text{real}}}{\dot{\gamma}_{\text{real}}} \quad (3.9)$$

3.1.2. Wall slip effect

The viscosity of liquids and polymer solutions flowing in microchannels has been observed to increase up to 80% near the wall of the channel. During the polymer flow this effect is believed to be due to high intermolecular interaction and disentanglement between bulk and wall chains [79, 80]. Effects like microscale viscosity, wall slip and surface tension need to be studied for a full comprehension of the rheological behaviour of the flow in microchannels [65].

The concept of wall slip was first addressed by Mooney (1931), who found that certain flow curves depended on the radius of the capillary once the shear stress exceeded a critical value [81]. The effect takes place when the shear stress at the microchannel wall exceeds a critical value, typically, above 0,1 MPa [65, 74, 82]. As the magnitude of the shear stresses varies, polymer melts flow in a way that is a superposition of slipping at the wall and shearing within the melt [83]. When at a critical wall shear stress wall slip occurs the flow curves (wall shear stress *versus* apparent shear rate) diverge from each other and become dependant on channel dimensions. Usually the boundary conditions at the wall are known and their influence on the flow behaviour close to the wall is relevant. Assuming a constant heat flux at the wall ($\partial T/\partial r = \text{constant}$ and $Bi(T_0 - T_w)$) without considering pressure or temperature dependence, a simplified power-law slip model (Equation 3.10) was introduced for the slip velocity [75]

$$u_s = \frac{a}{1 + (\tau_c / \tau_w)^{10}} \tau_w^m \quad (3.10)$$

where τ_w – wall shear stress,

τ_c – critical shear stress for slip,

a – scalar coefficient and

m – mass flow rate constancy equation given by:

$$m = 2\pi \int_0^R \rho \cdot v_z \cdot r \, dr \quad (3.11)$$

3.2. Experimental methods

3.2.1. Concept

Conventional capillary rheometers are difficult to operate with channels with dimensions at the micrometric region. Alternative experimental setups guaranteeing the flow through the microchannel must generate pressure high enough and support the high stresses developed during flow [64, 84]. A concept meeting these requirements consists of using a small injection mould structure with a set of interchangeable moulding blocks with calibrated microchannels, in an injection moulding machine. The operation of such a device requires accurate temperature control

during the heating and cooling phases of the moulding cycle, as well as pressure monitoring at the extremities of the microchannel. The concept is sketched in Figure 3.2.

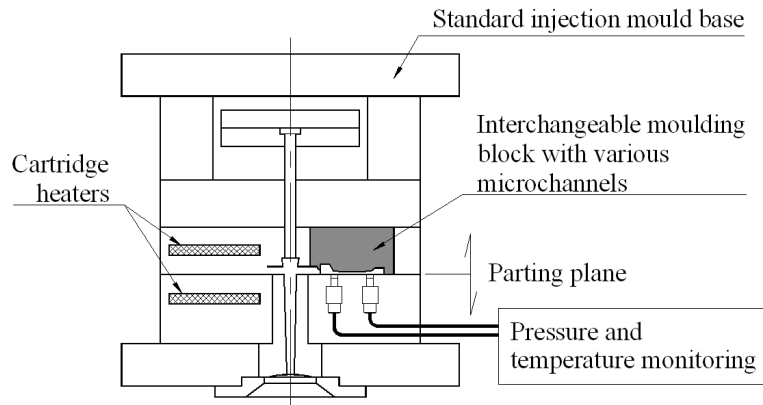


Figure 3.2. Concept of the tool for rheometric studies in microchannels

The use of miniature pressure sensors and a suitable data acquisition system makes it possible to gather the information required for rheological characterization of the flow in the microchannel as suggested in the Figure 3.3.

It must be stressed that equipment based on this concept is not exactly a microrheometer, but rather a setup capable to replicate flow conditions in actual micromoulding. More precisely it is a viscometer that can be used on standard injection moulding equipment to analyse the flow using processing parameters characteristic of microinjection moulding.

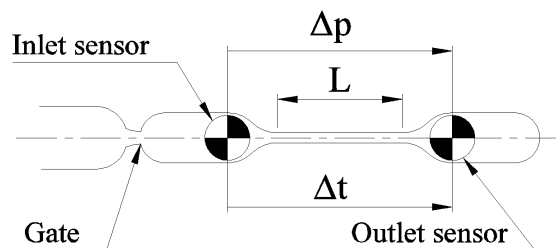


Figure 3.3. Variables for rheological assessment of the flow in microchannels.
 Δp – pressure drop; Δt – time interval; L – channel length

The pressure drop, Δp , measured from the pressure sensor data is required for calculating the shear stress using Equation 3.8. The average melt flow rate is derived from acquired data that yields the flow time between the locations of the pressure sensors, Δt . The shear rate can then be calculated using the equations already referred to.

3.2.2. Methodology

The studies on the flow in microchannels were developed using a commercial microinjection moulding cell and a research mould that are detailed in Chapter 4. The mould was designed to accommodate interchangeable moulding blocks, allowing the variation of the microcavities. Moulding blocks with two different microchannel cross sections were tested: a slit with rectangular cross section, 400 μm wide by 100 μm deep, and a 200 \times 200 μm square cross section to emulate the flow in a circular cross section. The length of the microchannel is 5 mm. The microchannel must be designed to meet the requirements of a slit flow, enabling pressure monitoring at both ends to generate specific experimental data. The general layout of the cavities is shown in Figure 3.4.

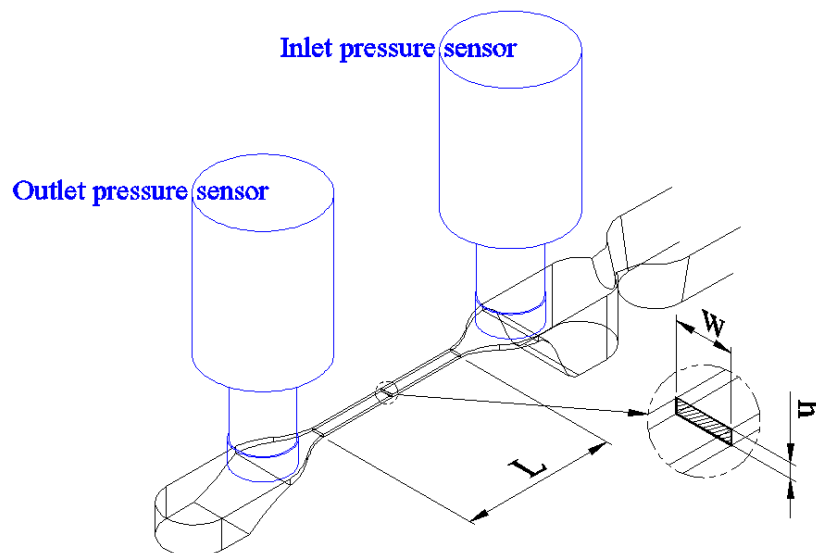


Figure 3.4. Layout of the microchannel with overall dimensions and pressure sensor location

The use of a rectangular or square cross section enables a future comparison with pressure data from a circular cross section with similar dimensions, since circular and square cross sections exhibit different areas, although, with a similar hydraulic diameter. The microchannel design is completed with two deposits, thicker volumes at each end, to provide melt flow stabilization. The transition between the deposits and the microchannel is as smooth as possible in order not to disturb melt flow within the microchannel itself.

Concerning the location of the pressure sensors, there is a source of error that must be addressed. The physical dimensions of the commercial sensors used are of a scale different from the microchannels. Hence, the microchannels are wider at both ends to allow the pressure reading by the sensors. However, this geometry variation influences the pressure drop and therefore an entry correction is required, hence, zero-length microchannels for each cross-section tested were implemented in two additional moulding blocks (Figure 3.5).

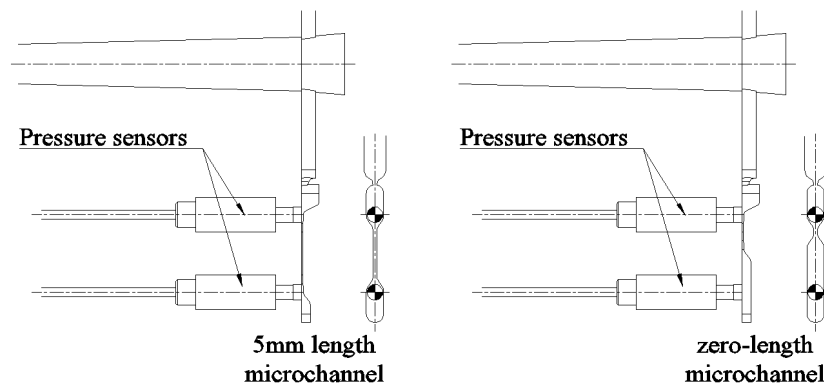


Figure 3.5. View of the $400 \times 100 \mu\text{m}$ microchannel showing the 5 mm length (on the left) and the zero-length versions (on the right)

When the moulding blocks with microchannels are implemented, the mould can be used as a high pressure viscometer enabling high injection pressures in the microchannels, which are difficult to be achieved in conventional viscometers [64, 65, 78, 84, 85]. Since the goal is to promote steady flow in microchannels, an external control unit for the heating system will provide the temperatures suitable for polymer injection at this scale, enabling quantitative flow evaluation at the same time and under the same processing conditions.

Algorithm for microrheometry evaluations

The rheometry evaluations performed with the microchannels followed a procedure that replicates the calculations required on capillary rheometry. The microchannel length used is 5 mm long, requiring the Bagley procedure to correct the entry effects since the location of the pressure sensors is outside the microchannel area due to the sensor dimensions. For that purpose, a zero-length microchannel for each cross-section was used to perform this correction.

Capillary rheometry relies on the variation of the piston speed to impose different shear rates, establishing the characteristic flow curves. In this particular case, such variation can only be made cycle by cycle and not, within the injection cycle, which requires several injection cycles with different melt speeds imposed. Each point of the flow curve must be obtained directly from a single standardized injection cycle.

The procedure for microrheometry evaluation is described step by step on the following list of tasks:

1. Obtain a sample set of pressure curves (inlet and outlet pressure) for each melt speed imposed for the 5 mm length microchannel;
2. Select the group of pressure curves (inlet and outlet pressure) which variation should be contained within the standard deviation of $\pm 5\%$;
3. Obtain the average pressure curves (inlet and outlet pressure);
4. Identify the time instant in which the melt touches the first pressure sensor (t_1);
5. Identify the time instant in which the melt touches the second pressure sensor (t_2);
6. Determine average melt velocity within the microchannel:
 - The distance between pressure sensors is $\Delta L = 9$ mm;
 - The average melt velocity is calculated by $V_{avg} = \frac{\Delta L}{\Delta t} = \frac{\Delta L}{t_2 - t_1}$;
7. Determine the average flow rate within the microchannel:
 - The volume of the microchannel is obtained from the 3D CAD model;

- The average flow rate is calculated by $Q_{avg} = \frac{Vol}{\Delta t} = \frac{Vol}{t_2 - t_1}$;

- From the average pressure curves, based on the values gathered by the data acquisition system, obtain the pressure drop (ΔP) between t_1 and t_2 , as shown on Figure 3.6;

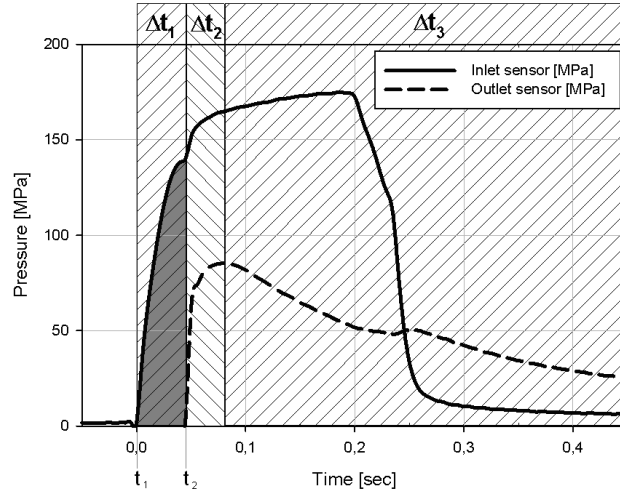


Figure 3.6. Pressure drop on the 200×200 μm microchannel between t_1 and t_2

- Obtain a sample set of pressure curves (inlet and outlet pressure) for each melt speed imposed for the zero-length microchannel;

- Steps **2 to 8** must be repeated for the zero-length microchannel;

- Calculate the corrected pressure drop $\Delta P_{real} = \Delta P_{L5} - \Delta P_{L0}$;

- Calculate the apparent shear stress $\tau_{w(app)} = \frac{h}{2} \left(\frac{-\Delta P_{real}}{L} \right)$;

- Calculate the apparent shear rate $\dot{\gamma}_{w(app)} = \frac{6Q}{w \cdot h^2}$;

- Calculate the index of non-Newtonian flow behaviour $n = \frac{\ln \sigma_{real_i} - \ln \sigma_{real_{i-1}}}{\ln \gamma_{app_i} - \ln \gamma_{app_{i-1}}}$;

15. Calculate the shear stress, applying the Rabinowitsch procedure

$$\dot{\gamma}_{w(\text{real})} = \frac{6Q}{w \cdot h^2} \left(\frac{2}{3} + \frac{1}{3}n \right);$$

16. Calculate the shear rate, applying the Bagley correction $\tau_{w(\text{real})} = \frac{w \cdot h}{2(w+h)} \left(\frac{-\Delta P_{\text{real}}}{L} \right);$

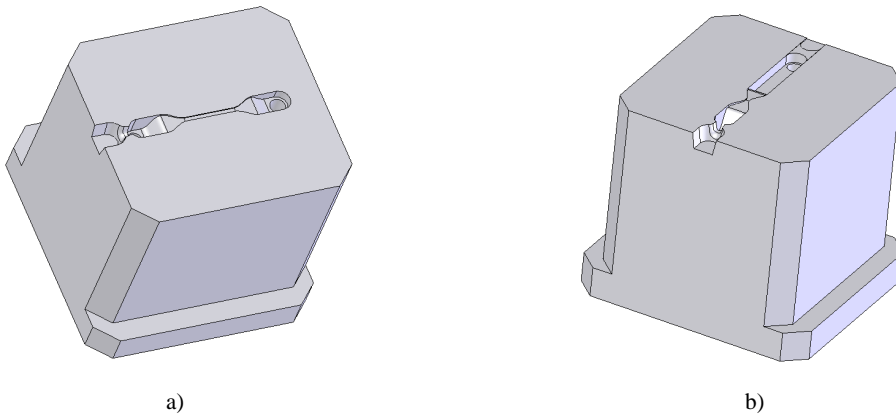
17. Based on the values for shear stress and shear rate calculated previously on steps **15** and

16, calculate viscosity $\eta_{(\text{real})} = \frac{\tau_{\text{real}}}{\dot{\gamma}_{\text{real}}};$

18. Plot viscosity *versus* shear rate on a logarithmic scale.

3.2.3. Moulding blocks for microchannels

The various microchannels cavities were obtained by micromilling in standard interchangeable moulding blocks of the research mould (details are included in Section 4.3). A view of the moulding blocks for the 400×100 μm cross-section, and 5 mm and zero-length microchannels is shown in Figure 3.7.



a) b)
Figure 3.7. Moulding blocks for the 400×100 μm microchannel.
a) 5 mm long microchannel; b) zero-length microchannel

3.2.4. Instrumentation

The rheological characterization of the polymer flow in the microchannel depends on the monitoring the melt pressure at the microchannel inlet and outlet using two miniature piezoelectric pressure sensors. The pressure drop between the two locations and the flow velocity are used to relate the shear viscosity to the shear rate [64, 78].

For each microchannel the data for analysis were those corresponding to full-shot mouldings, when pressure data were obtained by the pressure sensors. A typical set of pressure data is shown in the Figure 3.8.

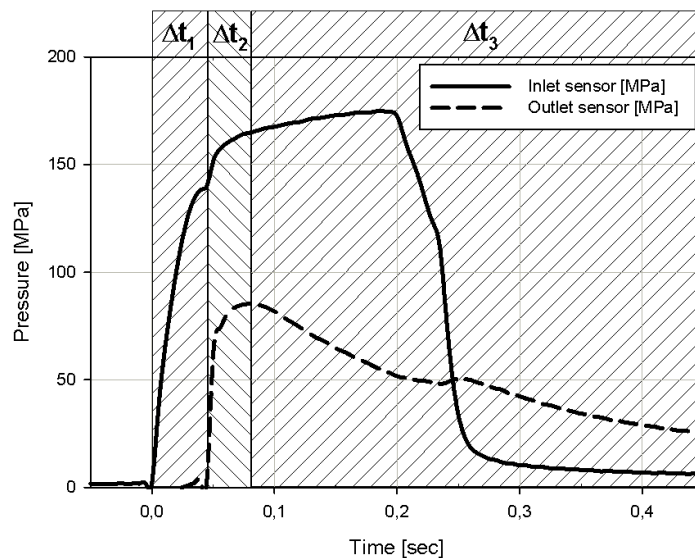


Figure 3.8. Sample pressure curves for the 200×200 μm microchannel moulding

Three different time frames, identified as Δt_1 , Δt_2 and Δt_3 , can be identified in this sample. The first time frame, Δt_1 , starts when the melt reaches the inlet pressure sensor at the entrance of the microchannel (solid line on the graph). The end of this interval corresponds to the instant when the melt reaches the outlet sensor at the exit of the microchannel (dashed line on the graph). After Δt_1 the flow is fully developed in the microchannel, as pressure signals are recorded on both sensors, and the measurements for the viscosity evaluation can be initiated. During the second time frame, Δt_2 , which ends when the outlet sensor reaches its peak, the melt has filled completely the impression. After this point, the melt flow stops and the microchannel freezes off, leading to the

pressure drop monitored by the two sensors. This phase occurs during the last time frame, Δt_3 , where the peak on inlet pressure sensor value corresponds to the solidification of the gate. After this point, pressure rapidly decreases as a result of the variation of the specific volume of the melt.

3.2.5. Materials

The injection tests were carried out with polyoxymethylene (POM), Hostaform C27021 (Ticona-Europe, Germany). This semi-crystalline polymer is a very easy flow injection moulding type with MFR of $24 \text{ cm}^3/10 \text{ min}$ (190°C , 2,16 kg) that is commonly used in microinjection moulding [57].

3.2.6. Microinjection moulding

The initial approach for the injection tests was close to conventional rheometry. The melt speed was increased gradually to establish the data required for shear rate and viscosity calculation.

The melt temperature, T_{inj} , used in the study is above the typical range for this POM grade. The material manufacturer recommends a melt temperature ranging from 190°C to 210°C . For the purpose of this research study, the melt temperature was set to 235°C to enable the complete filling of the microchannels.

The mould temperature, T_{mould} , was also set above the recommended temperature range. Despite the fact that this POM grade already requires a high mould temperature (from 80°C to 120°C), the injection moulding tests were performed at 145°C to enable the complete filling of the impressions. This was particularly critical with the thinnest $400 \times 100 \mu\text{m}$ slit microchannels.

The injection speed or melt speed was adjusted within the capability of the equipment, from 20 to 200 mm.s^{-1} , to reach several values for injection time, t_{inj} , leading to different values of shear rate on each microchannel.

Differently from the microinjection process, no packing pressure was used since the goal was only to obtain a fully established flow within the microchannel without pressure disturbances. The data was obtained from full mouldings, *i.e.*, short shots were discarded.

For each injection speed a time interval, Δt , defined as the time lag between the melt touching each pressure transducer, was measured, enabling the calculation of the average melt speed within

the microchannel. Pressure data from the inlet and outlet sensors, for typical injection moulding conditions, ($T_{inj}=205^{\circ}\text{C}$; $T_{mould}=145^{\circ}\text{C}$; $t_{inj}=0,35\text{s}$) are shown in Figure 3.12.

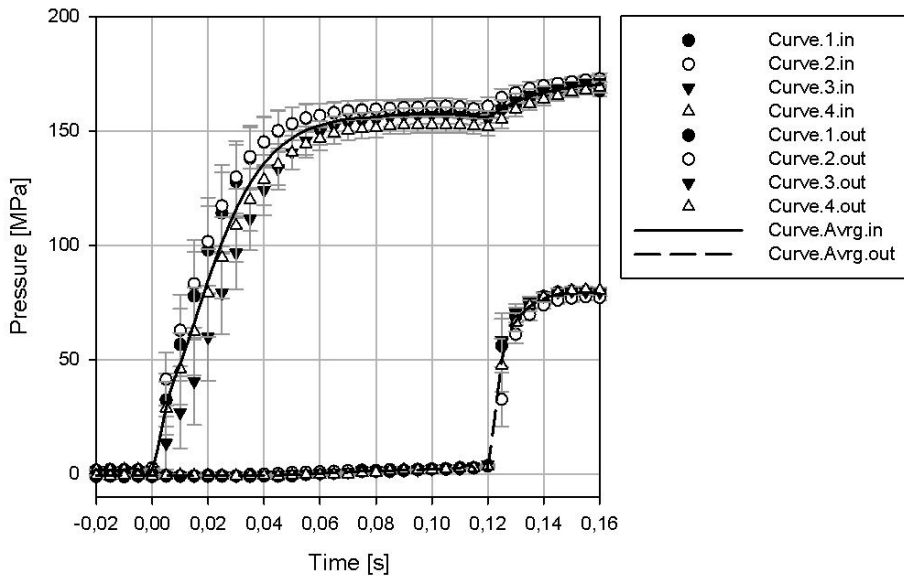


Figure 3.12. Typical pressure profiles during the flow in the microchannel. Suffix 'in' corresponds to the signal at the channel inlet and suffix 'out' at the channel outlet. The lines in this excerpt correspond to the average of 2000 experimental points for each curve.

During the tests the two pressure profiles were recorded, from the sensors at the inlet and the outlet of the microchannel. This information, as exemplified in Figure 3.13, allows obtaining the following information: a) the pressure drop between inlet sensor and microchannel inlet, Δp_1 ; b) the pressure drop on the microchannel itself, Δp_2 ; and c) the pressure drop between the microchannel outlet and the outlet sensor, Δp_3 . To determine Δp_2 , the value for Δp_1 must be removed from the total pressure drop value obtained assuming that Δp_3 is much smaller than $\Sigma \Delta p_i$. The zero-length microchannel (L0) is meant to determine its initial pressure drop, which will be equivalent to Δp_1 so the values for the 5 mm microchannel (L5) could be corrected (Figure 3.16).

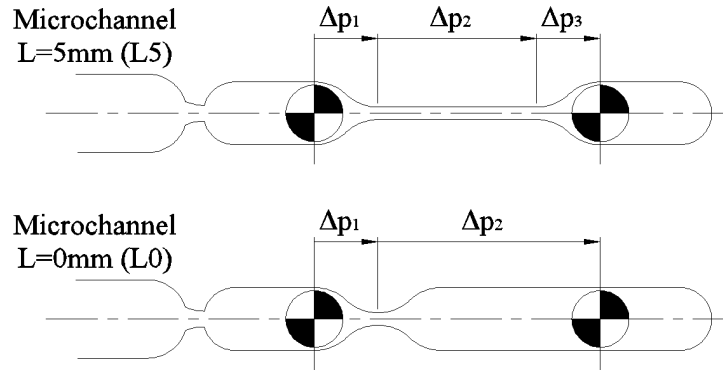


Figure 3.16. Determination of the effective pressure drop within the microchannel

3.3. Results and discussion

3.3.1. Conventional rheometry

The conventional characterization of the polymer was made with a twin-bore Rosand RH10 capillary rheometer (Malvern, UK). The determination of the flow curves were made at 180°C, 200°C, 220°C and 240°C. The flow activation energy was calculated since at these temperatures POM is a thermo-rheologically simple material and the time-temperature superposition (TTS) principle is expected to apply. For polymer melts this applies when the flow temperature is more than 100°C above the glass transition temperature. The shift factor for each temperature, a_T , can be expressed by an Arrhenius relation [86] as:

$$a_T = \exp\left(\frac{E}{R} \cdot \left(\frac{1}{T} - \frac{1}{T_0}\right)\right) \quad (3.12)$$

where E – flow activation energy,

R – gas constant and

T and T_0 – absolute temperatures.

As the TTS principle holds for the POM melt, the flow activation energy, E , is approximately 44,8 kJ/K.mol. The flow curves obtained from capillary rheometry are shown in Figure 3.14.

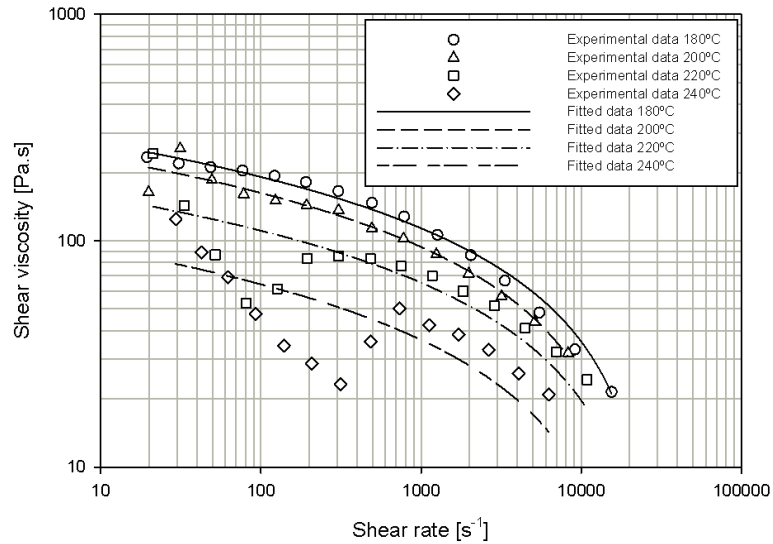


Figure 3.14. Flow curves from conventional capillary rheometry for the Hostaform® C 27021

The master curve is depicted in Figure 3.15, showing that the TTS principle is fully applicable to this material, confirming the previous assumption that this material grade is thermorheologically simple. This definition is based on the fact that the viscoelastic functions determined under isothermal conditions remained unaffected in shape, enabling the application of the TTS principle [71]. Therefore, it should be possible to establish a relation between any other flow curve and the temperature used to obtain it, considering the distance between curves on the plot. If such relation cannot be established, the TTS principle might not be applicable, raising the suspicion that the flow is occurring under non-isothermal conditions.

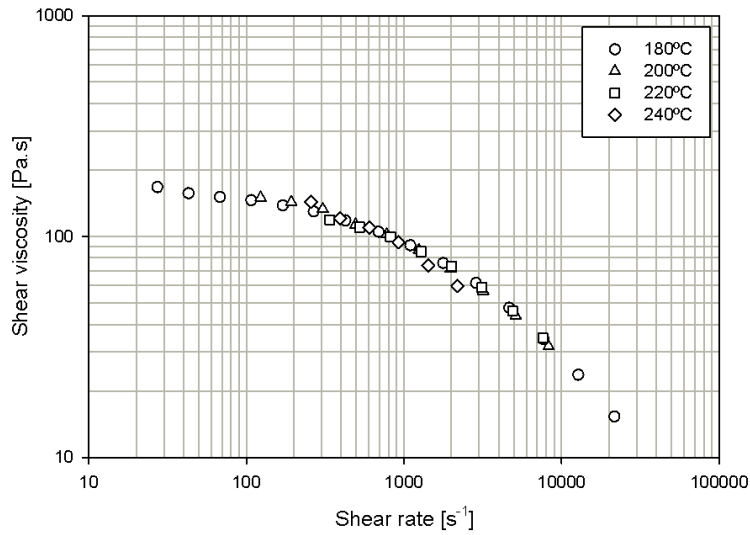


Figure 3.15. Master curve for Hostaform C 27021, observing the time-temperature superposition principle

3.3.2. Flow in microchannels

For each melt speed imposed, it was obtained a time difference, Δt , between the signals of the inlet and outlet pressure sensors that provided the flow rate value required for shear rate calculation from Equation 3.6. The pressure drop was also obtained, allowing the calculation of shear stress through Equation 3.8. With these two values for each melt speed, the shear viscosity was calculated as the ratio between shear stress and shear rate (Equation 3.9) and plotted as in Figure 3.17.

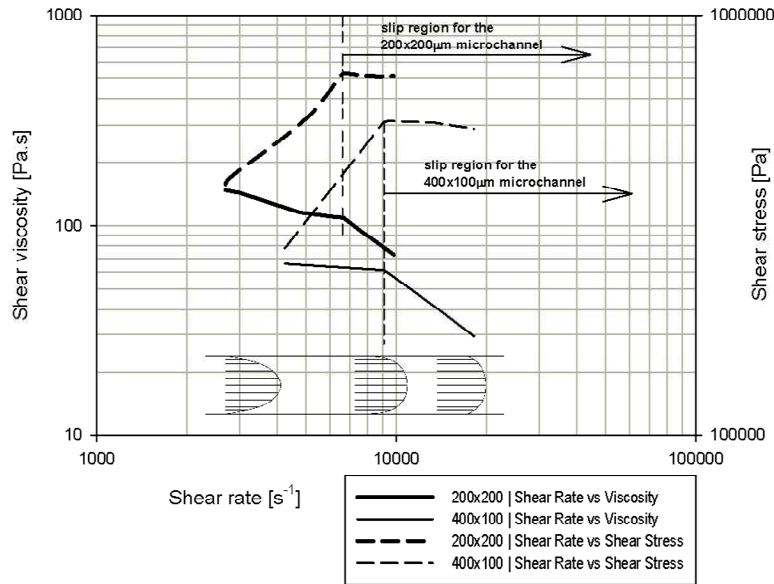


Figure 3.17. Flow curves based on the 200×200 μm and 400×100 μm microchannel pressure data

An immediate conclusion arises from the shape of the plotted curves since there is an abrupt change of the direction on both curves instead of a smooth set of experimental points for each curve. It is also possible to observe in this figure that the critical shear rate for this particular material in the 200×200 μm microchannel is around 5000 s⁻¹. The critical shear rate for the 400×100 μm microchannel, for which successful shots were difficult to obtain at lower melt speeds, is estimated to be approximately 6000 s⁻¹. After exceeding the correspondent critical shear rates, shear stress ceases to increase, keeping its value almost constant till the end of the curve.

3.3.3. Plug flow transition

There is an important change on flow behaviour on each microchannel as shear rate increases, as noticeable in the plot in Figure 3.17. Both curves show a transition from a normal flow to a new type of flow, although at different values of shear rate, where the index of non-Newtonian behaviour, n , is close to 1, indicating the onset of slip at the wall. The horizontal section of the curves, where the shear stress reaches a plateau, clearly indicating the change in behaviour from shear flow to plug flow. This transition is associated to the wall-slip effect. The non-horizontal

section of the curves, for both microchannels, corresponds to the shear flow regime, before the critical shear rate is reached.

The different shear rates at which the plug flow transition occurred in the two types of microchannels can be explained by their hydraulic diameter and the aspect-ratio of their cross-sections. The $200 \times 200 \mu\text{m}$ square section, with an aspect-ratio of 1:1, corresponds to an equivalent round section $200 \mu\text{m}$ in diameter. On the other hand, the $400 \times 100 \mu\text{m}$ section with an aspect-ratio of 4:1 has a hydraulic diameter of just $160 \mu\text{m}$, hence a less favourable flow geometry. This leads to a 36% decrease on the effective flow cross-section of the $400 \times 100 \mu\text{m}$ microchannel, causing it to reach its critical shear rate at lower values. After these critical values of shear rate, a plug flow is fully developed on both microchannels.

3.3.4. Interpreting the plug flow transition

Despite of the processing temperature used for the melt flow in the microchannels being of 235°C , the corresponding flow curve is located above the 180°C flow curve, as shown in Figure 3.18. This means that the real temperature on the microchannel is much lower than the imposed melt temperature.

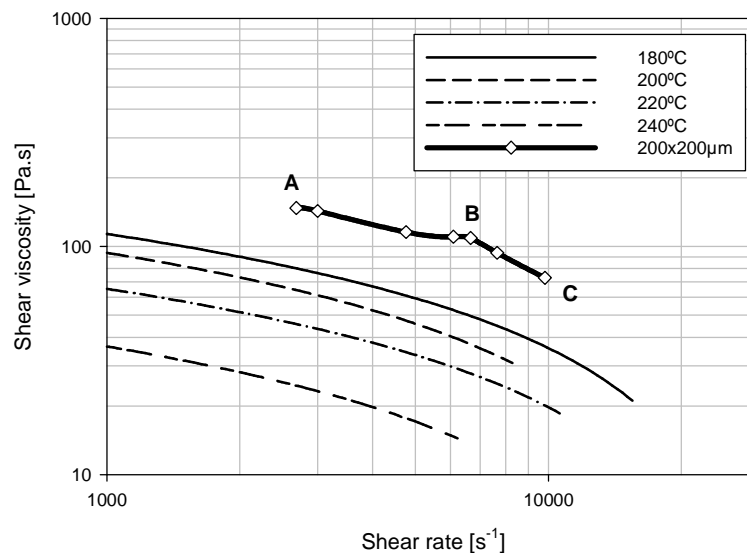


Figure 3.18. Plot data from conventional capillary rheometry and rheometry calculations based on the $200 \times 200 \mu\text{m}$ microchannel pressure data.

This incongruence is certainly due to the high surface area to volume ratio, which makes conventional heat transfer equations insufficient to describe what happens at this scale. Table 3.1 summarizes some geometric relevant values for comparison between rectangular/square and circular cross-sections microchannels.

Table 3.1. Comparison between different cross-section microchannels

Length [mm]	Width [μm]	Height [μm]	Hydraulic diameter [μm]	Cross-section area [mm^2]	Surface area [mm^2]	Volume [mm^3]	Surface area to volume ratio
5,000	200,000	200,000	200,000 (*)	0,040	4,000	0,200	20
	400,000	100,000	160,000 (*)	0,040	5,000	0,200	25
			400,000	0,126	6,283	0,628	10
			200,000	0,031	3,142	0,157	20
			160,000	0,020	2,513	0,101	25
			100,000	0,008	1,571	0,039	40

(*) Hydraulic diameters

The values corresponding to rectangular/square and circular cross-sections microchannels shown on Table 3.1 enable the analysis of the relevant geometric features. The decrease of the microchannel dimensions corresponds to the increase of the surface to volume ratio, enabling a high heat transfer rate to the mould wall [38, 87]. Furthermore, for similar dimensions, rectangular/square cross-section microchannels exhibit higher surface area than the circular cross-section, although their similar surface to volume ratio. In this case, since heat transfer is mainly through conduction, such effect depends directly on the contact surface, which is higher on the non-circular cross-sections.

Analyzing the flow curve corresponding to the $200 \times 200 \mu\text{m}$ microchannel, two sections can be observed as in Figure 3.18. From A to B, shear flow with its parabolic velocity profile is expected to develop. At the end of this section, B a transition takes place and the section B to C corresponds to a regime in which plug flow, with higher velocities close to the wall, progressively develops.

The faster cooling of the melt in the microchannel means that the temperature of the flowing melt is expected to be well below the initial 235°C . The amplitude of the temperature decrease, but, it

cannot be predicted from TTS, which is known to be valid for this material, as shown previously. In fact, an application of TTS to the microchannel flow data in order to superimpose it with the other data yields an apparent flow temperature of less than 80°C, which is impossible because not only it is more than 60 °C lower than the mould wall temperature, but is also lower than the no-flow temperature of POM, which in this case is the crystallite melting point of the material [88].

This fact clearly indicates that the heat transfer analysis that is normally used with injection moulding is not directly transferable to the microscale due to the high surface area to volume ratio. Comparing the rectangular/square cross-sections with the correspondent circular cross-sections (200×200 µm versus 200 µm and 400×100 µm versus 160 µm), it is possible to witness these facts. The particular case of the 400×100 µm microchannel shows a surface area which is the double of its correspondent 160 µm microchannel. Given their sub-millimetric dimensions, the microchannels exhibit a high heat diffusion rate which causes filling to occur almost isothermally [65]. In this particular case, there is effectively little or no bulk in the moulding, so our results indicate that heat transfer equations that are typically valid at the macroscale should be disregarded here.

The evaluation of the expected wall-slip velocity was made using Equation 3.10. The mass flow-rate consistency value was calculated through Equation 3.11, using the hydraulic radii of the microchannels. The melt front profile was estimated as a gradual shifting from shear flow to plug flow as shear stress increases.

The data obtained for the 400×100 µm microchannel might not be conclusive since there is not enough data in shear flow conditions to establish a reliable trend to this value. However, the few calculated local wall-slip velocities for this microchannel seem to corroborate the conclusions already obtained on the shear stress *versus* shear rate plot (Figure 3.19).

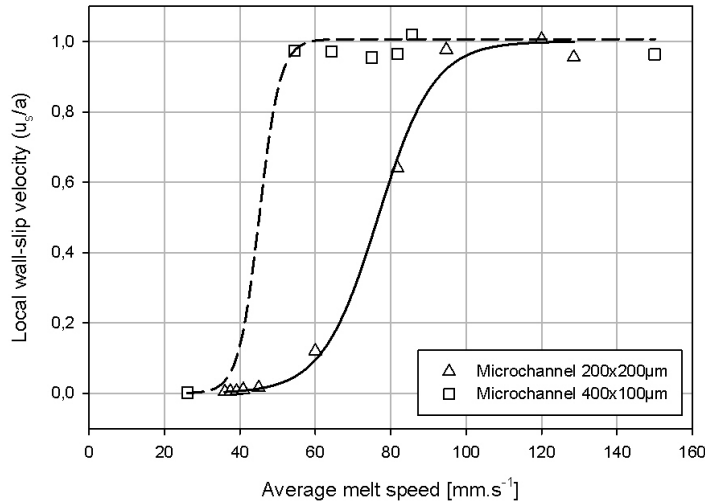


Figure 3.19. Plot of average melt speed versus reduced local wall-slip velocity

Nevertheless, the curves in Figure 3.19 show the same trend, when shear stress is less than the critical shear stress, the local wall-slip reduced velocity is nearly zero. As predicted, the local wall-slip reduced velocity becomes close to one if the shear stress keeps increasing [75].

An immediate conclusion of this study is that the flow in the micromould is non-isothermal, which means that the data eventually obtained is not to be regarded as quantitatively accurate rheometrical data. As stated before, the equipment setup in this study is not a microrheometer, but rather a viscometer that replicates the flow conditions in real flow situations, *i.e.*, it is a process analyser and simulator.

The use of a microinjection moulding tool for rheometry purposes provided the establishment of flow curves for POM at pressures higher than the ones obtained on traditional rheometry, enabling critical shear rate determination for each microchannel used.

Unlike conventional capillary rheometry devices, this setup used microinjection process parameters namely the injection speed to obtain different shear rates, enabling the plotting of flow curves. Therefore, the results could be easily applied onto the microinjection process itself or on microinjection simulation.

An important microscale effect such as wall-slip was detected and the critical values of shear rate were determined for both microchannels studied. Furthermore, local wall-slip velocity was

calculated and compared to the average melt velocity imposed on the process, to determine its relevance on the flow behaviour. It was noticed that the shifting between shear flow and plug flow is much more abrupt on the $400 \times 100 \mu\text{m}$ microchannel, due to the less favourable cross-section.

Chapter 4 – Design of the Micromould

This chapter describes in detail the design options considered for the micromould. The design constraints are referred, describing the mould technical specifications concerning the injection equipment in which it will be operating, the type and dimensions of the parts that will be produced as well as the type of research data that will be extracted from it, using an external data acquisition system.

4.1. Design constraints

The design of this particular mould was developed to meet some important requirements concerning the microinjection research work. The parts to be obtained by microinjection moulding are small (maximum 15 mm long), however, they include some microfeatures such as ultrathin walls or microdetails. Considering the research interest on testing several geometries, the mould design considered the use of interchangeable moulding blocks. Aspects such as the aspect-ratio of micromoulded parts can be tested afterwards, which causes the height of the moulding block to be higher than necessary at this point. The moulding area of the mould must enable the assembly of two Ø1,8 mm pressure sensors as well as its cables and connections to the data acquisition system. Such system will acquire the pressure data from the cavities, enabling its post-treatment for analysis. These interchangeable moulding blocks should be assembled on the ejection side to enable the assembly of the pressure sensors on the injection side. This assembly choice does not require the disassembly of the pressure sensors and enables the change of the moulding blocks with minimal setup time. Finally, another requirement is the injection equipment to be used. The mould was designed to work on a Boy 12A, regarding all the interface issues such as distance between columns, mould fixation on plates and relevant processing features such as minimum shot dosage.

4.2. The mould

The mould was built on a standard mould structure using components from HASCO series K, plate dimensions of 130×100 mm. It is equipped with two HASCO K100 centering rings: a Ø110 mm ring on injection side and a Ø60 mm ring on the ejection side, and a HASCO Z51 main injector with 40 mm radius. The closed mould height is of 155 mm for a minimum plate distance of 100 mm, providing a maximum mould opening of 145 mm (Figure 4.2). A complete 2D drawing of the mould, detailing all systems is attached in Annex A1.

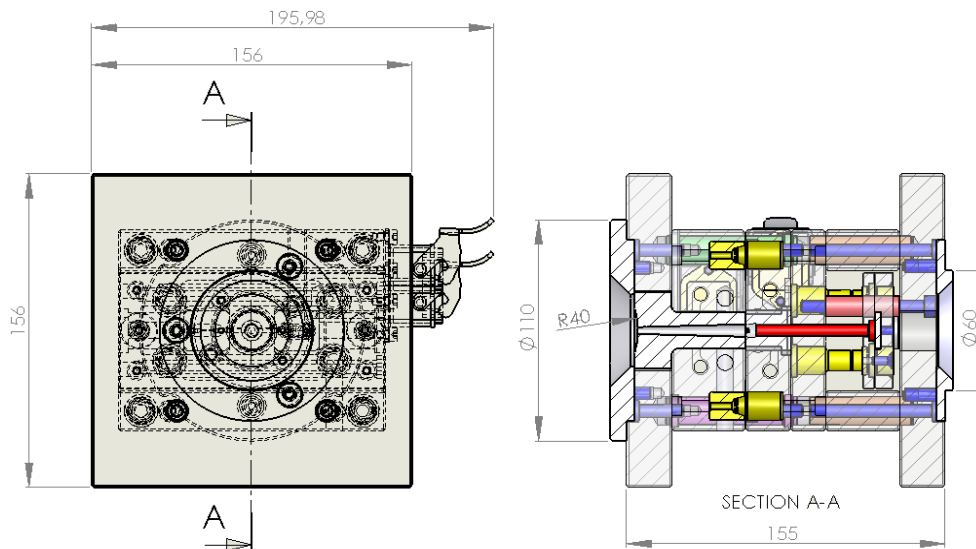


Figure 4.1. Cross-section view of the micromould

The thickness of the cavity plate was mainly selected to accommodate the pressure sensors. Concerning the moulding block interchangeability, the backing plate enables the disassembling of the moulding blocks mounted on the core plate. The spacer height resulted from the required ejection stroke, especially those foreseen for higher aspect-ratio parts. The centering system (Figure 4.2) is composed by a set of 4 guide pins, guide bushings and alignment pins.

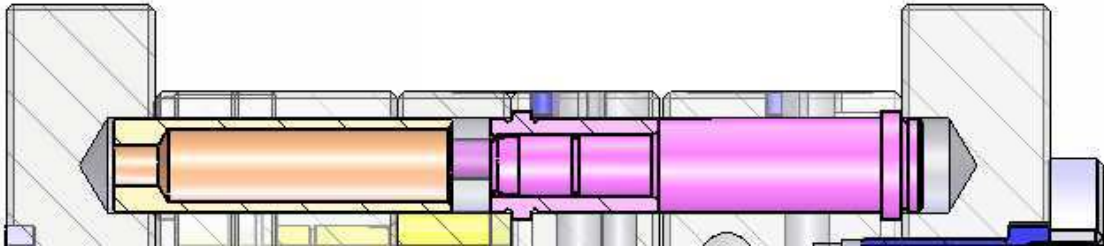


Figure 4.3. Mould guiding and centering system

The interlocking system consists of two conical interlocks from HASCO Z05 series. These are located so that thermal expansion is allowed without causing problems (Figure 4.3). The mouldings produced in this research do not require interlocking between both mould halves since the moulded part is fully contained on the ejection side. However, such feature might be required afterwards for further studies on higher parts.

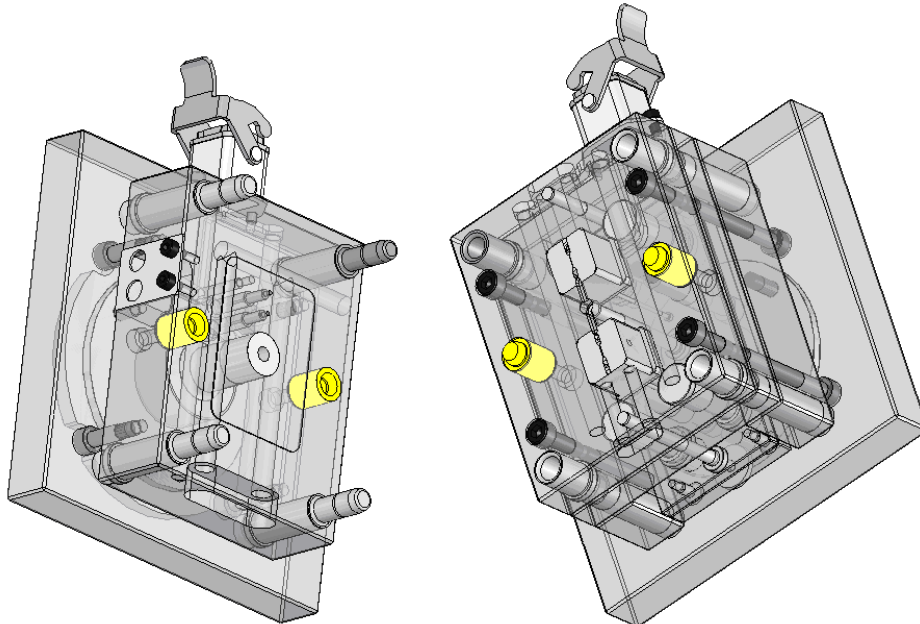


Figure 4.3. Interlocking system (highlighted in yellow)

4.3. Moulding blocks

The moulding blocks used in this mould have a geometry of a parallelepiped of $20 \times 22 \times 20,5$ mm. They are assembled in the core plate (3), with the general dimensions and tolerances shown in the Figure 4.4.

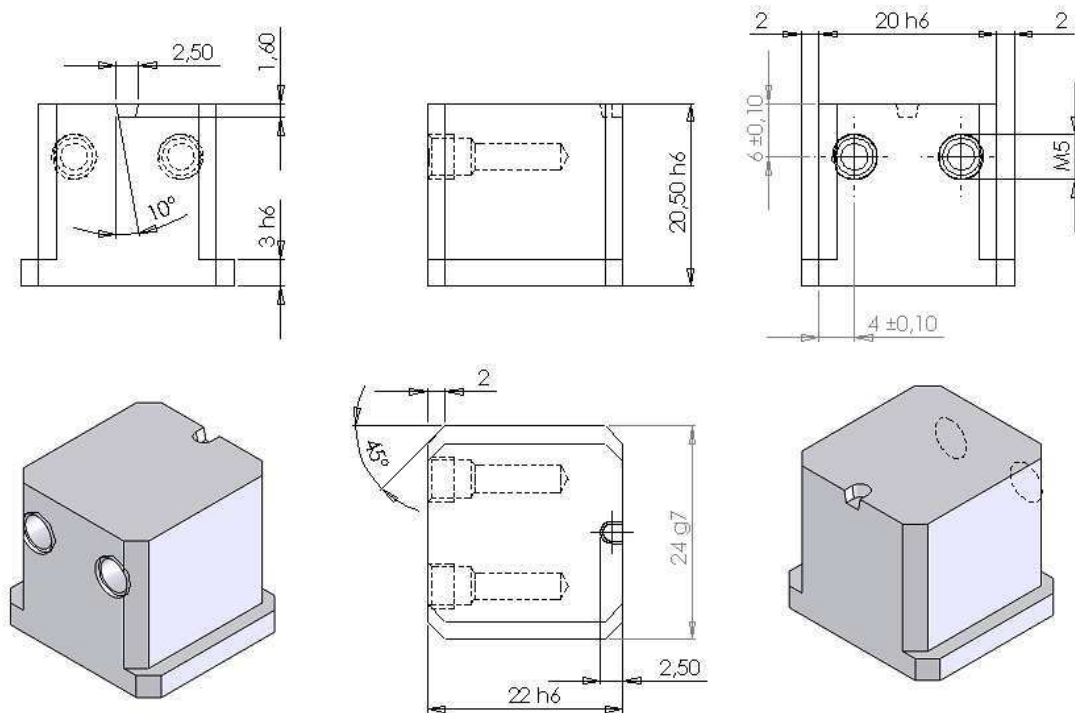


Figure 4.5. Blank moulding block

The use of interchangeable moulding blocks is motivated for maintenance and the need of testing various micromoulding geometries. In the current mould configuration it is only possible to use moulding blocks in the moving side of the mould. The injection side is flat and the cavity plate was designed to accommodate the data acquisition system.

The Figure 4.5 shows as an example the moulding block for a $400 \times 100 \mu\text{m}$ microchannel cavity, with the cooling channel and the thermocouple location.

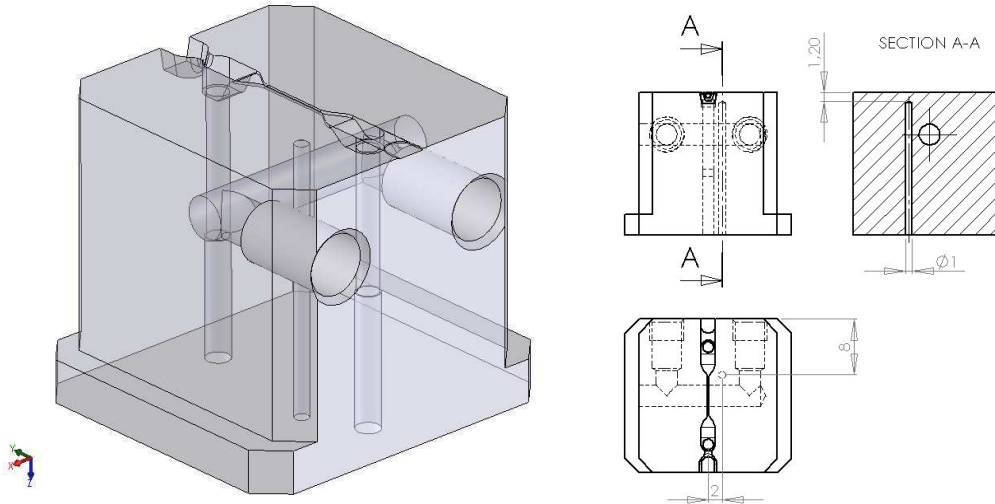


Figure 4.5. Moulding block showing the cooling circuit and the thermocouple location

4.4. Feed system

The cold runner system shown in Figure 4.6 consists of a conical sprue, a cold material trap, two runners, and the gates defined in the moulding blocks. This runner system has a total volume of $1,27 \text{ cm}^3$.

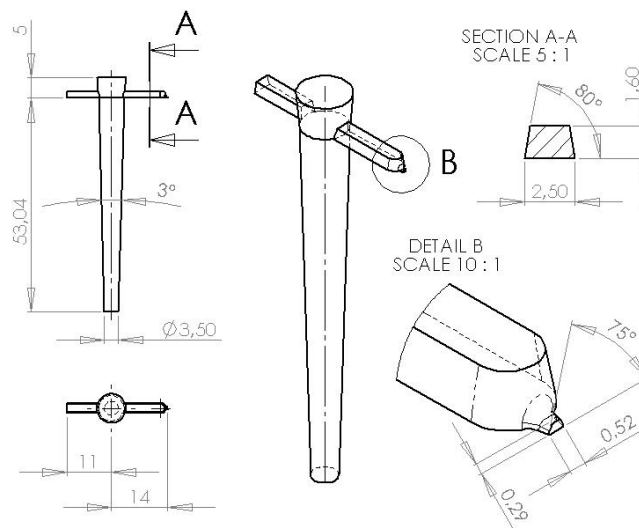


Figure 4.6. Feed system

4.5. Temperature control

The microinjection process is often characterised by the use of Variotherm systems for enabling quick changes in the mould [1]. In this study the temperature control system was only designed for heating before injection and cooling after the holding phase.

The heating is provided at two individually controlled zones, each including two 160 W \varnothing 6,5 mm cartridge heaters, and a type J thermocouple (Figure 4.7).

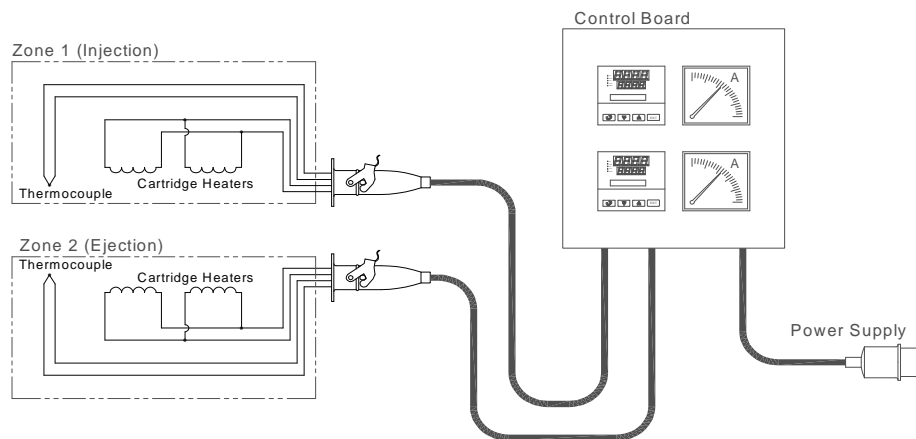
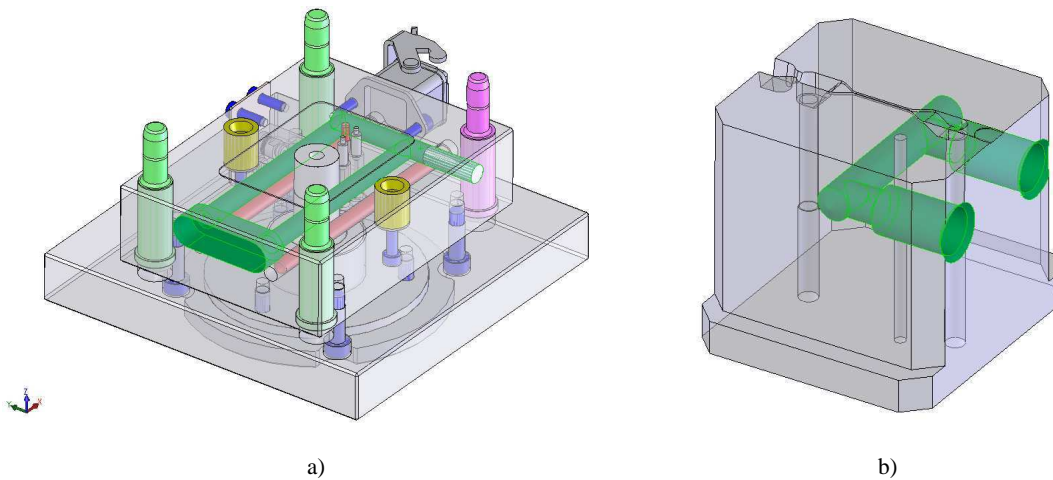


Figure 4.7. Electrical wiring scheme for temperature control

The temperature controller is located at the external control board. Zone 1 controls the temperature at the injection side, on the mould cavity plate. Since there are no moulding blocks at the injection side, the thermocouple is located as near as possible to the parting plane. In Zone 2, the resistances are located on the mould core plate. The moulding blocks are located in this plate and the thermocouple is mounted directly on one of them.

The micromould is also equipped with independent cooling circuits on injection and ejection side (see Fig. 4.8). A simple “U” shape circuit is designed in the moulding blocks since complex cooling channels are not easily implemented. M5 threads were made to receive the cooling connectors.



a) Figure 4.8. Cooling circuits on the micromould
 a) cooling circuit on the injection side; b) cooling circuit on the moulding block

4.6. Ejection system

Standard ejector pins from HASCO, Z40 series were used for the ejection system, namely Z40/5,5×100 for the return pins, Z40/5,5×058 for the sprue ejector, and Z40/1,5×061 (gate side) and Z40/1,5×062 (exit side) for the cavity ejectors (Figure 4.9).

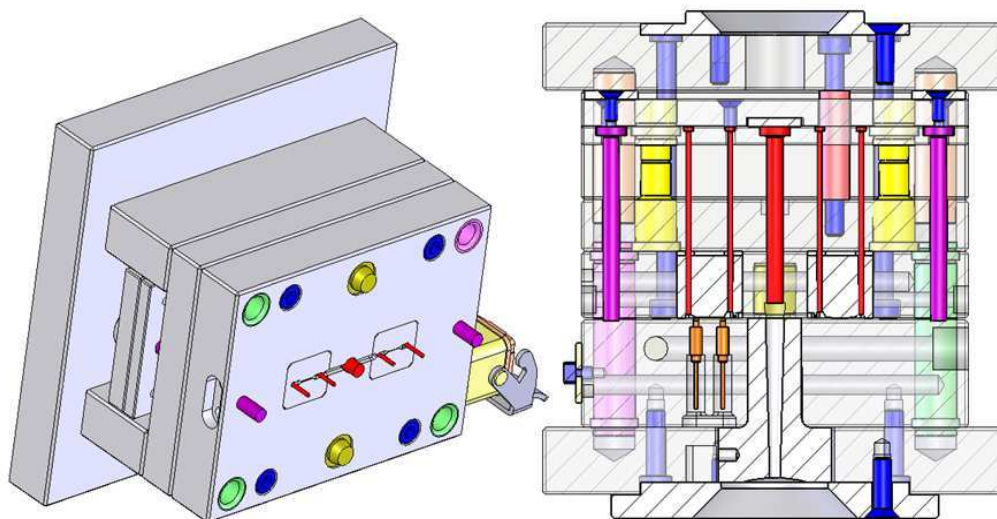


Figure 4.9. Mould view with the ejection system actuated (left) and the cross-section view of the ejection system (right)

4.7. Venting

The air vents are machined directly in the moulding block parting plane. Furthermore, the location of the last ejector pin also contributes to the venting of the impression (Figure 4.10).

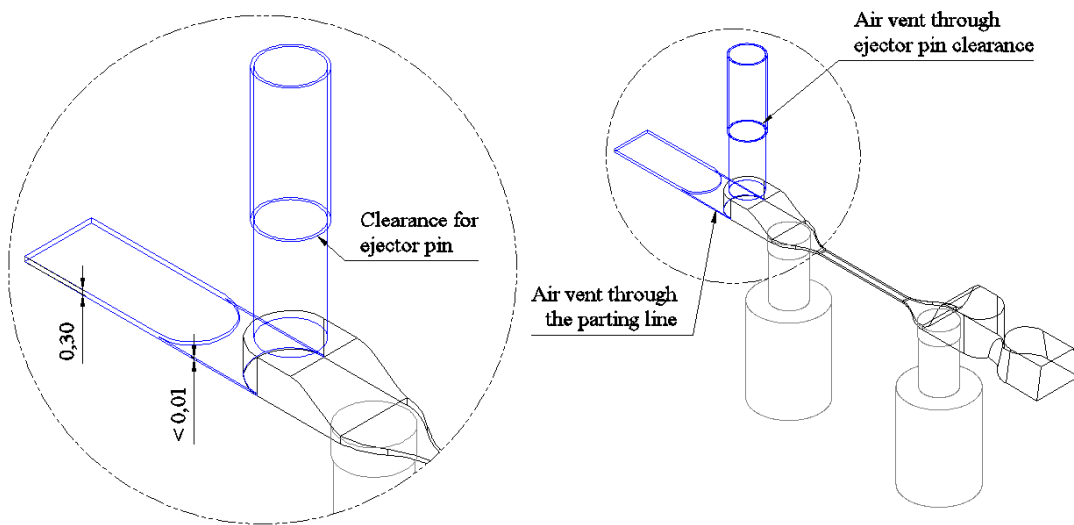


Figure 4.10. Example of the air vent at the end of the microchannel cavity.

4.8. Pressure and temperature monitoring

The monitoring of the injection moulding cycle is made in terms of temperature and pressure. The melt pressure in the mould is monitored with $\varnothing 1,8\text{mm}$ pressure sensors Priamus, model 6006B0,2 (Switzerland), located as shown in Figure 4.11.

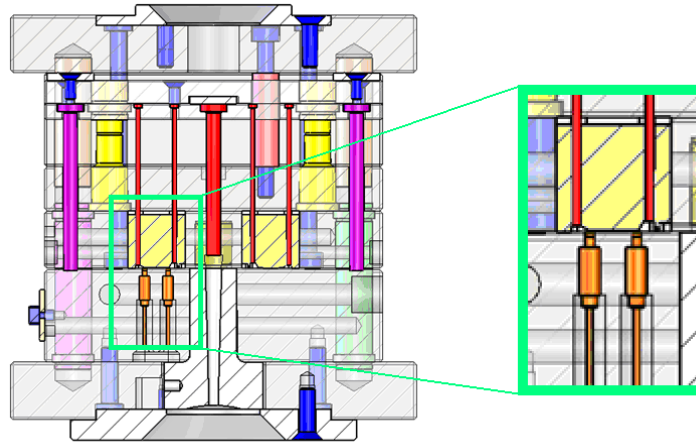


Figure 4.11. Location of the pressure sensors with respect to the surface of one of the moulding blocks

The data acquisition unit consists of two physical units, the input module Priamus Multi DAQ 8101A and the amplifier module Priamus Mobile DAQ 8001B. The user interface is ensured by the Priamus Molding Monitor software, which results page is depicted on Figure 4.12.

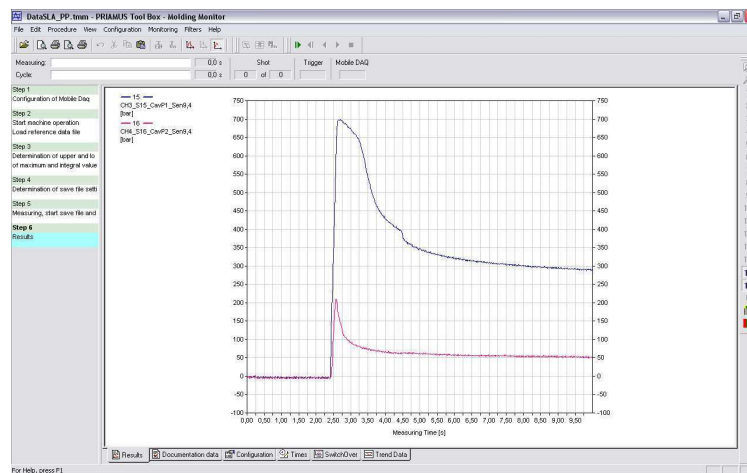


Figure 4.12. Results page of the Priamus Molding Monitor software

The thermocouples installed on the moulding blocks enable mould temperature control. As described on the Temperature Control item, the thermocouples used are type J, with a working range from -200°C to 750°C , according to manufacturer data. Considering the space available, the thermocouple used on the injection side is larger than the one used on the ejection side.

For the injection side, a Resitec TC.002 model (Leiria, Portugal) was selected for assembly on mould plate (2). The thermocouple is positioned on the plate so it can perform the temperature reading on the moulding block area, as shown on Figure 4.13.

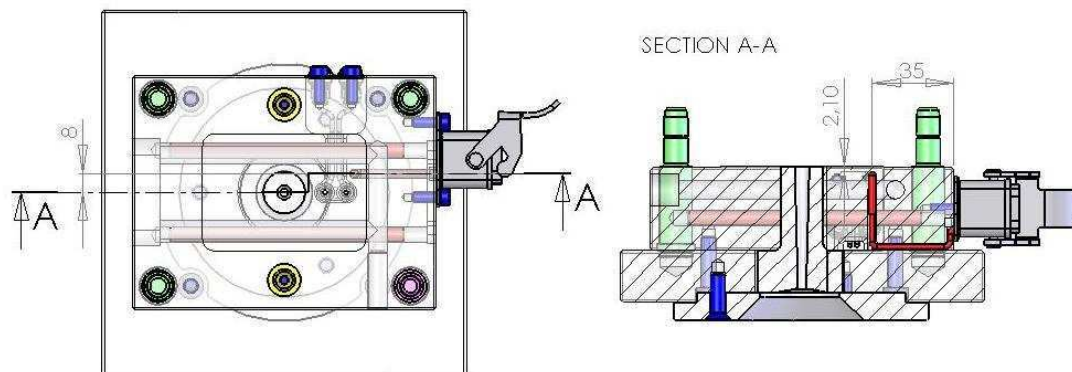


Figure 4.13. Location of the thermocouple on the injection side

The body of this thermocouple does not allow any bending operations. Therefore, its length was selected to enable all curves to be imposed on the cable. An overview of the thermocouple assembly on the injection side is shown on Figure 4.14.

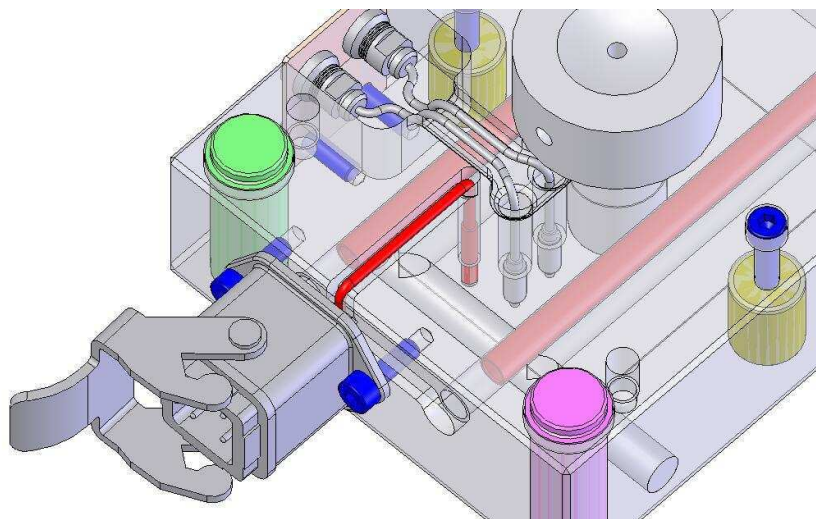


Figure 4.14. Overview of the thermocouple assembly on mould plate (2)

On the ejection side, due to the geometry requirements, it was necessary to select a flexible thermocouple that could be bent in order to reach the minimum distance between the thermocouple and the moulding surface. For that purpose, a Resitec TC.001 model (Leiria, Portugal) with 50 mm in length and 1 mm in diameter was selected for assembly on the moulding blocks. Underneath each moulding block, there is a spacer to enable the thermocouple to be assembled, as shown on Figure 4.15.

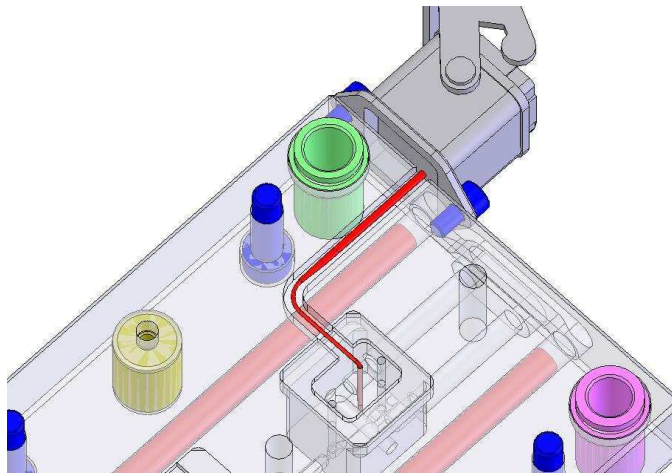


Figure 4.15. Overview of the thermocouple assembly on the moulding block

As shown previously, to reach to the appropriate reading area, the body of this thermocouple was bent twice with suitable radius, in order to avoid damaging the thermocouple (Figure 4.16).

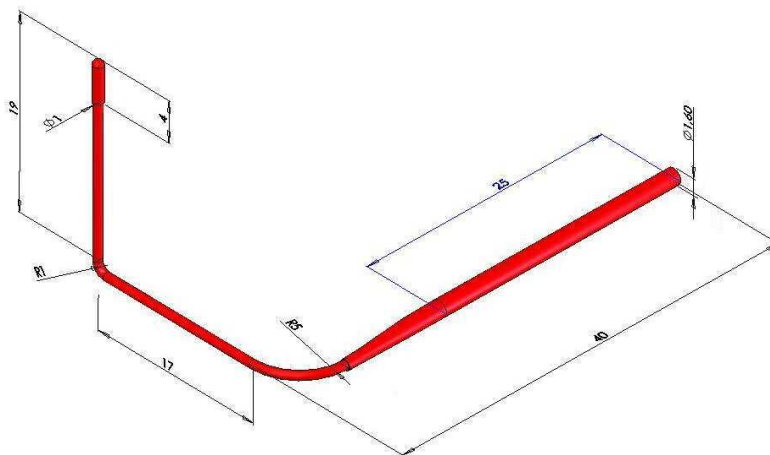


Figure 4.16. Overview and general dimensions of the thermocouple

4.9. The microinjection moulding cell

The mould already described is to be used in a injection moulding machine Boy 12 A (Dr Boy, Neustadt-Fernthal, Germany). The equipment features are appropriate for the microinjection tests since the maximum shot weight is rather small, only 4,45 grams, using polystyrene as a reference material. Given the nature of the parts to be obtained by microinjection moulding, the equipment has clamping force of 129 kN, much more than required. The relevant features of the Boy 12 A model (Euromap size 129-15) are detailed on Table 4.1.

Table 4.1. Equipment features for Boy 12A (Euromap size 129-15)

Injection unit		
Screw diameter	14,0	mm
Screw length-diameter ratio	18,0	
Maximum stroke volume (theoretical)	4,5	cm ³
Maximum shot weight in PS	4,45	g
Injection force	37,1	kN
Injection flow	30,6	g/s
Maximum specific injection pressure	241,3	MPa
Maximum screw stroke	40,0	mm
Maximum screw speed	500,0	min ⁻¹
Clamping unit		
Clamping force	129,0	kN
Maximum plate daylight	300,0	mm
Minimum mould height	100,0	mm

The main dimensions of the equipment that are relevant for the mould assembly are shown in Figure 4.17. This cross-section view shows the diameters for the centering rings of the mould as well as the adjustable distance for the injection nozzle.

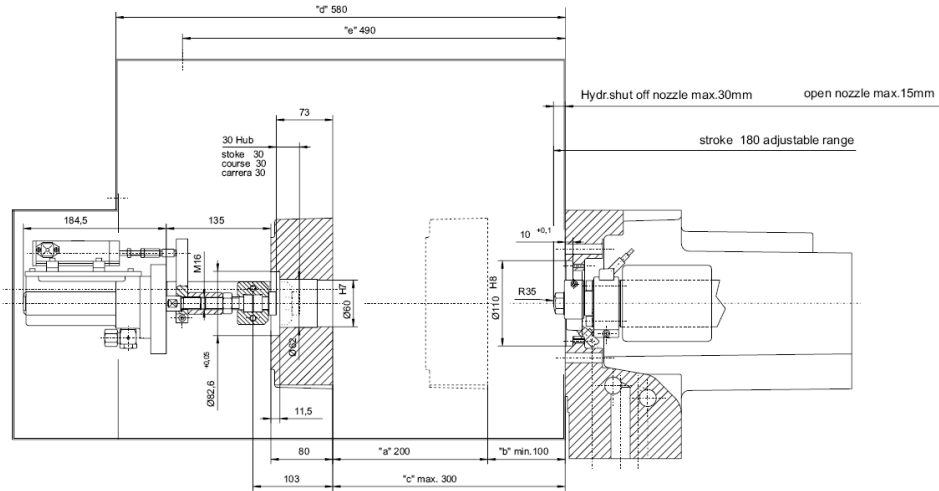


Figure 4.17. Daylight dimensions of the Boy 12 A

The microinjection moulding cell incorporates other equipments, namely for temperature control and pressure monitoring, as shown on Figure 4.18.

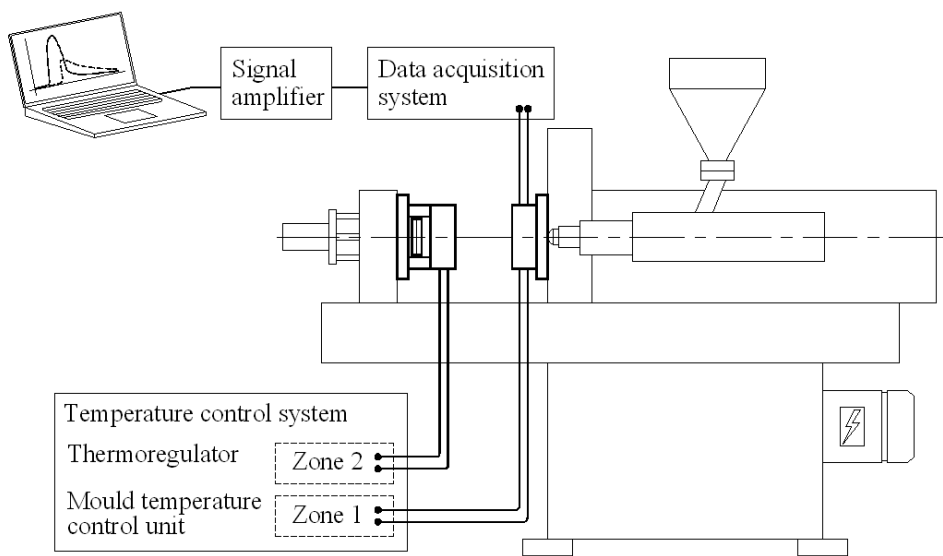


Figure 4.20. The microinjection moulding cell

The mould is equipped with two connections for the pressure sensors. The signals are acquired by the data acquisition module and are processed by the amplifying module. The signals from the

pressure sensors are input afterwards in the software and can be exported to worksheets for post-treatment.

Concerning temperature control, the mould is divided in two control zones, for heating and for cooling, enabling the operation with different temperatures on cavity and core sides.

The electrical connections are located on the top side of the mould, away from coolant connections to prevent problems in case of leaks. The connections for the data acquisition system are located opposite to the operator side, liberating the operator side for handling, assembly or maintenance operations. The general layout for all mould external connections is shown in Figure 4.19.

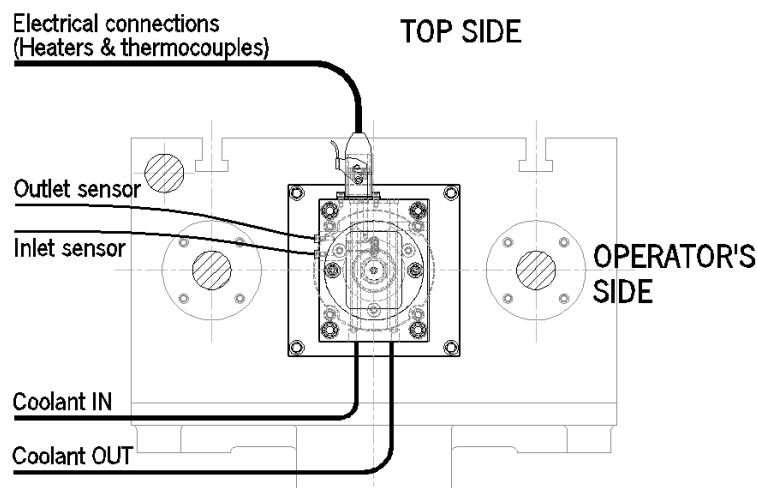


Figure 4.19. Electrical and coolant connections (injection side)

Figure 4.20 shows the complete setup of the microinjection moulding cell and Figure 4.21 shows the micromould open.

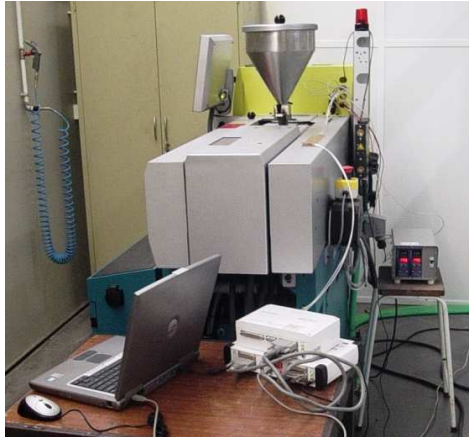


Figure 4.20. Full view of the complete setup for the microinjection tests



Figure 4.21. Micromould showing electrical and sensor connections

4.10. Process control data sheet

The injection process can be suitably described on a process data sheet, where all processing parameters are summarized. This data sheet may include not only the parameters imposed by the user, but also the values given by the equipment. Table 4.2 details the process parameters to be recorded for further analysis.

Table 4.2. Process control data sheet

Plastic material/grade	Mould temperature [°C]		Cooling fluid temperature [°C]	Cooling fluid flow rate [cm ³ .s ⁻¹]	Melt temperature [°C]	Injection speed [mm.s ⁻¹]	Injection pressure [MPa]	Dosage [mm]	Cushion [mm]	Holding pressure [MPa]	Holding time [s]	Cooling time [s]	Barrel temperatures (zones 1 to 5) [°C]	Injection time [s]	Cycle time [s]
	Injection side	Ejection side													

↪ Elements supplied by the user

↪ Parameters for introduction on the mould temperature control unit

↪ Parameters for introduction on the thermoregulator

↪ Parameters for introduction on the microinjection equipment

Values retrieved from the microinjection equipment ↪

4.11. Microinjection moulding cell operation procedures

The microinjection moulding cell requires preliminary procedures before operation. These procedures are important since they contribute for an accurate data acquisition.

The cables of all systems must be connected following the good practices. Equipments are powered off at this moment and all electrical connections, after established, should be blocked by a latch lock or by a blocking nut to prevent accidental disconnection during operation.

After setting up all systems, the microinjection equipment can be powered on. In order to operate with maximum accuracy, the equipment requires the stabilization of the hydraulic system, by performing a few movement cycles to promote oil circulation at adequate temperature.

Barrel temperature must also be stabilized before operation. At the micrometric level, where temperature control is definitely very important, tight tolerances on the temperature setpoint of each barrel zone are recommended to enable melt injection at the intended temperature. This simple precaution is even more important when sensitive materials with narrow processing window are being used.

A similar procedure should be carried out for mould temperature. The mass of the mould is very small and heat transfer through convection is high due to the exposed area. Mould temperature control and thermoregulator should be initialized with appropriate values. Mould temperature should be then stabilized with the mould closed in order to achieve the temperature setpoint faster and uniformly both on cavity and core side.

The data acquisition system requires trigger tuning up before initialization. The trigger is a capacitive detector that should be positioned to sign out the 'mould closed' position and start data acquisition. If the trigger is not positioned over the mould parting line, it can be positioned outside, attached to the column of the moving plate so it detects the closing of the mould, the event that signals the beginning of a new injection cycle.

The data acquisition should be initialized by setting up the channels that are currently connected. Preliminary checking of the sensors datasheet is recommended for a proper setup of the reading range. Acquisition frequency should also be setup considering the accuracy required for analysis. A compromise between accuracy and the size available on the hard disk must be considered.

Chapter 5 – Experimental techniques and methods

This chapter describes the materials, the manufacturing and characterization techniques and the equipments used in this work. Furthermore, the test methods, the injection tests and the simulation analyses are also detailed herein.

5.1. Tooling

5.1.1. Subtractive technologies

The concept of the moulding blocks obtained by subtractive technologies came from the cooperation with similar studies aiming at the evaluation of the performance of micromanufacturing technologies. Therefore, compatible moulding blocks were produced for common interest studies. For that purpose, a simple part was designed containing a vertical rib enabling aspect-ratio evaluation both from the manufacturing and replication points of view. The standard blank moulding block which was already discussed in Chapter 4 (Figure 4.4) is shown on Figure 5.1.

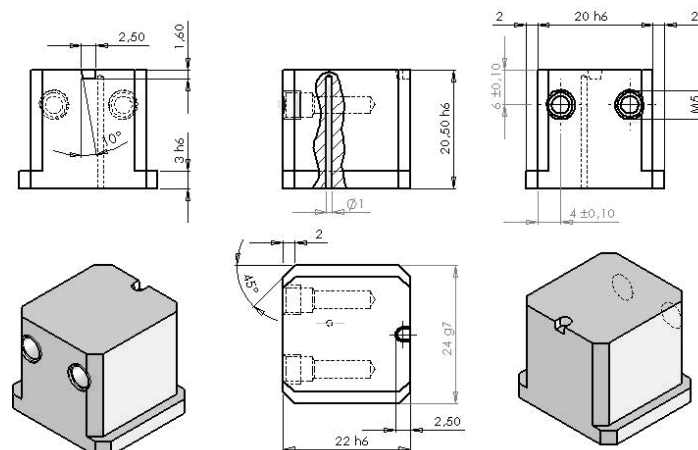


Figure 5.1. Standard moulding block with main dimensions and features

The moulding blocks have a blank volume of 478,51 mm³ and were produced using micromilling, microEDM and laser milling, depending on the aspect ratio of the features to be machined, as shown on Table 5.1.

Table 5.1. Dimensions achievable with the manufacturing technologies used

Technology	W _{bottom} [μm]	W _{top} [μm]	Height [μm]	Aspect ratio
Micromilling	100	100	1000	10:1
MicroEDM	100	60	1500	15:1
Laser milling	100	60	400	4:1

Four cavities were implemented in the moulding blocks. Given the dimensions, two mouldings were designed comprehending the adequate feed system for two cavities in each one (Figure 5.2).

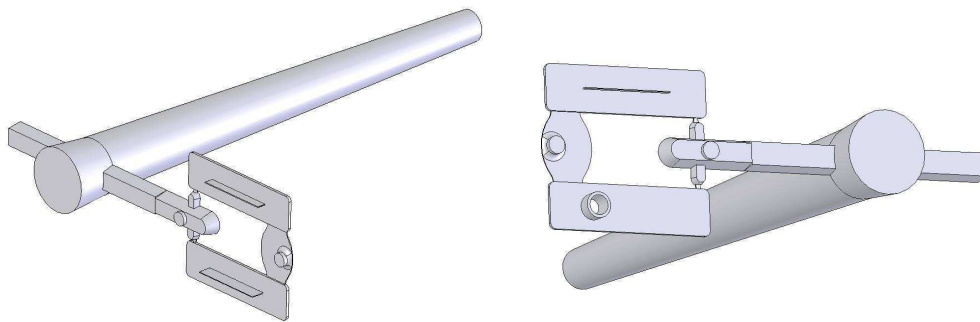


Figure 5.2. 3D models of the parts to be obtained on the moulding blocks produced by subtractive technologies

In the first block (Figure 5.3) two similar cavities were produced using micromilling and microEDM. They differ in the aspect ratio of the ribs and the manufacturing technology used in each of them.

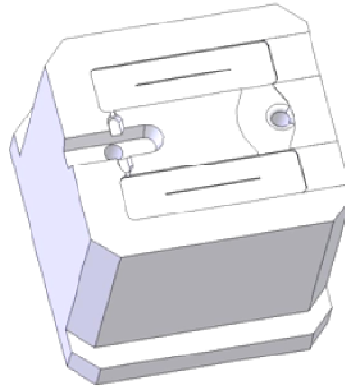


Figure 5.3. Moulding block with ribs produced by micromilling and microEDM

The second block has two cavities, one similar to the previous ones, but produced by laser milling, the second, a round protrusion produced by micromilling, with a through hole to study weld-line formation (Figure 5.4).

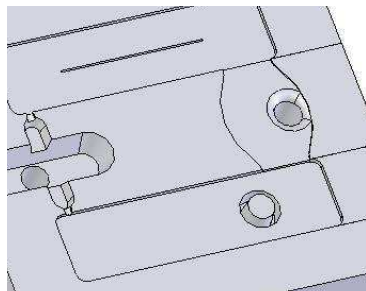


Figure 5.4. Moulding block with rib produced by laser milling and protrusion produced by micromilling

The dimensions of the ribs produced by micromilling, microEDM and laser milling in each cavity were detailed in Table 5.1 along with the aspect ratios of each rib.

The micromilling operations were made with a FIDIA HS644 High Speed Micro Machining Centre (Torino, Italy) with a spindle speed of 36.000min^{-1} . Other relevant of machine features are rapid acceleration and high axis feeds and sophisticated algorithms of the Fidia C1 numerical control. With these solutions, the equipment is capable of milling hard materials that have been traditionally machined by EDM, exhibiting good results in terms of surface roughness, accuracy and execution times. The parameters used for manufacturing are listed in Table 5.2.

Table 5.2. Micromilling processing parameters

Parameter	Units	Values
Cutting Speed (V_c)	$m.min^{-1}$	68
Spindle Speed (n)	min^{-1}	36.000
Feed per tooth (f_z)	μm	4
Width of cut (a_c)	μm	4

For laser beam machining, a Deckel-Maho DML 40 SI (Bielefeld, Germany) with 100 W Nd:YAG-type pulsed laser with wavelength of 1064 nm was used. Several parameters can be considered when producing 3D microfeatures. With this specific equipment, it is possible to change processing parameters such as pulse frequency, scanning speed, machining strategy, cutting depth and hatching on industrial environment. The operating parameters used for manufacturing are listed in Table 5.3.

Table 5.3. Laser beam machining processing parameters

Parameter	Units	Values
Pulse frequency	kHz	30
Cutting depth	μm	2
Hatching	μm	10

The microEDM was performed with an AgieCharmilles Hyperspark (Geneve, Switzerland). Removal and surface roughness determine the pulse time requirement. In the case of EDM, the objective is always to optimise the material removal performance and to reach the surface quality of the workpiece being processed. The operating parameters are described in Table 5.4.

Table 5.4. μ EDM processing parameters

Parameter	Units	Values
Current Intensity	A	0,8
Voltage	V	120
Pulse time	μs	7,5 - 32
Pause time	μs	2,4

From hereon these moulding blocks will be referred to as MS01, the one with identical cavities, and MS02 that with the rib and the circular feature. A view of these moulding blocks is shown in Figure 5.5.

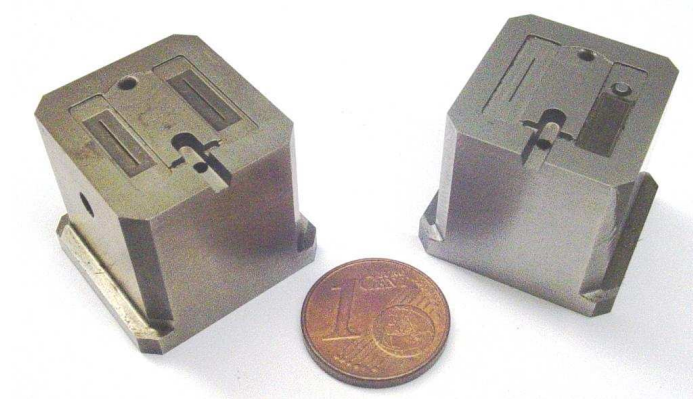


Figure 5.5. Moulding blocks manufactured by subtractive technologies, MS01 at the left and MS02 at the right

5.2. Additive technologies

In view of the brittleness and cost of the parts produced by additive technologies, a base insert was designed to assemble moulding blocks manufactured in this way (Figure 5.6). This base insert was manufactured in 1.2767 (X45NiCrMo4) tempered steel.

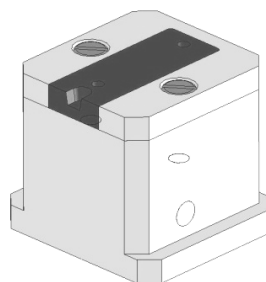


Figure 5.6. Moulding block base for inserts produced by additive technologies

The block is attached to the base by a fixing ring which is fixed on the main body by two screws (Figure 5.7). This setup is required to provide suitable fixation on the base insert and also to minimize the construction volume. For an appropriate temperature monitoring, this assembly must

consider the location of the thermocouple on the additive moulding block itself. Therefore, the base insert is equipped with a through hole to enable this type of assembly for the thermocouple.

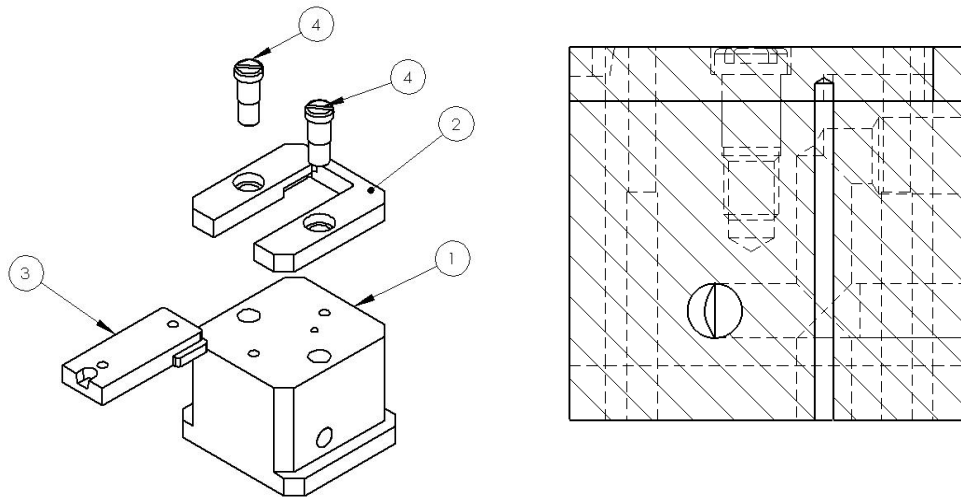


Figure 5.7. Exploded view of the moulding block base (1), fixing ring (2), moulding insert (3), fixing screws (4) and a cross-section showing the hole for the thermocouple

The moulding insert obtained by additive technologies has a maximum height of 3 mm, this dimension being suitable for construction in each of the technologies selected. The dimensions for the blank moulding block insert are shown on Figure 5.8.

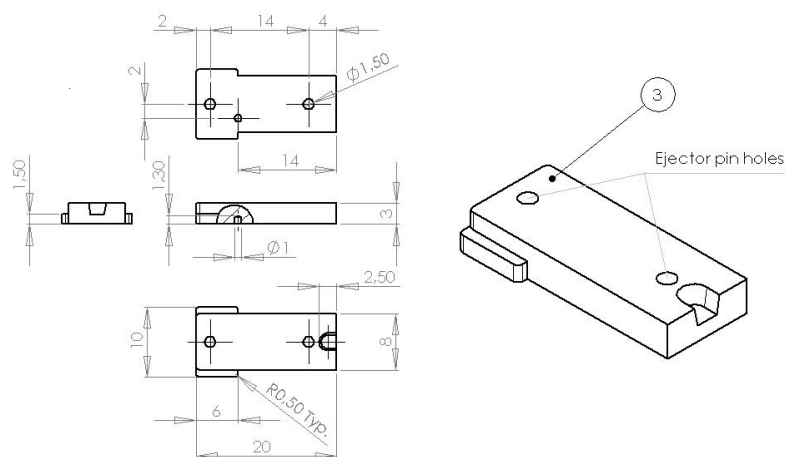


Figure 5.8. Blank moulding block insert

Three inserts were designed to be manufactured by additive technologies enabling the evaluation of several problems that could occur during the injection procedure. These aspects were the mechanical resistance to flow effects during filling (Figure 5.9 a); the evaluation of the replication of microfeatures (Figure 5.9 b); and the evaluation of the effect of ejection forces (Figure 5.9 c). These moulding blocks hereon will be identified with the prefix “BA” followed by two digits according to the shapes illustrated there in. It is also added the suffix “SLA” or “SLM” to identify the technology used in rapid prototyping, Stereolithography and Selective Metal Melting, respectively.

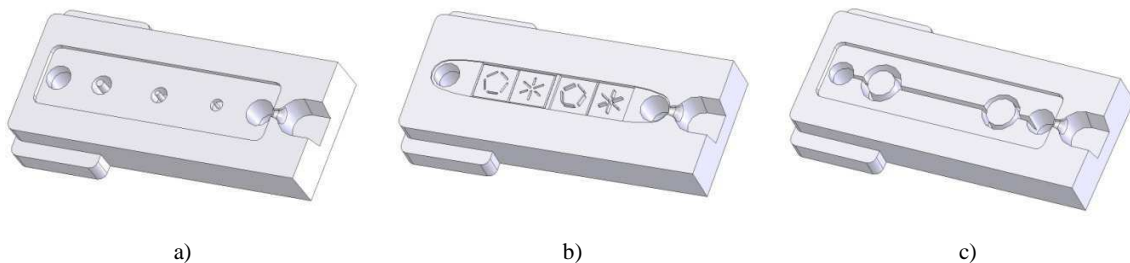


Figure 5.9. Moulding block obtained by additive technologies: a) BA01; b) BA02; c) BA03.

The BA01 moulding block is meant to evaluate the mechanical resistance to flow effects during cavity filling, therefore, a set of pins of different aspect-ratios were designed. The replication of microfeatures is going to be studied with the BA02 moulding block, where two institutional logos were used in low relief, closer to the gate, and in high relief next to the end of the cavity. The microdetails have a minimum width of 100 μm . Finally, for the evaluation of the mechanical strength offered by this type of mould insert on the ejection phase, the BA03 moulding block features two annular sections and a connecting rib between them, which creates a large contact area therefore causing difficulties resulting from the friction forces involved.

5.3. Materials

5.3.1. Subtractive technologies

The material selected for the moulding blocks produced by subtractive technologies is typical steel used by the mouldmaking industry, 1.2767 (X45NiCrMo4). This steel is widely used due to its excellent properties concerning finishing and machinability operations. The main properties are described on Table 5.5.

Table 5.5. Mechanical and thermal properties for the 1.2767 steel (manufacturer data)

Property	Unit	Hardness [HRC]		
		58	55	50
Tensile strength	MPa	1960	1860	1620
Compressive strength	MPa	2745	2450	2060
		Temperature		
		20°C	200°C	
Density	kg/m ³	7750	7700	
Coefficient of thermal expansion from 20°C	µm/m°C	-	11,6	
Thermal conductivity	W/m.K	26,1	27,1	

5.3.2. Additive technologies

Stereolithography

Despite some handicaps of the stereolithography resins, namely low thermal conductivity leading to longer cycle times and limited mechanical strength, they have been considered a viable solution in rapid tooling [89, 90]. In this work, the resin NanoForm 15120 from DSM Somos (Hoek van Holland, The Netherlands), an epoxy resin filled with ceramic nanoparticles that produces strong and stiff parts, was chosen for producing the inserts in the moulding blocks. It has been used successfully in injection moulding for short to medium run production [90, 91]. The mechanical

and thermal properties of the material are listed on Table 5.6, where the post-cure treatments effects are considered.

Table 5.6. Mechanical and thermal properties of DSM Somos Nanoform 15120

	ASTM method	Property	Unit	After UV post-cure	After UV + Thermal post-cure	
Mechanical properties	D638M	Tensile strength	MPa	48	53	
		Elongation at break	%	2,1%	1,2%	
		Modulus of elasticity	C	5000	5900	
	D790M	Flexural strength	MPa	98	129	
		Flexural modulus	MPa	3630	4450	
	D256A	Izod impact-notched	J/cm	0,15	0,159	
	D695-02a	Compressive strength	MPa	137	234	
		Compressive modulus	MPa	4510	4680	
D1004	Hardness	Shore D	93	92		
Thermal properties	E831-00	Coefficient of thermal expansion	0° to 50°C	µm/m.K	111,9	50,9
			50°C to 100°C	µm/m.K	143,6	84,0
			100°C to 150°C	µm/m.K	106,3	128,6
	E1545-00	Glass transition temperature	°C	39	80	
	D648-98c	Heat deflection temperature @ 0,455 MPa	°C	65,5	269	
		Heat deflection temperature @ 1,82 MPa	°C	52,9	115	

Selective Laser Melting

The material used with this rapid prototyping/manufacturing method is a pre-alloyed stainless steel fine powder GP1 from EOS (Germany). It corresponds to the European classification 1.4542 (X5CrNiCuNb16-4) and is characterized by good chemical and mechanical properties for which it is widely used in engineering applications. The GP1 powder has an average grain size of 30 µm, and the minimum layer thickness recommended for processing is 20 µm. The mechanical and thermal properties of GP1 are detailed in Table 5.7.

Table 5.7. Mechanical and thermal properties of EOS GP1 powder

		Properties	Values
Mechanical properties	Tensile strength	Horizontal direction (MPIF 10)	1050 ±50 MPa
		Vertical direction (modified MPIF 10)	980 ±50 MPa
	Yield strength	Horizontal direction (MPIF 10)	540 ±50 MPa
		Vertical direction (modified MPIF 10)	500 ±50 MPa
	Elongation at break (MPIF 10)		25 ±5%
	Modulus of elasticity (MPIF 10)		170 ±20 GPa
	Hardness (DIN EN ISO 6507-1)		230 ±20HV
Thermal properties	Coefficient of thermal expansion 20° to 600°C		14 µm/m.K
	Thermal conductivity	@ 20°C	13 W/m.K
		@ 100°C	14 W/m.K
		@ 200°C	15 W/m.K
	Maximum operating temperature		550°C

5.3. Polymers for microinjection moulding

Materials already used by other authors in microinjection studies, e.g. [57, 72, 92] were used in this work. For assessing the effect of the crystallinity, amorphous (PS) and semi-crystalline (PP and POM) materials were chosen. The Moplen PP was supplied by Lyondell Basell (The Netherlands), the Polystyrol PS by BASF (Germany), and the Hostaform POM by Ticona-Europe (Germany). The relevant properties of these materials are listed in Table 5.8.

Table 5.8. General properties of the thermoplastics

Material	Grade	Density [kg/m ³]	MVR [cm ³ /10min]	Mould shrinkage [%]	Thermal conductivity [W/m.K]	Specific heat [J/kg.K]
PP	Moplen HP548R	905	31	1,8 – 2,0 (estimated)	0,202	1900
PS	Polystyrol 145D	1046	15	0,3 – 0,6 (D955)	0,15	2300
POM	Hostaform C27021	1410	24	1,8 – 1,9 (ISO 1133)	0,155	2210

5.4. Rapid prototyping

Laser micro sintering has been used in microinjection tooling [4]. The selection of the additive process more suitable for a given tool depends on the type of materials to process. Metallic powders suffer from limitations associated to the binding mechanisms [93, 94], namely the surface roughness. In this aspect stereolithography using polymeric resins is a very precise method. Thus, high-resolution stereolithography, and selective laser melting of metal powders were selected for manufacturing moulding blocks.

5.4.1. High-resolution stereolithography

The equipment used to produce the components was a Viper Si² by 3D Systems (Valencia, USA). The main equipment features are summarized on Table 5.9.

	Type	Solid state Nd:YVO4
Laser	Wavelength	354,7 nm
	Power at vat	100 mW
	Process	Zephyr TM recoating system
Recoating system	Beam diameter (standard)	0,250 ±0,025 mm
	Beam diameter (hi-res mode)	0,075 ±0,015 mm
Optical and scanning	Vertical resolution	0,0025 mm
	Position repeatability	0,0076 mm
	Build velocity	5 m.s-1

The NanoForm components were outsourced at SIRRIS (Gosselies, Belgium) and subjected to an UV post-cure right after manufacturing. The mechanical and thermal properties are improved with no significant variation on hardness, allowing finishing operations.

As shown in Table 5.6, material properties can be enhanced by performing an additional post-cure treatment. Since deviations are expected after this thermal treatment, all correction operations were postponed until a new dimensional analysis was performed. The thermal post-cure was programmed according to SIRRIS recommendations, by following the temperature profile depicted on Figure 5.10.

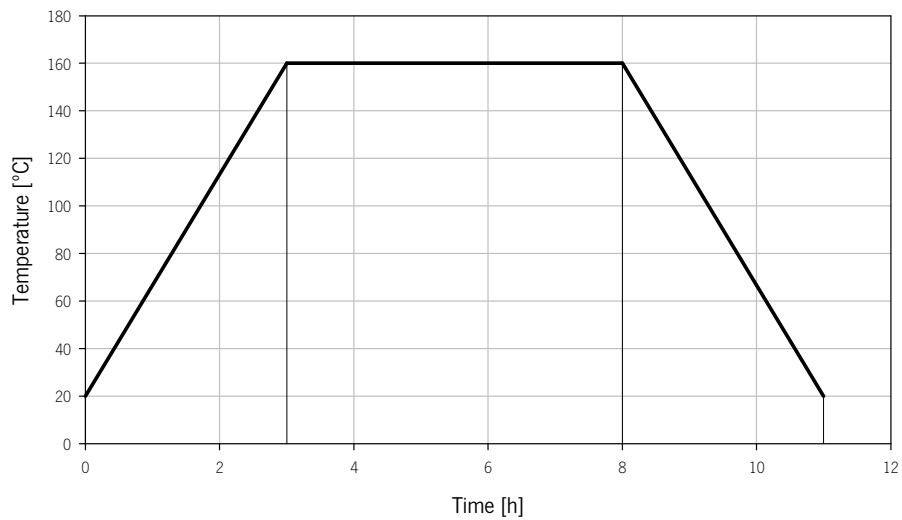


Figure 5.10. Temperature profile for the thermal post-cure of NanoForm 15120

The thermal treatment was performed in a furnace under controlled temperature, with the components immersed in glass beads. This enables uniform heating of the components, avoiding hot spots that could promote warpage of the components upon relieving internal stresses. Furthermore, according to the manufacturer data, it increases the glass transition and the heat deflection temperatures, enabling its use on microinjection moulding.

5.4.2. Selective laser melting

The parts obtained by SLM of metals were outsourced at Fundación Prodentec (Gijon, Spain). The equipment used was an EOSINT M270, by EOS (Krailling, Germany). The main features of the equipment are summarized in Table 5.10.

Table 5.10. System specifications of EOS EOSINT® M270

Laser	Type	Yb-Fibre laser
	Power	200 W
Optical	Variable focus diameter	100 to 500 μm
	Scan speed	Up to 7,0 m.s^{-1}
	Precision optics	F-theta-lens, high speed scanner
Platform	Layer thickness (material dependant)	20 to 100 μm
	Build velocity (material dependant)	2 to 20 m.s^{-1}

The sintering process occurs at 80°C in nitrogen atmosphere at 0,15 kPa. Oxygen levels are kept below 0,7% to prevent reaction with gases generated during processing and oxidation of the parts.

For the sintering, three parts were produced simultaneously and positioned so that the recoating unit could not introduce any positioning error. By placing the parts on a diagonal pattern and rotating them by just 10° it is enough to prevent the recoating unit from colliding with all the parts at the same time and, for each one of them, to enable a smooth recoating operation, from one corner to the opposite one (Figure 5.11).

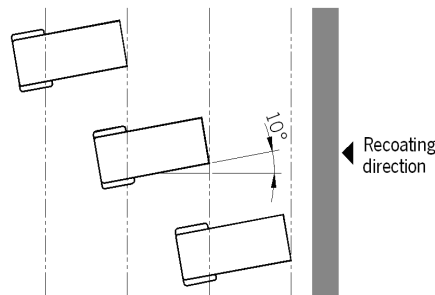


Figure 5.11. Parts positioning for the selective laser melting process

The process performs an initial laser scan on the slice contour, to contain the sintering area of the slice. Then, a hatch scan is performed inside that area using a hatch angle which is going to be increased in every slice to prevent unwanted orientation effects on mechanical properties and dimensional variations. At the end of each slice, a post-contouring scan for a final definition of the sintered area on the slice is performed (Figure 5.12).

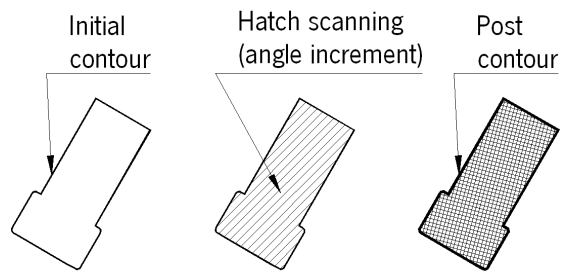


Figure 5.12. Processing phases used by the EOSINT® M270

The parts were built on support pillars to facilitate the separation from the platform. Finishing operations are required to remove the pillars and to ensure overall dimensions and tolerances of the sintered parts. Figure 5.13 shows two sets of parts still attached to the building platform.

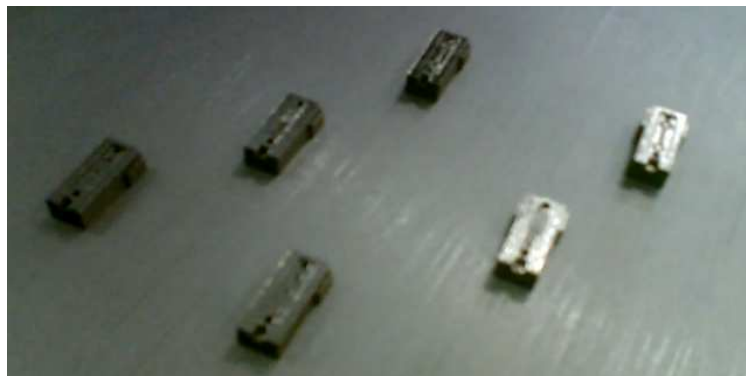


Figure 5.13. Parts processed at the EOSINT M270

5.5. Capillary rheometry

The preliminary evaluation of viscosity for all polymers was carried out in a twin-bore Rosand RH10 capillary rheometer from Malvern Instruments (Malvern, UK). The determination of standard flow curves was carried from 180°C to 250°C, covering the range of processing temperatures used in the microinjection tests.

The capillary rheometry tests were performed with a Ø1 mm bore, using two dies: a) 16 mm long die for calculating the pressure drop and b) zero-length die for the entry correction and Bagley procedure.

5.6. Microinjection moulding

The injection tests were performed on a microinjection moulding cell based on a 129 kN clamping force Boy 12 A injection moulding machine already described in Chapter 4, Section 4.9.

5.6.1. Injection moulding program

The test planning considered the different moulding blocks tested as well as the polymer to be moulded. The setting of the processing conditions, particularly concerning to the melt temperature, mould temperature and the maximum working temperature of the Nanoform 15120 resin was taken into account in the case of the stereolithography moulding blocks. For the metallic blocks, the temperatures were raised to enhance the process performance.

The processing conditions used with the moulding blocks manufactured by subtractive technologies are summarized on Table 5.11.

Table 5.11. Processing conditions for the materials used on the MS00 moulding blocks

	Material	Melt temperature [°C]	Mould temperature [°C]	Injection pressure [MPa]	Holding pressure [MPa]	Flow rate [cm ³ .s ⁻¹]
MS01	PP	230	80	6	3	123
	PS	240	60	12	0,2	154
	POM	200	95	10	0,2	154
MS02	PP	230	80	8	5	123
	PS	240	60	12	0,2	154
	POM	200	100	10	0,2	208

The processing conditions for the SLA Nanoform 15120 are summarized in Table 5.12, referring to the BA00SLA blocks.

Table 5.12. Processing conditions for the materials used on the BA00SLA moulding blocks

	Material	Melt temperature [°C]	Mould temperature [°C]	Injection pressure [MPa]	Holding pressure [MPa]	Flow rate [cm ³ .s ⁻¹]
BA01SLA	PP	240	50	4	2	77
	PS	240	60	12	0,2	154
	POM	215	75	4	2	77
BA02SLA	PP	240	50	4	2	77
	PS	240	60	12	0,2	154
	POM	215	90	4	2	139
BA03SLA	PP	240	50	4	2	77
	PS	240	60	12	0,2	154
	POM	205	80	4	3	66

In the case of the SLM moulding blocks, due to the similarity of thermal conductivity and thermal expansion of the GP1 material to steel, the processing conditions were closer to those on Table 5.11. The processing conditions for the BA00SLM blocks are summarized in Tables 5.13.

Table 5.14. Processing conditions for the materials used on the BA00SLM moulding blocks

	Material	Melt temperature [°C]	Mould temperature [°C]	Injection pressure [MPa]	Holding pressure [MPa]	Flow rate [cm ³ .s ⁻¹]
BA01SLM	PP	240	70	6	5	231
	PS	240	60	12	0,2	154
	POM	215	100	6	2	231
BA02SLM	PP	240	70	6	5	231
	PS	240	60	12	0,2	154
	POM	215	100	6	2	231
BA03SLM	PP	240	70	6	5	231
	PS	240	60	12	0,2	154
	POM	215	100	6	2	231

5.7. Characterization

The dimensions of the moulding blocks as well as the microdetail dimensions required several characterization operations to support this research work. This subtopic describes the characterization methods used.

5.7.1. Microscopy

The assessment of the integrity of the moulding blocks, after production or post-treatment was performed by optical and hybrid microscopy. The optical microscopy analyses were done with a Axiotech 100HD microscope from Carl Zeiss (Göttingen, Germany) (Figure 5.14).

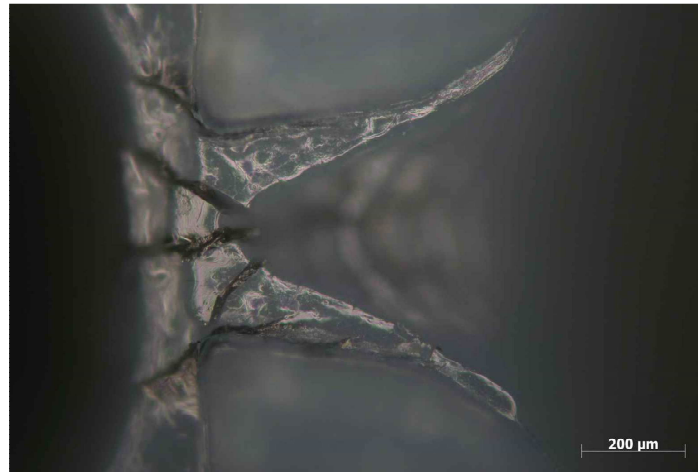


Figure 5.14. Sample of optical microscopy obtained with the Carl Zeiss Axiotech 100HD

The SLA blocks were examined with a VHX-500F hybrid microscopy system from Keyence (New Jersey, USA). This equipment is capable of obtaining high resolution images, up to 2,11 Mpixels through a CCD image sensor (Figure 5.15).



Figure 5.15. Sample of hybrid microscopy measurements obtained with the Keyence VHX-500F

5.7.2. Roughness evaluation

The surface roughness evaluation of the moulding blocks was performed by contact and non-contact solutions. For the contact tests, a perthometer Mahr Marsurf M2 (Göttingen, Germany) was used on the MS00 and BA00SLM blocks, whose material enables a roughness contact measurement without damaging the part. A typical roughness profile is shown in Figure 5.16.

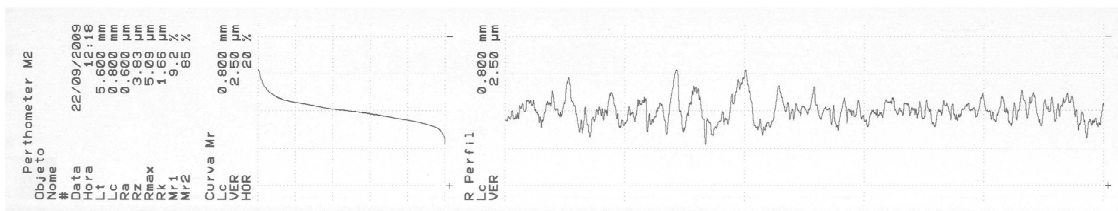


Figure 5.16. Sample of roughness profile obtained with the Mahr Marsurf M2

For preserving the integrity of the BA00SLA blocks, it was used a non-contact solution for the surface roughness evaluation and surface characterization. A laser perthometer Rodenstock RM600-3D (Munich, Germany) was used. This equipment enables the full mapping of 3D surfaces, based on the data acquired by an automatically focused infrared optic sensor. The data was post-treated with the Gwyddion[®] software, which enables the improvement on the graphical representation of the surfaces' topography (Figure 5.17).

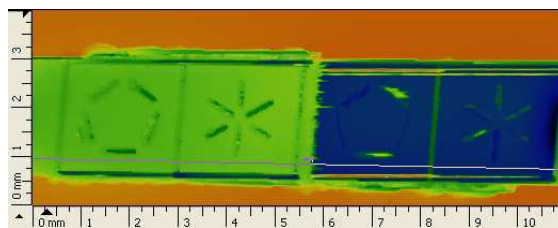


Figure 5.17. Sample of the 3D mapping of the surface obtained with the Rodenstock RM600-3D

5.7.3. SEM and X-ray spectroscopy

SEM scans were performed with a scanning electron microscope FEG-SEM, Nova Nano SEM 200 (Hillsboro, USA). SEM scanning was used to obtain detailed images of the microfeatures on BA00SLA moulding blocks. The sample was attached to an aluminium pin with a double face

tape. The SEM analysis was carried out at low vacuum without any coating of the samples and using an acceleration tension of 5 keV (Figure 5.18).

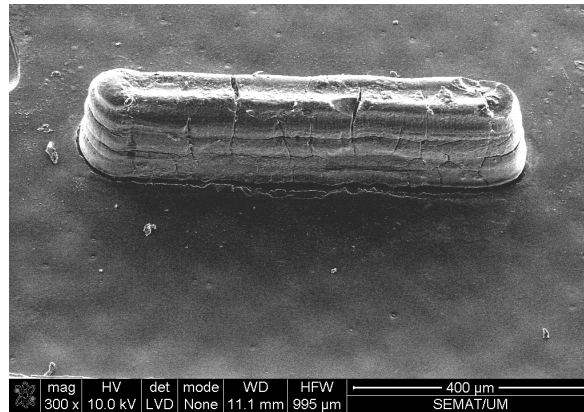


Figure 5.18. Sample SEM images of the microdetails obtained with the Nova Nano SEM 200

The elemental analysis was carried out with a EDAX integrated X-ray microanalysis system to perform elemental analysis by energy dispersive X-ray spectroscopy, using a Si(Li) detector (New Jersey, USA). This elemental analysis was performed to determine which material was present on the SEM images. Elemental analysis occurred at an internal chamber pressure of 90 Pa with an acceleration tension of 10 keV. An example of an elemental analysis carried out on polymer particle reveals traces of Nanoform resin and POM, as shown in Figure 5.19.

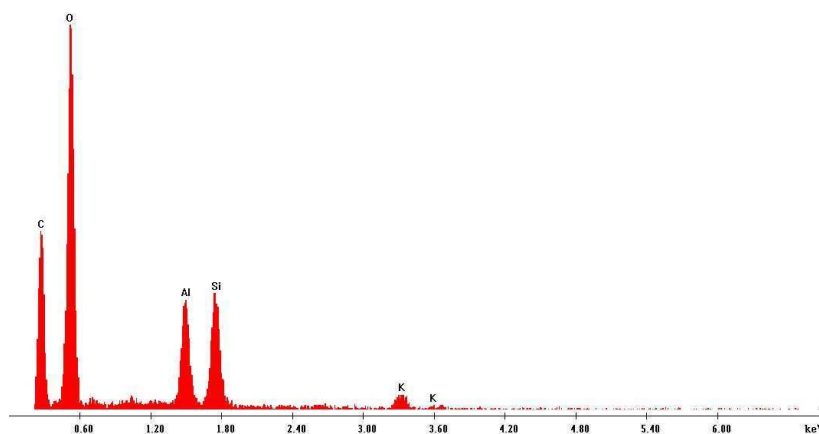


Figure 5.19. Sample elemental analysis obtained with the EDAX X-ray analyser

5.8. Numerical simulation

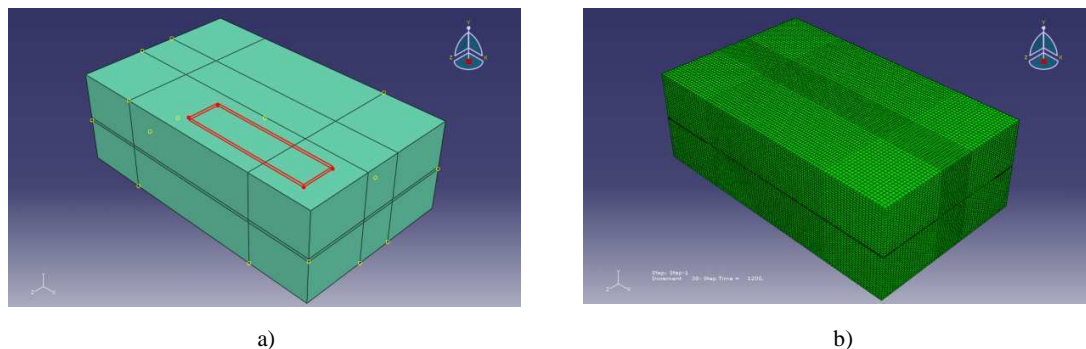
Mathematical modelling of phenomena enables early assessment of what is likely to happen to a system or to a component limited by known boundary conditions when submitted to predictable loads or thermal and flow fields. In which concerns microinjection moulding, there is still insufficient data for a precise prediction of polymer flow at the microscale. Therefore, heat transfer simulation is recommendable prior to the filling simulation, in order to improve the results.

5.8.1. Heat transfer simulations

Heat transfer is one of the variables less known at the microscale. It was already mentioned in Chapter 3 that in microinjection moulding some departure from conventional heat transfer models should be reviewed at this scale. Thus, a simple 3D model of an injection moulded bar was considered to evaluate heat transfer. In the analysis it is assumed that filling of the cavity has just ended and the analysis is focused on the heat transfer from the polymer to the cavity and core materials.

Simulation model

The simulations were performed on Abaqus, release 6.7. The 3D model for the heat transfer simulation is depicted in Figure 5.20.



a) mould with highlight of the impression; b) simulation mesh with 277245 nodes and 264000 elements

This model consists of three elements: the impression filled with melt, the cavity and the core. The moulding is a thin parallelepiped of 16×4×0,3 mm that was meshed so that at least 3 elements exist through the thickness, which implies an average mesh size of 0,1 mm. The element DC3D8 type selected on Abaqus is an eight-node brick element, able to support heat transfer through convection and diffusion. The cavity and the core were also meshed with this type of element. These meshes were refined to match the impression surface, leaving the corner volumes with a coarse mesh size since the contact area between both sections is null.

The properties of the material can be input in each part of the simulation volume, enabling the test of various material combinations. The materials used in the simulations were EOS GP1, Nanoform 15120 and 1.2767 tool steel. The relevant properties of these materials are listed in Table 5.14.

Table 5.14. Thermal properties

Material	Property		
	Thermal Conductivity [W/m.K]	Density [kg/m ³]	Specific Heat [J/m ³ .K]
1.2767 tool steel	32 @293K (34 @423K)	7850	460
Nanoform 15120 *	0,307 @293K	1380	1582
EOS GP1	13 @293K (14 @373K)	7800	460
Hostaform C27021	0,155 @293K	1410	2210

* Material data supplied by supplied by SIRRIS (Belgium)

Loads and boundary conditions

In this particular case, the loads are the imposed temperatures. Considering that only the cooling phase is going to be analyzed at this point, this simulation was prepared under the following assumptions:

- The cavity has just been filled, so, the polymer melt has suffered only the temperature drop corresponding to the heat dissipated on the sprue and channels;
- The cavity and core sections are subject to a initial temperature of 90°C, a typical mould temperature imposed in several injection tests;
- The outside air temperature is 25°C enabling the temperature drop.

Heat transfer simulation planning

The goal of this heat transfer simulation is to establish the magnitude of the heat flows verified in each combination of materials. The following material combinations tested are shown in Table 5.15.

Table 5.15. Planning for the heat transfer simulations

Section	Initial temperature	Simulation 1	Simulation 2	Simulation 3	Simulation 4
Cavity	90°C	1.2767 Steel	1.2767 Steel	1.2767 Steel	Nanoform 15120
Moulding	180°C	POM Hostaform C27021			
Core	90°C	1.2767 Steel	EOS GP1	Nanoform 15120	Nanoform 15120

5.8.2. Filling simulations

The software packages to simulate the injection moulding procedure are based on conventional governing equations. Preliminary results (as reviewed in Chapter 2), showed that current software packages cannot accurately predict the results of the microinjection procedure without incorporating the effects of microscale phenomena.

The software Moldex 3D (Core-Tech, Taiwan) was used for comparing filling simulation of various impressions with the pressure data obtained from the instrumented mould.

Simulation models

Considering the different cavities to be submitted to a filling simulation for comparison with the experimental data obtained, two different sprue configurations were modeled for compatibility both with the “MS00” and the “BA00” moulding blocks: 1) a double-gate sprue and 2) a single-gate sprue, respectively (Figures 5.21 and 5.22).

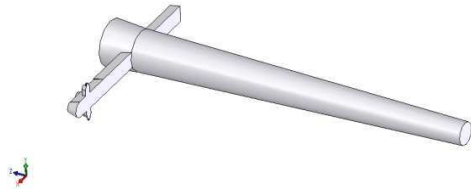


Figure 5.21. 3D model of the double gate runner used on the “MS00” moulding blocks

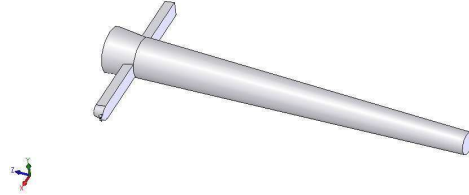


Figure 5.22. 3D model of the single gate runner used on the “BA00” moulding blocks

For this particular type of simulation, Moldex 3D recommends a three-dimensional hybrid type of mesh, the Boundary Layer Mesh (BLM), incorporating prismatic and tetrahedral elements. This mesh incorporates different topological elements enabling the full description of the non-continuous temperature distribution at both sides of the interface between the melt and the mould [95].

Furthermore, all part models were meshed ensuring that the number of elements across the part thickness was equal or above 5, causing the decrease of element size and consequently, the increase of the number of elements. The example illustrated on Figure 5.23 shows a broken-out section of the MS01 model mesh. In this particular location, the part thickness at the base is 300 μm and the rib is 100 μm wide. Two layers of prismatic elements at the interface are combined with tetrahedral elements on the core, all over the part.

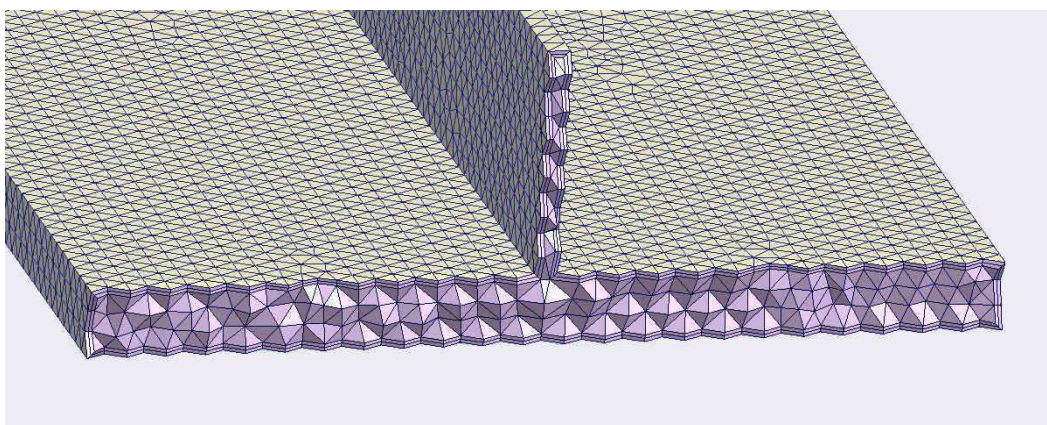


Figure 5.23. Broken-out section of the MS01 model mesh

Filling simulations planning

The performed numerical simulations were made using the processing conditions used in the experimental program described in Section 5.5.2. All mesh models incorporated two node sensors on the exact location of the pressure sensors located on the mould impression, enabling the comparison of pressure data from both sources.

From the range of moulding geometries tested were selected three models considered as representative for the numerical analysis, a) MS01, b) BA02 and c) BA03. The filling simulation planning for these models are described on Table 5.16.

Table 5.16. Filling simulations planning

Mesh model	Technology	Filling	Packing	Warping
MS01	Subtractive	Yes	Yes	Yes
BA02	SLA	Yes	Yes	If relevant
	SLM			
BA03	SLA	Yes	Yes	If relevant
	SLM			

Chapter 6 – Results and discussion

The experimental results of this research work are reviewed and analyzed in this chapter. Although some preliminary conclusions were possible after each experiment, only the correlation between results in different areas will provide the required data for final conclusions. The discussion hereupon is organized into the following topics: a) production of moulding blocks; b) microinjection moulding; c) replicability; d) surface wear; and e) numerical simulation.

6.1. Moulding blocks

The technologies and equipments used for the manufacture of the moulding blocks were described on Chapter 5. Although it is relevant to compare these processes, the manufacturing approach of each technology must be addressed separately since specific features are not directly comparable.

Considering the processes that rely on a top-to-bottom approach, in this case, micromilling, microEDM and laser beam machining, there is an important limitation concerning feature size since none of these processes is able to obtain a 3D feature below 10 μm . From these processes, micromilling and microEDM provide the best surface finishing and microEDM achieves the maximum aspect-ratio [19]. On laser beam machining, the use of an optical tool enables higher scanning speeds and expectably, higher material removal rates. However, a compromise between these parameters is required to improve surface finishing [96].

The key issue for processes whose manufacturing approach is bottom-to-top is the mechanical behaviour of its products. The SLM process enables the manufacture of full density metal parts, its products exhibiting good mechanical properties [94]. Material improvements have enabled SL to use photocurable resins with ceramic nanofillers to improve the mechanical properties of the products [97]. Other parameters such as scanning strategy and laser power are conditioning factors for surface finishing on the SLM process [98]. Concerning the replication of the microdetails addressed in work, high precision SLA is more effective than SLM.

On an overall comparison between all these processes, three key features arise, a) freeform geometry, b) mechanical integrity of the products upon use and c) manufacturing time.

The capacity of producing a full freeform geometry is the domain of rapid prototyping/rapid manufacturing and specific alternative materials must be used to enable that capacity. However, concerning the mechanical behaviour, only metallic products are able for long term use. Finally, the flexibility of RPT shortens manufacturing time, although some of the products may require some post-processing operations.

6.1.1. Cavity geometries

The MS type geometries present a challenge concerning the manufacturing of the moulding blocks and the success of microinjection. The MS01 (a) and MS02 (b) moulding blocks are shown on Figure 6.1.

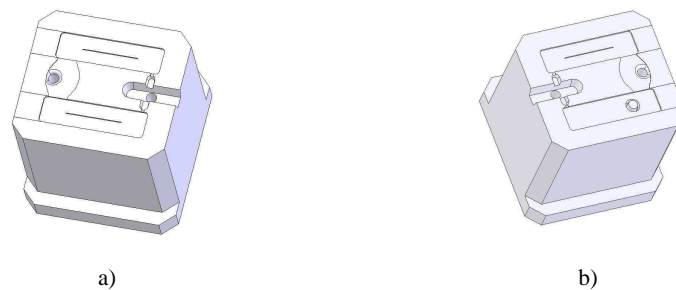


Figure 6.1. Steel moulding blocks

From the manufacturing point of view, it is relevant to determine if subtractive processes could yield the intended geometries from a single block of material, without using any inserts. The aspect ratio of the rib features makes it interesting also for microinjection considering that the rib width is small enough to be considered as a thin-wall. However, the manufacturing approach caused an additional problem in microinjection since air vents could only be created at the parting plane and not on the top of the ribs, as it is common on conventional injection moulding. Filling simulation will be performed, in order to determine if the predicted polymer flow behaves as in reality.

The BA type geometries present several difficulties regarding manufacturing. The use of materials with rather different mechanical properties requires specific processing conditions. This is particularly true for the moulding blocks manufactured by high precision stereolithography. On the other hand, the surface finishing achieved by each manufacturing technology along with its replication on the moulded parts will cause additional difficulties during microinjection.

The aims of the BA01 geometry are: a) from the manufacturing point of view, to determine if it would be possible to build the pins; b) from the microinjection point of view, to determine the capacity of filling the protrusions and c) from the mechanical integrity point of view, to determine if the pins could withstand the effect of polymer flow (Figure 6.2).

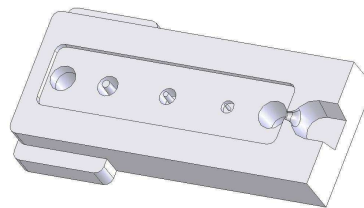


Figure 6.2. BA01 geometry

The BA02 geometry presents a challenge concerning the filling of the microfeatures that define the logos. An additional challenge is imposed since polymer must fill first the thin-walls that connect the microfeatures. The mechanical behaviour of the moulding block microfeatures is also a issue, especially in the case of Nanoform 15120 as a base material (Figure 6.3).

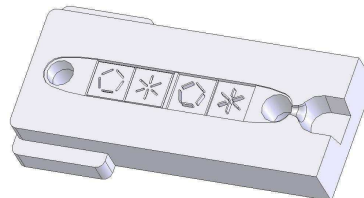


Figure 6.3. BA02 geometry

The BA03 geometry was designed to evaluate the behaviour of the moulding block upon ejection. Such evaluation is certainly more relevant with the BA00SLA blocks due to mechanical properties of the SLA resin. In this case, the main issue lies on the surface finishing of the moulding block and on how it affects the moulded parts (Figure 6.4).

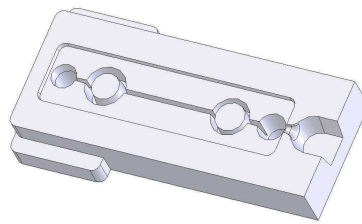


Figure 6.4. BA03 geometry

6.1.2. Steel moulding blocks

The MS01 moulding block has two cavities, each one containing a longitudinal rib with different aspect ratio: a) 10:1 for the rib manufactured by micromilling and b) 15:1 for the rib manufactured by microEDM (see Table 5.1). However, a factor to be accounted for is the draft angle of each rib since the aspect ratio definition does not include that feature, which is relevant for mouldability.

The rib manufactured by micromilling has its walls perfectly vertical. Contrarily, the rib manufactured by microEDM has a small draft angle. In this case, the existence of vertical walls on the rib manufactured by micromilling benefited from a smaller aspect-ratio. The rib manufactured by microEDM has the highest aspect-ratio and benefits from the existence of a draft angle to enable ejection.

The steel moulding blocks group, manufactured from 1.2767 tempered steel, are not likely to suffer wear or abrasion in operation.

Like MS01, the MS02 moulding block has two cavities. The first cavity features a longitudinal rib manufactured by laser milling with aspect ratio of 4:1. Concerning mouldability, there is a generous draft angle to enable a smooth ejection operation. The second cavity has a similar base but instead of a rib, it has a round protrusion with a through hole. Ejection problems may occur

since the only draft angle exists inside the through hole. The outside wall of the round protrusion is vertical, without any draft angle.

6.1.3. RPT moulding blocks

In this section, the preliminary evaluation of the moulding blocks manufactured by rapid prototyping/tooling technologies such as SLA and SLM is described.

SLA moulding blocks

The BA00SLA group gathers the moulding blocks manufactured by high-precision stereolithography. This group is particularly interesting since it provided excellent replication of microdetails and a rather good surface finishing in the preliminary evaluation. However, the combined effect of melt temperature, melt flow and ejection will certainly be relevant on a future use of this type of moulding blocks. Considering those effects, less aggressive processing parameters were used that could preserve the integrity of these moulding blocks. Figure 6.5 shows the set of BA00SLA moulding blocks, ready to be assembled on the micromould.

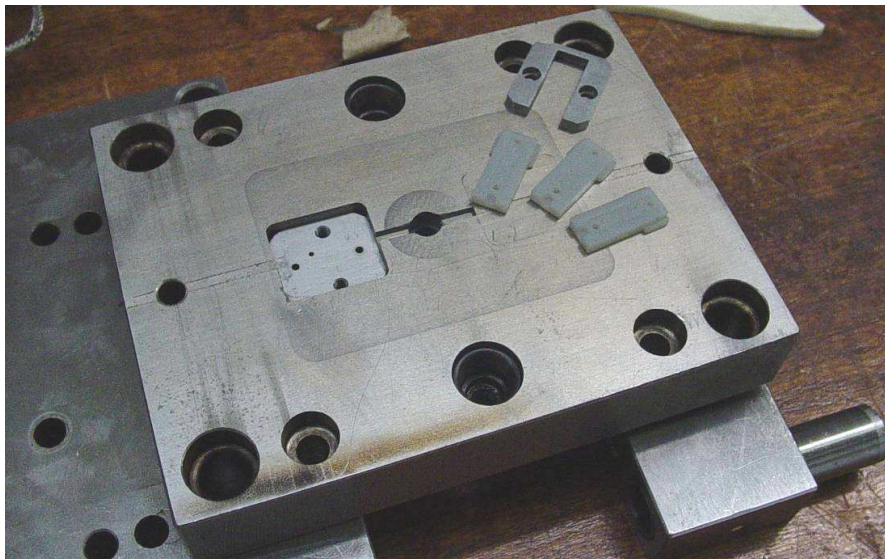


Figure 6.5. BA00SLA moulding blocks

Preliminary dimensional analysis of the components showed some dimensional or other geometric variations that require further analysis after the thermal post-cure.

The initial dimensional analyses were performed with an optical microscopy device Keyence VHX-500F. The critical dimensions for assembly were controlled to determine the dimensional compatibility with the support mould insert, concerning block external dimensions, ejector pin holes diameter and location. An example of the preliminary dimensional analysis for the SLA moulding blocks are shown on Figures 6.6 and 6.7.



Figure 6.6. BA01SLA moulding block, top side (magnified 10×)

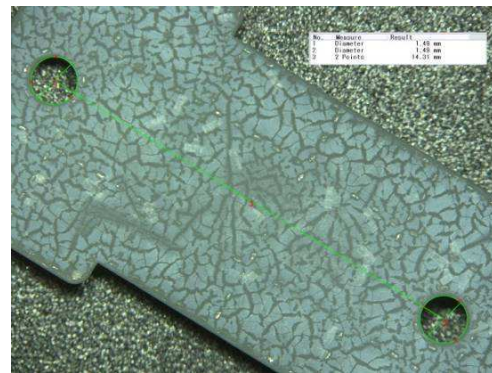


Figure 6.7. BA01SLA moulding block, bottom side (magnified 20×)

The metrology data of all BA00SLA moulding blocks are summarized in Table 6.1.

Table 6.1. Optical microscopy measurements of BA00SLA moulding blocks (units in mm)

Dimension	Nominal	BA01SLA	BA02SLA	BA03SLA
L	20,00	20,43	20,43	20,10
W	8,00	8,17	8,17	8,04
T	3,00	3,10	3,03	3,06
C	14,00	14,31	14,54	14,19
\varnothing_1	1,50	1,49	1,50	1,47
\varnothing_2		1,49	1,50	1,45

Concerning external dimensions, length (L), width (W) and thickness (T), all moulding blocks show excess material that need to be removed for assembly with the support base. Ejector pin holes, on the other hand, show some deviation especially considering their relative position. The distance between the ejector pin holes (C) should be exactly 14 mm but for all cases that distance

shows deviations up to 3,85%. The ejector pin hole diameters (\varnothing_1 and \varnothing_2) however, are according to the 3D model or even smaller, which requires a small preliminary correction on the hole diameters before assembling the ejector pins. After the thermal treatment, no significant dimensional deviations were noticed with respect to the nominal dimensions. Therefore, the same observations made before are now also valid, concerning assembly purposes and components compatibility with ejector pins, especially the holes diameter and the distance between centres. The results of the metrology analysis performed after the thermal post-cure are detailed in Table 6.2.

Table 6.2. Optical microscopy measurements of BA00SLA moulding blocks after thermal post-cure

Dimension	BA01SLA			BA02SLA			BA03SLA		
	Before	After	Variation	Before	After	Variation	Before	After	Variation
L	20,43	20,49	+0,29%	20,43	20,29	-0,69%	20,10	20,32	+1,09%
W	8,17	8,20	+0,37%	8,17	8,15	-0,24%	8,04	8,16	+1,49%
T	3,10	3,10	0%	3,03	3,02	-0,33%	3,06	3,02	-1,31%
C	14,31	14,32	+0,07%	14,54	14,42	-0,83%	14,19	14,32	+0,92%
\varnothing_1	1,49	1,50	+0,67%	1,50	1,50	0%	1,47	1,50	+2,04%
\varnothing_2	1,49	1,49	0%	1,50	1,52	+1,33%	1,45	1,50	+3,45%

The BA00SLA blocks built from Nanoform™ 15120, even after the thermal post-cure, exhibit a glass transition temperature of 80°C, which determines the decrease of processing temperatures to enable the use of these materials in moulding blocks. Therefore, one of the goals in the initial tests was to establish lower limits of the mould temperatures.

The BA01SLA moulding block consists on a series of three cylindrical/conical cavities with pins inside, with different feature dimensions but similar aspect-ratio, in order to mould annular protrusions on the plastic part. However, ejection was not properly considered since the contact area of these pins *versus* the area of the ejection pins caused several problems. The high contact area between pins and moulded part may generate enough friction to cause damage.

The BA02SLA moulding block features a series of 100 µm wide microdetails, depicting the logos of the School of Engineering (from now on designated as *SE* logo) and the University of Minho (from now on designated as *UM* logo), both in high-relief and low-relief. The high-relief and low-

relief areas are connected through a thin wall which required additional injection pressure to make the polymer reach the outlet pressure sensor. Considering the moulding block material, such increase is likely to have damaging effects on the microdetails.

The BA03SLA moulding block has a series of almost vertical walls, meant to evaluate the ejection effects on the moulding block. Basically, besides the two protrusions where the ejector pins acts, the cavity features two annular protrusions connected by ribs, creating a high contact surface. The part itself does not represent a challenge for microinjection, however, the effects of ejection over the Nanoform composite are still to be determined since the results obtained so far with such material indicate that the layer effect due to the manufacturing process and draft angle should be optimized to enhance the moulding block performance [97].

SLM moulding blocks

The BA00SLM group includes the moulding blocks manufactured by selective laser melting, using the same 3D models. From this particular group of moulding blocks and considering the manufacturing process used to produce them, no major damage is expected on the moulding blocks. However, the surface finishing already found on the preliminary characterization, allowed the suspicion that the ejection procedure on these moulding blocks would be rather problematic. On a selective laser melting process, even the debris gets fully attached, decreasing the surface finishing of the part. In which concerns to microinjection processing, the material of these moulding blocks supports the use of high melt and mould temperatures. The EOS GP1 exhibits mechanical and thermal properties similar to stainless steel, enabling processing parameters similar to the ones previously used on the MS moulding blocks.

6.1.4. Moulding block assessment

The moulding blocks were topographically assessed before the microinjection tests to determine initial conditions for future reference. Concerning the MS type moulding blocks in particular, there are some surface roughness results that require attention. On both moulding blocks micromilling was used, so the surface finishing of both areas where the process was applied should be similar. Nevertheless, the MS02 moulding block shows a much higher surface roughness on the

micromilled areas, which is somehow related to the milling strategy. As expected, microEDM and micromilling show the best results while LBM shows only a reasonable surface finishing. Table 6.3 summarizes the surface roughness measurements performed on the MS moulding blocks.

Table 6.3. Preliminary roughness measurements on the MS type moulding blocks

Moulding block	Cavity	Average roughness (Ra)	Mean peak-to-valley height (Rz)	Max. roughness height (Rmax)
MS01	microEDM	0,075 μm	0,59 μm	0,13 μm
	microMilling	0,083 μm	0,69 μm	0,21 μm
MS02	LBM	0,588 μm	3,48 μm	3,82 μm
	microMilling	0,221 μm	1,62 μm	1,85 μm

An optical microscopy analysis of these moulding blocks enabled the evaluation of rib radius and width at the base, as shown on Figures 6.8 and 6.9.



Figure 6.8. Rib detail on the MS01 moulding block manufactured by microEDM

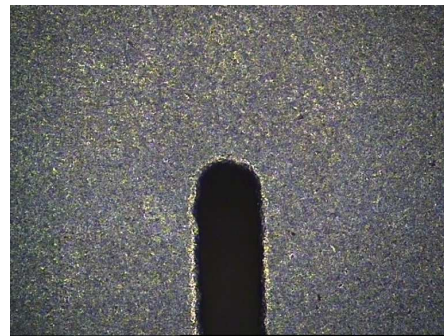


Figure 6.9. Rib detail on the MS02 moulding block manufactured by microMilling

The BA00SLA moulding blocks showed interesting results concerning surface finishing. Although these roughness measurements were taken on the bottom face of the cavity, where no layer effect could be noticed, the surface finishing is only reasonable despite the smooth appearance. Only the BA03SLA moulding block shows excellent surface quality. The results are detailed on Table 6.4.

Table 6.4. Preliminary roughness measurements on the “BA00SLA-type” moulding blocks

Moulding block	Average roughness (Ra)	Mean peak-to-valley height (Rz)	Max. roughness height (Rmax)
BA01SLA	0,645 μm	4,33 μm	4,89 μm
BA02SLA	0,600 μm	3,83 μm	5,09 μm
BA03SLA	0,193 μm	0,95 μm	1,03 μm

The microscopy analysis enables to determine the state of the microdetails prior to the microinjection tests. Figure 6.10 shows the detail of the smallest pin, Pin 1, built with an aspect ratio of 3:1, 200 μm diameter at the base and 600 μm height. Figure 6.11 shows the high-relief and the low-relief logos, where the high-relief is built with microdetails of 120 μm width by 200 μm height.

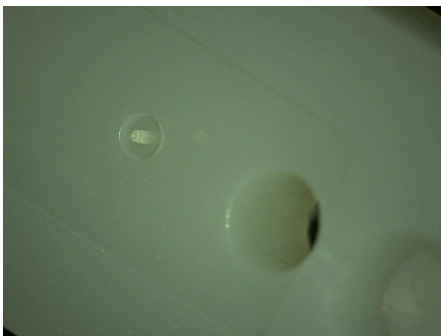


Figure 6.10. Detail of the Pin 1 on the BA01SLA moulding block

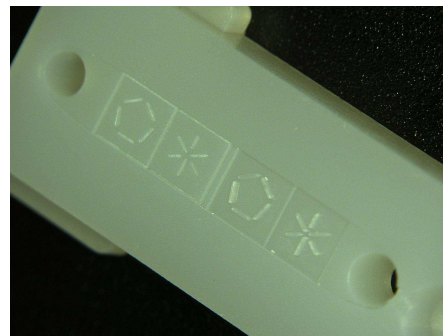


Figure 6.11. Detail of the high-relief and low-relief logos on the BA02SLA moulding block

The BA00SLM type moulding blocks showed the least interesting results concerning surface finishing, this being expectable. Nevertheless, it is relevant to notice that the BA03SLM moulding block shows a quite interesting surface quality. Comparing to the other two moulding blocks also manufactured by SLM, the obvious difference concerning processing is the laser scanning strategy, which may have caused a poor surface quality since both cavities have more details built on them. Table 6.5 summarizes the surface roughness measurements performed on BA00SLM moulding blocks.

Table 6.5. Preliminary roughness measurements on the BA00SLM type moulding blocks

Moulding block	Average roughness (Ra)	Mean peak-to-valley height (Rz)	Max. roughness height (Rmax)
BA01SLM	4,121 μm	19,3 μm	22,5 μm
BA02SLM	5,083 μm	23,02 μm	45,3 μm
BA03SLM	0,936 μm	4,61 μm	5,21 μm

The surface roughness results are confirmed by the microscopy analysis. Surface quality is in fact poor, but, no polishing process was intentionally performed. The elevated edge effect due to the SLM processing can be noticed on all edges [98], as noticed in Figures 6.12 and 6.13.

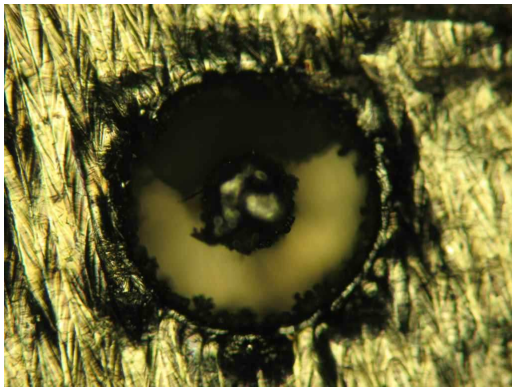


Figure 6.12. Detail of Pin 3 in BA01SLM

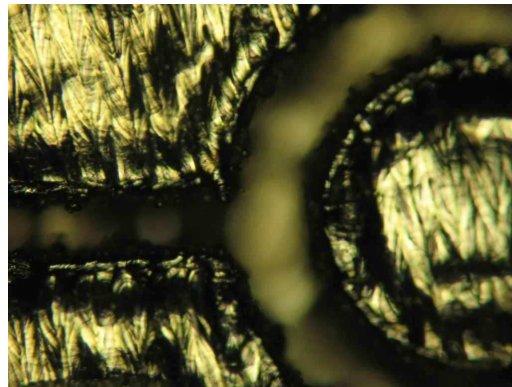


Figure 6.13. Detail of rib wall in BA02SLM

6.2. Microinjection moulding

This section refers to the microinjection moulding procedures, from thermoplastic materials characterization through rheometry techniques, pressure sensor position on the cavity, processing parameters analysis, mouldability on the several moulding blocks tested, cycle time and process repeatability.

6.2.1. Polymer characterization

The thermoplastic materials used on this research were preliminarily characterized through capillary rheometry. The flow curves obtained were then compared to the rheological database for the same thermoplastic materials from Moldex 3D[®], which is the numerical tool selected for the filling simulations.

Considering the range of dimensions that are the subject on this work, capillary rheometry was chosen as the most representative of the type of geometry that is going to be submitted to the microinjection tests. The group of test materials that were subject to capillary rheometry was already described in Chapter 5. The same procedure for preparing the analysis was used on all materials. For each material it was defined a reference temperature (T_{ref}) and from that, additional temperatures: $T_{ref} - 40^{\circ}C$, $T_{ref} - 20^{\circ}C$, $T_{ref} + 20^{\circ}C$ and $T_{ref} + 40^{\circ}C$, that were used depending on the width of the conventional processing temperature range of each material. The capillary rheometry results for the PP Moplen HP548R are shown in Figure 6.14 and Figure 6.15 shows the data for the same material from the Moldex 3D database. Despite some initial instability at $220^{\circ}C$ in capillary rheometry, the polymer behaviour on both flow curves is quite similar especially at higher shear rates.

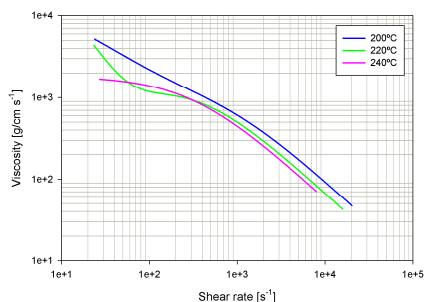


Figure 6.14. Flow curves from capillary rheometry for PP Moplen HP548R

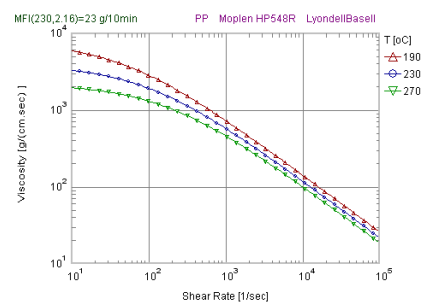


Figure 6.15. Rheological data from Moldex 3D database for PP Moplen HP548R

For the PS Polystyrol 145D, the reference temperature used was 230°C and here also were obtained two other temperatures, respectively at $T_{ref} + 20^\circ\text{C}$ and $T_{ref} - 20^\circ\text{C}$. However, the 230°C flow curve resulted too unstable and it was neglected. Therefore, only the 210°C and the 250°C flow curves are shown in Figure 6.16. The comparison with the Moldex 3D® data (Figure 6.17) shows also similarities on the high shear rate area, however, the index of non-Newtonian flow is higher on capillary rheometry since viscosity decays much faster with the increase of shear rate.

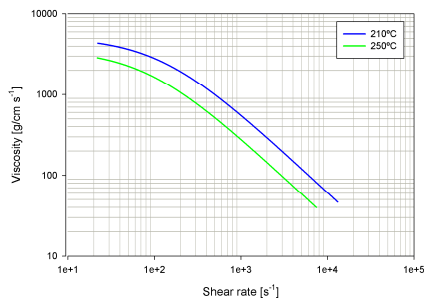


Figure 6.16. Flow curves from capillary rheometry for PS Polystyrol 145D

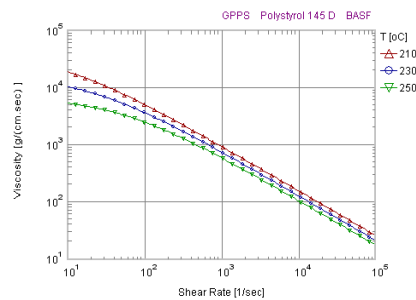


Figure 6.17. Rheological data from Moldex 3D database for PS Polystyrol 145D

Finally, for the POM Hostaform C27021, the reference temperature used was 200°C and three additional characterization temperatures were used, $T_{ref} - 20^\circ\text{C}$, $T_{ref} + 20^\circ\text{C}$ and $T_{ref} + 40^\circ\text{C}$. The resulting flow curves are depicted on Figure 6.18 and there is some significant differences to the Moldex 3D data for the same material (Figure 6.19). The flow curves from capillary rheometry do not form a plateau at lower shear rates and there is a much sudden increase on the index of non-Newtonian flow at higher shear rates. Such behaviour may indicate an important trend for this POM grade since it might slip at lower shear rates and lower temperatures than the other materials studied here.

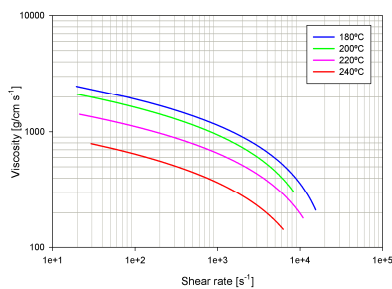


Figure 6.18. Flow curves from capillary rheometry for POM Hostaform C27021

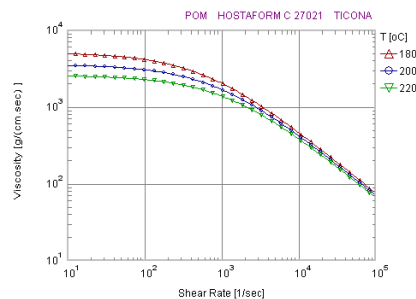


Figure 6.19. Rheological data from Moldex 3D database for POM Hostaform C27021

6.2.2. Instrumentation

The sensors selection for the instrumentation setup was conditioned by the existence of a data acquisition unit from Priamus. Therefore, to ensure full compatibility, the pressure sensors were acquired to the same manufacturer. This sensor have a sensitivity of less then 2 pC.bar^{-1} , which makes it quite suitable for high precision pressure measurement.

Considering the application to microinjection moulding, it would require sensors as small as possible. In this case, the smallest pressure sensor available from Priamus has $\text{Ø}1,8 \text{ mm}$, making it possible to use on this application. These pressure sensors can also give some indications on process repeatability by providing pressure information inside the cavity. For the same processing conditions, pressure curves are quite similar, indicating that the process is stable, concerning times, pressure peaks and the format of both curves. All data is compared with numerical simulations. In this case, Figure 6.20 shows a sample set of average curves for Hostaform C27021 with the BA02SLA moulding block where two effects can be noticed. The first effect is the sudden decay of pressure at the inlet pressure right after 2 seconds, indicating the end of packing pressure. The second effect is given by the higher value of outlet pressure at the end, indicating the absence of air vents.

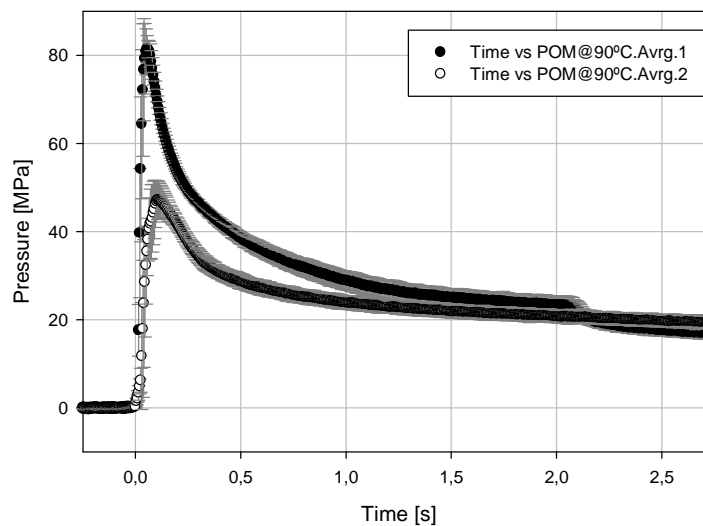


Figure 6.20. Sample pressure curves from the BA02SLA moulding block using Hostaform C27021

The high sensitivity of these pressure sensors also caused some difficulties during the microinjection tests. Noise reduction would be required to isolate the electrical signal from the noise. In particular, the determination of the instant when the melt touched the sensor was quite difficult and required detailed analysis of the pressure curves.

Concerning pressure data acquisition, all moulding blocks were designed to have at least one pressure sensor directly on the cavity. In the case of the MS blocks, given the two gating solution, one pressure sensor is directly located at the predictable location of a weld line. Figure 6.21 shows the pressure sensors location at the cavities of the MS01 and MS02 blocks.

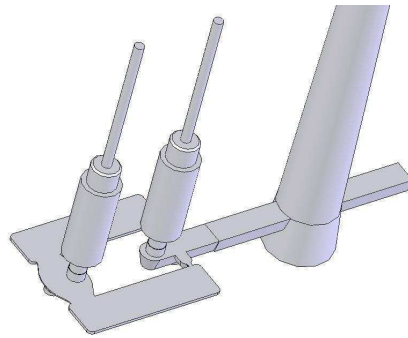


Figure 6.21. Pressure sensors location at the cavities for the MS01 and MS02 moulding blocks

The evaluation of the process temperature was limited to the use of temperature sensors. However the purpose of these is simply to control temperature at the moulding blocks and not the temperature of the flowing polymer by itself. The use of such device would be highly recommendable but commercial solutions are currently inexistent or unaffordable. The smallest temperature sensor available is extremely reliable, it has $\text{Ø}0,6$ mm, but basically is a contact sensor, which means that it reads temperature on the interface mould/part. Concerning temperature on microinjection, the core temperature of the polymer is quite significant as shown earlier on Chapter 3. A solution for evaluating core temperature could be the use of infrared thermal sensors, although, the size ($\text{Ø}4,0$ mm minimum) of the actual commercial sensors available makes it impossible to adopt since there is no suitable location for it, given the dimensions of the plastic parts.

6.2.3. Mouldability

In this section are summarized the problems on microinjection related to mouldability of the parts along with the surface conditions provided by each moulding block, considering the manufacturing process involved.

Steel moulding blocks

The steel moulding block consist of vertical ribs and protrusions whose aspect-ratio created some problems on ejection. On the MS01 moulding block, the rib manufactured by micromilling has the same width at top and bottom, therefore, the draft angle is null. On the other hand, the rib manufactured by microEDM has a draft angle per side of $0,764^\circ$. Concerning conventional injection moulding, such draft angle would be enough for an adequate part ejection considering its height. However, in this case, the draft angle of each rib was clearly insufficient, especially considering the few injection tests done with PS. The friction between the plastic and cavity on the central area rib often caused the parts to get blocked on the moulding block and the successfully ejected parts were bent upon ejection. Another fact that caused this problem is that, for compatibility reasons, the ejector pins actuate outside the part and not on the part itself. Figure 6.22 shows the moulded parts on this moulding block, a) the part injected with the POM and b) the part injected with PP.

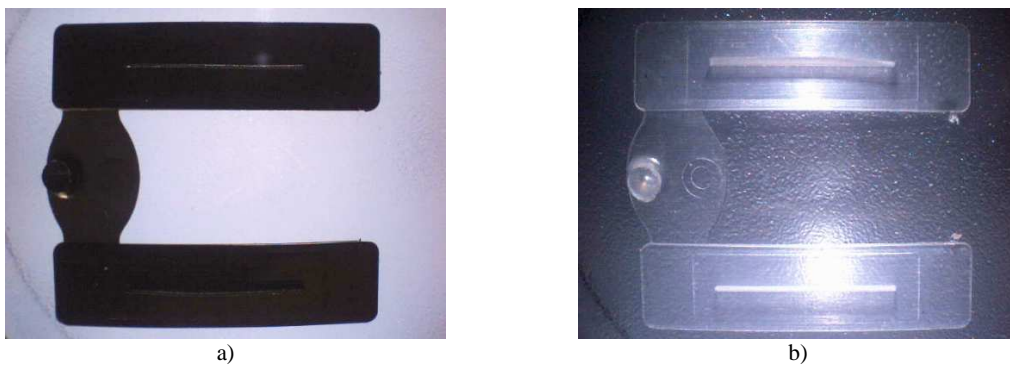


Figure 6.22. Plastic parts obtained from the MS01 moulding block
a) POM and b) PP

The moulded parts were then separated to analyze the geometry of the ribs. Figure 6.23 shows details of the ribs moulded on POM, depicting some filling defects. In Figure 6.23a is shown the end corner of the $1500\ \mu\text{m}$ height rib, where a small unfilled area appears, resulting on a rounded

corner. However, only a detailed analysis of the cavity would confirm if it is in fact a filling defect. For the 1000 μm height rib, Figure 6.23b shows a similar defect on the corner which is consistent with a frozen melt front. At the base of the rib, another unexpected defect appears resulting on a small gap, which is a clear evidence of the melt speed difference, at the base and inside the rib.

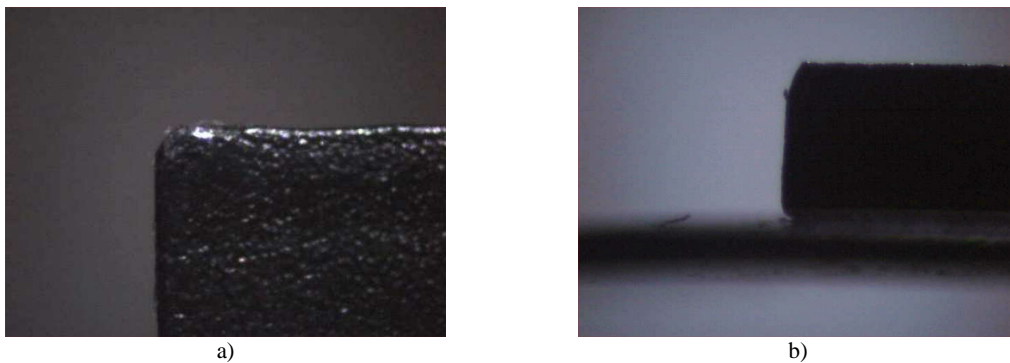


Figure 6.23. Rib analysis of the POM parts moulded on the MS01 moulding block

The same analysis was performed for the PP parts. Both ribs exhibit a similar filling defect on the end corner as shown in Figure 6.24. The 1500 μm height rib (Figure 6.24a) illustrates as well some irregularities on the top surface of the rib. On the 1000 μm height rib (Figure 6.24b), only the unfilled area on the corner of the rib was noticeable.

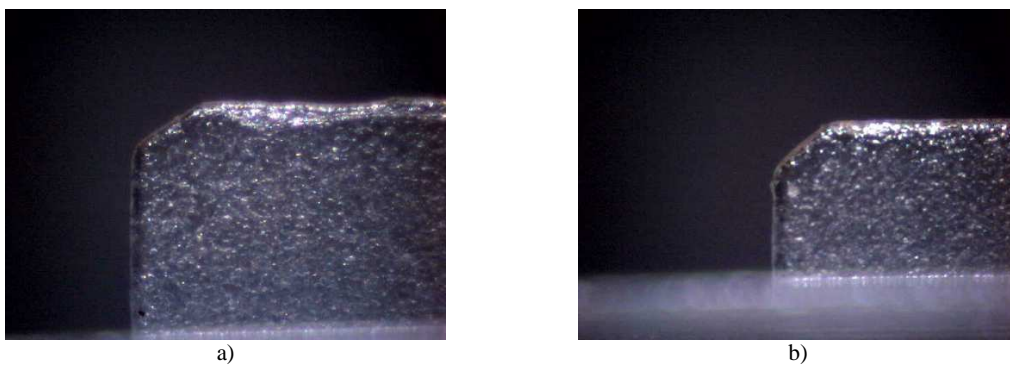


Figure 6.24. Rib analysis of the PP parts moulded on the MS01 moulding block

The filling defects present on the corner of the ribs, despite the injected material, are consistent with the absence of air vents. Nevertheless, a detailed analysis on the moulding blocks is recommendable, although such analysis, given the aspect-ratio of the rib cavities, would require

the destruction of the blocks for a proper topographic characterization. Like the MS01, the MS02 block has two cavities. The first cavity contains a longitudinal rib manufactured by laser milling. Concerning mouldability, the rib dimensions result on a generous draft angle of $2,86^\circ$. The second cavity has a similar base but instead of a rib, it has a round protrusion with a through hole. Ejection problems occurred since the only draft angle exists inside the through hole. The outside wall of the round protrusion is normal to the base, without draft angle. Figure 6.25 shows the parts obtained with the MS02 moulding block.

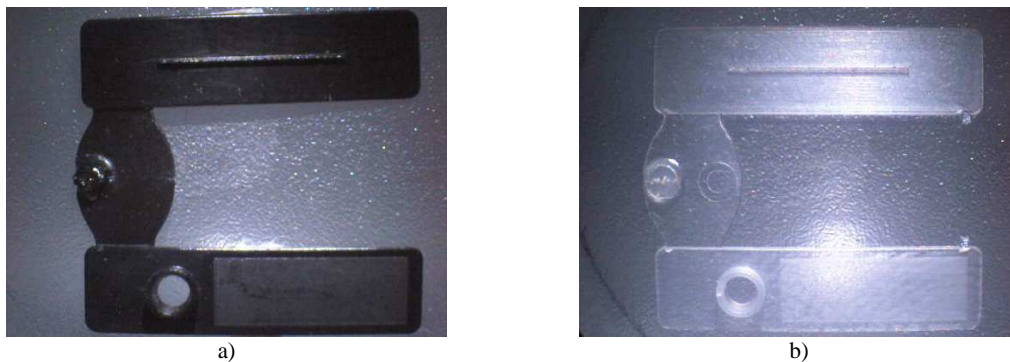


Figure 6.25. Plastic parts obtained from the MS02 moulding block

The analysis of the $400\ \mu\text{m}$ high rib on the two materials showed that there are some anomalies at the bottom of the rib cavity. In this particular case, the rib cavity was manufactured with laser beam machining, whose surface finishing is clearly the worst of the subtractive processes tested here. The POM part shows a small bump on the top surface of the rib (Figure 6.26a). The same defect appears on the PP part and another sign of the poor surface finishing arises since a small piece of material was trapped at the cavity due to the debris (Figure 6.26b).

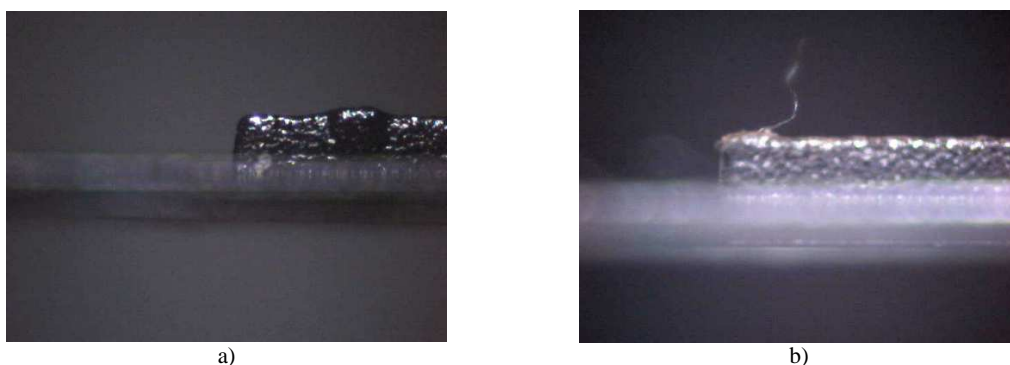


Figure 6.27. Analysis of the $400\ \mu\text{m}$ height rib for the parts moulded on the MS02 moulding block

Concerning the surface finishing of the moulding blocks, both exhibited the lowest roughness, enabling the ejection of the rib features despite their aspect ratio. The major ejection problems could have occurred on the rib manufactured by laser beam machining, but this rib was designed with the lowest aspect ratio.

SLA moulding blocks

The BA01SLA moulding block enabled only a few injection runs from which fully filled parts resulted. The parts obtained with this moulding block are shown on Figure 6.27. Due to the fractured pins and the consequent damaging of this moulding block, only the POM was tested. Figure 6.27a shows a general view of the moulded part and Figure 6.27b highlights the different heights of the protrusions despite the warpage resultant from ejection.



Figure 6.27. Plastic parts obtained from the BA01SLA block

All the few produced parts resulted in full-shots, enabling the preliminary conclusion that the geometry of this cavity was not the most difficult to fill. Despite the existence of the protrusions created by the pins, the typical wall thickness of the part was kept constant. Figures 6.28 and 6.29 show the top face of the protrusions moulded by the Pin 1 and Pin 2 cavities, respectively.

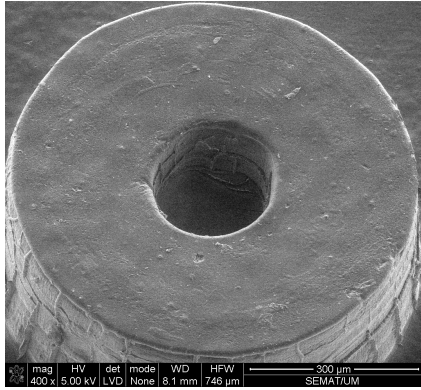


Figure 6.28. General view of Pin 1 protrusion

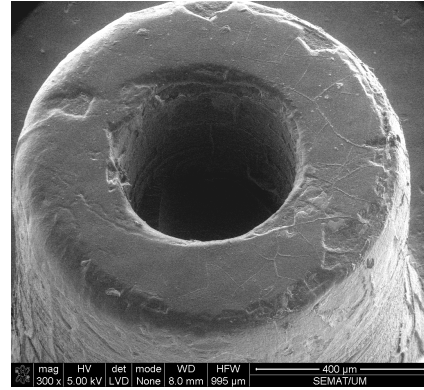


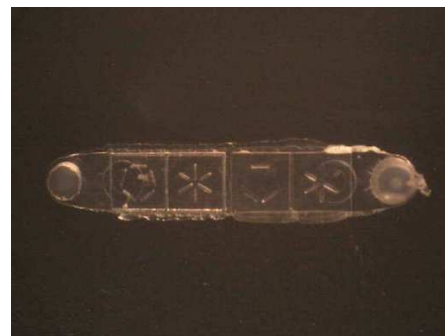
Figure 6.29. General view of Pin 2 protrusion

The top face of the protrusion generated by Pin 1 is perfectly flat. On the other hand, the same face on the protrusion of Pin 2 suggests that delamination of resin layers has occurred. Another important aspect is that the edges of Pin 1 protrusion have been kept while on Pin 2 protrusion, the edge was totally lost.

The plastic parts moulded with the BA02SLA block, both on POM and PP, show a high replication level of the microfeatures. In fact, even the damages noticed on the previous topic were well replicated on the plastic parts. General view of the plastic parts moulded in POM (a) and PP (b) are shown on Figure 6.30.



a)



b)

Figure 6.30. Plastic parts obtained from the BA02SLA block

This moulding block revealed some difficulties on filling the cavity since the second half of the part has a thickness of 100 µm, which resulted in many short-shots with the initial sets of processing parameters. Figure 6.31 shows flashing through the parting plane with both materials. However, the increase of mould temperature played an important role despite the limitation

imposed by the Nanoform 15120 T_g, enabling the full filling of the cavity. Figures 6.31 to 6.34 show detailed views of the microfeatures replicated onto the POM plastic parts.



Figure 6.31. Detail view of the low-relief UM logo on POM (10×)



Figure 6.32. Detail view of the low-relief SE logo on POM (10×)

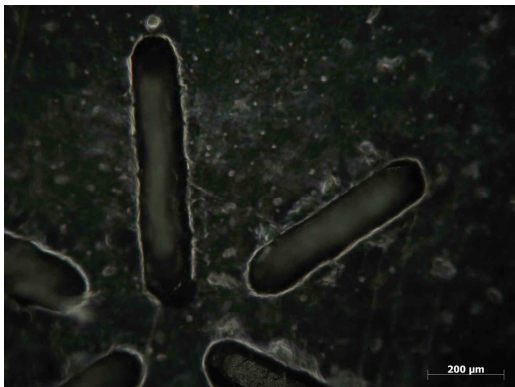


Figure 6.33. Detail view of the high-relief UM logo on POM (10×)



Figure 6.34. Detail view of the high-relief SE logo on POM (10×)

This POM grade exhibits an excellent replicability of microdetails, both on high and low-relief areas of the part, even considering that some damage has occurred. Figure 6.32 shows the replication of the fracture surface onto the plastic parts. Another damage replication is shown in Figure 6.34, on the almost closed area formed by the walls of the *SE* logo.

The parts injected with PP are depicted in Figures 6.35 to 6.38, showing detailed views of the microdetails.



Figure 6.35. Detail view of the high-relief UM logo on PP (10×)



Figure 6.36. Detail view of the high-relief SE logo on PP (10×)



Figure 6.37. Detail view of the low-relief UM logo on PP (10×)

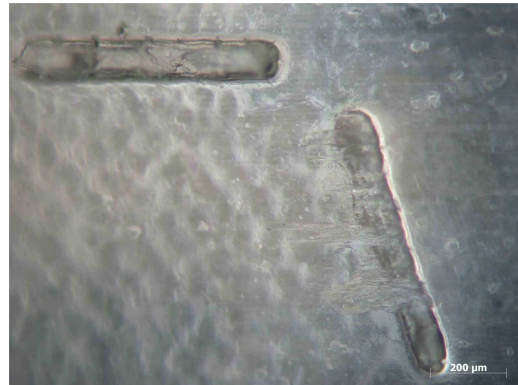


Figure 6.38. Detail view of the low-relief SE logo on PP (10×)

The low-relief area of the part shows some problems due to the damage suffered by the moulding block, as detected already on the parts injected with POM. In the high-relief area, the *UM* logo shows a reasonable replication level. The detailed view of the *SE* logo confirms that PP was the material trapped inside the cavity, since traces of torn material appear here as well.

The BA03SLA moulding block produced only one part and failed. That part was trapped inside the cavity and the ejection system released only the extremities of the part. The contact area on the core side for this moulding block is very large. Considering the surface area of the cylindrical walls as well as the surface area of the ribs that connect them, the friction forces are certainly higher than the ejection force transmitted. The ejection force is concentrated on the two ejector pins which are clearly insufficient to remove this part [89].

The contact area between part and cavity, based on measurements on the 3D model, is 131 mm², which is roughly more than 67% of the total surface area of the part. Furthermore, the ejector pins

area is very small ($3,5 \text{ mm}^2$) and the ejection force is only applied at the extremities, as depicted on Figure 6.39, which causes the part to bend when ejection takes place.

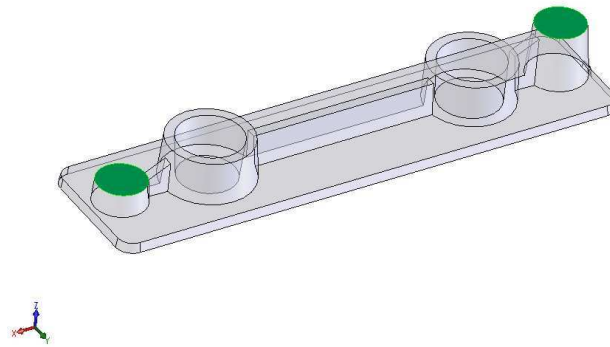


Figure 6.39. Ejector pins' area (highlighted in green) for the BA03SLA part

SLM moulding blocks

The surface quality of the BA01SLM moulding block foresees the predictable quality of their plastic parts. The debris accumulated at the surface damages the moulded parts upon ejection. The details of the only part moulded in POM are shown on Figures 6.40 and 6.41.

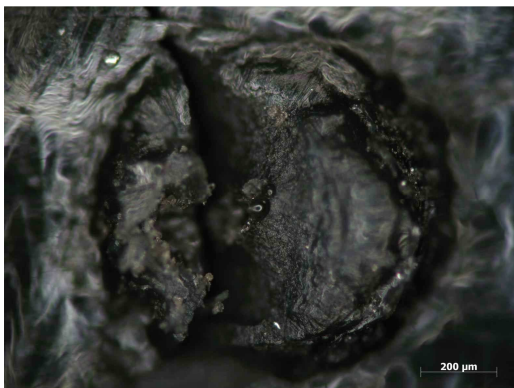


Figure 6.41. Detail view of Pin 1 moulded with POM on the BA01SLM block (10×)



Figure 6.42. Detail view of Pin 2 moulded with POM on the BA01SLM block (10×)

The parts moulded in PP show similar surface quality. However, the higher shrinkage exhibited by this material caused damage during the ejection procedure (Figure 6.42 and 6.43).



Figure 6.42. Detail view of Pin 1 with PP on the BA01SLM block (10×)

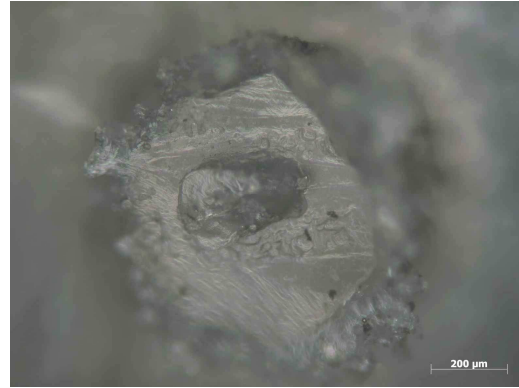


Figure 6.43. Detail view of Pin 2 with PP on the BA01SLM block (10×)

All plastic parts, regardless of the material used, were ejected manually, suffering damages and fractures. Therefore, it was impossible to get complete parts from the BA01SLM moulding block in order to obtain a trend on weight evolution.

The building problems on the manufacturing process concerning microdetails made the BA02SLM moulding block just a reasonable replication tool. Therefore, the quality of the moulded parts is below the quality of the cavity itself, as shown on Figures 6.44 and 6.45, when POM was injected.

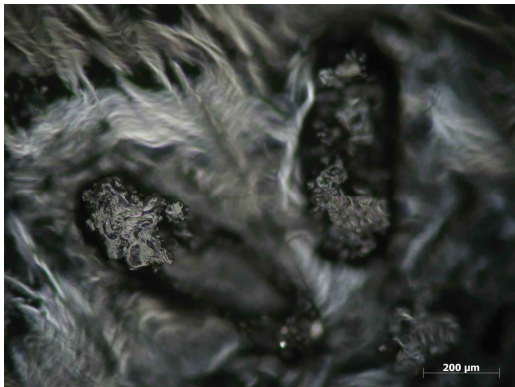


Figure 6.44. Top view of the high-relief SE logo on POM (10×)

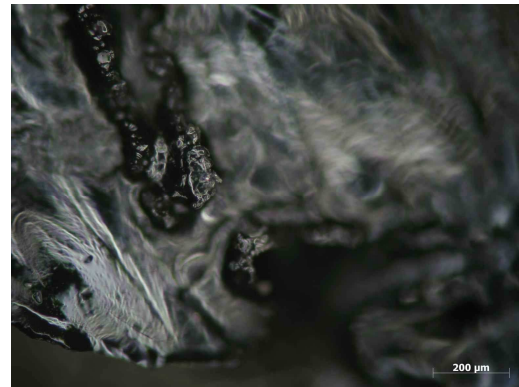


Figure 6.45. Top view of the high-relief UM logo on POM (10×)

The results obtained with PP are not much better than the previous ones. The microdetails are now more visible, indicating that the PP parts were less damaged during ejection (Figure 6.46). As suggested before, this material shows the highest shrinkage, which in this case may have played an important role. On Figure 6.47, there is an indisputable proof that PP was injected after the POM, since a small remaining piece of POM is seen on the PP part.

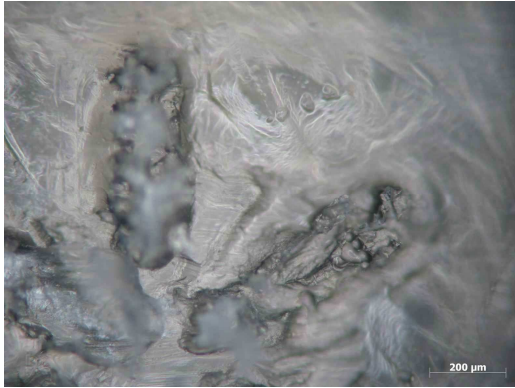


Figure 6.46. Top view of the high-relief SE logo on PP (10×)



Figure 6.47. Top view of the high-relief UM logo on PP (10×)

The parts obtained are consistent with the surface finishing of the BA03SLM moulding block shown previously. Therefore, all moulded parts were damaged upon the ejection procedure disabling the possibility of a stable injection operation. The parts were fully filled, enabling the acquisition of pressure curves. However, the contact area of the part together with the poor surface finishing resulted on seriously damaged parts, with rib walls plucked away as shown in Figure 6.48.

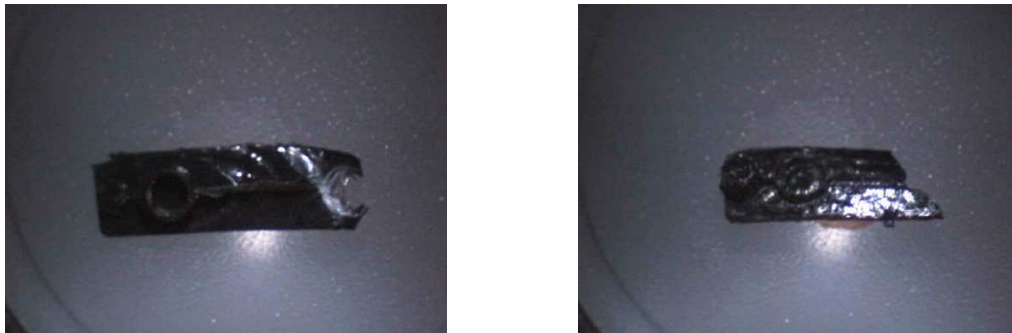


Figure 6.48. Damaged parts obtained from the BA03SLM moulding block

6.2.4. Moulding repeatability

The repeatability of the microinjection process of all types of moulding blocks used was assessed. Processing conditions were stabilized enabling data retrieval concerning injection time and part weight. Considering the difficulties noticed on the ejection of the BA00SLM parts, it was not possible to establish a trend for the moulding due to the reduced number of samples. On the BA00SLA moulding blocks there was also a limited number of complete parts which causes the sample to be insufficient to establish a trend. Nevertheless, all data is based on a minimum sampling of 10 parts. Figure 6.49 shows the weight dispersion for the MS01 moulding block using PP Moplen HP548R.

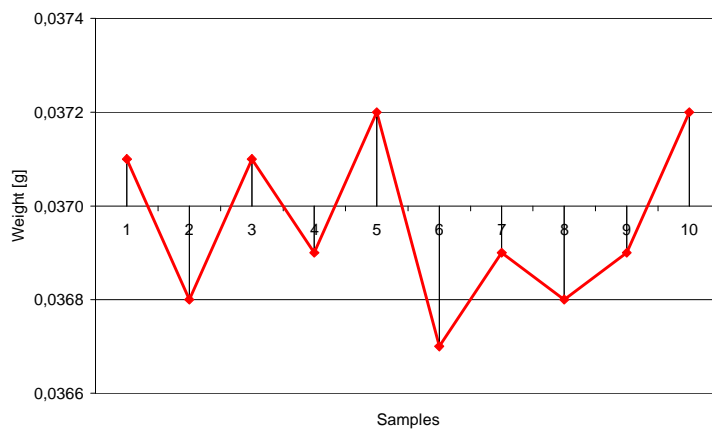


Figure 6.49. Weight sampling for the MS01 moulding block using PP

The data of average injection time and part weight for all moulding blocks and thermoplastic materials tested are detailed on Table 6.6.

Table 6.6. Average injection time and part weight

Moulding block	Injected Material	Average Injection Time [s]	Average Weight [g]	Weight Standard Deviation [g]
MS01	Hostaform C27021	1,08	0,0588	±0,0003
	Moplen HP548R	0,33	0,0370	±0,0002
	Polystyrol 145D	0,17	Not enough samples	Not enough samples
MS02	Hostaform C27021	0,29	0,0577	±0,0005
	Moplen HP548R	0,19	0,0344	±0,0002
	Polystyrol 145D	0,17	Not enough samples	Not enough samples
BA01SLA	Hostaform C27021	0,21	Not enough samples	Not enough samples
	Moplen HP548R	Not available	Not available	Not available
BA02SLA	Hostaform C27021	0,21	0,0211	±0,0005
	Moplen HP548R	0,24	0,0150	±0,0001
BA03SLA	Hostaform C27021	0,20	Not enough samples	Not enough samples
	Moplen HP548R	Not available	Not available	Not available
BA01SLM	Hostaform C27021	0,21	Not enough samples	Not enough samples
	Moplen HP548R	0,25	0,0297	±0,0005
BA02SLM	Hostaform C27021	0,19	Not enough samples	Not enough samples
	Moplen HP548R	0,27	0,0147	±0,0003
BA03SLM	Hostaform C27021	0,20	Not enough samples	Not enough samples
	Moplen HP548R	0,28	Not enough samples	Not enough samples

In the case of the MS moulding blocks, the PS was the only material that created difficulties on the ejection. This polystyrene grade exhibits the lowest shrinkage, compared to the other materials (as in Table 5.8 of Chapter 5). This caused the material to be trapped in the cavity several times, causing damage on the parts upon ejection.

Concerning the few moulded parts with BA01SLA, it was not possible to establish a reliable trend. Although it might not be representative, the POM mouldings exhibited an average weight of 33,7 mg.

Despite the initial difficulties, the BA02SLA moulding block enabled full automation of the process. The microfeatures of the part have a low aspect ratio and no major problems occurred during ejection.

Concerning weight evolution in the case of the BA02SLM moulding block, the POM parts were very damaged and even fractured. Thus, no whole parts were obtained to establish a trend on this

parameter. The only set of whole parts, suitable to establish a trend on weight throughout processing was obtained when moulding with PP.

In the case of the BA03SLA, BA01SLM and BA03SLM moulding blocks, only few injections were possible since the thermoplastic material was trapped inside the cavity. Therefore, it was not possible enough mouldings to establish a trend.

6.3. Moulding surface replication

The replicability of the moulding blocks surfaces on the plastic parts was assessed through optical microscopy and scanning electron microscopy.

Concerning the replication of the cavity surface of the MS01 moulding block, it is possible to notice the eroded surface generated by the microEDM process. Figure 6.50 shows the texture of the 1500 μm height rib wall of the POM part. A detail of the microEDMed surface obtained with the same processing parameters is shown on Figure 6.51.



Figure 6.50. Replication of microEDM surface on to the rib of MS01 moulding block with POM

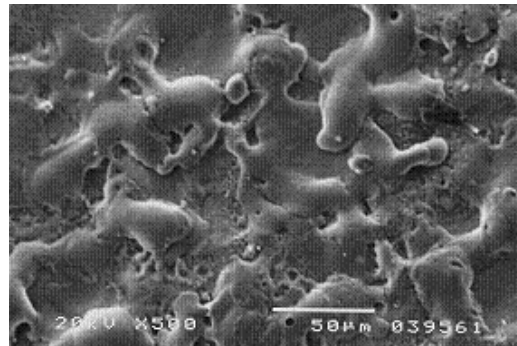


Figure 6.51. SEM micrograph detail of a sample microEDMed steel surface

The surface texture of the 400 μm height rib of the MS02 moulding block (Figure 6.52) clearly shows the effect of the debris left on the cavity surface processed by laser beam machining on a POM part (Figure 6.53). In fact, considering the feature geometry, it is possible to believe that surface finishing inside the rib cavity could be even worse since the evacuation of the expelled particles may not have been effective [99].



Figure 6.52. Replication of LBM surface on to the rib of MS02 moulding block with POM

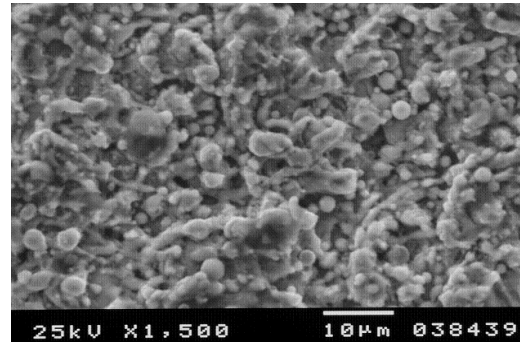


Figure 6.53. SEM micrograph detail of a sample LBMed steel surface

In which concerns to the parts produced on the SLA moulding blocks, the surface finishing is similar for all parts. These moulding blocks were produced at the same time under the same processing parameters; therefore, surface quality is also similar. The analysis of cavity surface replication onto the part (Figure 6.54), the Pin 3 cavity at the BA01SLA moulding block (Figure 6.55) shows a particular pattern that will be further discussed when analyzing the structural integrity of the moulding block. However, it is noticeable that the bottom of the cavity is fully replicated onto the top of the POM plastic feature.

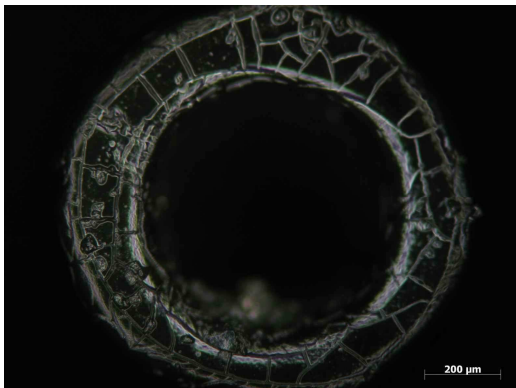


Figure 6.54. Microscopy image of Pin 3 obtained with POM

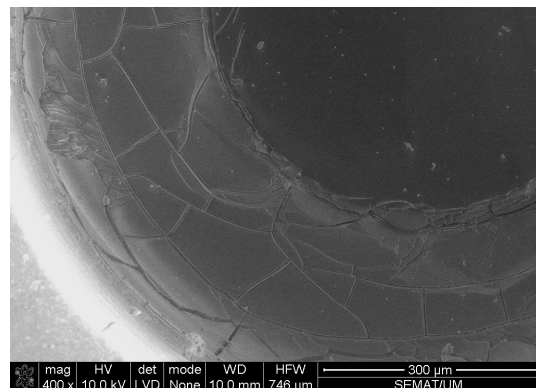


Figure 6.55. SEM micrograph detail of the bottom of the Pin 3 cavity

The surface analysis of the BA02SLA moulding block enables the evaluation of the replicated texture of plane surfaces and featured microdetails. Figure 6.56 shows a low-relief detail of the plastic parts making perceptible the surface quality provided by the high-precision

stereolithography process. The SEM image depicted in Figure 6.57 shows the correspondent high-relief microdetail as well as the surface quality on the cavity itself.



Figure 6.55. Microscopy image of a low-relief microdetail on the POM plastic part

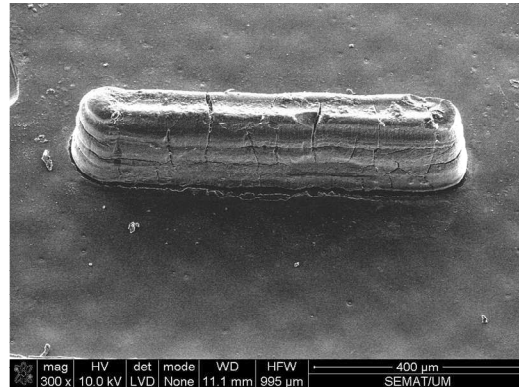


Figure 6.56. SEM micrograph of a high-relief microdetail on the SLA cavity

The final quality of the plastic parts produced on the SLM moulding blocks does not allow the comparison between surface quality of the moulding block and the parts. However, it is possible that the moulded material has replicated the cavity surface but ejection damaged it. Analyzing the part feature (Figure 6.58) and the correspondent cavity (Figure 6.59), it is almost impossible to establish a relation concerning replication.



Figure 6.58. Microscopy image of Pin 1 moulded with PP

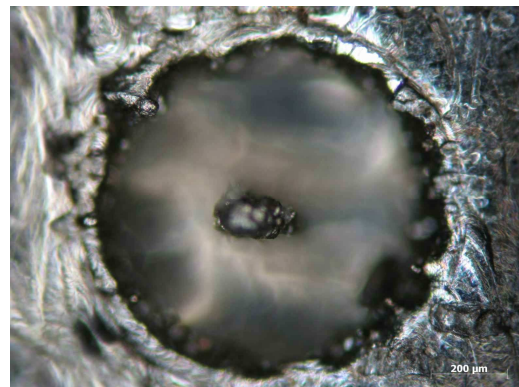


Figure 6.59. Microscopy image of the Pin 1 cavity on the BA01SLM block

Regarding to the BA02SLM moulding block, the same situation occurs. Only the surface of the part (Figure 6.60) is shown as a replication of the cavity surface (Figure 6.61), since the surface

quality is in both cases equally poor. The replication of the microdetails that form the UM logo is quite bad, making it hard to make a plausible comparison.

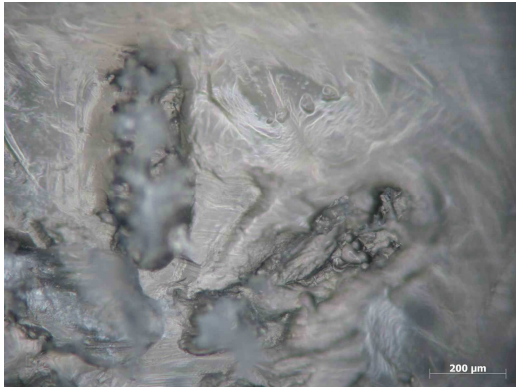


Figure 6.59. Microscopy image of the high-relief *UM* logo on the plastic part

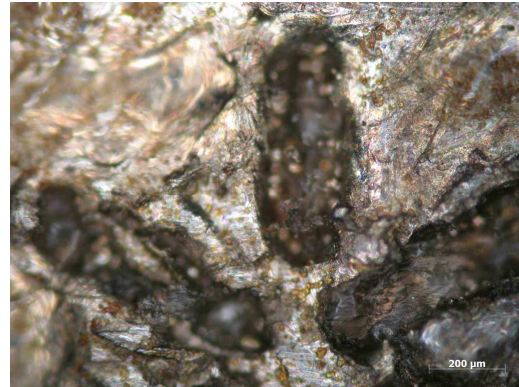


Figure 6.60. Microscopy image of the low-relief cavity for the *UM* logo

6.4. Surface wear

The surface roughness of the MS01 moulding block was evaluated prior to the microinjection tests. Although it is not expected any wear of the surface, roughness measurements were made before and after moulding to determine if the polymer flow produced any significant change on the moulding surfaces. The results are detailed on Table 6.7.

Table 6.7. Roughness measurements on the MS01 moulding block

Cavity	Average roughness (Ra)			Mean peak-to-valley height (Rz)			Max. roughness height (Rmax)		
	Before	After	Variation	Before	After	Variation	Before	After	Variation
µEDM	0,075 µm	0,014 µm	-81,3%	0,59 µm	0,11 µm	-81,4%	0,84 µm	0,13 µm	-84,5%
µMilling	0,083 µm	0,023 µm	-72,3%	0,69 µm	0,14 µm	-79,7%	1,06 µm	0,21 µm	-80,2%

The results above show that a significant change on surface roughness occurs despite the excellent surface finishing provided by the subtractive technologies used. The average roughness (Ra) is known to be less sensitive to surface topography; however, it agrees with the variations of the Rz and Rmax parameters.

The surface roughness of the MS02 moulding block was also evaluated prior to the microinjection tests. The results, before and after the injection, are detailed on Table 6.8.

Table 6.8. Roughness measurements on the MS02 moulding block

Cavity	Average roughness (Ra)			Mean peak-to-valley height (Rz)			Max. roughness height (Rmax)		
	Before	After	Variation	Before	After	Variation	Before	After	Variation
LBM	0,588 μm	0,485 μm	-17,5%	3,48 μm	2,55 μm	-26,7%	3,82 μm	3,25 μm	-14,9%
$\mu\text{Milling}$	0,221 μm	0,022 μm	-90,0%	1,62 μm	0,15 μm	-90,7%	1,85 μm	0,17 μm	-90,8%

The surface roughness decrease on micromilled surfaces occurs also on the MS02 moulding block. However, the changes on the laser beam machined surface are much smaller, despite the initial low surface finishing obtained, when compared with other subtractive technologies. While the trend on surface roughness is similar on all parameters for the micromilled surface, the LBM surface presents a significant variation of Rz and Rmax, indicating the presence of surface defects. However, considering the nature of the micromanufacturing process used, such defects are likely to appear, requiring a post-treatment to prevent this situation. Regardless of the manufacturing process, the improvement of the surface finishing of both moulding blocks is certainly due to the polymer flow and the high melt speeds imposed. Although it may be possible, there is not enough data to support the existence of an influencing flow effect, namely wall-slip, that could cause this change on surface roughness. These results have been presented in the conference Polymer and Moulds Innovation 2010 (Ghent, Belgium). A copy of the paper is attached in Annex A5.

6.5. Structural integrity

The moulding blocks structural integrity was considered an issue especially in the case of the use of SLA as a manufacturing technology. Despite that Nanoform 15120 having already been used before for mould tooling purposes, its mechanical properties, although enhanced by the ceramic nanoparticles, are still limited. Considering medium to long production run, failure is likely to appear due to the stresses imposed by injection moulding [97].

After 5 injection cycles, the BA01SLA moulding block got damaged. The ejection phase was often accomplished manually before the next injection cycle. During one of these procedures, the bigger pins, Pins 2 and 3, got fractured, seriously damaging the mould insert. Figure 6.61 shows Pin 3 trapped on the part. More detail is shown on the SEM image at Figure 6.63.

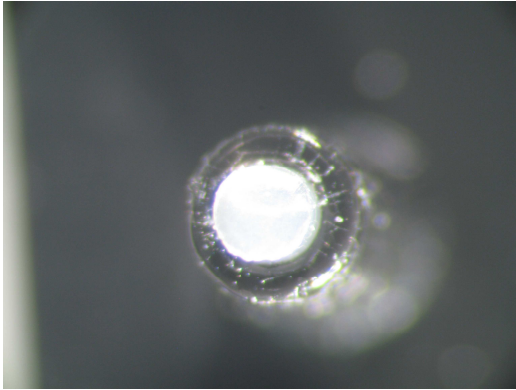


Figure 6.62. Detail of Pin 3 (10×) showing the Nanoform 15120 pin inside the part

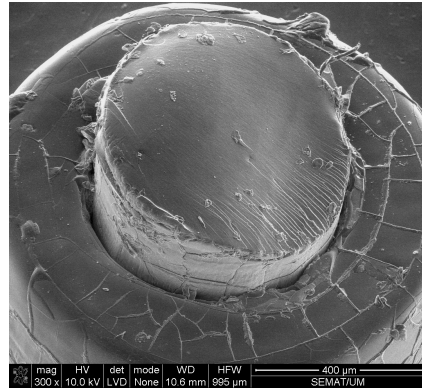


Figure 6.63. SEM image of Pin 3 trapped in the part showing its fracture surface

Although the fractured pin is already visible on the microscopy image, the SEM image gives additional information, namely a significant amount of cracks at the bottom of this pin cavity.

An elemental analysis with the X-ray microanalyzer, confirmed that the piece of material trapped inside the plastic part was in fact a piece of Nanoform 15120. Figure 6.64 shows the result of the spectroscopic analysis where carbon appears as the main constituent and silicate, denoting the presence of the ceramic nanoparticles.

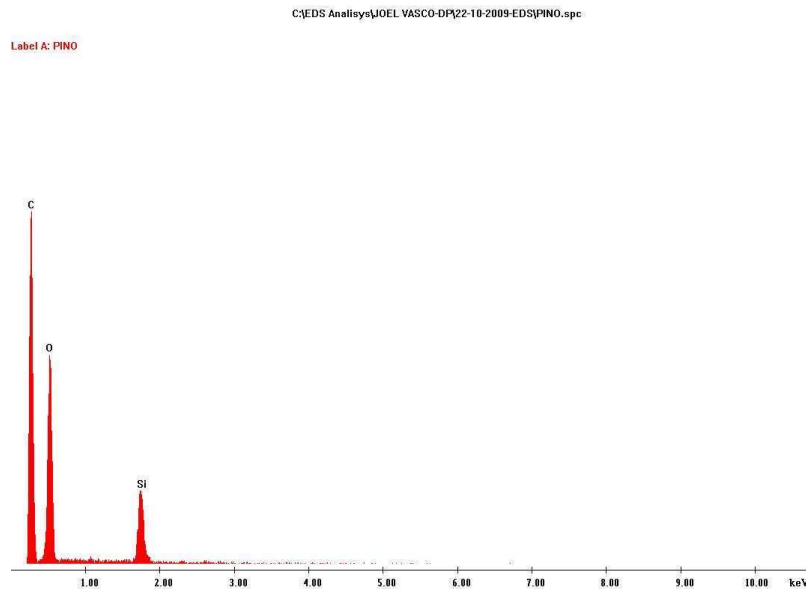


Figure 6.64. Spectroscopic analysis of the trapped material

Considering the integrity of the moulding block, further SEM analyses were performed to check if additional cracks appear in the cavity. Figures 6.65 and 6.66 show images obtained at the Pin 3 cavity.

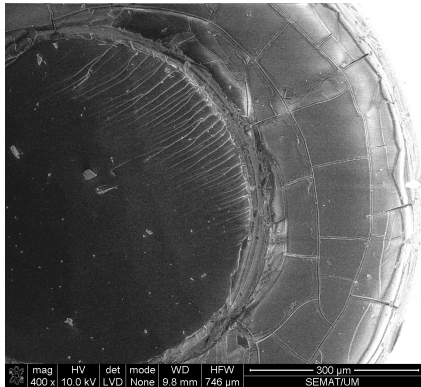


Figure 6.64. Top view of the Pin 3 cavity

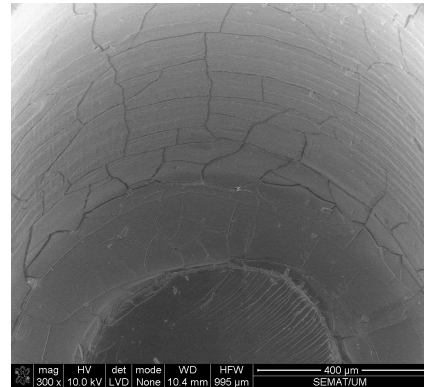


Figure 6.65. General view of the Pin 3 cavity

Cracks are visible in the two SEM images. The top view clearly shows the fracture lines. At the bottom, the cracks that were detected on the POM moulding are also visible here. On the general view, cracks are also noticed on the side wall, as a result of the pressure applied on this cavity. Another issue here is the absence of air vents at this location, causing the pressure increase of the air trapped inside the impression.

Similar problems were also detected when analyzing the Pin 2 cavity. This pin did not fracture at the root, probably due to the manual intervention in the ejection process. Only nearly half of the pin was fractured, as shown on Figures 6.67 and 6.68.

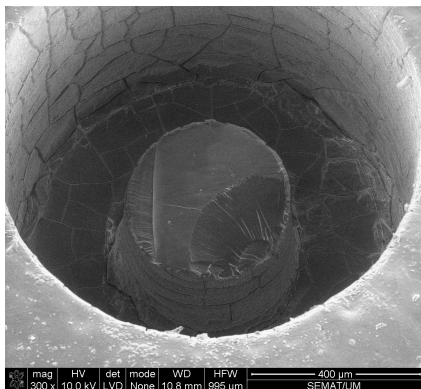


Figure 6.66. General view of Pin 2 cavity

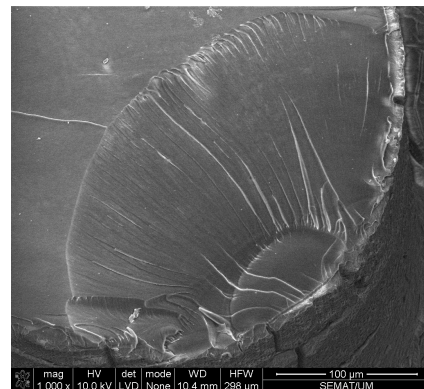


Figure 6.67. Top view of Pin 2, detailing primary fracture surface

A clear fracture surface is noticed in the two SEM images. Figure 6.67 shows two fracture surfaces, the primary one, shown in detail in Figure 6.68 and a smaller one, the secondary fracture surface, on the opposite side of the pin (Figure 6.69). Similarly to the Pin 3 cavity, cracks were also detected at the bottom of the cavity and at the side wall (Figure 6.70).

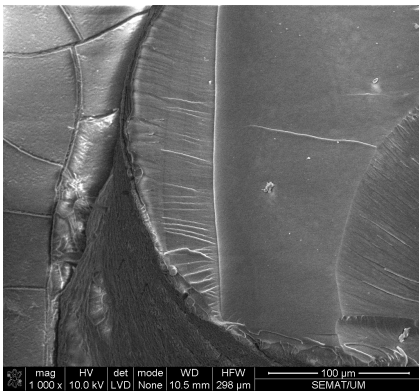


Figure 6.69. Top view of Pin 2, detailing the secondary fracture surface

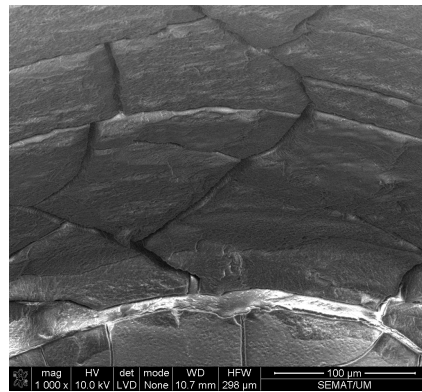


Figure 6.70. Side wall detail of Pin 2

The first pin, Pin 1, was the most fragile in spite of having the same aspect ratio as all others. It seems that it supported the mechanical loads but suffered some damage. Figures 6.71 and 6.72 show the fractured pin and cracks are visible at the side walls of the pin cavity and not at the bottom face.

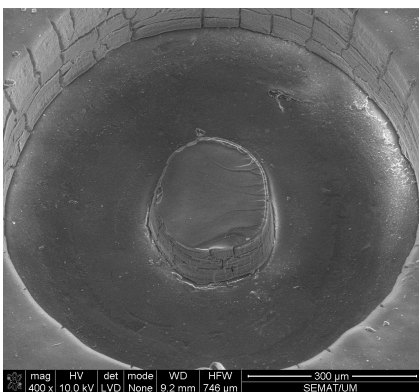


Figure 6.71. General view of Pin 1 cavity

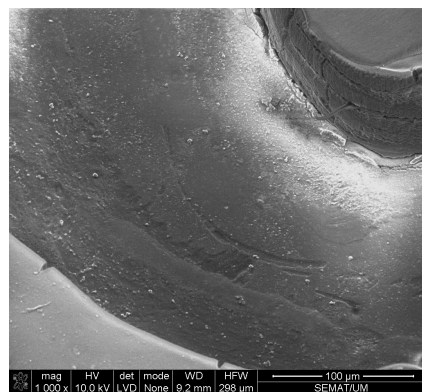


Figure 6.72. Bottom face of Pin 1 cavity

In Figure 6.71, at the top of Pin 1 a fractured surface appears, but the overall height of the pin is kept. This fracture can be caused by delamination of the Nanoform 15120 resin. The moulding

blocks from the BA series were built layer-wise in the vertical direction, *i.e.*, along the axis of the pin. The polymer flow could be damaging enough to cause a fracture between layers of resin. Other pressure effects can be observed at the gate location. At the parting plane, the gate appears well defined and undamaged (Figure 6.73). But at the bottom of the gate (Figure 6.74), cracks are evident, showing that, even if the pins were kept intact, this moulding block would become seriously damaged in the short term.

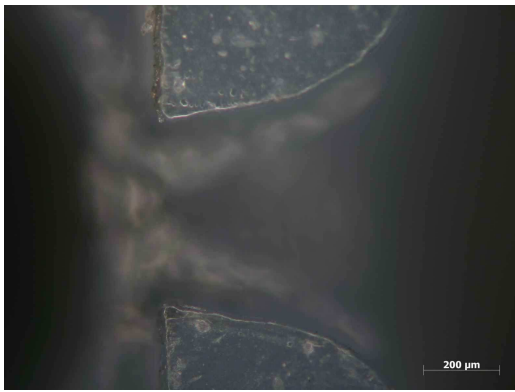


Figure 6.73. Gate detail of the BA01SLA at the parting plane (10×)

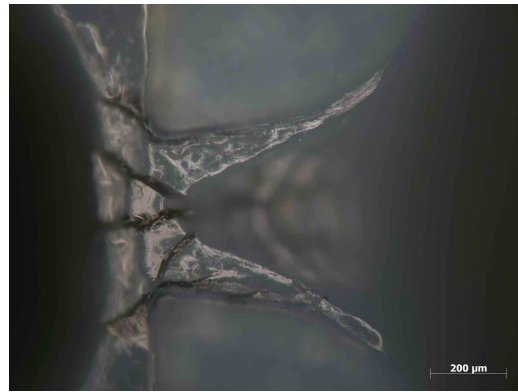


Figure 6.74. Gate detail of the BA01SLA at the bottom of the gate (10×)

Generally, the effect of the melt flow pressure seems to be present in all analyzed areas. With the exception of Pin 1, where the bottom face is flat, all other faces are cracked. All pins were designed with the same aspect-ratio and the higher pins, Pin 2 and Pin 3, have less material underneath, as shown in Figure 6.75. Therefore, it is possible to conclude that in this case, the moulding block height should be higher to increase the structural integrity of the moulding block.

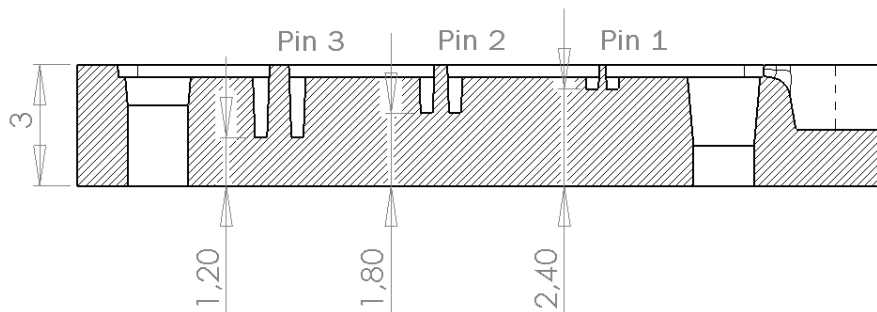


Figure 6.75. Cross-section of the BA01SLA moulding block (dimensions in mm)

The BA02SLA block was designed to evaluate not only the replication of microdetails on the plastic parts but also the integrity of microfeatures of the cavity itself. In particular, the low-relief area of the plastic part replicates the high-relief microfeatures of the cavity. These features may be considered fragile despite their small aspect ratio (below 3:1) since they have a typical top width of 100 μm and height of 300 μm (Figure 6.76).

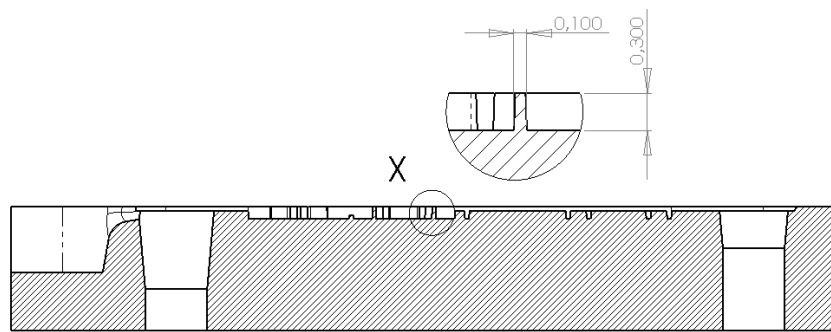


Figure 6.76. Cross-section of the BA02SLA cavity and detail of a microfeature (dimensions in mm)

These features are located close to the gate side which makes them more exposed to polymer flow effects. However, before these features, there is a thin wall that protects the microfeatures from being swept away by the polymer flow.

Optical microscopy enabled the detection of some fracture surfaces in both logos, as shown in Figures 6.77 and 6.78. However, it was not possible to evaluate the height of the fracture surface or even to determine a possible cause for it.



Figure 6.77. Top view of high-relief SE logo at the low-relief area of the part (10 \times)

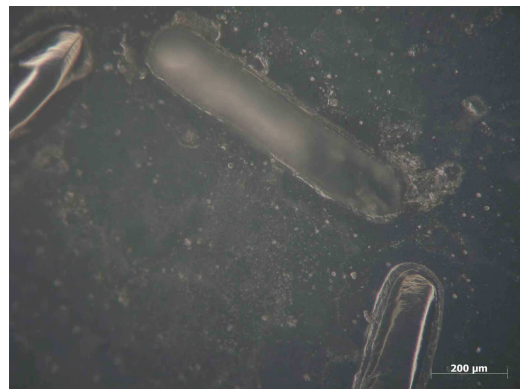


Figure 6.78. Top view of high-relief UM logo at the low-relief area of the part (10 \times)

Further analyses were required to evaluate these foreseeable damages. Figure 6.79 shows the preliminary topographic analysis made with the laser perthometer.

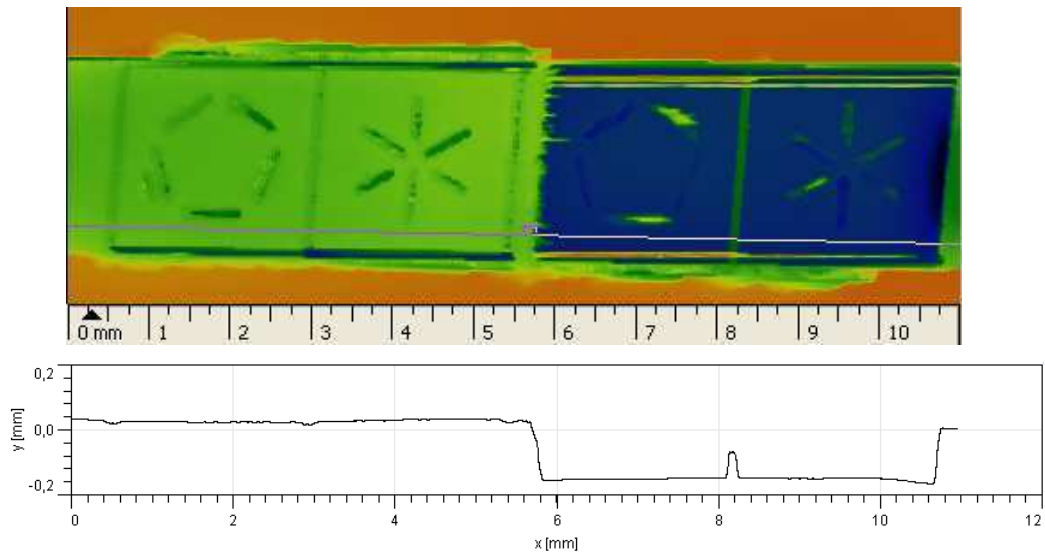


Figure 6.79. General topographic analysis of the BA02SLA cavity

Each logo on the low-relief area was then analyzed and roughness measurements were carried out on the entire cavity. Figures 6.80 and 6.81 show the two surface topographies.

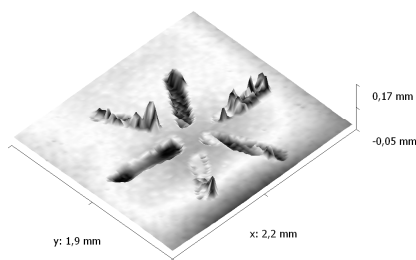


Figure 6.80. Topographic analysis of the high-relief SE logo

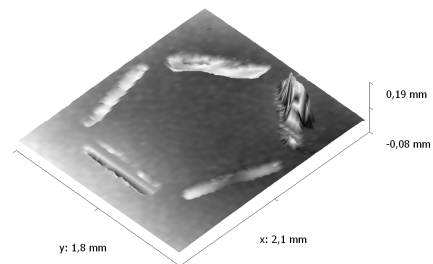


Figure 6.81. Topographic analysis of the high-relief UM logo

These topographic analyses showed that this moulding block had already suffered serious damage at this area. Some microfeatures were completely plucked away, which is more visible in the case of the *UM* logo since the layout of these features creates a closed loop, therefore, imposing more

resistance to polymer flow. At the next region to fill, there is the high-relief area of the plastic part, or the low-relief area of the cavity. Here, the microfeatures consist of through holes with similar dimensions as in the previous logos. However, the integrity of this region would be very different since no protrusions exist. The same topographic analysis was performed over this area and the results are shown on Figures 6.82 and 6.83.

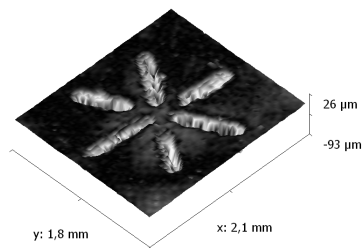


Figure 6.82. Topographic analysis of the low-relief UM logo

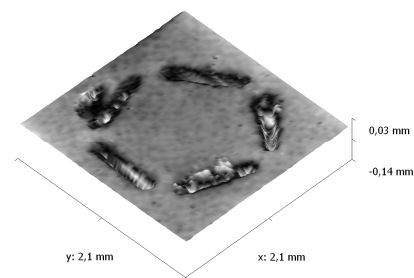


Figure 6.83. Topographic analysis of the low-relief SE logo

From these topographic analyses, it is possible to conclude that the depth of the features was not correctly replicated. Therefore, it is reasonable to suspect that remains of polymer were trapped within, filling the microfeatures. Additional SEM scans were performed to determine which walls were in fact intact at the cavity of the moulding block. Figure 6.84 shows the general view of the high-relief SE logo and Figure 6.85 shows a detail of a fractured wall on the logo.

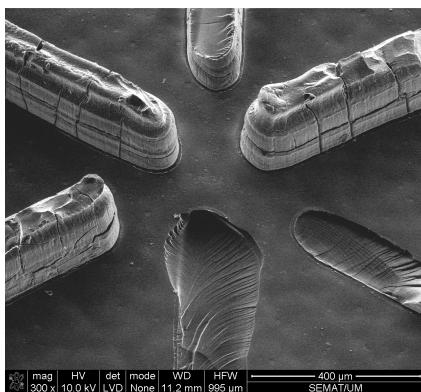


Figure 6.83. General view of the high-relief SE logo

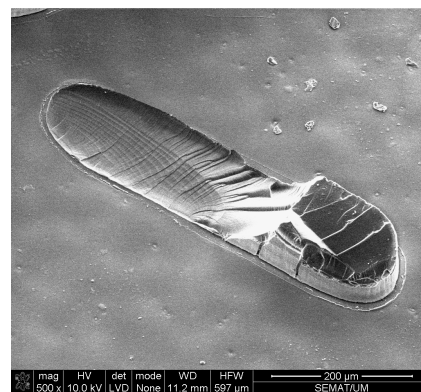


Figure 6.84. Detail view of fractured wall on the high-relief SE logo

In all features, fracture surfaces are visible. At the intact walls, however, layer-wise cracks are also visible that could be the source for this problem. In this logo, at least, three walls are intact allowing the conclusion that they generated less resistance to the polymer flow.

On the high-relief *UM* logo, as stated earlier, the walls form an almost closed loop, imposing more resistance to flow. As shown in Figure 6.86, four out of five walls are fractured. The fifth wall is intact because it is oriented in the same direction as the polymer flow. Figure 6.86d shows oriented fracture lines in the same direction of the polymer flow.

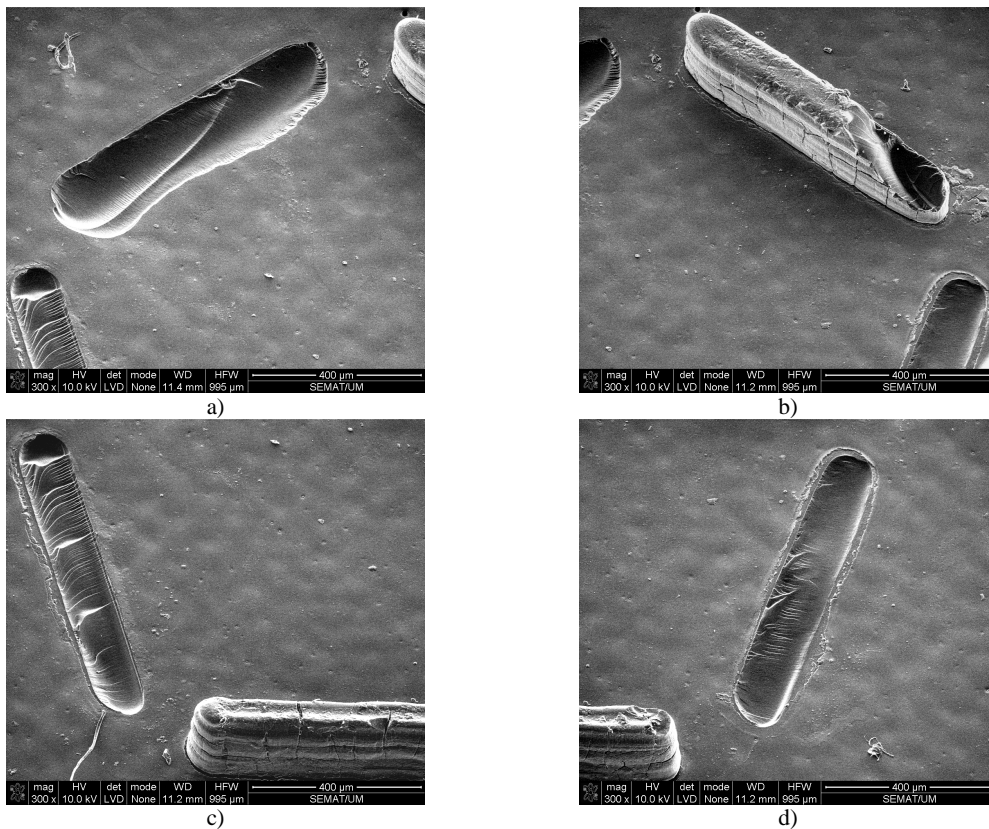


Figure 6.86. Detail view of fractured walls on the high-relief SE logo

Concerning the high-relief area of the part, or low-relief of the cavity, the preliminary analysis with the laser perthometer allowed the conclusion that there is material trapped inside the cavities. Figure 6.87 shows two of the cavities of the low-relief *UM* logo where vertical cracks are visible, denoting that the melt pressure had an effect on these features.

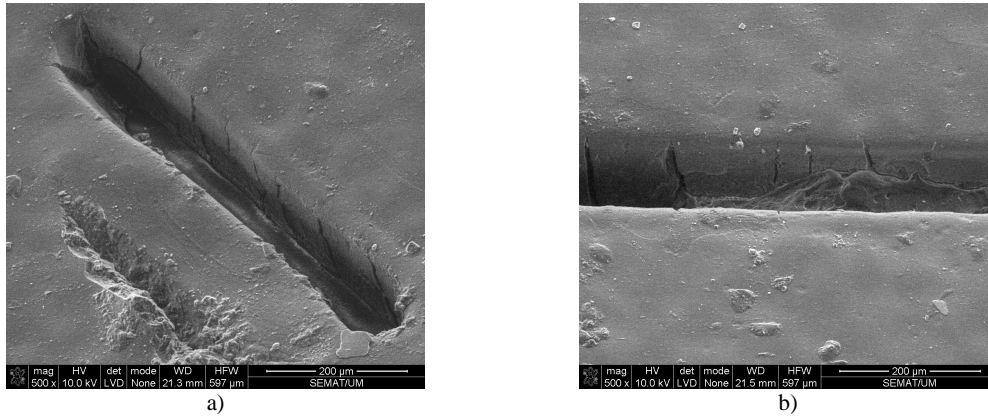


Figure 6.87. Detail view of the cavities on the low-relief UM logo

In the case of the *SE* logo, the same vertical cracks exist but there is material trapped inside the cavities. The cavity details, shown in Figures 6.88 and 6.89, confirm the existence of foreign material. The draft angle on these cavities is generous, 3° per side, but it seems to be insufficient for a proper ejection. In Figure 6.88, besides the trapped material, a residue is visible near the edge of the cavity. Considering that in Figure 6.89 is shown a piece of ripped material that probably occurred on ejection, it is possible that such residue is also a result of a ripped piece of plastics.

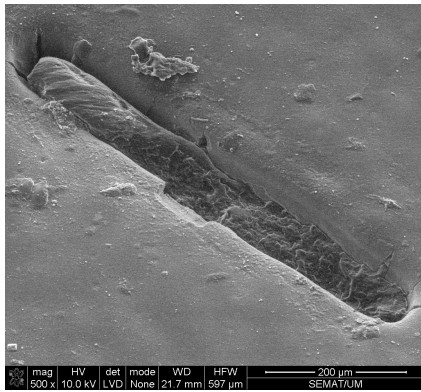


Figure 6.88. Detail (1) view of filled cavity wall on the low-relief SE logo

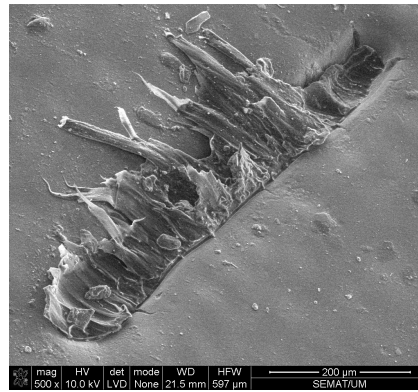


Figure 6.89. Detail (2) view of filled cavity wall on the low-relief SE logo

Since this moulding block was used for the injection of POM and PP, the X-ray microanalyzer was used to determine which material was in fact present. Figures 6.90 to 6.91 show the results of the spectroscopic analysis conducted on the low-relief *SE* logo.

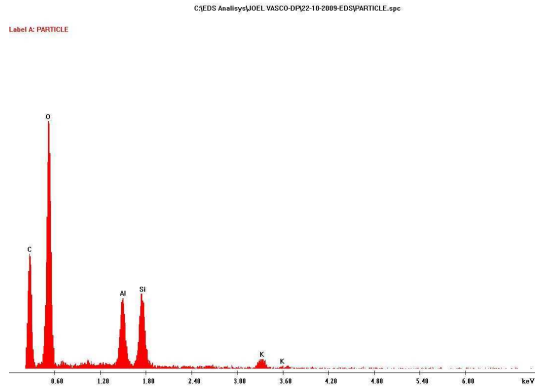


Figure 6.90. Spectroscopic analysis of the particle depicted on Figure 6.87

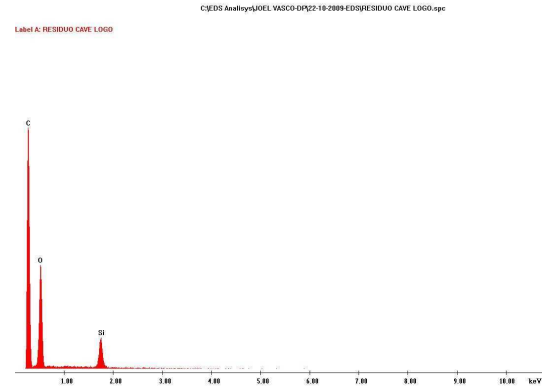


Figure 6.91. Spectroscopic analysis of the residue depicted on Figure 6.88

The elemental analysis of the particle illustrated on Figure 6.90 reveals that its main constituents are oxygen, carbon, silicate and aluminum, therefore, traces of both Nanoform 15120 and POM.

The elemental analysis of the residue shown in Figure 6.89 is not conclusive since the dragged material shown should belong to a polymeric material but few traces of it were found.

The BA03SLA moulding block became unusable after the first injection test with POM because the moulding was trapped inside the cavity. The part broke at the middle zone and it is trapped inside the cavity, as shown on Figure 6.92.



a)



b)

Figure 6.92. Small piece of the plastic part trapped inside the BA03SLA cavity

6.6. Numerical simulation

The simulations described in this topic include the filling analyses with Moldex 3D R9.1 and the heat transfer simulations with Abaqus 6.7 EF. The heat transfer simulations are performed, not to simulate the microinjection process, but to determine the effect of heat transfer in the thermal performance of the moulding blocks.

6.6.1. Injection moulding simulation

In this particular case, the simulation of the microinjection process with a numerical tool gives an insight on polymer flow at the microscale. Envisaging industrial applications at the microscale, this capacity is relevant for the optimization of process tools and the process itself, minimizing costs and shortening development and operation time [100].

Moulding cycle

The melt fill time, in the case of the cavity of the MS01 moulding block was in agreement with the microinjection tests for all materials and processing conditions imposed. Figure 6.92 shows a) the melt front time and b) the shear rate for the POM Hostaform C27021. A copy of the Moldex 3D simulation report with the MS01 moulding block is attached in Annex A2.

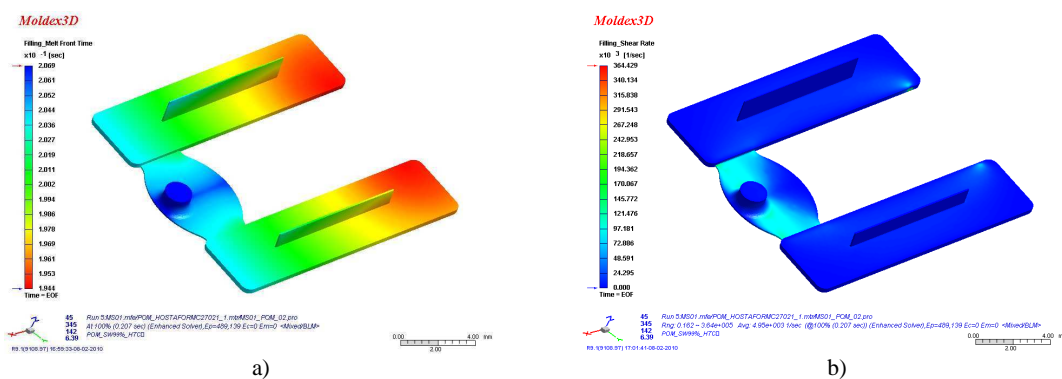


Figure 6.93. Numerical results for POM on the MS01 moulding block

Table 6.9 summarizes the information from all simulations performed on the MS01 moulding block geometry. Concerning shear rate, the highest values appear at the gate area, as expected. However, significant values occur also at the thin-wall near the end of filling.

Table 6.9. Simulation results analysis on the MS01 moulding block

Material	Mould temperature	Melt front time		Maximum shear rate	
		Input value	Numerical	Value	Location
PP	70°C	0,33 s	0,331 s	$15,1 \times 10^5 \text{ s}^{-1}$	Gate
PP	80°C	0,17 s	0,171 s	$18,0 \times 10^5 \text{ s}^{-1}$	Gate
				$\sim 95 \times 10^4 \text{ s}^{-1}$	Thin-wall
POM	100°C	0,20 s	0,207	$36,4 \times 10^4 \text{ s}^{-1}$	Gate
				$\sim 20 \times 10^4 \text{ s}^{-1}$	Thin-wall
PS	60°C	0,17 s	0,171 s	$19,1 \times 10^5 \text{ s}^{-1}$	Gate

The filling of the impression of the BA02SLM moulding block was also in agreement with the microinjection tests for all materials and processing conditions. Figure 6.94 shows a) the melt front time and b) the shear rate for the PP Moplen HP548R. The presence of several thin-walled sections caused a significant increase on the shear rate, up to $7,3 \times 10^5 \text{ s}^{-1}$. A study including this part as a case-study was presented on the 26th Meeting of Polymer Processing Society (Banff, Canada). A copy of the paper is attached in Annex A4.

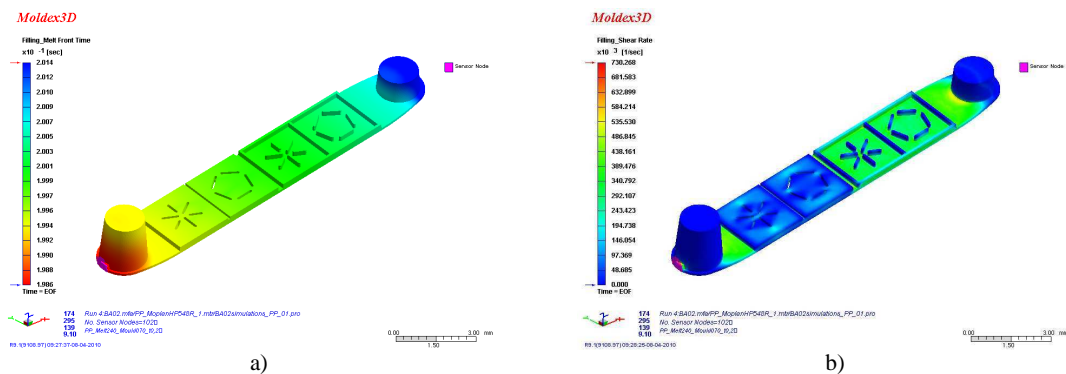


Figure 6.94. Numerical results for PP on the BA02SLM moulding block

Table 6.10 summarizes the information from all simulations performed on the BA02SLM moulding block geometry. Shear rate reached significant values for all materials. In all cases, this increase was found on the thin-walled sections at the base of the moulding.

Table 6.10. Simulation results analysis on the BA02SLM moulding block

Material	Mould temperature	Melt front time		Maximum shear rate	
		Input value	Numerical	Value	Location
PP	70°C	0,20 s	0,201 s	$73,0 \times 10^4 \text{ s}^{-1}$	Gate
				$\sim 60 \times 10^4 \text{ s}^{-1}$	Thin-wall
POM	100°C	0,25 s	0,270 s	$89,0 \times 10^4 \text{ s}^{-1}$	Gate
				$\sim 55 \times 10^4 \text{ s}^{-1}$	Thin-wall
POM	110°C	0,19 s	0,209 s	$65,3 \times 10^3 \text{ s}^{-1}$	Gate
				$\sim 37 \times 10^3 \text{ s}^{-1}$	Thin-wall

The filling of the impression of the BA03SLM moulding block also agreed with the microinjection tests. Again, using the data from the microinjection tests, the cavity filling was predicted correctly. Figure 6.95 shows a) the melt front time and b) the shear rate for the PP grade Moplen HP548R.

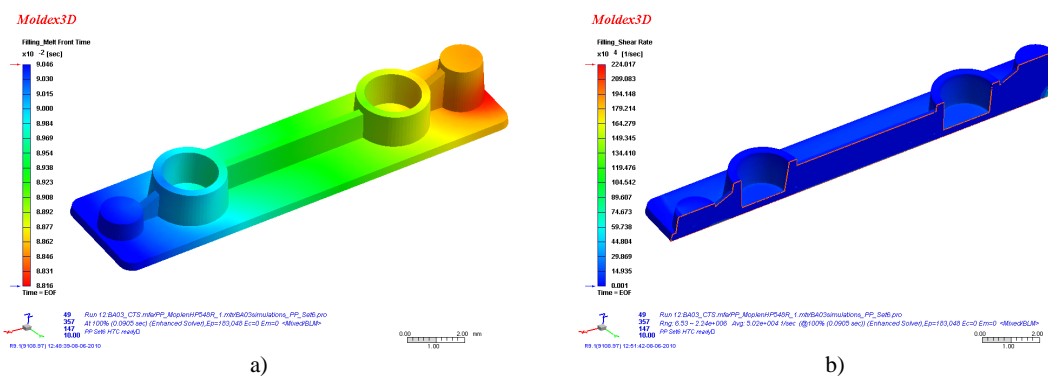


Figure 6.95. Numerical results for PP on the BA03SLM moulding block

Table 6.11 summarizes the information from all simulations with the BA03SLM moulding block geometry. The part has a typical thickness of 300 μm , therefore, it is not predictable that the geometry might origin a shear rate increase. Additional processing conditions for the PP were tested on Moldex 3D according to the experimental microinjection tests, resulting on parameter Sets 1 to 7. Fill time was correctly predicted in all situations despite the variations on the processing conditions. As expected, the higher values of shear rate were verified when injection speed and injection pressure were pushed up, which occurred on the simulations that used processing parameters Sets 4 and 6).

Table 6.11. Simulation results analysis on the BA03SLM moulding block

Material	Flow rate	Injection pressure	Melt front time		Maximum shear rate	
			Input value	Numerical	Value	Location
POM	231 cm ³ .s ⁻¹	60 MPa	0,20 s	0,204 s	48,2×10 ⁴ s ⁻¹	Gate
PP Set 1	231 cm ³ .s ⁻¹	60 MPa	0,27 s	0,271 s	85,1×10 ⁴ s ⁻¹	Gate
PP Set 2	108 cm ³ .s ⁻¹	80 MPa	0,30 s	0,301 s	76,6×10 ⁴ s ⁻¹	Gate
PP Set 3	108 cm ³ .s ⁻¹	100 MPa	0,32 s	0,321 s	71,8×10 ⁴ s ⁻¹	Gate
PP Set 4	123 cm ³ .s ⁻¹	120 MPa	0,25 s	0,251 s	$\frac{92,0 \times 10^4 \text{ s}^{-1}}{\sim 10 \times 10^4 \text{ s}^{-1}}$	Gate Base
PP Set 5	46 cm ³ .s ⁻¹	120 MPa	0,52 s	0,522 s	44,1×10 ³ s ⁻¹	Gate
PP Set 6	277 cm ³ .s ⁻¹	120 MPa	0,09 s	0,090 s	$\frac{22,4 \times 10^5 \text{ s}^{-1}}{\sim 55 \times 10^4 \text{ s}^{-1}}$	Gate Base
PP Set 7	277 cm ³ .s ⁻¹	30 MPa	0,15 s	0,153 s	$\frac{66,3 \times 10^4 \text{ s}^{-1}}{\sim 80 \times 10^3 \text{ s}^{-1}}$	Gate Base

Filling

The ribs of the MS01 geometry are the only features which require some analysis concerning filling. Despite the obvious difficulty, the rib cavities were filled without major problems. Nevertheless, some filling defects detected on the moulded parts showed some differences comparing to the numerical results. The rib corners closer to the gate are easily filled, but the simulation shows the presence of air traps in both locations. At the opposite side, the rib corners are also filled but the melt front profile of the POM grade (Figure 6.96) exhibits some differences, considering the assessment of the moulded parts discussed previously in Section 6.2.3.

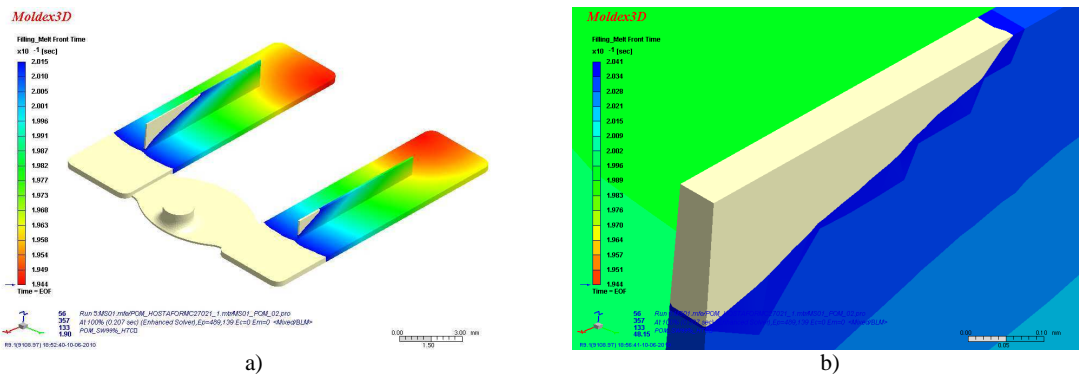


Figure 6.96. Numerical filling results for POM on the MS01 geometry

The BA02 geometry has several microfeatures which filling capacity should be assessed. In this case, the second half of the part consists of thin walls which make this geometry the most difficult to fill [85]. The filling simulation enabled a detailed analysis of each microfeature, but no filling problems were detected except for the existence of air traps on the last areas to fill. Figure 6.97 shows two sequences of filling for the PP grade, a) at the high-relief UM logo and b) at the high-relief SE logo.

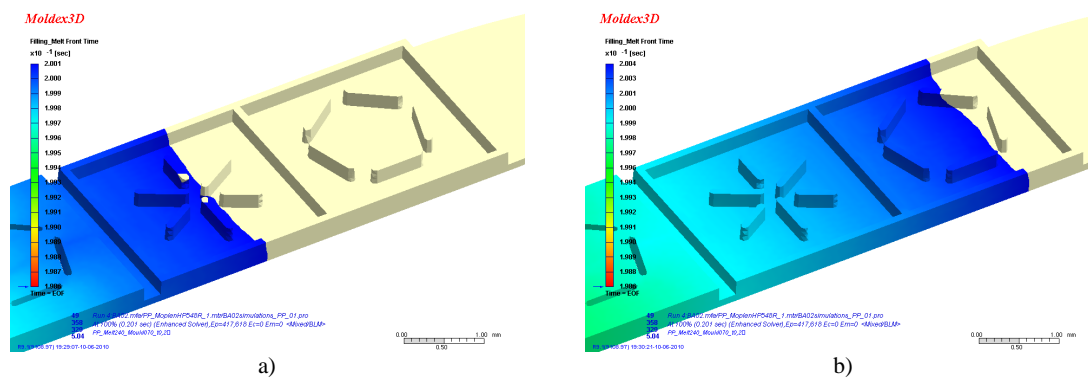


Figure 6.97. Numerical results for PP on the BA02SLM moulding block

The BA03 geometry has no details that could be considered as difficult to fill. Considering the overall part dimensions, wall thickness is large enough to enable full filling of the impression without problems. The only issue is the formation of two weld-lines at the annular protrusions, as shown in Figure 6.98. Consequently, the mould temperature should be increased to prevent the local weakening of the moulding [101].

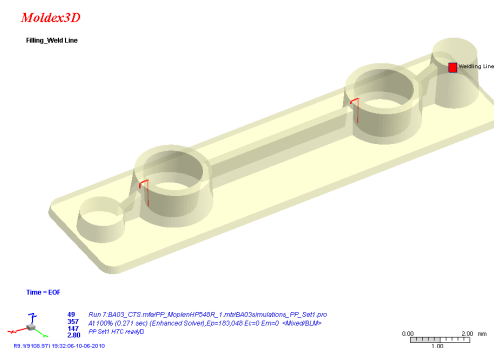


Figure 6.98. Numerical results for PP on the BA03SLM moulding block

Temperature

The analysis of the maximum temperature on the MS01 geometry enables the conclusion that the viscous heating affected all materials, since the core temperature was significantly higher than the melt temperature. Figure 6.99a shows the particular areas where skin temperature raised above the processing temperature. The core temperature at the ribs area is shown in Figure 6.99b where different temperature profiles are noticeable.

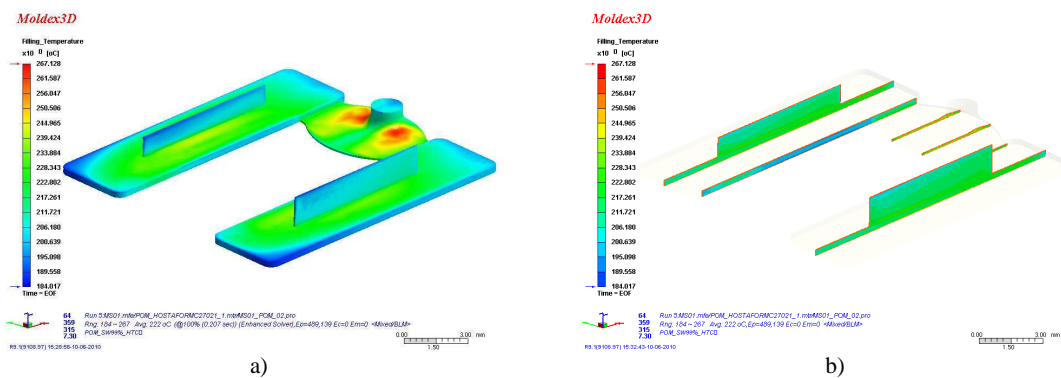


Figure 6.99. Filling temperature simulation for POM using the MS01 moulding block

The temperature rise due to the viscous heating effect appears on the maximum melt front temperature with gains of approximately 20°C on every simulation. The results from all simulations are summarized in Table 6.12.

Table 6.12. Simulation results analysis on the MS01 moulding block

Maximum temperature			
Simulation	Input value	Core	Melt front
PP@70°C	230°C	300,11°C	247,60°C
PP@80°C	230°C	318,55°C	253,09°C
POM@100°C	200°C	267,13°C	226,80°C
PS@60°C	230°C	308,32°C	251,46°C

As noticed previously, the thin-walled sections on the BA02 geometry caused relevant effects on shear rate and therefore, on melt core temperature as well. Analyzing the second half of the part length it is possible to notice that the PP temperature is predicted to increase locally above 300°C

due to viscous heating and that shear rate reaches values closer to $600\,000\text{ s}^{-1}$. The criticalness of that temperature can be evaluated comparing the melt speeds measured experimentally and numerically. Moldex 3D results showed filling discrepancies compared to experimental results when using the same processing conditions. In the numerical simulation, the impression was only fully filled upon the application of packing pressure. The last simulation comprehends an attempt to optimize the process by increasing mould and melt temperatures. The skin a) and core temperature b) are shown on Figure 6.100.

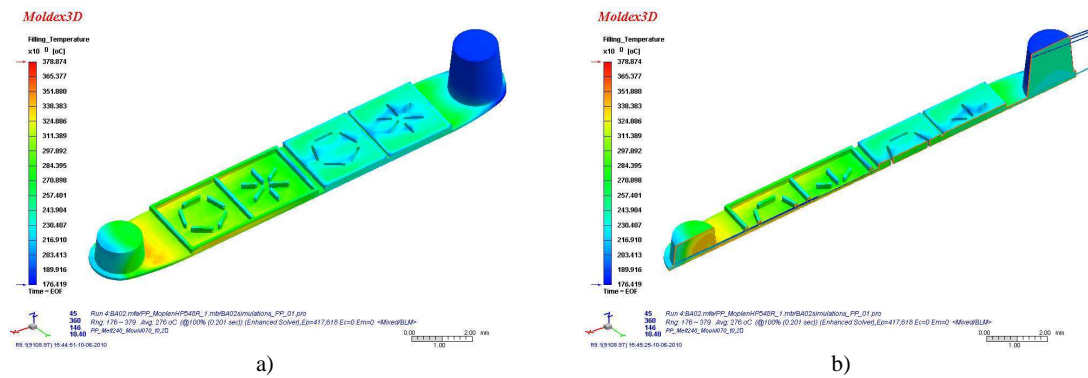


Figure 6.100. Numerical temperature results for PP on the BA02SLM moulding block

The viscous heating effect is much more evident with this geometry, since the base of the second half of the part is a $100\ \mu\text{m}$ thick wall. The temperature rise for PP at the melt front and core were significant, as shown on Table 6.13. On the other hand, POM behaved quite differently. This material show lower temperature rise and the increase of the mould temperature enabled the decrease of maximum temperatures, both at skin and core.

Table 6.13. Simulation results analysis on the BA02SLM moulding block

Maximum temperature			
Simulation	Input value	Core	Melt front
PP@70°C	240°C	378,87°C	324,99°C
POM@100°C	215°C	273,47°C	261,60°C
POM@110°C	220°C	268,41°C	252,52°C

The BA03 geometry consists on several features with a typical thickness of 300 μm . Once again, the viscous heating effect can be noticed, although, with a different magnitude. However, it is now possible to observe significant differences between skin and core temperature, since the typical wall thickness is large enough for such difference to be noticed. Figure 6.101 shows the skin temperature a) and the core temperature b). Analyzing the middle rib, it is noticeable that the temperature difference achieves more than 40°C on a 300 μm thick wall.

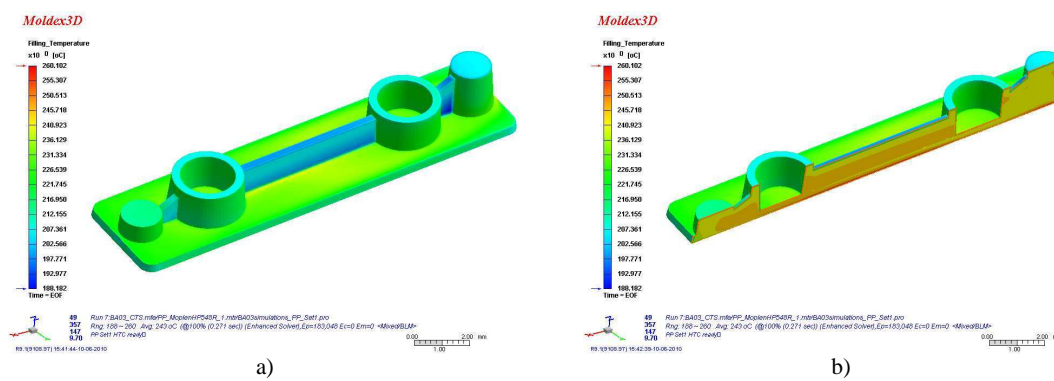


Figure 6.100. Numerical temperature results for PP on the BA03SLM moulding block

The data from all simulations is summarized in Table 6.14 and it shows the differences between the processing temperature, the core temperature and the melt front temperature. For the POM grade, the mould temperature was kept at 100°C. For PP, the mould temperature was kept at 70°C. In both cases, the temperature difference between skin and core is increased with a lower mould temperature or with the increase of flow rate and injection pressure imposed on Parameter Set 6.

Table 6.14. Simulation results analysis on the BA03SLM moulding block

Maximum temperature			
Simulation	Input value	Core	Melt front
POM	215°C	273,81°C	240,77°C
PP Set 1		260,10°C	251,46°C
PP Set 2		259,02°C	250,44°C
PP Set 3		259,95°C	249,91°C
PP Set 4	240°C	261,04°C	252,13°C
PP Set 5		254,48°C	246,18°C
PP Set 6		283,56°C	265,82°C
PP Set 7		260,29°C	252,27°C

Pressure

The use of pressure sensors on the mould enabled the comparison between experimental and numerical results. The results for both pressure data on the MS01 geometry are shown in Figure 6.102a. The pressure at the end of filling phase is shown in Figure 6.102b for the POM Hostaform C27021.

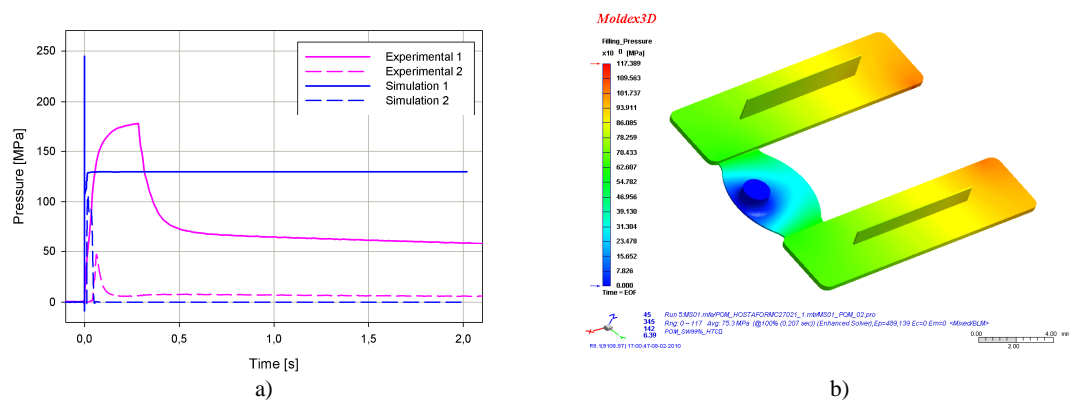


Figure 6.102. Numerical results for POM on the MS01 moulding block

As depicted on Figure 6.102a, the inlet pressure in the simulation shows a peak completely different from the experimental. This may be due to the inlet sensor location on the runner and not on the part itself. The same occurs in the simulation, causing the sensor node to be located on a runner-type mesh instead of a part-type mesh, which may have caused a peak with such magnitude. A similar situation occurred in all other simulations and therefore, the inlet signal from the simulation was discarded.

The pressure results obtained on the numerical simulation for all materials and processing conditions are summarized in Table 6.15.

Table 6.15. Numerical pressure results analysis on the MS01 moulding block

Simulation	Maximum outlet sensor pressure [MPa]		Maximum numerical pressure [MPa]		Time span between sensors	
	Experimental	Numerical	End of filling	End of packing	Experimental	Numerical
PP@70°C	36,33	107,23	106,81	113,50	35 ms	10,2 ms
PP@80°C	40,82	123,28	120,56	128,42	40 ms	5,36 ms
POM	46,39	106,46	117,39	126,39	45 ms	11,6 ms
PS	25,59	120,21	117,80	126,63	40 ms	5,37 ms

Comparing the pressure peaks on the outlet sensor, a much higher value results from the numerical simulation. The same occurs for the maximum pressure at the end of the filling and packing phases. All numerical pressure values are much higher than those measured experimentally. However, analyzing the last two columns in Table 6.15, it is possible to observe that the melt speed is also rather different. Considering the path between the two sensors, it is not possible to perform an accurate speed measurement, although it is possible to conclude that the flow regime is quite different on simulation. This fact may also contribute to explain the pressure peaks on the simulations.

Figure 6.103 shows the simulation for the PP with the BA02 geometry concerning a) the pressure at the end of filling phase and b) the pressure at the end of packing phase. The end of packing shows some interesting results. The part has several abrupt section variations, increasing pressure drop and causing packing to be ineffective at the end of the part. Considering the volume part compared with the overall volume, the pressure switch-over was set to 99,8% of filled volume to prevent the packing pressure from acting too soon [102].

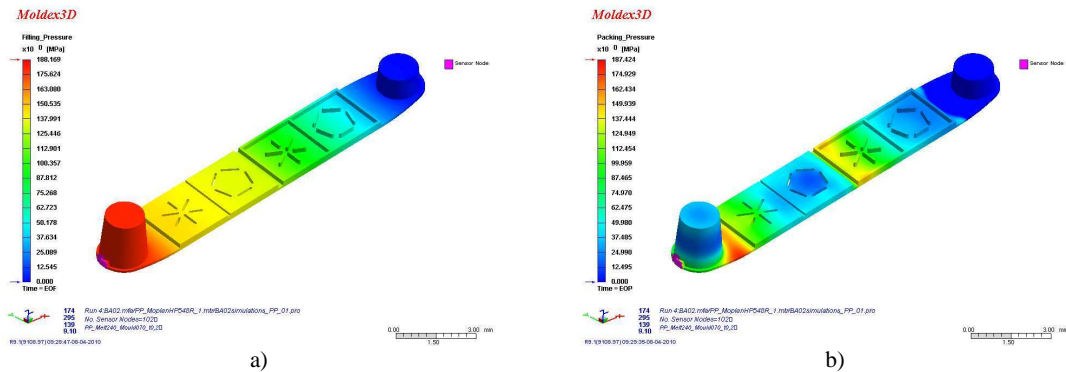


Figure 6.103. Pressure numerical results for PP on the BA02SLM moulding block

The comparison of experimental and numerical values for the PP grade on Figure 6.104 shows that the two sets of curves are different. Contrarily, the POM grade exhibited a similar behaviour (Figure 6.105), especially considering the pressure peaks that are similar.

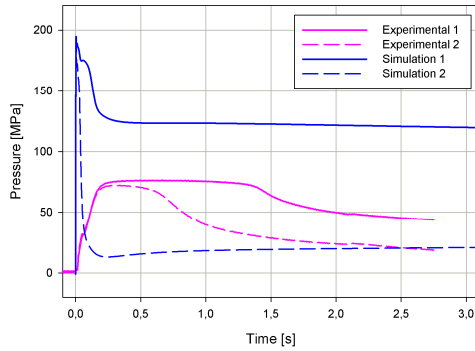


Figure 6.104. Comparison between pressure experimental and numerical results for the PP grade on the BA02SLM moulding block

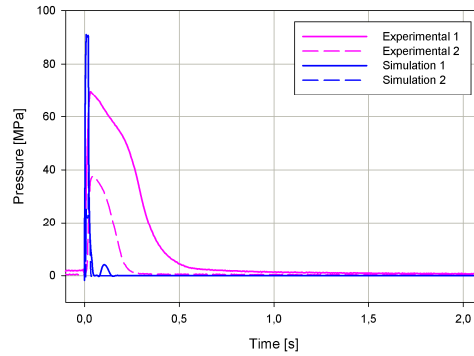


Figure 6.105. Comparison between pressure experimental and numerical results for the POM grade on the BA02SLM moulding block

These curves enable the comparison of the experimental time span between sensors with the same value estimated on the numerical simulation. By making this comparison, it is possible to foresee if shear rate reaches in fact critical values that could promote a flow regime change. These results obtained on the numerical simulation for all materials and processing conditions are summarized on Table 6.16.

Table 6.16. Numerical pressure results analysis on the BA02SLM moulding block

Simulation	Maximum sensor pressure [MPa]		Maximum numerical pressure [MPa]		Time span between sensors / Average speed					
	Experimental Inlet	Numerical Outlet	Inlet	Outlet	End of filling	End of packing	Experimental		Numerical	
							Time	Speed	Time	Speed
PP@70°C	76,37	72,36	194,78	192,68	188,17	187,42	20 ms	0,45 m.s ⁻¹	0,95 ms	~ 9 m.s ⁻¹
POM@100°C	69,55	37,57	91,02	25,86	113,01	0,0	15 ms	0,60 m.s ⁻¹	6,72 ms	~ 1,3 m.s ⁻¹
POM@110°C	64,26	7,62	76,10	19,69	94,42	0,0	25 ms	0,36 m.s ⁻¹	9,10 ms	~ 1 m.s ⁻¹

The simulation pressure data for POM, despite the obvious differences, are closer to the experimental values than those obtained for PP. Considering pressure at the end of packing, the POM simulations show a null value as in the experimental tests, noticing that packing time was too long for this application. On the same parameter, PP exhibits a different behaviour at the end of the packing phase. Although numerical simulation predicts a much higher value at the inlet sensor, the outlet signal, both experimental and numerical, seems to converge to a value close to 20 MPa.

These two materials show excellent ability for microinjection since they exhibit easy flow capacity, achieving high melt speeds with good replication of microdetails. However, the simulation of average melt speed is completely different than the experimental data, allowing the conclusion that the shear rates calculated in the numerical simulation are not as critical as they seem to be.

The simulation results for the BA03 geometry for the PP Moplen HP548R are shown in Figure 6.106 concerning a) the pressure at the end of filling phase and b) the pressure at the end of packing phase. In this case, the geometry is easier to fill and enabled a more effective packing phase.

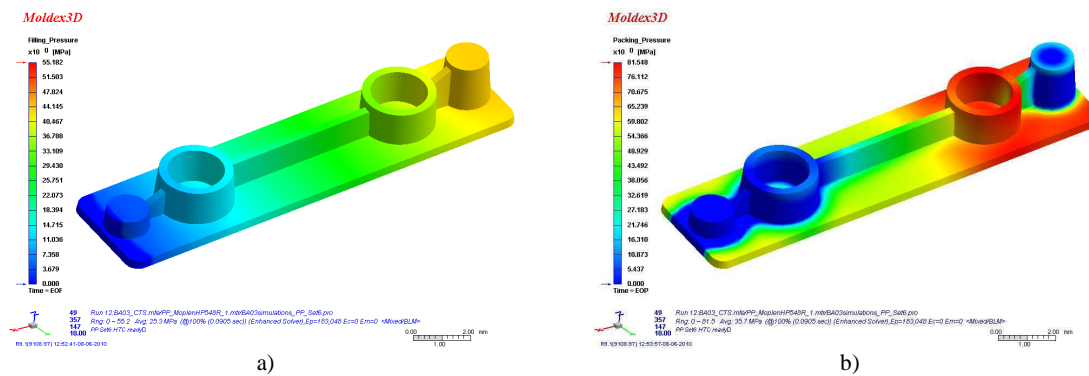


Figure 6.106. Pressure numerical results for PP on the BA03SLM moulding block

The comparison between experimental data and simulations for this moulding block showed similar results. Despite the different pressure profiles, Moldex 3D has predicted comparable values. Figure 6.107 illustrates the comparison of experimental and numerical values for the POM grade where the pressure peak values for the inlet sensor are quite similar. The pressure decay on both simulation curves is much faster than in reality; however, the trend leads to values similar experimental. The PP grade exhibited also some similarities with simulation curves (Figure 6.108). The pressure peaks are similar, at the inlet and at the outlet, but the pressure decay has different profiles. Nevertheless, the decay on the inlet sensor does not reach zero, which also occurred on the simulation, although with a much higher value. The pressure decay on the outlet sensor has also a different profile, but its trend is identical to the experimental profile, which is stabilized slightly below 40 MPa.

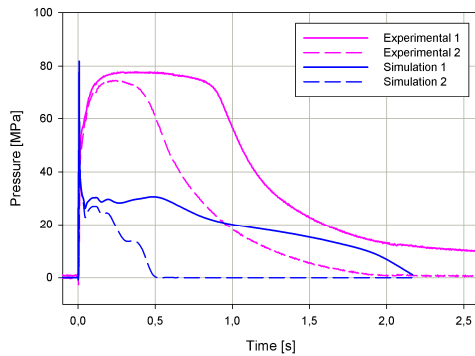


Figure 6.107. Comparison between pressure experimental and numerical results for the POM grade on the BA03SLM moulding block

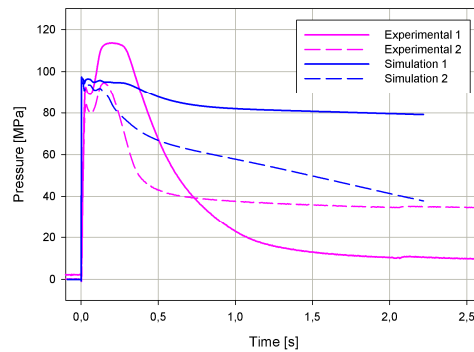


Figure 6.108. Comparison between pressure experimental and numerical results for the PP grade on the BA03SLM moulding block on Set 6

All other parameter sets for PP (Parameter Sets 1 to 5 and Set 7) resulted in significant differences between the experimental pressure curves and the numerical ones. In all cases, the pressure data predicted numerically were always lower than the experimental. Furthermore, the profile of the curves, especially the geometry of the pressure peak and pressure decay were different, although keeping a similar trend. The results obtained on the numerical simulation for all materials and processing conditions are summarized on Table 6.17.

Table 6.17. Numerical pressure results analysis on the BA03SLM moulding block

Simulation	Maximum sensor pressure [MPa]				Maximum numerical pressure [MPa]		Time span between sensors / Average speed			
	Experimental		Numerical		End of filling	End of packing	Experimental		Numerical	
	Inlet	Outlet	Inlet	Outlet			Time	Speed	Time	Speed
POM	77,83	74,71	81,84	75,33	72,22	15,33	10 ms	0,90 m.s ⁻¹	4,35 ms	~ 2 m.s ⁻¹
PP Set 1	72,97	52,47	50,74	49,06	28,97	31,81	20 ms	0,45 m.s ⁻¹	3,59 ms	~ 2,5 m.s ⁻¹
PP Set 2	105,41	51,44	33,22	31,85	27,48	10,33	15 ms	0,60 m.s ⁻¹	3,37 ms	~ 2,7 m.s ⁻¹
PP Set 3	118,38	66,60	36,13	33,40	26,62	14,84	15 ms	0,60 m.s ⁻¹	4,24 ms	~ 2,1 m.s ⁻¹
PP Set 4	107,82	58,57	45,24	43,53	30,25	25,57	15 ms	0,60 m.s ⁻¹	3,29 ms	~ 2,7 m.s ⁻¹
PP Set 5	111,64	56,61	29,83	26,14	21,81	5,72	25 ms	0,36 m.s ⁻¹	6,89 ms	~ 1,3 m.s ⁻¹
PP Set 6	113,45	93,56	97,44	96,60	55,18	81,55	5 ms	1,80 m.s ⁻¹	1,21 ms	~ 7,4 m.s ⁻¹
PP Set 7	47,78	42,95	28,90	26,40	26,04	0,00	10 ms	0,90 m.s ⁻¹	3,33 ms	~ 2,7 m.s ⁻¹

Considering the pressure peaks at the sensors, Table 6.17 confirms that the greater similarities between experimental and numerical values appear in the POM simulations and also in the PP

simulation, using Parameter Set 6. All other simulations show great discrepancies on pressure peak values. In which concerns to the average melt speed inside the cavity, other significant differences arise, since numerical simulation predicts melt speeds much higher than those measured experimentally.

6.6.2. Heat transfer simulation

The heat transfer simulations were prepared to evaluate the magnitude of the heat flux under transient conditions on moulding blocks for microinjection. Therefore, a simple impression was generated using a sample part consisting of a thin feature with approximate dimensions of the base of the BA01 and BA03 type parts. For that purpose, a simple mesh model was generated and a transient analysis was defined on Abaqus 6.7 EF to clarify this phenomenon, as described earlier in Chapter 5.

Heat transfer on elements of the moulding blocks

The first simulation was carried out, using the same material in the core and the cavity, *i.e.* steel 1.2767 (Job 1), to establish a reference for future comparison with other material setups. Analyzing the longitudinal cross-section of the moulding block and considering the temperature boundary conditions imposed, it can be noticed that temperature variations occurs mainly at interfaces Steel/Air and Steel/POM,. Despite the difference between the POM temperature – 180°C – and the outside air temperature, 25°C, there is no significant heat transfer on the moulding block itself. Both moulding blocks were kept at 90°C. They have suffered a decrease on the Steel/Air interface but only a slight temperature increase is noticed at the Steel/POM interface.

The second simulation was carried out with the same material setup as the microinjection tests performed with the Nanoform 15210 moulding blocks (Job 2). Here also, the moulding blocks were kept at 90°C due to the thermal limitation imposed by the composite resin. The simulation results for this material setup are shown on Figure 6.109.

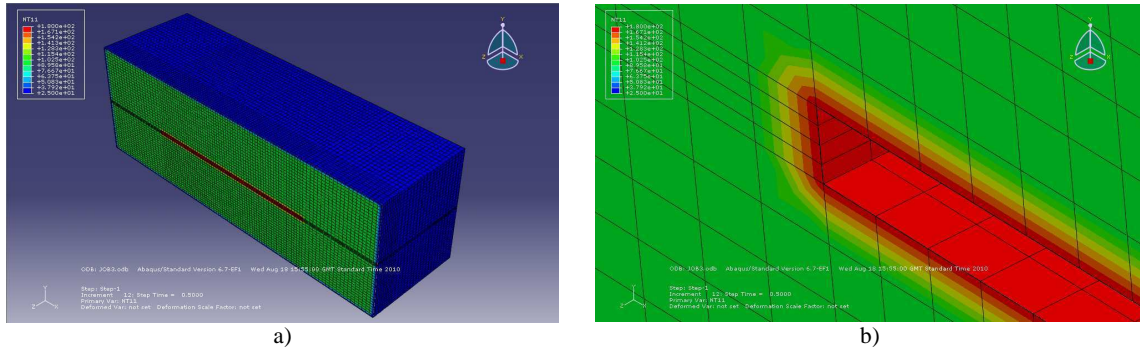


Figure 6.109. Job 2 heat transfer simulation results

a) cross-section view of the moulding blocks; b) detail of cross-section view of cavity

This simulation uses a mixed material setup; hence, it would be expectable to notice differences on the thermal affected area due to the different conductivities. However, such effect is not easily noticed. The composite resin is a much worse thermal conductor than steel and thus, an asymmetric thermal profile would be expectable instead of a symmetrical one. One of the reason for this may be the short simulation time, but most microinjection tests occurred much faster than this. The other plausible reason is the low surface to volume ratio of the part and the moulding blocks. Although the part surfaces are set initially at 180°C, such thermal load is not enough to promote a significant heat transfer on the moulding block.

The third simulation was carried out using the same material with the core and the cavity, *i.e.* Nanoform 15210 and it is designated as Job 3. Given the previous results on Job 2, it is important to analyze the importance of heat transfer on moulding blocks when both are made from less conductive materials such as a composite resin. The simulation results show similar thermal profiles as in previous heat transfer simulations. Here, it would be expectable a symmetric thermal profile, although, with a much lower magnitude than the one noticed on Job 1, using a Steel/Steel combination. Also, the moulding blocks have suffered a decrease at the Nanoform/Air interface but only a slight temperature increase is noticed at the Nanoform/POM interface.

Heat transfer on nodes of the moulding blocks

The previous simulation results based on elements were not conclusive regarding the use of alternative materials such as the composite resin Nanoform 15210. In fact, the use of a less conductive material did not resulted on a significantly poorer heat transfer as expected. Therefore, the heat transfer simulation for the Steel/EOS GP1 setup was discarded. The EOS GP1 is

equivalent to a stainless steel, which is less conductive than a common steel but much more conductive than the Nanoform 15210 resin, as shown on Table 5.15.

Since the previous heat transfer results showed some ambiguity for all material setups, a nodal temperature analysis was carried out to determine the temperature variation on relevant nodes of the mesh. The nodes selected for the temperature analysis are located on the longitudinal section cut and are shown in Figure 6.110. The nodes from the cavity side are noted as “Ca” and the ones from the core side are noted as “Co”, both followed by two characters separated by a dot. The first character indicates the node position at the interface between part and cavity/core. The second character indicates the node position in the mesh: 1 means that the node is at the interface and the value grows as the node is located further away from the interface.

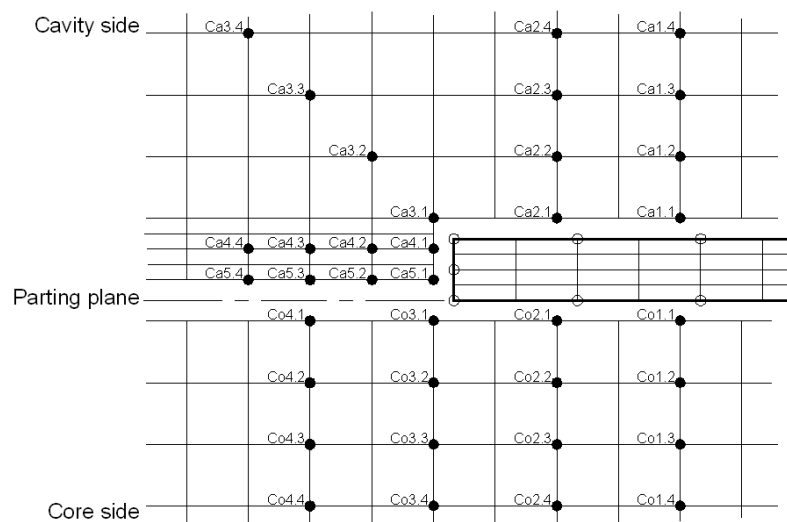


Figure 6.110. Nodes selected for temperature analysis

Preliminary node temperature analysis showed that all interface nodes Ca1.1, Ca2.1, Ca3.1, Ca4.1, Ca5.1, Co1.1, Co2.1 and Co3.1, except for the Co4.1 node, suffered only a slight temperature decrease while the correspondent level 2 nodes (Ca1.2, Ca2.2, Ca3.2, Ca4.2, Ca5.2, Co1.2, Co2.2 and Co3.2) have just suffered a slight temperature increase. Therefore, level 1 nodes are closer to 180°C and level 2 nodes are closer to 90°C. It is important to notice that the distance between level 1 and level 2 nodes, except for the Ca3 nodes, is just 266 μm. Therefore, the mesh size can be considered tight enough to observe changes on nodal temperature concerning materials conductivity. However, for the same reason it is useless to compare nodal temperatures from

level 1 and level 2 nodes on the same line. Level 3 and 4 nodes are not significantly affected and may be overlooked in this analysis.

The nodal temperatures extracted from Job 1 simulation results showed the nodal temperature variation on cavity level 1 nodes (Figure 6.111). Except for the Ca4.1 node, the other nodes show a temperature decrease. After 0,5 seconds, none of the selected cavity interface nodes drops more than 0,0125°C.

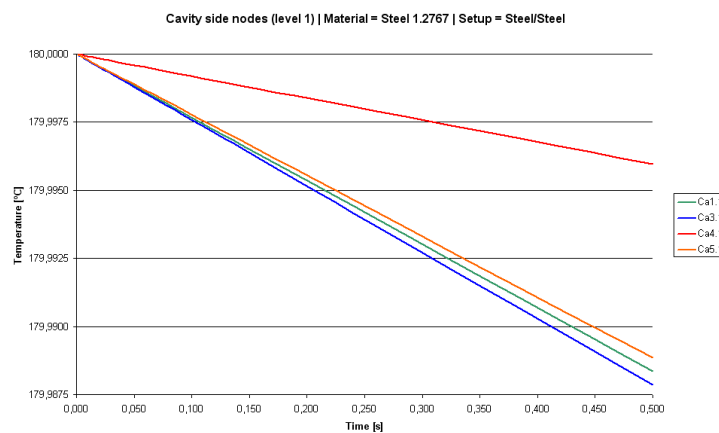


Figure 6.111. Nodal temperature variation for cavity level 1 nodes

The Ca4.1 node shows the smaller temperature decrease followed by the Ca5.1 node, both located near the parting plane. This interface, although it is formed by a Steel/Steel combination may have contributed to this thermal behaviour.

On the core side, this material setup showed similar results. Nodal temperature decreased similarly for Co1.1, Co2.1 and Co3.1 nodes. On the level 2 nodes, both on cavity and core, nodal temperature increase is always below 0,9%. Level 3 nodes show even lower temperature increase and finally, level 4 nodes are not thermally affected at all by the heated polymer.

The nodal temperature analysis of the Job 2 results shows the noticeable effect of material setup (Figure 6.112). Cavity nodes belong to the less conductive material and so, the temperature decrease is much smaller on the interface nodes Ca1.1 to Ca4.1. The Ca5.1 node shows a higher temperature decrease due to its contact with a better conductive material, *i.e.* Steel.

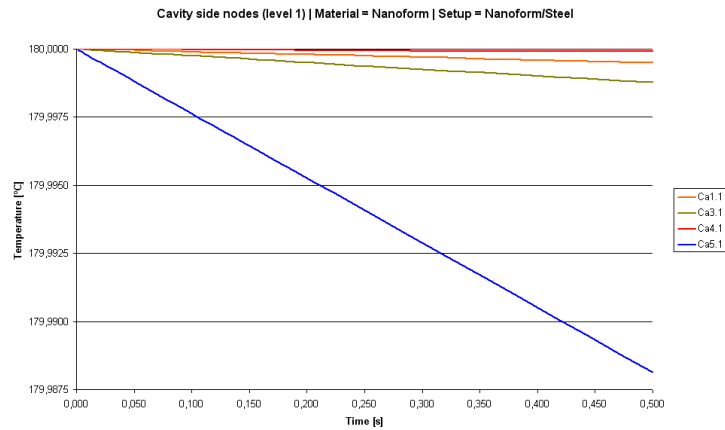


Figure 6.112. Nodal temperature variation for cavity level 1 nodes

On the core side, the behaviour is quite similar to that on the Job 1 nodal analysis. Co2.1 curve overlaps the Co1.1 curve and the corner node – Ca3.1 – shows now a slightly higher decrease, although it is not significant since it only drop 0,0125°C, as previously noted.

The last nodal analysis, based on Job 3 results, shows the effect of this all Nanoform setup on heat transfer. The temperature drop is expected to be reduced due to the thermal properties of the material. Such fact is confirmed by the cavity nodal analysis depicted on Figure 6.113. The temperature decrease is now below 0,001%. After 0,5 s, the Ca4.1 node shows the higher temperature, followed by the Ca1.1 node. The corner nodes, Ca3.1 and Ca5.1 show similar decreases since the interface at the parting plane is now from the same material.

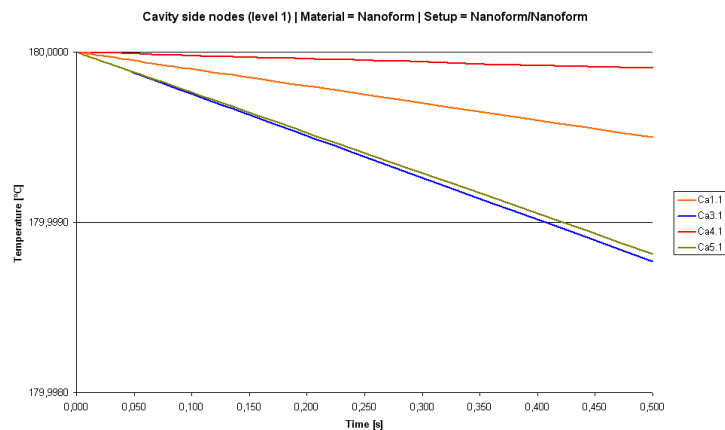


Figure 6.113. Nodal temperature variation for cavity level 1 nodes

The nodal analysis on the core side followed the same trend, keeping temperature decreases very small.

A last set of heat transfer analysis was performed, motivated by the short simulation time imposed initially, 0,5 s. Although this simulation time corresponds to field results, it was decided to perform simulations with extended time to determine if the temperature decrease would be higher and if heat transfer would be more effective or not, depending on the material setup. For that purpose, 2 s were added to the simulation time, corresponding to the most used packing time in the microinjection tests. Therefore, the simulation time is now 2,5 s and initial time step was set to 5 ms.

Two simulations were prepared to evaluate the effect of a longer simulation time: Jobs 1 and 3, respectively for the material setups Steel/Steel and Nanoform/Nanoform. These simulations were repeated for the new simulation time. It is possible to notice that no major differences occur on the thermal behaviour. The interface walls are equally heated despite the different material conductivities.

As expected, the longer simulation time resulted on higher temperature decrease on the two material setups. Nevertheless, the Steel/Steel setup still shows the highest temperature drop (Figure 6.114).

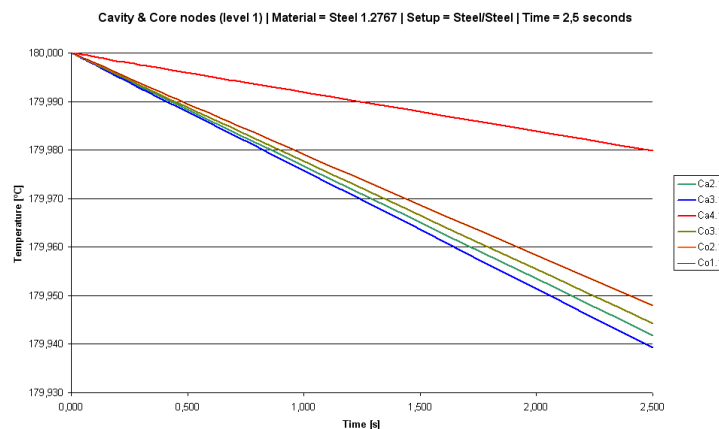


Figure 6.114. Nodal temperature variation for cavity and core level 1 nodes for 1.2767 Steel

On the other hand, the Nanoform/Nanoform setup shows the lowest temperature after 2,5 s on the Ca3.1 node with a temperature drop of 0,0061°C (Figure 6.115).

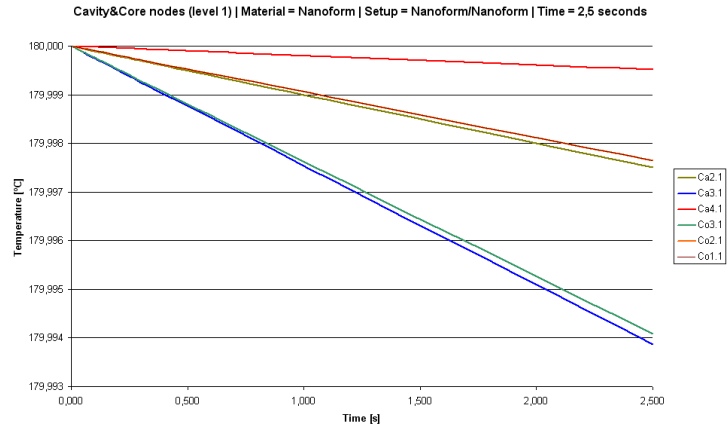


Figure 6.115. Nodal temperature variation for cavity and core level 1 nodes for Nanoform 15210

The results of the heat transfer analysis here performed enabled the preliminary conclusion that heat transfer on the moulding blocks was not significant despite the different thermal properties of the materials. Even a detailed analysis on mesh nodes showed that the interface temperature is highly influenced by the temperature of the hottest element. Therefore, the filling and packing simulations performed with Moldex 3D can be considered valid for both material types.

Conclusions

The opportunity of this research emerges from the interest gathered by microinjection in growing sectors of application. Injection moulding as a mass replication process along with its flexibility shows great potential for the production of microcomponents and microsystems. Characterizing the polymer flow at the microscale is a topic that still requires development. In this work the microinjection tests conducted in microchannels, ultrathin walls and filling of microdetails, both experimentally and numerically enabled the gathering of useful data for integration on commercial software packages. The micromouldings were produced with a production cell based on a Boy 12A injection moulding machine capable of metering with precision the small dosage volumes required in microinjection moulding. The simulations were performed using the software Moldex 3D, adapting the mesh models and the heat transfer coefficients to the process.

Micromilling, laser beam machining, microEDM, high-precision stereolithography and selective laser melting were the manufacturing technologies used to produce the moulding blocks.

The results of this research suggest a number of conclusions:

1. Considering the materials used, the moulding blocks produced by high precision stereolithography were the most fragile, even considering that they were built with Nanoform 15120, a photocurable resin filled with ceramic nanoparticles.

Other conclusions may be organised according to the following topics

i) Assessment of the injection moulding flow at the microscale

2. It is possible to state that the use of a microinjection moulding tool for rheometry purposes provided the establishment of flow curves at higher pressures than the ones obtained on traditional rheometry, enabling critical shear rate determination for each microchannel used.
3. A tool for the quantitative evaluation of the rheological behaviour of polymer melts under typical microinjection moulding conditions was developed. Unlike conventional capillary

rheometry devices, this setup used microinjection process parameters, namely the injection speed to obtain different shear rates, enabling the plotting of flow curves. Therefore, the results could be easily applied onto the microinjection process itself or on microinjection simulation.

4. Wall slip as a microscale effect was detected and the critical values of shear rate were determined. Furthermore, the local wall slip velocity was calculated and compared to the average melt velocity imposed on the process, to determine its relevance to the flow behaviour. It was noticed that the shifting between the shear flow and plug flow is more abrupt on the $400 \times 100 \mu\text{m}$ microchannel than in $200 \times 200 \mu\text{m}$ square microchannels, due to the less favourable cross-section.
5. These results proved the validity of the experimental concept and also suggested that the heat transfer phenomena in ultrathin microinjection mouldings with a large surface area/volume ratio play an important role.
6. The validity of the TTS principle at this scale is also questionable, allowing the conclusion that heat transfer mathematical models will require further study.

ii) Design and manufacturing of the research micromould

7. A specific moulding tool was enabling interchangeable moulding blocks manufactured by each technology being used. Such flexibility enabled a preliminary study on microrheometry since polymer flow at the microscale still requires further knowledge. The moulding tool is equipped with two pressure sensors, located strategically that were used to evaluate pressure peaks, pressure drop, and melt speed.
8. Two microchannel cross sections, $200 \times 200 \mu\text{m}$ and $400 \times 100 \mu\text{m}$, were tested to evaluate critical shear rate values. This setup enabled the moulding tool to operate as a microrheometer, fully compatible with any industrial injection equipment, enabling polymer flow characterization on site. However, it is important to clear that this equipment setup is not a microrheometer, but rather a viscometer that replicates the flow conditions in real flow situations, i.e., it is a process analyser and simulator.

iii) Assessment of additive processes and moulding geometries

9. Two types of parts/moulding blocks were designed to validate the capacity of the manufacturing technologies to operate at the microscale. The first type presented a challenge concerning the aspect-ratio achievable by each manufacturing technology. The same challenge is also valid for microinjection since the filling of high aspect-ratio microfeatures and thin-walls revealed some issues. These moulding blocks were manufactured by micromilling, laser beam machining and microEDM. The challenge for the second type was to manufacture the microdetails, to evaluate the moulding blocks integrity after the microinjection tests and to evaluate the moulding surface replication onto the plastic parts. These moulding blocks were manufactured by high-precision stereolithography and selective laser melting.
10. Surface finishing arises as one of the most significant parameters, having great influence in the injection process. Subtractive technologies are capable of excellent surface finishing, even if no post-processing is applied. Some wear was noticed on these moulding blocks related to the debris left by the processing technique, indicating that a polishing process would be desirable.
11. The surface quality provided by additive technologies depended on the process. High-precision stereolithography achieved a good surface roughness while selective laser melting generated a poor surface quality. However, in which concerns to material, selective laser melting can use metallic powder with similar properties as stainless steel, making its products fully functional right after manufacture. In this case, a post-processing such as shot-peening or electron beam polishing would be highly recommendable to enhance surface quality. Nanoform 15120 besides the UV cure, required an additional thermal cure to enhance the mechanical properties.

iv) Rheological characterization, flow and heat transfer simulation

12. The filling simulation using Moldex 3D brought additional knowledge to the experimental work. In general, the filling simulations had similar results as experimental tests, concerning fill time and the full filling of cavities. Nevertheless, the comparison of

numerical data and experimental data concerning pressure reveals several discrepancies that need to be addressed.

13. Despite all the refinements imposed to the model meshing and analysis setup, the pressure peaks inside the impression were not similar in all cases. However, an important aspect is that in the experimental work, larger piezoelectric pressure sensors with physical dimensions, namely the diameter, are used. The pressure reading on this type of sensors is proportional to the area covered by the melt front, disabling the possibility of reading a peak value directly. Therefore, the pressure reading may differ naturally from experimental to numerical.
14. For the parts incorporating thin walls, the pressure values were quite similar, regarding to pressure peaks and pressure profile along the moulding cycle. The analysis of the moulded parts on thin rib walls revealed that melt front profile is different on numerical analysis. These parts appeared as fully filled and only a microscopic analysis enabled the detection of those flow effects.
15. The heat transfer simulations with Abaqus enabled the conclusion that heat transfer on the moulding blocks is less important than the fill time. The use of different materials with different thermal conductivities is not significantly important on the injection phase.
16. A less conductive material like Nanoform can be rather useful on the packing phase since it delays melt cooling enabling packing pressure to be more effective. On the other hand, this delay makes cycle time longer which is certainly undesirable on industrial applications.
17. The heat transfer from the melt to the outside was not significant since the moulding block was heated up, as good microinjection practices recommend.

v) Structural integrity of the moulding blocks

The microinjection tests performed using several types of moulding blocks, enabled the comparison between the manufacturing techniques.

18. The steel moulding blocks have not sustained any damage; however, the micromilled surfaces suffered some wear. The milling strategy left some debris, noticeable on the SEM

images, and polymer flow acted as a surface polishment. Such effect would be also expectable on the LBMed surfaces, since they exhibit the higher values of surface roughness: this process is thermal-based and thus the laser beam hardened a superficial layer of material. The debris left on that area during processing became fully attached to the surface and only a slight wear was detected.

vi) Microproduct assessment

The plastic parts were obtained from commercial thermoplastic grades. Three materials were selected, a) two semi-crystalline materials, polypropylene and polyoxymethylene and b) an amorphous material, polystyrene.

19. Injection mouldings with PS revealed to be very difficult due to lowest shrinkage value of this material combined with unsuitable draft angles on the cavities of the moulding blocks. The semi-crystalline materials showed good flow and ejection behaviour.
20. The microinjection tests with steel moulding blocks showed that the selection of the manufacturing technology is important to improve the performance of the moulding tool. The higher is the aspect-ratio of the feature; the better should be the surface finishing. Therefore, if the geometry of the feature makes any post-processing operation inefficient, the technology must achieve a suitable surface quality.
21. Manufacturing time must also be considered and a balance between these two factors or even the integration of technologies to accomplish the geometry may be the adequate approach.
22. The use of the SLA moulding blocks on microinjection was interesting in terms of the the replication of microdetails and the overall good surface quality. However, some moulding features were too demanding upon ejection. The draft angles should be higher considering the aspectratio and the contact surface. In some cases, these ejection problems resulted on damaged features or on permanently damaged moulding blocks. Polymer flow also caused damage to microdetails. The measured melt speed in these regions reached values close to 1 m.s^{-1} suggesting a drag force large enough to pluck way the features that were not oriented in the flow direction. Other damaged areas appear on the gate area of the moulding blocks, especially when high pressure values were required to obtain a fully

- filled cavity. As major limitation, these moulding blocks worked under a mould temperature similar to the Nanoform glass transition temperature to prevent the deterioration of the resin.
23. The tests with the SLM moulding blocks led to poor results. The moulding surface quality was very poor and the microdetails were inefficiently built since the minimum dimension of the microfeatures (100 μm) is equal to the laser spot size.
 24. Considering the state-of-the-art of the process, the feature dimensions were too ambitious. The moulding block that exhibited the best surface roughness has rib cavities where there is accumulated debris. Despite the generous draft angle, the poor surface quality inside the rib cavity caused the plastic parts several times to be blocked.
 25. The analysis of the moulded parts and moulding blocks through optical microscopy, laser topography and scanning electron microscopy are suitable for this application domain. Although not all this equipment is suitable for on site characterization, these techniques are very important to assess the quality of the moulded parts given the high demanding level of several domains of application such as microfluidics or microoptics.
 26. As a final note, the manufacturing time of these additive processes may enable the shortening of time-to-market. Considering short-runs, Nanoform and SLA are suitable solutions for microtools, as long as the part design contains geometries that allow the enhancement of tool life. The SLM process is also evolving and both laser and material developments will surely bring new features that might become useful in micromanufacturing. Its use on less demanding applications concerning the dimensional range of the tools is certainly important since the mechanical properties of the material are quite suitable for a long-run tool.

Future work

The work here developed studied the polymer flow on microinjection and its effects on moulding blocks manufactured by additive and subtractive technologies. However, it also brought up other related subjects that need to be addressed, requiring further studies. The following proposals are originated on the knowledge gathered throughout this work.

- The heat transfer phenomena on the polymer revealed to be highly significant in microrheometry and in microinjection. Further understanding of the phenomena requires studies using sensing equipment adapted to the micrometric scale. The future miniaturization of infrared temperature sensors will bring new prospects to this analysis;
- The microrheometry tool developed enables the characterization of other materials that might be considered to be used on microinjection. Critical shear rates can be obtained to determine suitable processing conditions for newly developed materials;
- The microinjection process control may benefit from new developments on Variotherm systems, incorporating fast response devices/materials for heating and cooling;
- The use of subtractive technologies, complemented with a suitable post-finishing process or with the use of coatings to enhance surface properties is required to establish guidelines concerning plastic part design and manufacturing process selection;
- The capacities of additive manufacturing will certainly be incremented through technological and/or material developments. Considering the particular case of metallic materials, the use of a post-finishing process was intentionally missed in this work but technologies such as shot-peening or electron beam polishing could prove to be useful;

- The development of a microinjection knowledge database comprising the guidelines for material and manufacturing technologies selection would certainly become rather useful to support both academia and industry.

References

1. Piotter, V., K. Mueller, K. Plewa, R. Ruprecht, and J. Haußelt, *Performance and simulation of thermoplastic micro injection molding*. Microsystem Technologies, 2002. **8**: p. 387-390.
2. Young, W.-B., *Simulation of the filling process in molding components with micro channels*. Microsystem Technologies, 2005. **11**: p. 410-415.
3. Young, W.-B., *Analysis of filling distance in cylindrical microfeatures for microinjection molding*. Applied Mathematical Modelling, 2007. **31**: p. 1798-1806.
4. Regenfuss, P., L. Hartwig, S. Klotzer, R. Ebert, T. Brabant, T. Petsch, and H. Exner, *Industrial freeform generation of microtools by laser micro sintering*. Rapid Prototyping Journal, 2005. **11**(1): p. 18-25.
5. Galantucci, L.M., F. Lavecchia, and G. Percoco. *Study of compression properties of topologically optimized FDM made structured parts*. in *CIRP Annals 2008*. 2008.
6. Dimov, S.S., C.W. Mathews, A. Glanfield, and P. Dorrington, *A roadmapping study in Multi-Material Micro Manufacture*. Elsevier, 2006.
7. Löhe, D. and J. Haußelt, *Microengineering of Metals and Ceramics - Part I, Advanced Micro & Nanosystems*. Vol. 3. 2005, Weinheim: Wiley-VCH Verlag GmbH & Co. KGaA.
8. Piotter, V., T. Hanemann, R. Ruprecht, and J. Haußelt, *Injection molding and related techniques for fabrication of microstructures*. Microsystem Technologies, 1997: p. 129-133.
9. Martin, M.T., B. Whiteside, P.D. Coates, P.S. Allan, G. Greenway, and P. Hornsby. *Micromoulding: Consideration of Processing Effects on Medical Materials*. in *ANTEC 2003 - 61st Annual Technical Conference & Exhibition*. 2003.
10. Kukla, C., H. Loibl, and H. Detter, *Micro-Injection Moulding, The aims of a Project Partnership*, in *Kunststoffe Plastic Europe*. 1998. p. 1331-1336.
11. Evans, B. and R. Mehalso, *How Small is Small?: A Guide to the New Microfabrication Design and Process Techniques*, in *Medical Device & Diagnostic Industry*. 2001.
12. Kupka, R.K., F. Bouamrane, C. Cremers, and S. Megtert, *Microfabrication: LIGA-X and applications*. Applied Surface Science, 2000. **164**: p. 97-110.
13. Pouzada, A.S., *Hybrid moulds: A case of integration of alternative materials and rapid prototyping for tooling*. Virtual and Physical Prototyping, 2009. **4**(4): p. 195 - 202.
14. Martinho, P.M., P.J. Bártolo, and A.S. Pouzada, *Hybrid moulds: effect of the moulding blocks on the morphology and dimensional properties*. Rapid Prototyping Journal, 2009. **15**(1): p. 71-82.
15. Rajurkar, K. and M. Madou, *Processes*, in *WTEC Panel Report on International Assessment of Research and Development in Micromanufacturing*, WTEC, Editor. 2005, WTEC. p. 39-64.
16. Petsch, T., P. Regenfuß, R. Ebert, L. Hartwig, S. Klötzer, T. Brabant, and H. Exner. *Industrial laser micro sintering*. in *23th International Congress on Applications of Lasers and Electro-Optics*. 2004.
17. Kruth, J.P., B. Vandenbroucke, J. Van Vaerenbergh, and I.P. Mercelis. *Benchmarking of different SLS/SLM processes as rapid manufacturing techniques*. in *International Conference on Polymers & Moulds Innovations (PMI)*. 2005. Ghent, Belgium.
18. Malek, C.K. and V. Saile, *Applications of LIGA technology to precision manufacturing of high-aspect-ratio micro-components and -systems: a review*. Microelectronics Journal, 2004. **35**: p. 131-143.
19. Uriarte, L., A. Herrero, A. Ivanov, H. Oosterling, L. Staemmler, P. Tang, and D. Allen, *Comparison between microfabrication technologies for metal tooling*. Proceedings of the Institution of Mechanical Engineers, Part C: Journal of Mechanical Engineering Science, 2006. **220**(11): p. 1665-1676.
20. Bourell, D. and K. Rajurkar, *Materials*, in *WTEC Panel Report on International Assessment of Research and Development in Micromanufacturing*, WTEC, Editor. 2005, WTEC. p. 21-38.

21. Bertsch, A., S. Jiguet, P. Bernhards, and P. Renaud, *Microstereolithography: a review*, in *Materials Research Society Symposium 758*, M.R. Society, Editor. 2003, Materials Research Society.
22. Bertsch, A., S. Jiguet, P. Bernhards, and P. Renaud. *Microstereolithography: a review*. in *Materials Research Society Symposium 758*. 2003: Materials Research Society.
23. Neumeister, A., S. Czerner, and A. Ostendorf. *Metal and polymer micro parts generated by laser rapid prototyping*. in *4th International Congress on Laser Advanced Materials Processing*. 2006.
24. Wohlers, T., *Part 3: System Manufacturers*, in *Wohlers Report 2005*, Wohlers_Associates_Inc., Editor. 2005.
25. Cheng, Y.-L., M.-M. Li, J.-H. Lin, J.-H. Lai, C.-T. Ke, and Y.-C. Huang. *Development of a Dynamic Mask Photolithography System*. in *2005 IEEE International Conference in Mechatronics*. 2005. Taiwan.
26. Houbertz, R., L. Frölich, M. Popall, U. Streppel, P. Dannberg, A. Bräuer, J. Serbin, and B. Chichkov, *Inorganic-Organic Hybrid Polymers for Information Technology: from Planar Technology to 3D Nanostructures*. *Advanced Engineering Materials*, 2003. **8**: p. 553-558.
27. Kou, H., A. Asif, W. Shi, Z. Jiang, and W. Huang, *A novel hyperbranched polyester acrylate used for microfabrications*. *Polymers for Advanced Technologies*, 2004. **15**: p. 192-196.
28. Stute, U., J. Serbin, C. Kulik, and B. Chichkov. *Three-dimensional nanostructure fabricated by two-photon polymerization of hybrid polymers*. in *1st International Conference on Advanced Research on Virtual and Rapid Prototyping*. 2003. Leiria.
29. Kruth, J.P., I.P. Mercelis, J. Van Vaerenbergh, L. Froyen, and M. Rombouts. *Advances in Selective Laser Sintering*. in *1st International Conference on Advanced Research on Virtual and Rapid Prototyping*. 2003. Leiria, Portugal.
30. Kruth, J.-P., B. Vandenbroucke, J. Van Vaerenbergh, and P. Mercelis, *Benchmarking of Different SLS/SLM Processes as Rapid Manufacturing Techniques*, in *International Conference Polymers & Moulds Innovations (PMI) 2005*. 2005: Ghent, Belgium.
31. Wohlers, T., *Part 5: Metal parts and tooling*, in *Wohlers Report 2009*, Wohlers_Associates_Inc., Editor. 2009.
32. Santos, E.C., M. Shiomiya, K. Osakada, and T. Laoui, *Rapid manufacturing of metal components by laser forming*. *International Journal of Machine Tools & Manufacture*, 2006. **46**: p. 1459-1468.
33. Grujicic, M., Y. Hu, G.M. Fadel, and D.M. Keicher, *Optimization of the LENS Rapid Fabrication Process for In-Flight Melting of Feed Powder*. *Journal of Materials Synthesis and Processing*, 2001. **9**(5): p. 223-233.
34. Hensiger, D.M., A.L. Ames, and J.L. Kuhlmann. *Motion Planning for a Direct Metal Deposition Rapid Prototyping System*. in *2000 IEEE International Conference on Robotics & Automation*. 2000.
35. Hofmeister, W., M. Wert, J. Smugeresky, J.A. Philliber, M. Griffith, and M. Ensz, *Investigating Solidification with the Laser-Engineered Net Shaping (LENSTM) Process*. *The Journal of The Minerals, Metals & Materials Society*, 1999. **51**(7).
36. Ochiai, H., M. Watanabe, M. Arai, H. Yoshizawa, and Y. Saitou, *Development of Coating and Cladding Technology, MSCOating®, Using Electro-Discharge Energy*. *IHI Engineering Review*, 2006. **39**(1).
37. Hiemenz, J., *EBM offers a new alternative for producing Titanium parts and prototypes*, in *Time-Compression Technologies*. 2006. p. 16-20.
38. Sha, B., S.S. Dimov, D.T. Pham, and C.A. Griffiths, *Study of Factors Affecting Aspect Ratios Achievable in Micro-injection Moulding* in *4M2005 Conf. on Multi-material Micro Manufacture*. 2005, Elsevier: Karlsruhe. p. 107-110.
39. Hornes, J., J. Göttert, K. Lian, Y. Desta, and L. Jian, *Materials for LIGA and LIGA-based microsystems*. *Nuclear Instruments and Methods in Physics Research*, 2003. **B**(199): p. 332-341.
40. Bischofberger, R., H. Zimmerman, and G. Stauffert, *Low-Cost HARMS Process*. *Sensors and Actuators*, 1997. **A61**: p. 392-399.
41. Munnik, F., F. Benninger, S. Mikhailov, A. Bertsch, P. Renaud, H. Lorenz, and M. Gmür, *High aspect ratio, 3D structuring of photoresist materials by ion beam LIGA*. *Microelectronic Engineering*, 2003. **67**: p. 96-103.

42. Lawes, R.A., A.S. Holmes, and F.N. Goodall, *The formation of moulds for 3D microstructures using excimer laser ablation*. Microsystem Technologies, 1996. **3**(1): p. 17-19.
43. Nishi, N., T. Katoh, H. Ueno, and S. Sugiyama, *Study on three-dimensional micromachining using synchrotron radiation etching*. Microsystem Technologies, 2002. **9**: p. 1-4.
44. Katoh, T. and Y. Zhang, *High aspect ratio micromachining by synchrotron radiation direct photo-etching*. Microsystem Technologies, 1998. **4**: p. 135-138.
45. Park, M.S. and C.N. Chu, *Micro-electrochemical machining using multiple tool electrodes*. Journal of Micromechanics and Microengineering, 2007. **17**: p. 1451-1457.
46. Reyntjens, S. and R. Puers, *A review of focused ion beam applications in microsystem technology*. Journal of Micromechanics and Microengineering, 2001. **11**: p. 287-300.
47. Pham, D., L. Tonge, J. Cao, J. Wright, M. Papiernik, E. Harvey, and D. Nicolau, *Effects of polymer properties on laser ablation behaviour*. Smart Materials and Structures, 2002. **11**: p. 668-674.
48. Pflieger, W., W. Bernauer, T. Hanemann, and M. Torge, *Rapid fabrication of microcomponents - UV Laser assisted prototyping, laser micromachining of mold inserts and replication via photomolding*. Microsystem Technologies, 2002. **9**: p. 67-74.
49. Kim, J.T., B.C. Kim, M.Y. Jeong, and M.S. Lee, *Fabrication of a micro-optical coupling structure by laser ablation*. Journal of Materials Processing Technology, 2004. **146**: p. 163-166.
50. Friedrich, C. and M. Vasile, *The micromilling process for high aspect ratio microstructures*. Microsystem Technologies, 1996. **2**: p. 144-148.
51. Lu, Z. and T. Yoneyama, *Micro cutting in the micro lathe turning system*. International Journal of Machine Tools & Manufacture, 1999. **39**: p. 1171-1183.
52. Beltrami, I. *Wire electrical discharge machines*. in *ISEM XV - 15th International Symposium on Electromachinig*. 2007. Pittsburgh, USA.
53. Benavides, G., L. Bieg, M. Saavedra, and E. Bryce, *High aspect ratio meso-scale parts enabled by wire micro-EDM*. Microsystem Technologies, 2002. **8**: p. 395-401.
54. Murali, M. and S. Yeo, *Rapid biocompatible micro device fabrication by micro electro-discharge machining*. Biomedical Microdevices, 2004. **6**(1): p. 41-45.
55. Cohen, A., G. Zhang, F.-G. Tseng, U. Frodis, F. Mansfeld, and P. Will. *EFAB: Rapid, low-cost desktop micromachining of high aspect ratio true 3-D MEMS*. in *MEMS '99. Twelfth IEEE International Conference*. 1999.
56. Sharon, A., A. Bilsing, L. G., and X. Zhang, *Manufacturing of 3D microstructures using novel UPSAMS process for MEMS applications*, in *Material Research Society Symposium 741*, M.R. Society, Editor. 2003. p. 151-156.
57. Heckeles, M. and W.K. Schomburg, *Review on micro molding of thermoplastic polymers*. Journal of Micromechanics and Microengineering, 2004. **14**: p. R1-R14.
58. Piotter, V., A.E. Guber, M. Heckeles, and A. Gerlach, *Micro Moulding of Medical Device Components*, in *Medical Device Manufacturing & Technology*. 2004.
59. Piotter, V., W. Bauer, T. Benzler, and A. Emde, *Injection molding of components for Microsystems*. Microsystem Technologies, 2001. **7**: p. 99-102.
60. Worgull, M., J.-F. Héту, K.K. Kabanemi, and M. Heckeles, *Modeling and optimization of the hot embossing process for micro and nanocomponent fabrication*. Microsystem Technologies, 2006. **12**: p. 947-952.
61. Chang, J.-H. and S.-Y. Yang. *Development of rapid heating and uniformly pressing system for micro hot embossing*. in *ANTEC 2004 Plastics: Annual Technical Conference*. 2004.
62. Heckeles, M., A. Gerlach, A.E. Guber, and T. Schaller. *Large area polymer replication for microstructured fluidic devices*. in *SPIE 2001*. 2001.
63. Song, M.C., Z. Liu, M.J. Wang, T.M. Yu, and D.Y. Zhao, *Research on effects of injection process parameters on the molding process for ultra-thin wall plastic parts*. Journal of Materials Processing Technology, 2007. **187**: p. 668-671.
64. Chien, R.-D., W.-R. Jong, and S.-C. Chen, *Study on rheological behavior of polymer melt flowing through micro-channels considering the wall-slip effect*. Journal of Micromechanics and Microengineering, 2005. **15**: p. 1389-1396.

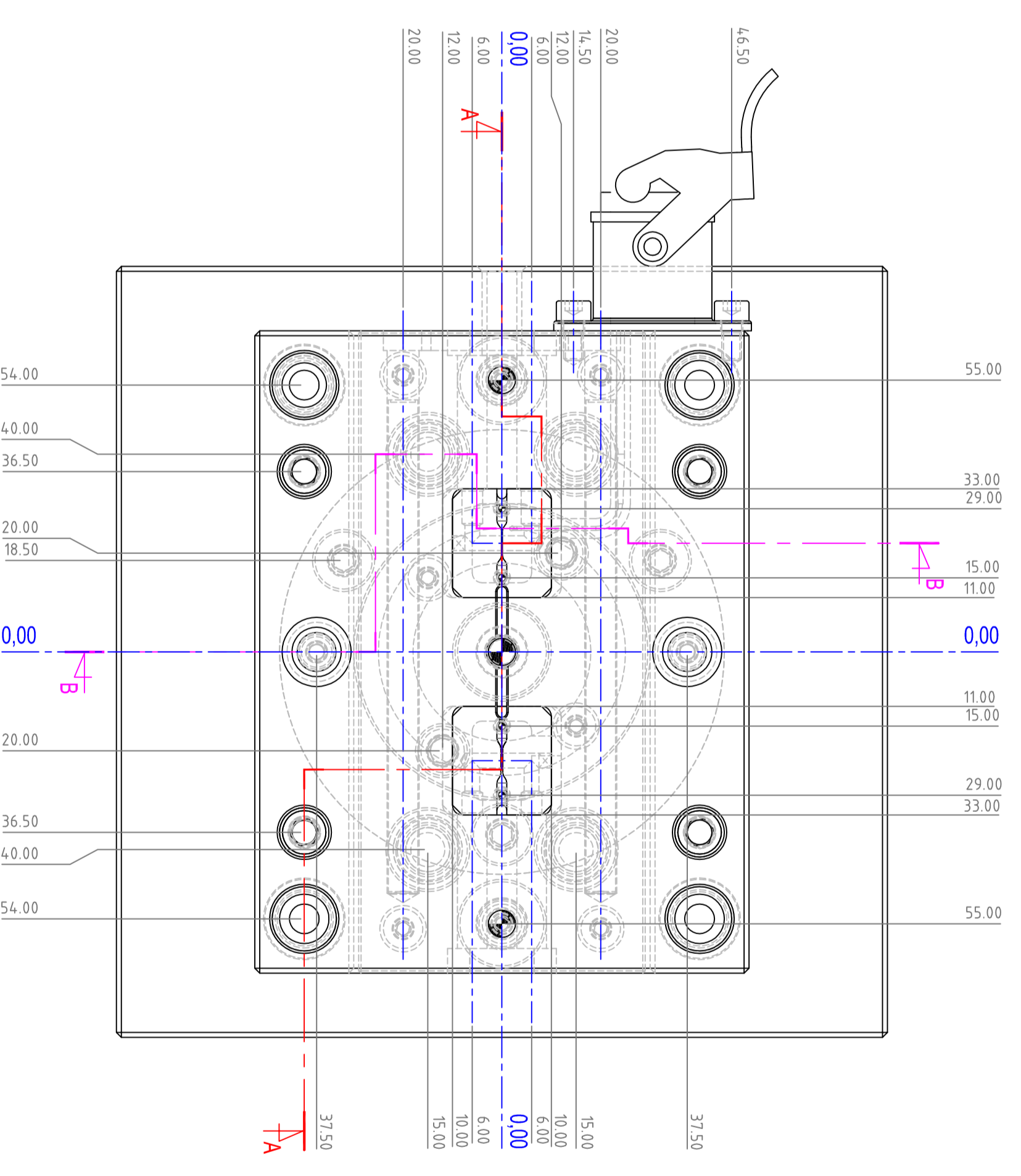
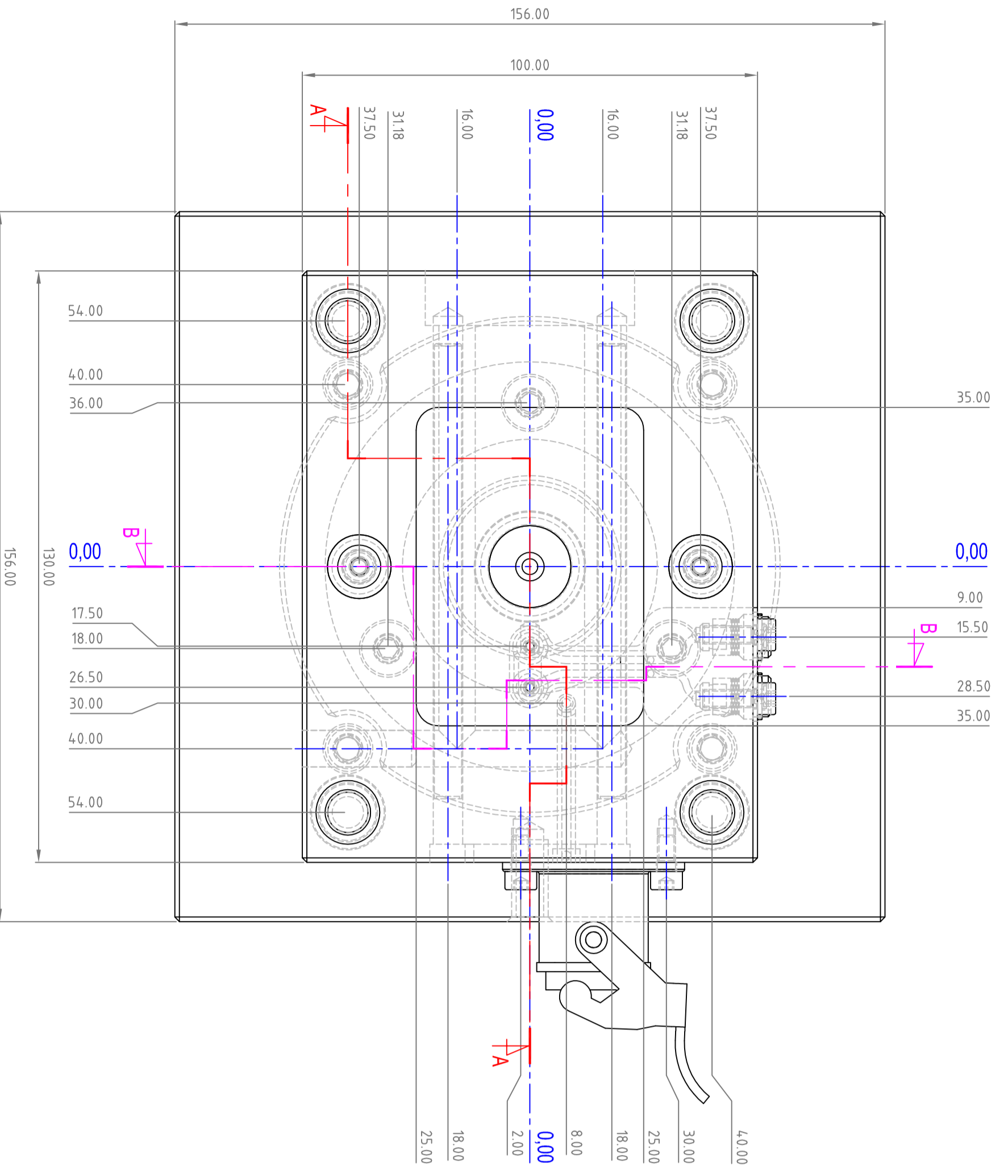
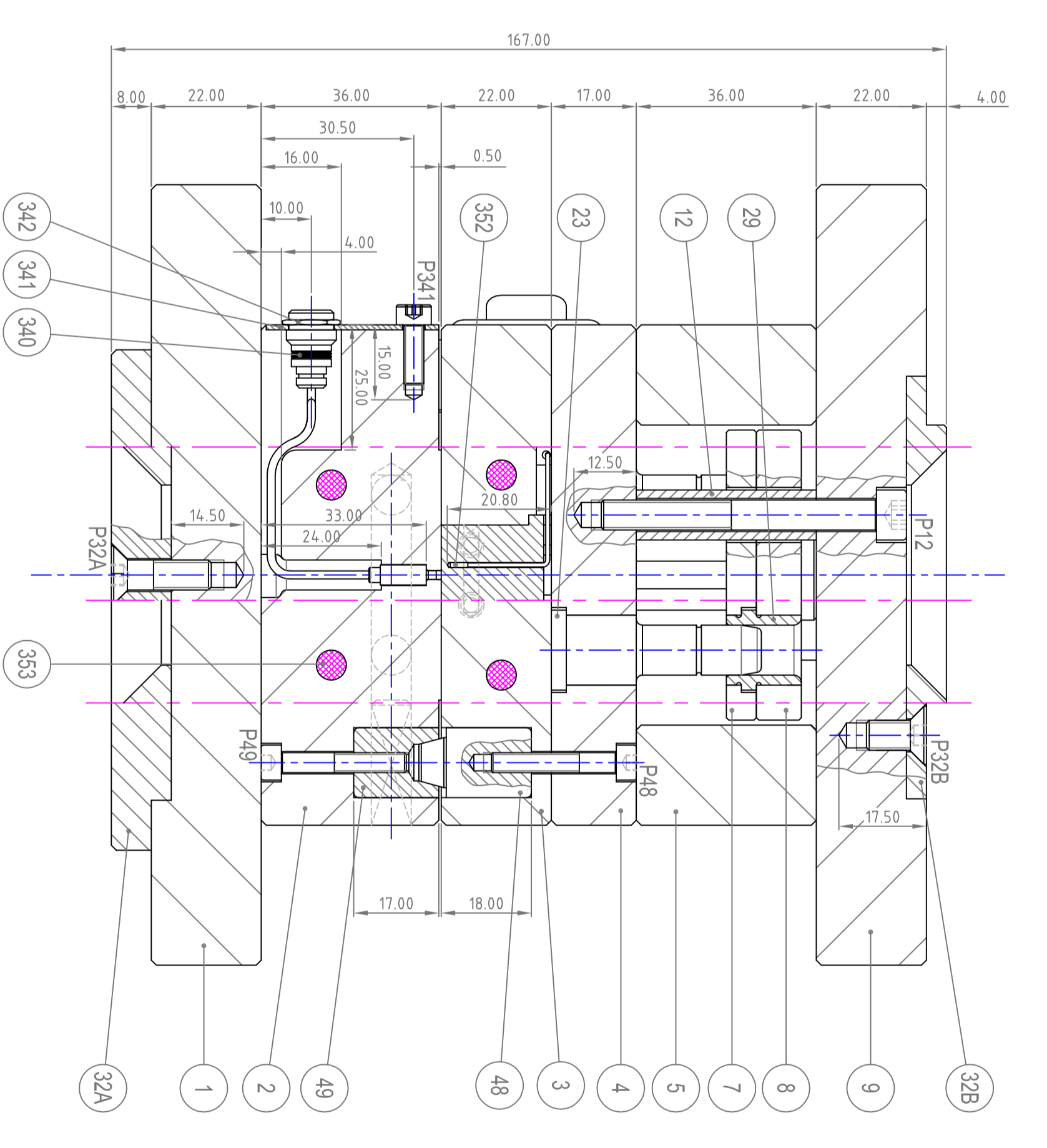
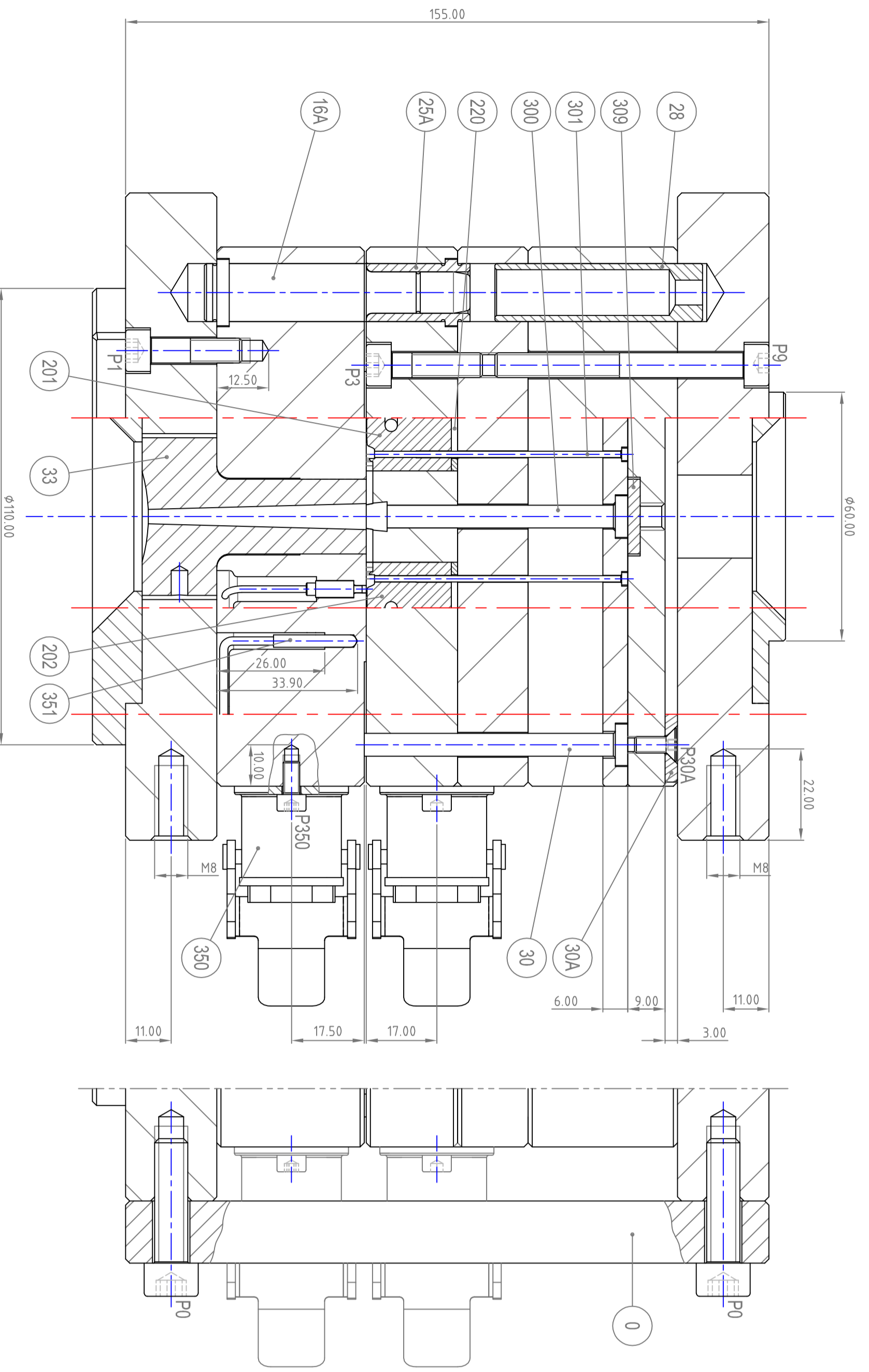
65. Yao, D. and B. Kim, *Simulation of the filling process in micro-channels for polymeric materials*. Journal of Micromechanics and Microengineering, 2002. **12**: p. 604-610.
66. Tanner, R.I., *Wall slip, Engineering Rheology*. 2nd Edition ed. Oxford Engineering Science Series. 2000, Oxford: Oxford University Press. 559.
67. Yu, L., J. Lee, and K.W. Koelling. *Flow and heat transfer simulation of thin-wall injection molding with microstructures*. in *ANTEC 2003 - 61st Annual Technical Conference & Exhibition*. 2003.
68. Kim, D.S., K.-C. Lee, T.H. Kwon, and S.S. Lee, *Micro-channel filling flow considering surface tension effect*. Journal of Micromechanics and Microengineering, 2002. **12**: p. 236-246.
69. Mosaddegh, P. and D.C. Angstadt, *Micron and sub-micron feature replication of amorphous polymers at elevated mold temperature without externally applied pressure*. Journal of Micromechanics and Microengineering, 2008. **18**: p. 1-10.
70. Kennedy, P., *Flow Analysis of Injection Molds*. 1995, Munich: Hanser Publishers. 237.
71. Zheng, R., P. Kennedy, N. Phan-Thien, and X.J. Fan, *Thermoviscoelastic simulation of thermally and pressure-induced stresses in injection moulding for the prediction of shrinkage and warpage for fibre-reinforced thermoplastics*. Journal of Non-Newtonian Fluid Mechanics, 1999. **84**(2-3): p. 159-190.
72. Mehta, N.M., C.M.F. Barry, D.T. Bibber, and D. Tully. *Validation of flow simulation for micromolded parts*. in *ANTEC 2003 - 61st Annual Technical Conference & Exhibition*. 2003.
73. Su, Y.-C., J. Shah, and L. Lin, *Implementation and analysis of polymeric microstructure replication by micro injection molding*. Journal of Micromechanics and Microengineering, 2004. **14**: p. 415-422.
74. Hatzikiriakos, S.G. and J.M. Dealy, *Wall slip of molten high density polyethylenes II. Capillary rheometer studies*. Journal of Rheology, 1992. **36**(4): p. 703-741.
75. Rosenbaum, E. and S. Hatzikiriakos, *Wall slip in the capillary flow of molten polymers subject to viscous heating*. AIChE Journal, 1997. **43**: p. 598-608.
76. Sha, B., S.S. Dimov, D.T. Pham, and C.A. Griffiths. *Study of Factors Affecting Aspect Ratios Achievable in Micro-injection Moulding*. in *International Conference 4M2005*. 2005: Elsevier.
77. Carreau, P.J., D. De Kee, and R. Chhabra, *Capillary rheometry, Rheology of polymeric systems - Principles and applications*. 1997, München: Hanser.
78. Chen, C.-S., S.-C. Chen, W.-L. Liaw, and R.-D. Chien, *Rheological behavior of POM polymer melt flowing through micro-channels*. European Polymer Journal, 2008. **44**: p. 1891-1898.
79. Eringen, A.C. and K. Okada, *A lubrication theory for fluids with microstructure*. International Journal of Engineering Science, 1995. **33**(15): p. 2297-2308.
80. Awati, K.M., Y. Park, E. Weisser, and M.E. Mackay, *Wall slip and shear stresses of polymer melts at high shear rates without pressure and viscous heating effects*. Journal of Non-Newtonian Fluid Mechanics, 2000. **89**: p. 117-131.
81. Lee, K. and M.R. Mackley, *The significance of slip in matching polyethylene processing data with numerical simulation*. Journal of Non-Newtonian Fluid Mechanics, 2000. **94**: p. 159-177.
82. Mitsoulis, E., I. Kazatchkov, and S. Hatzikiriakos, *The effect of slip in the flow of a branched PP melt: experiments and simulations*. Rheological Acta, 2005. **44**: p. 418-426.
83. Gleissle, W. and E. Windhab, *The "Twin capillary" a simple device to separate shear- and slip-flow of fluids* Experiments in Fluids, 1985. **3**(3): p. 177-180.
84. Vincent, M., C. Mnekbi, and J.-F. Agassant, *Polymer Rheology at High Shear Rate for Microinjection Moulding*, in *The 26th Annual Meeting of the Polymer Processing Society*. 2010: Banff, Canada.
85. Song, M.C., Z. Liu, M.J. Wang, T.M. Yu, and D.Y. Zhao, *Research on effects of injection process parameters on the moulding process for ultra-thin wall plastic parts*. Journal of Materials Processing Technology, 2007. **187**: p. 668-671.
86. Wagner, M.H., V. Schulze, and A. Göttfert, *Rheotens - Mastercurves and drawability of polymer melts*. Polymer Engineering and Science, 1996. **36**(7): p. 925-935.
87. Su, Y.C., J. Shah, and L.W. Lin, *Implementation and analysis of polymeric microstructure replication by micro injection molding*. Journal of Micromechanics and Microengineering, 2004. **14**(3): p. 415-422.

88. Greener, J. and R. Wimberger-Friedl, *Experimental analysis of microfetaure injection molding*, in *Precision injection molding: process, materials, and applications*. 2006, Carl Hanser Verlag: Munchen.
89. Hopkinson, N. and P. Dickens, *A comparison between stereolithography and aluminium injection moulding tooling*. Rapid Prototyping Journal, 2000. **6**: p. 253-258.
90. Ribeiro, A.S., N. Hopkinson, and C.H. Ahrens, *Thermal effects on stereolithography tools during injection moulding*. Rapid Prototyping Journal, 2004. **10**(3): p. 176-180.
91. Koster, R. and K. Ragaert. *Bioplastics injection moulding and modern mould opportunities*. in *International Conference on Polymers & Moulds Innovations (PMI)*. 2007. Ghent, Belgium.
92. Zhao, J., R.H. Mayes, G. Chen, H. Xie, and P.S. Chan, *Effects of Process Parameters on the Micro Molding Process*. Polymer Engineering and Science, 2003. **43**(9): p. 1542-1554.
93. Kruth, J.P., I.P. Mercelis, J. Van Vaerenbergh, L. Froyen, and M. Rombouts, *Advances in Selective Laser Sintering*, in *1st International Conference on Advanced Research on Virtual and Rapid Prototyping*. 2003: Leiria, Portugal. p. 59-70.
94. Mercelis, I.P., J.P. Kruth, and V. Vaerenbergh, *Feedback control of selective laser melting*, in *ISEM XV - 15th International Symposium on Electromachinig*. 2007: Pittsburgh. p. 421-426.
95. Chang, C.-Y., H.-W. Hung, W.-H. Yang, S.-C. Shen, L.-C. Su, and T. Neves, *Simulating Micro Injection Molding aided by variotherm technology*, in *RPD - Rapid Product Development 2008*. 2008: Marinha Grande.
96. Yasa, E. and J.-P. Kruth, *Investigation of laser and process parameters for Selective Laser Erosion*. Journal of Precision Engineering, 2010. **34**(1).
97. Koster, R. and K. Ragaert, *Bioplastics injection moulding and modern mould opportunities*, in *PMI - Polymer and Mould Innovations*. 2007: Ghent, Belgium.
98. Yasa, E., J. Deckers, T. Craeghs, M. Badrossamay, and J.-P. Kruth, *Investigation on occurrence of elevated edges in SLM*, in *Solid Freeform Fabrication (SFF) Symposium*. 2009: Austin, Texas, USA.
99. Pham, D.T., S.S. Dimov, P.V. Petkov, and T. Dobrev, *Laser Milling for Micro Tooling*, in *VIII LAMDAMAP Conference 2005*. 2005: Cranfield. p. 362-371.
100. Piotter, V., K. Mueller, K. Plewa, R. Ruprecht, and J. Hausselt, *Performance and simulation of thermoplastic micro injection molding*. Microsystem Technologies, 2002. **8**(6): p. 387-390.
101. Wu, C.-H. and W.-J. Liang, *Effects of geometry and injection-molding parameters on weld-line strength*. Polymer Engineering and Science, 2005: p. 1021-1030.
102. Mehta, N.M., C.M.F. Barry, D.T. Bibber, and D. Tully, *Validation of flow simulation for micromolded parts*, in *ANTEC 2003 - 61st Annual Technical Conference & Exhibition*. 2003. p. 3550-3554.

Annex A1

Mould Design

Item No.	Designation	Qty.	Manufacturer / Part Number
0	Security/transport strap	1	156x20x15
1	Clamping plate injection	1	HASCO K10 100x130x22
2	Cavity plate	1	HASCO K20 100x130x36
3	Core plate	1	HASCO K20 100x130x22
4	Core backing plate	1	HASCO K30 100x130 17
5	Spacer	2	HASCO K40 100x130 36
7	Ejector's plate	1	HASCO K60 100x130x06
8	Ejector's clamping plate	1	HASCO K70 100x130x09
9	Clamping plate ejection	1	HASCO K10 100x130x22
12	Support pillar	2	HASCO Z00/36/10x36
16A	Locating guide pillar	3	HASCO Z00/36/10x25
18	Locating guide pillar	3	HASCO Z00/36/10x30
23	Ejection guide pillar	4	HASCO Z03/17/10x30
25A	Guide bushing	3	HASCO Z10/17/10
25B	Guide bushing	1	HASCO Z20/17/10
28	Centering sleeve	4	HASCO Z10/17/09
29	Ejection guide bushing	4	HASCO Z10/17/209
30	Return pin	2	HASCO Z40/5 5x65
30A	Sealing washer	2	HASCO Z50/18x3
32A	Centering ring injection	1	HASCO K100/110x12 typeC
32B	Centering ring ejection	1	HASCO K100/08x08 typeA
33	Main ejector	3	HASCO Z51/18x36/3 5/40
48	Interlock cavity	2	HASCO Z05/14 female
49	Interlock core	2	HASCO Z05/14 male
201	Core insert microchannel 400x100µm	1	24x22x0.5
202	Core insert microchannel 200x200µm	1	24x22x0.5
220	Core insert spacer	2	24x22x1.5
300	Main ejector	1	HASCO Z40/5 5x058
301	Ejector 1	2	HASCO Z40/1 5x061
302	Ejector 2	2	HASCO Z40/1 5x062
309	Spacer main ejector	1	Ø18x3
340	Piezoelectric pressure sensor	2	PRIMUS 60068
342	Sensor mounting plate	1	PRIMUS 6581A
350	Signal housing 4 contacts	2	HASCO Z108/74
351	Thermocouple core	1	RESITEC TC102 Ø1.5x60
352	Thermocouple cavity	1	RESITEC Ø6.5x100
353	Cartridge Heater	4	HASCO Z31 M8x30
P1	Socket head cap screw	2	HASCO Z31 M8x22
P2	Socket head cap screw	4	HASCO Z31 M8x22
P3	Socket head cap screw	4	HASCO Z31 M8x22
P8	Countersunk head cap screw	6	HASCO Z31 M6x16
P9	Socket head cap screw	4	HASCO Z31 M6x65
P12	Socket head cap screw	2	HASCO Z31 M6x55
P30A	Countersunk head cap screw	2	HASCO Z33 M4x10
P32A	Countersunk head cap screw	3	HASCO Z33 M6x20
P32B	Countersunk head cap screw	3	HASCO Z33 M6x12
P48	Socket head cap screw	2	HASCO Z31 M4x25
P49	Socket head cap screw	2	HASCO Z31 M4x25
P341	Socket head cap screw	2	HASCO Z31 M4x12
P350	Socket head cap screw	4	HASCO Z31 M4x8



DESIGNER		DATE		REVISION	
NAME	DESIGN TIME	DATE			
CHKD	L.C. Wong				
APPD	A.S. Poon				
DRG	Frank S.A.				
QA	Frank S.A.				

UNIVERSITY OF MINHO SCHOOL OF ENGINEERING
Mould for microtechnological analysis and microinjection
Mould Phd Fill 2D

Annex A2

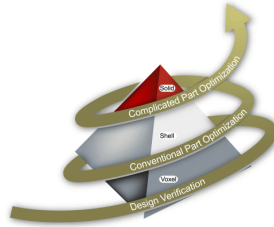
Moldex 3D Simulation Report

Microinjection simulation on 1.2767 steel moulding block

Material: PolyPropylene | Lyondell-Basel Moplen HP548R

Melt/Mould temperatures: 230°C/70°C

Moldex3D Moldex3D Report-Run06



Company Name: Joel Vasco
Project Name: MDXProject20100304
Software: Moldex3D R9.1 (9108.97)
Author: Joel Vasco
Date: Tuesday, August 03, 2010

True 3D CAE for Injection Molding

Moldex3D Summary

- Summary of the project

Microinjection simulation on 1.2767 steel moulding block

Material: PP | Lyondell-Basel Moplen HP548R

Melt/Mould temperatures: 230°C/70°C

1.1. Summary table

Mesh	MS01.mfe
Material(Part)	PP_MoplenHP548R_1.mtr
Process	MS01_PP70_02.pro
Computation parameters	MDXProject2010030406.cmx

True 3D CAE for Injection Molding

Moldex3D Summary - Mesh

2.1. Summary table - Mesh

Mesh Type	Mixed/BLM
No. cooling channel	0
Part dimension	15.50 x 14.00 x 1.80 (mm)
Mold dimension	41.00 x 14.00 x 58.04 (mm)
Cavity(Part) volume	0.0418247 (cc)
Cold runner volume	1.27905 (cc)
Element number	489139
Part elements	489139
Node number	172935

True 3D CAE for Injection Molding

Moldex3D Summary - Material

3.1. Summary table - Material

Material type	Thermoplastic
Generic name	PP
Supplier	LyondellBasell
Trade name	Moplen HP548R
MFI	MFI(230,2.16)=23 g/10min
Fiber percent	0.00 (%)
Melt temperature range	190 - 270 (oC)
Mold temperature range	20 - 50 (oC)
Ejection temperature	148 (oC)
Freeze temperature	168 (oC)

True 3D CAE for Injection Molding

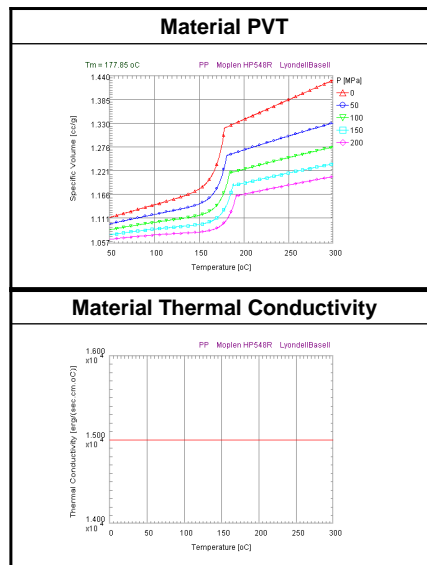
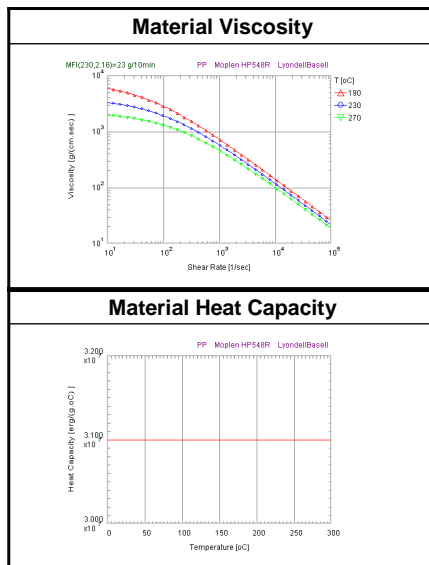
Moldex3D Summary - Process Condition

4.1. Summary table - Process Condition

Filling Time	0.3300 (sec)
Melt Temperature	230.0 (oC)
Mold Temperature	70.0 (oC)
Injection Pressure	130.00 (MPa)
Injection Volume	1.32087 (cc)
Packing Time	2.0000 (sec)
Packing Pressure	130.00 (MPa)
VP Switch by volume(%) filled	99.00 (%)
Mold Opening Time	5.0000 (sec)
Ejection temperature	147.8 (oC)
Air Temperature	25.0 (oC)

True 3D CAE for Injection Molding

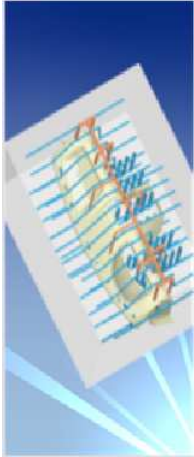
Moldex3D 1. Material figures



True 3D CAE for Injection Molding

Moldex3D Process - Filling/Packing Settings

Filling/Packing Settings



Filling setting

Filling time : 0.33 sec

Flow rate profile (1)...

Injection pressure profile (1)...

VP switch-over

By volume(%) filled as 99 %

Packing setting

Packing time : 2 sec

Packing pressure refer to end of filling pressure

Packing pressure profile (1)...

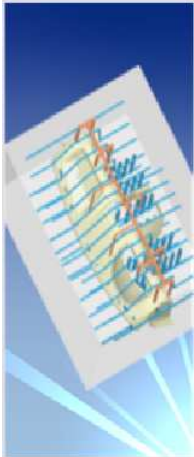
Melt Temperature	230	oC
Mold Temperature	70	oC

Advanced Setting...

True 3D CAE for Injection Molding

Moldex3D Process - Cooling Settings

Cooling Settings



Item	Value	Unit
Air Temperature	25	oC
Eject Temperature	147.85	oC
Cooling Time	20	sec
Mold-Open Time	5	sec

Cooling Channel/Heating Rod... Mold Metal Material...

Eject Criteria... Part Insert Initial Temperature...

Estimate Cooling Time...

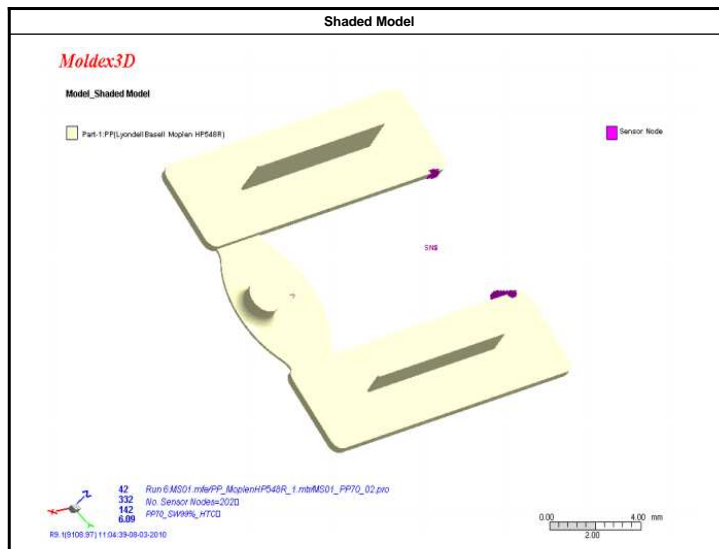
True 3D CAE for Injection Molding

Moldex3D Process - Summary

Summary	
[Filling]	
Filling time (sec)	0.33
Melt Temperature (oC)	230
Mold Temperature (oC)	70
Maximum injection pressure...	130
Injection volume (cm ³)	1.32087
[Packing]	
Packing Time (sec)	2
Maximum packing pressure ...	130
[Cooling]	
Cooling Time (sec)	20
Mold-Open Time (sec)	5
Eject Temperature (oC)	147.85
Air Temperature (oC)	25
[Miscellaneous]	
Cycle time (sec)	27.33

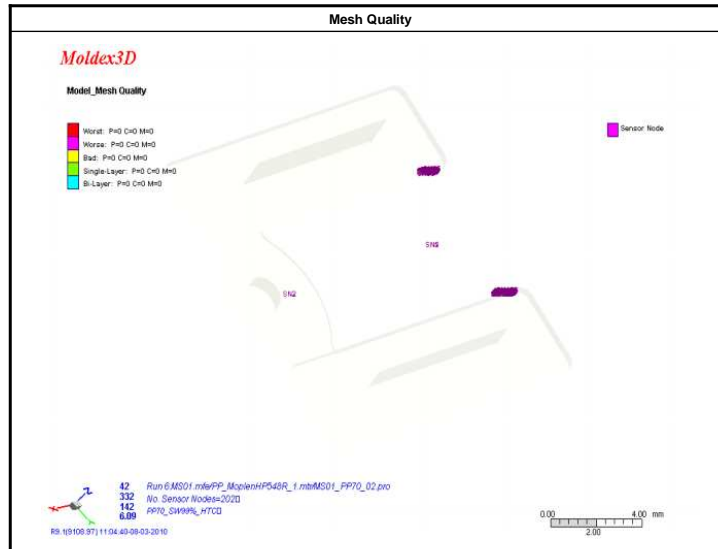
True 3D CAE for Injection Molding

Moldex3D Model-Shaded Model



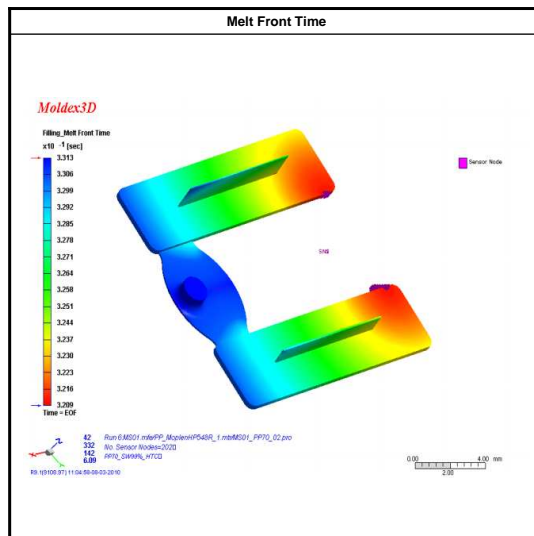
True 3D CAE for Injection Molding

Moldex3D Model-Mesh Quality



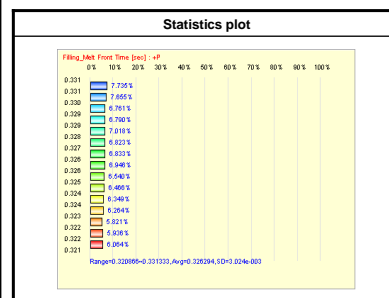
True 3D CAE for Injection Molding

Moldex3D Filling-Melt Front Time



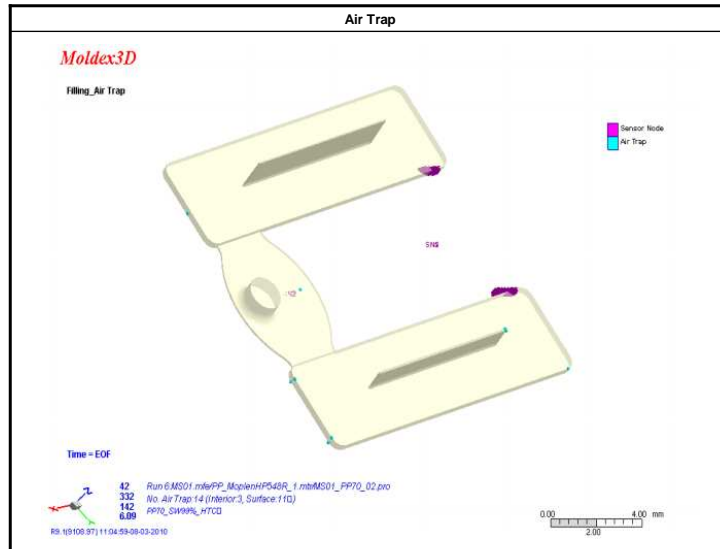
Melt front advancement is a position indicator as melt front boundary movement in different time duration in the filling process. From the melt front advancement one can:

- Examine the filling pattern of the molding
- Check potential incomplete filling (short shot) problem
- Identify weld line locations
- Identify air trap locations
- Check gate contribution for runner balance
- Check proper gate location to balance flow and eliminate weldline.



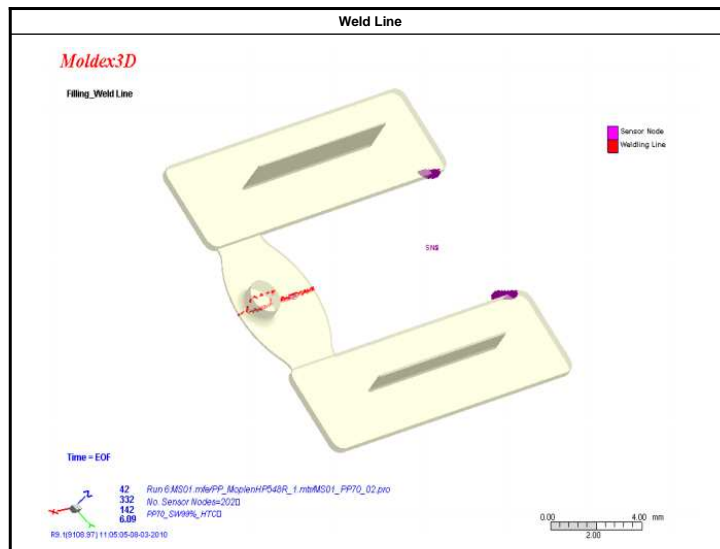
True 3D CAE for Injection Molding

Moldex3D Filling-Air Trap



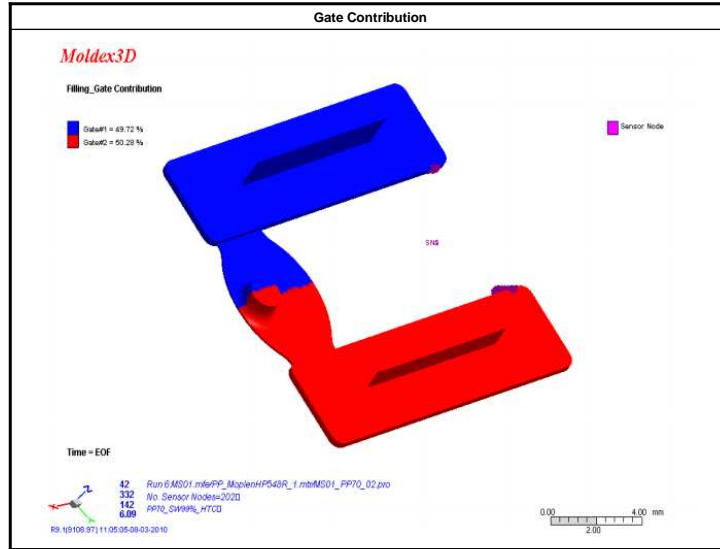
True 3D CAE for Injection Molding

Moldex3D Filling-Weld Line



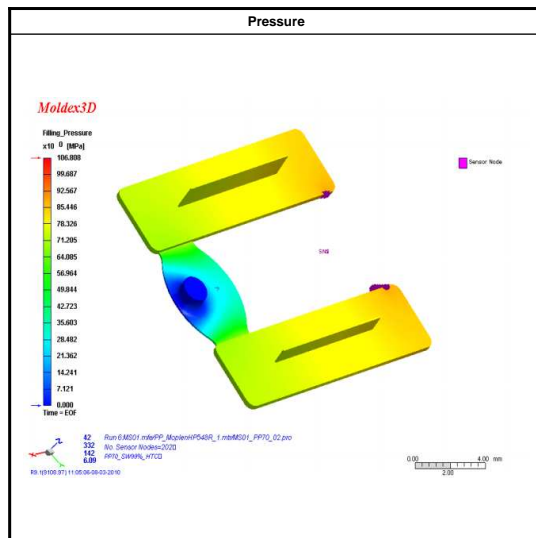
True 3D CAE for Injection Molding

Moldex3D Filling-Gate Contribution



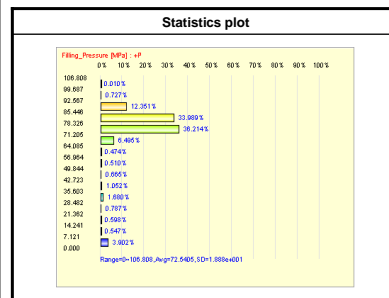
True 3D CAE for Injection Molding

Moldex3D Filling-Pressure



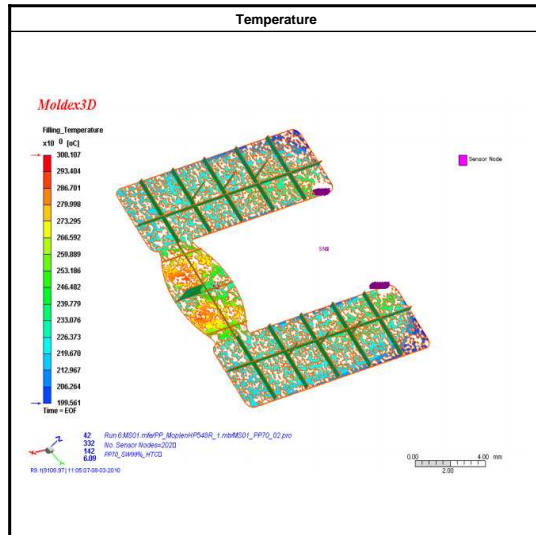
Pressure distribution of the cavity is shown in different colors at current instant. Based on the pressure drop and distribution, users can revise the part and mold design. From the pressure distribution one can:

- Check the pressure transmission situation
- Check runner system pressure drop
- Check flow balance of the design
- Avoid overpacking and flashing of melt
- Examine the extent of packing/holding.

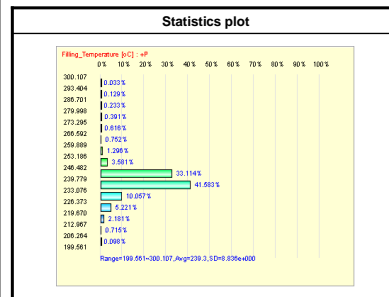


True 3D CAE for Injection Molding

Moldex3D Filling-Temperature

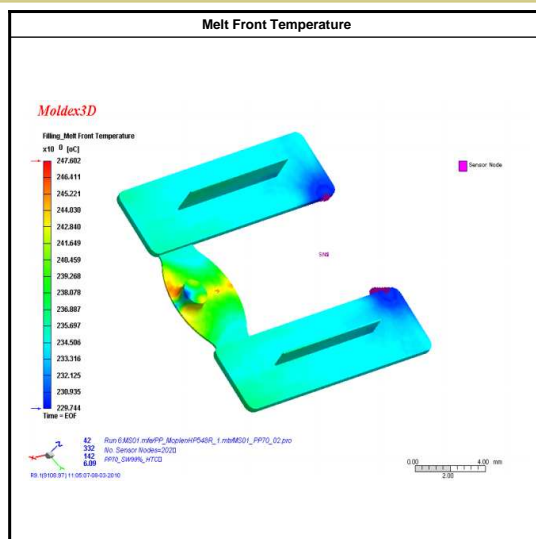


Plastic melt temperature distribution at current instant. For 3D calculation, the temperature distribution expresses temperatures in all three dimensional for the fully cavity.

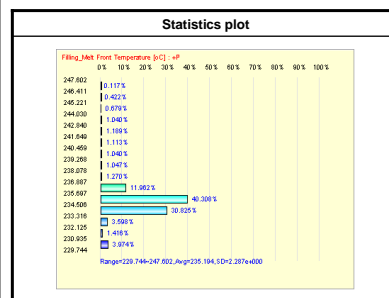


True 3D CAE for Injection Molding

Moldex3D Filling-Melt Front Temperature

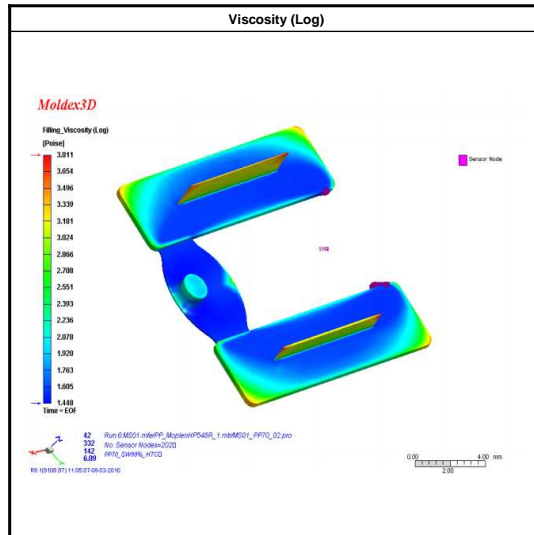


Melt front temperature is the temperature value of the plastic melt as it reaches the given point. This value indicates how heat is conveyed and dissipated during the molding phases.

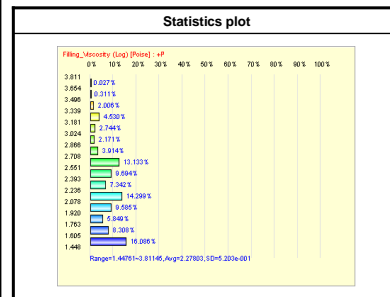


True 3D CAE for Injection Molding

Moldex3D Filling-Viscosity (Log)

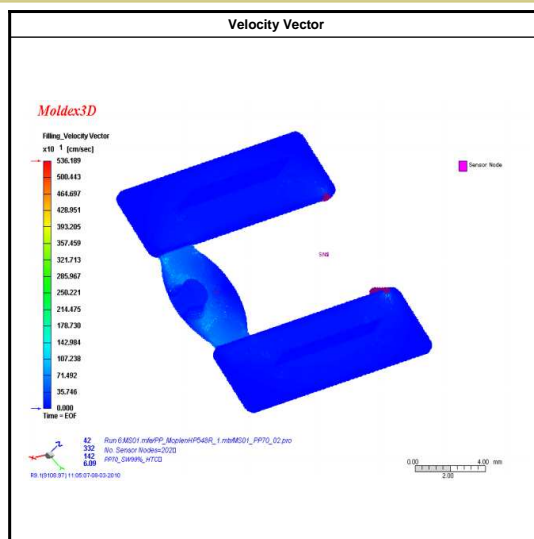


Viscosity is an important property in fluids which can be considered as the resistance of flow. In polymers, both temperature and shear rate will influence the value of viscosity. The viscosity is constant at low shear rate, and then the viscosity will decrease with increasing shear rate. Also, the viscosity will decrease as temperature increases.

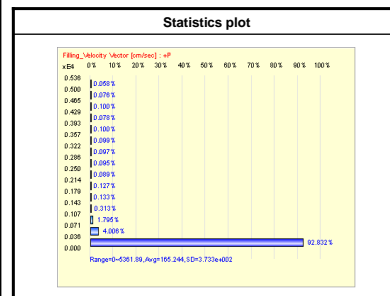


True 3D CAE for Injection Molding

Moldex3D Filling-Velocity Vector

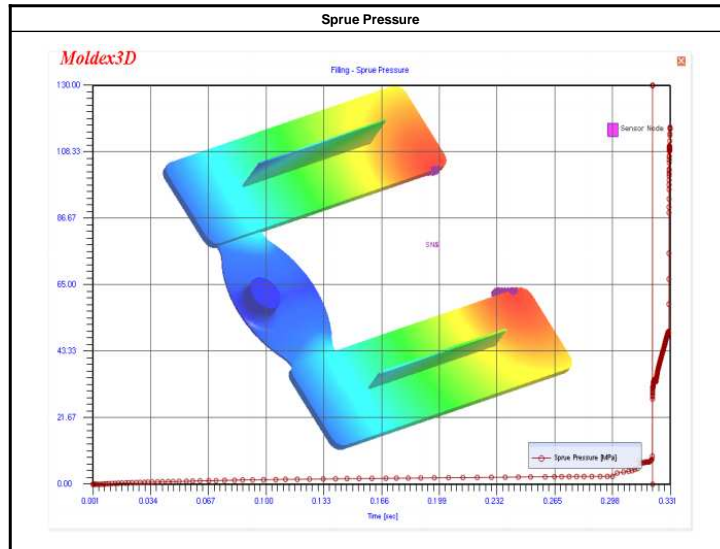


Velocity vector is the vector plot of the velocity vector at current instant.



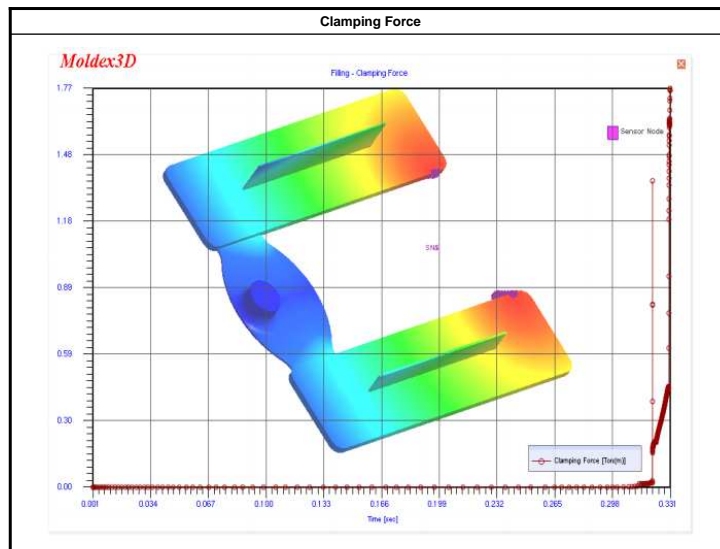
True 3D CAE for Injection Molding

Moldex3D Filling - Sprue Pressure XY Curve



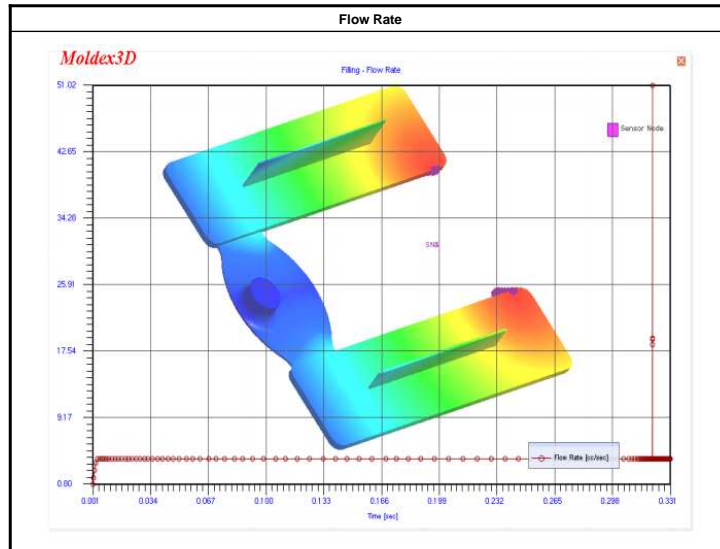
True 3D CAE for Injection Molding

Moldex3D Filling - Clamping Force XY Curve



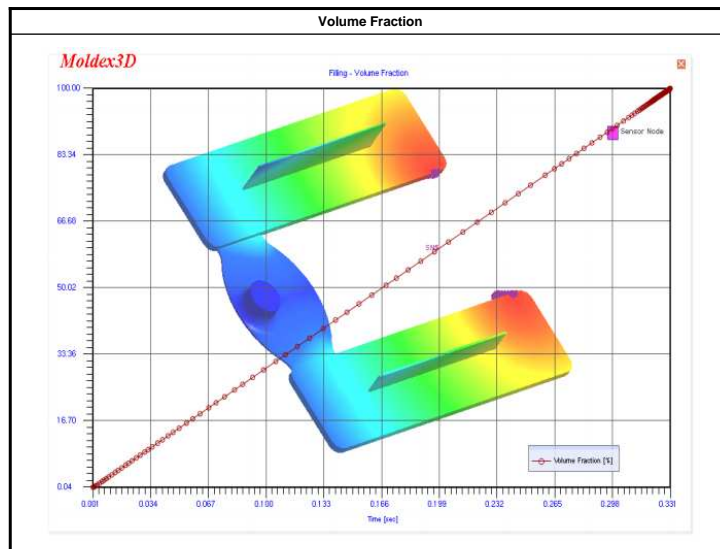
True 3D CAE for Injection Molding

Moldex3D Filling - Flow Rate XY Curve



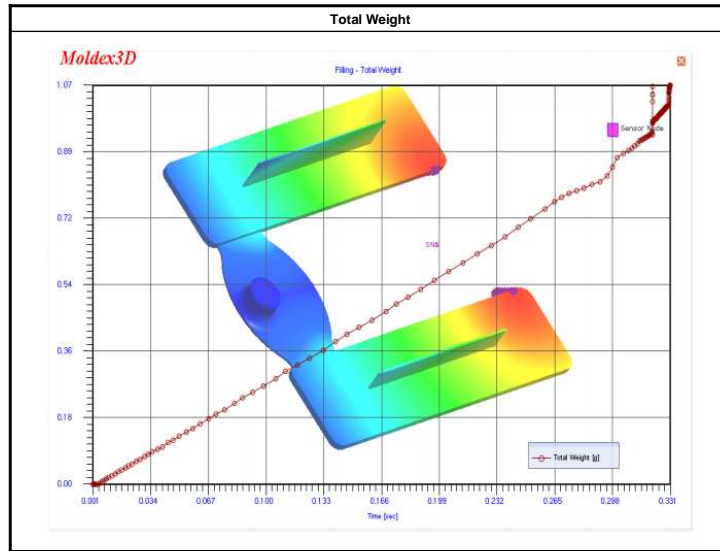
True 3D CAE for Injection Molding

Moldex3D Filling - Volume Fraction XY Curve



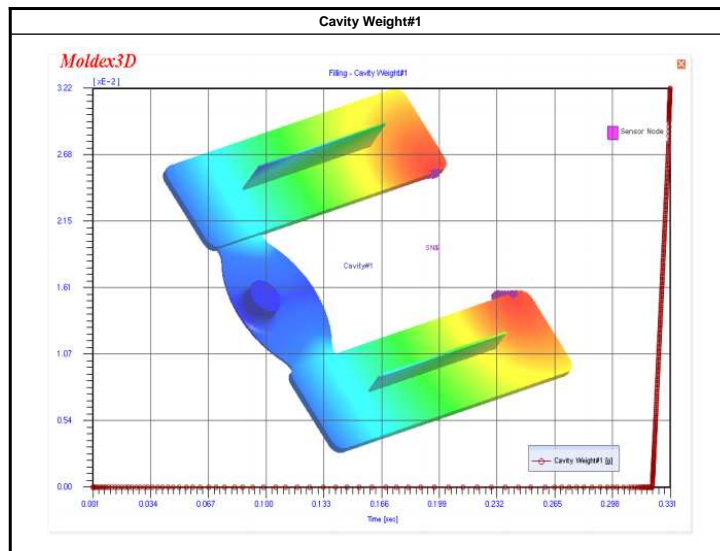
True 3D CAE for Injection Molding

Moldex3D Filling - Total Weight XY Curve



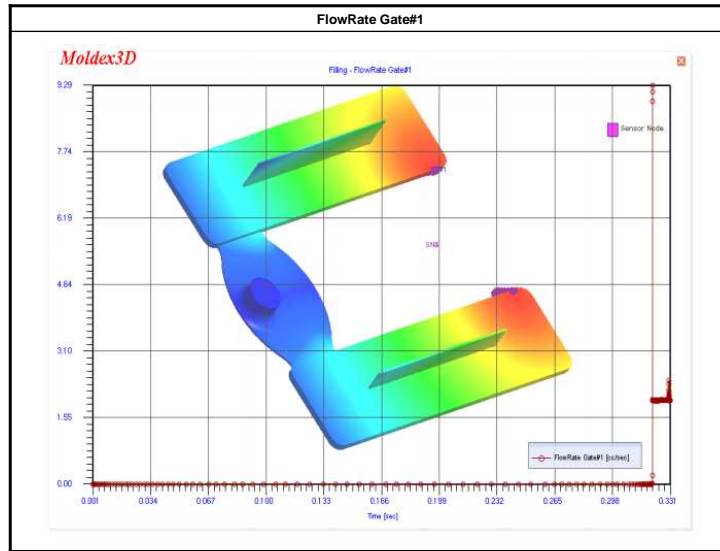
True 3D CAE for Injection Molding

Moldex3D Filling - Cavity Weight#1 XY Curve



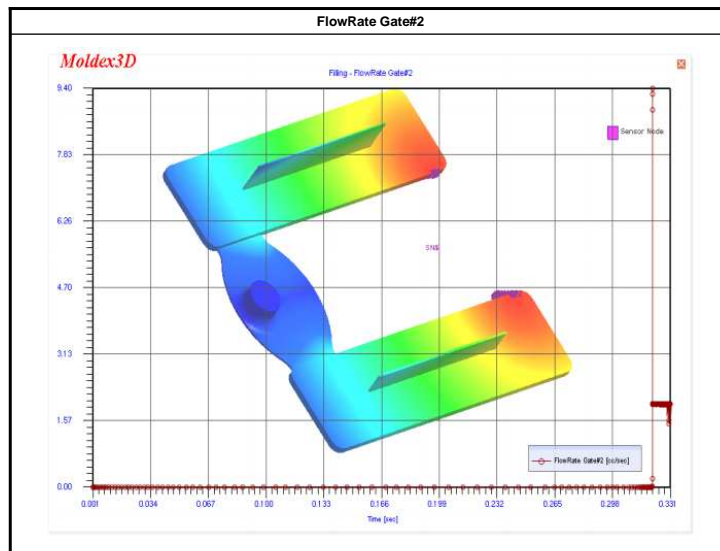
True 3D CAE for Injection Molding

Moldex3D Filling - FlowRate Gate#1 XY Curve



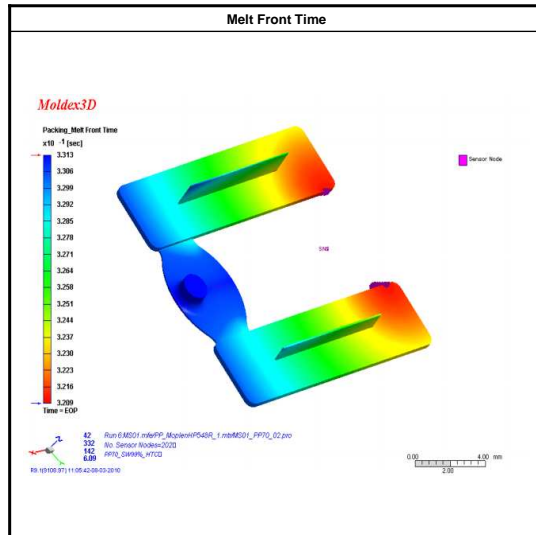
True 3D CAE for Injection Molding

Moldex3D Filling - FlowRate Gate#2 XY Curve



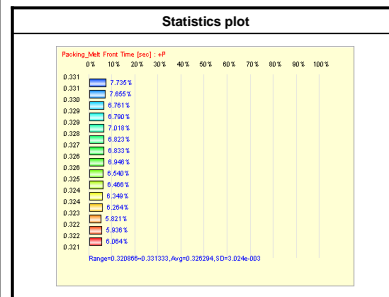
True 3D CAE for Injection Molding

Moldex3D Packing-Melt Front Time



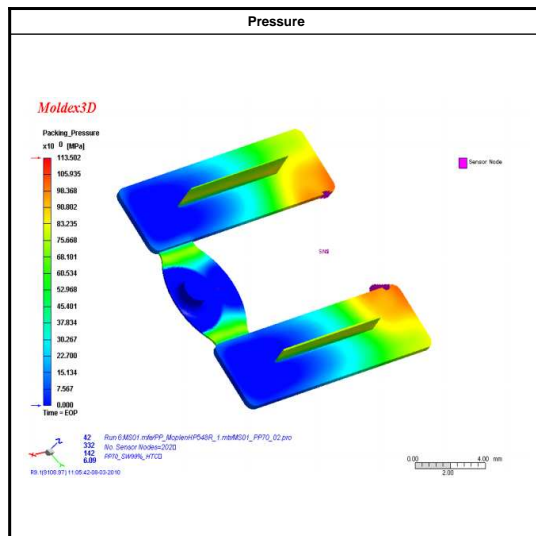
Melt front advancement is a position indicator as melt front boundary movement in different time duration in the filling process. From the melt front advancement one can:

- Examine the filling pattern of the molding
- Check potential incomplete filling (short shot) problem
- Identify weld line locations
- Identify air trap locations
- Check gate contribution for runner balance
- Check proper gate location to balance flow and eliminate weldline.



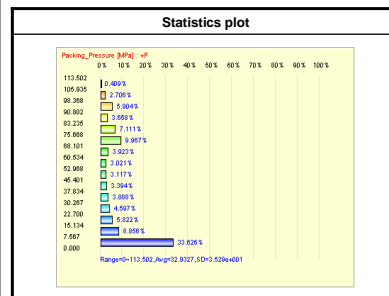
True 3D CAE for Injection Molding

Moldex3D Packing-Pressure



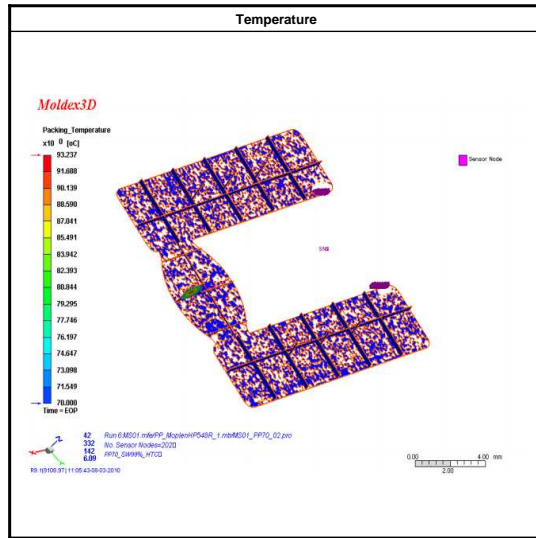
Pressure distribution of the cavity is shown in different colors at current instant. Based on the pressure drop and distribution, users can revise the part and mold design. From the pressure distribution one can:

- Check the pressure transmission situation
- Check runner system pressure drop
- Check flow balance of the design
- Avoid overpacking and flashing of melt
- Examine the extent of packing/holding.

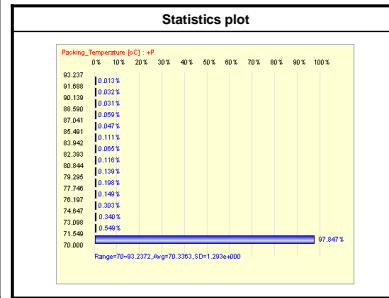


True 3D CAE for Injection Molding

Moldex3D Packing-Temperature

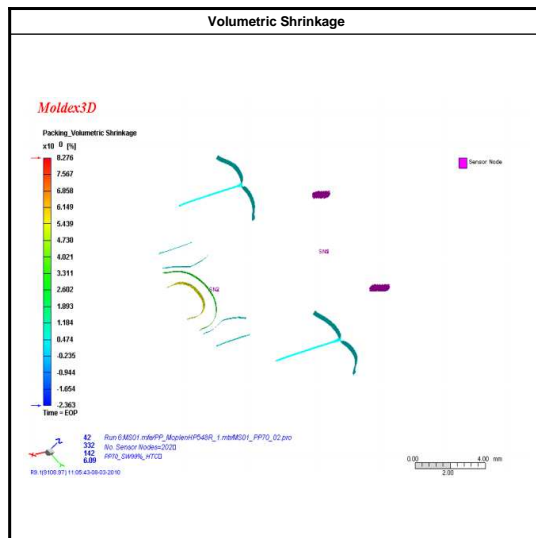


Plastic melt temperature distribution at current instant. For 3D calculation, the temperature distribution expresses temperatures in all three dimensional for the fully cavity.

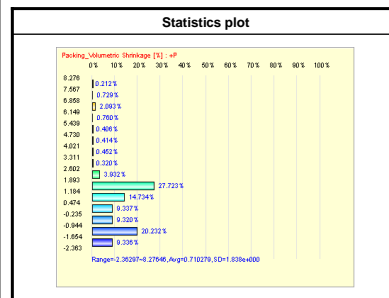


True 3D CAE for Injection Molding

Moldex3D Packing-Volumetric Shrinkage

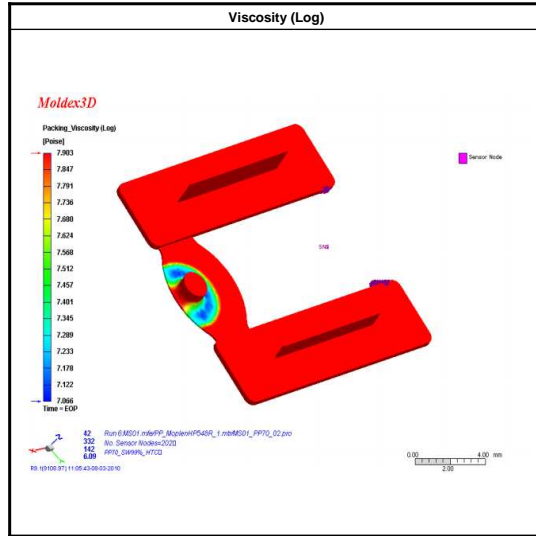


Volumetric shrinkage shows the percentage of part volume change due to PVT change as the part is cooled from high temperature, high pressure conditions at current instant to room temperature, ambient pressure conditions. Positive value represents volume shrinkage while negative value represents volume expansion due to over-pack. Non-uniform volumetric shrinkage will lead to warpage and distortion of demolded parts.

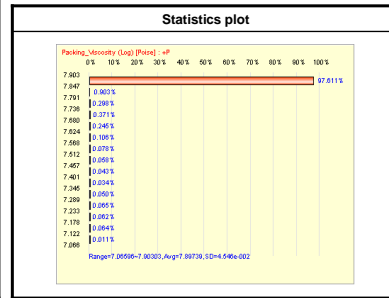


True 3D CAE for Injection Molding

Moldex3D Packing-Viscosity (Log)

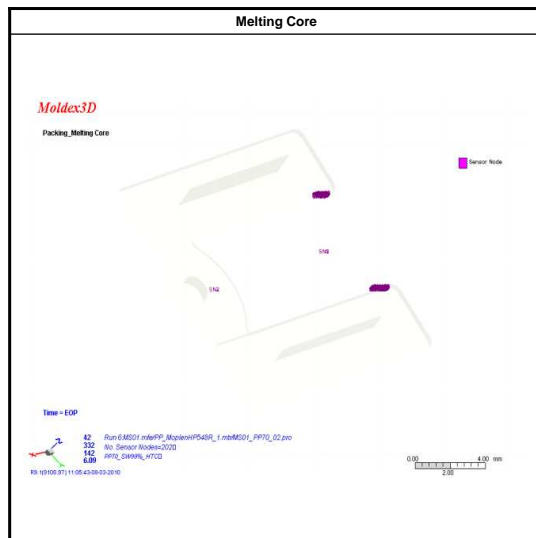


Viscosity is an important property in fluids which can be considered as the resistance of flow. In polymers, both temperature and shear rate will influence the value of viscosity. The viscosity is constant at low shear rate, and then the viscosity will decrease with increasing shear rate. Also, the viscosity will decrease as temperature increases.



True 3D CAE for Injection Molding

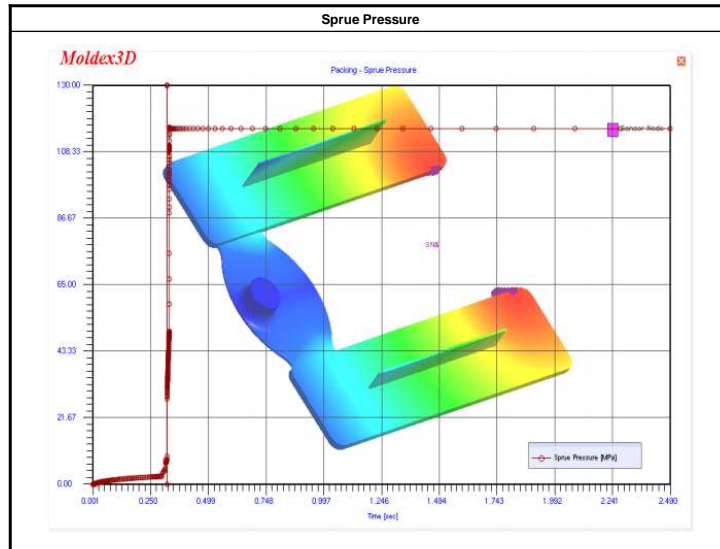
Moldex3D Packing-Melting Core



It demonstrates the Iso-surface of the freeze temperature of plastic melt at current instant. The enclosed region has the iso-surface with the temperature higher than the freeze temperature specified in the process condition.

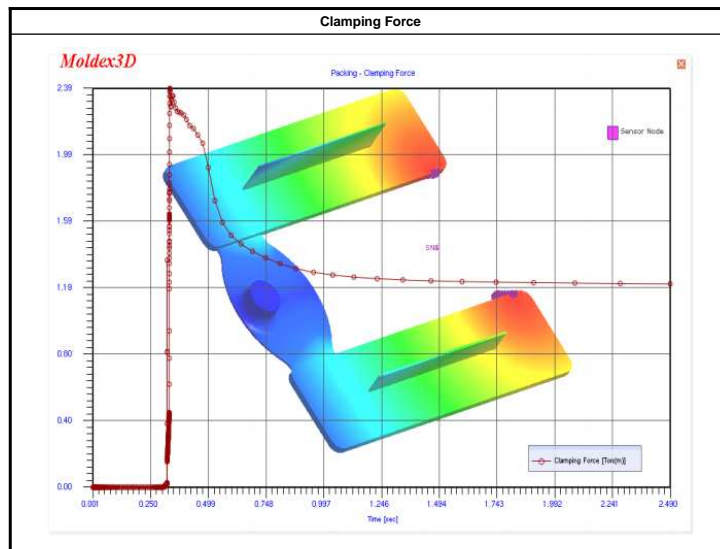
True 3D CAE for Injection Molding

Moldex3D Packing - Sprue Pressure XY Curve



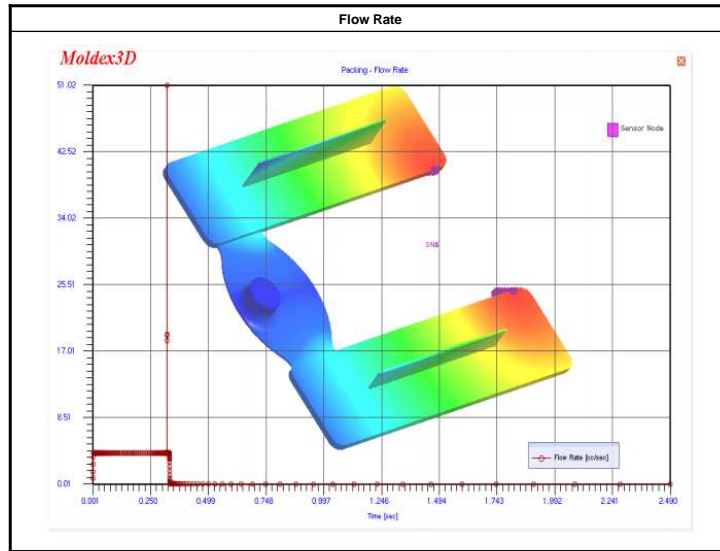
True 3D CAE for Injection Molding

Moldex3D Packing - Clamping Force XY Curve



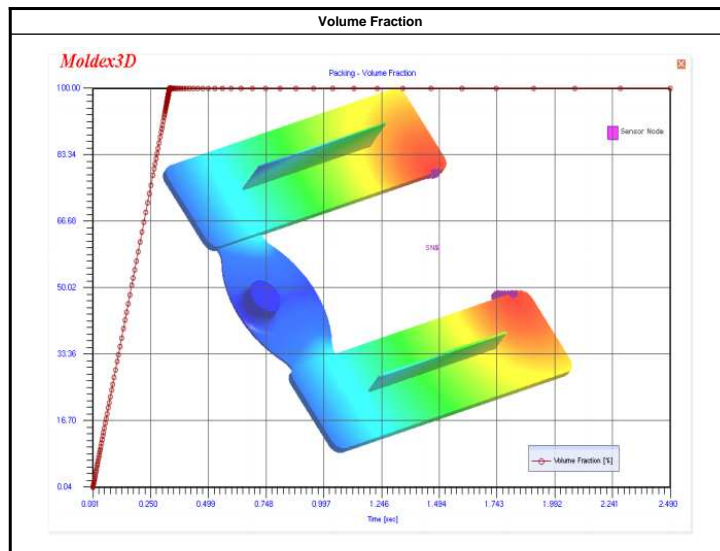
True 3D CAE for Injection Molding

Moldex3D Packing - Flow Rate XY Curve



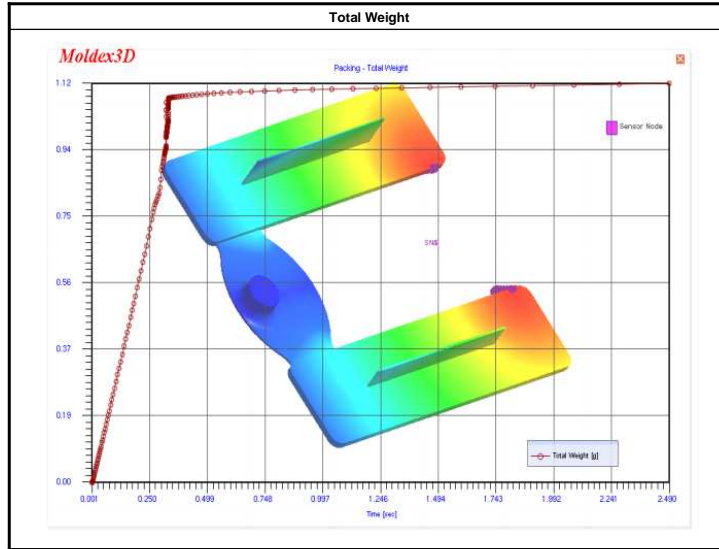
True 3D CAE for Injection Molding

Moldex3D Packing - Volume Fraction XY Curve



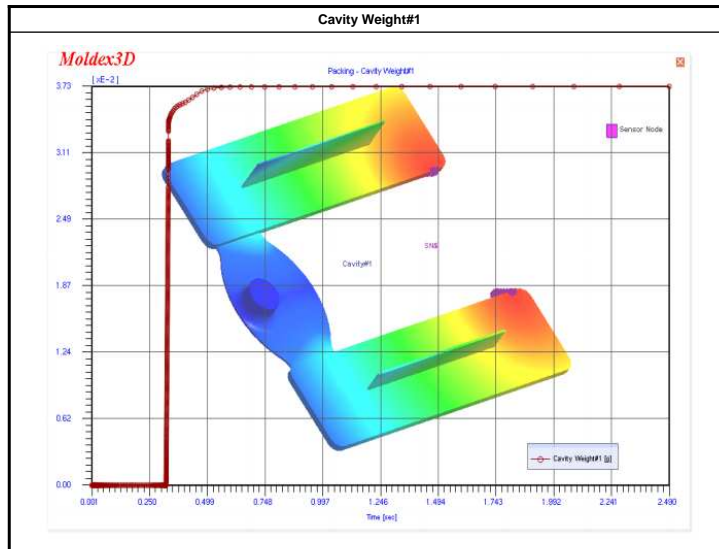
True 3D CAE for Injection Molding

Moldex3D Packing - Total Weight XY Curve



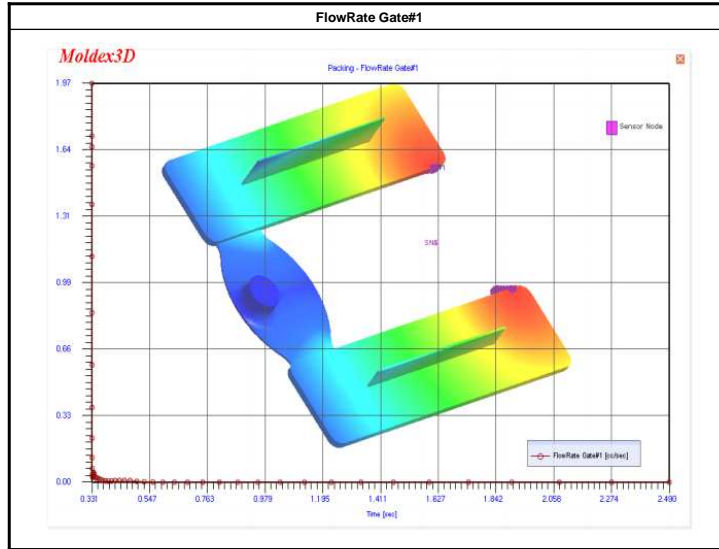
True 3D CAE for Injection Molding

Moldex3D Packing - Cavity Weight#1 XY Curve



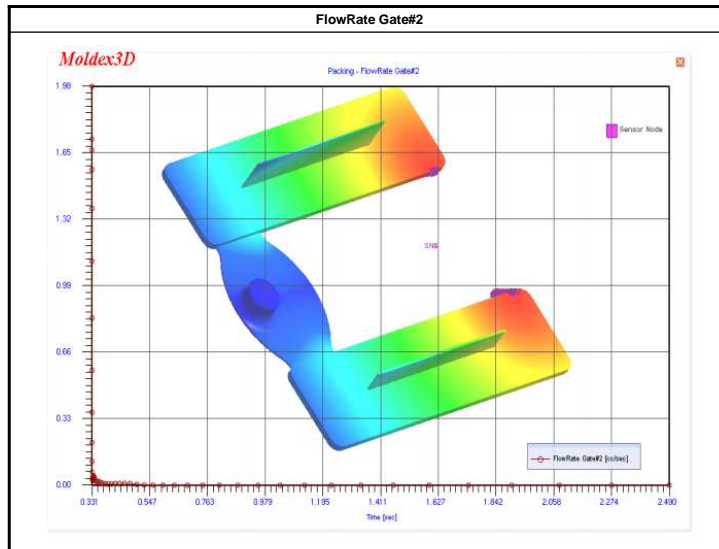
True 3D CAE for Injection Molding

Moldex3D Packing - FlowRate Gate#1 XY Curve



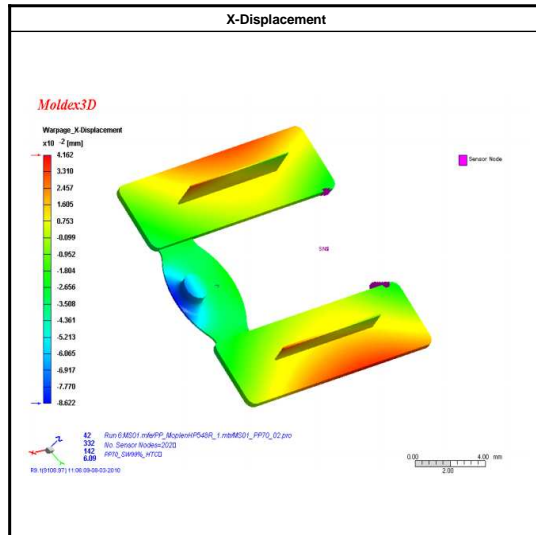
True 3D CAE for Injection Molding

Moldex3D Packing - FlowRate Gate#2 XY Curve

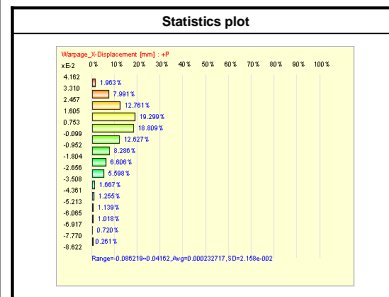


True 3D CAE for Injection Molding

Moldex3D Warpage-X-Displacement

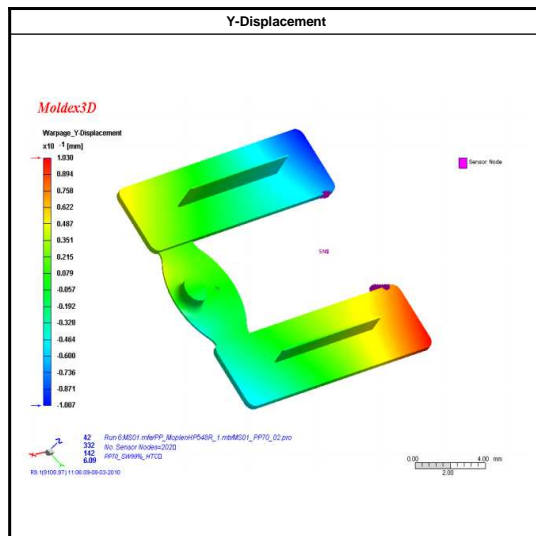


Shows the X-component of the total displacement (All effects are considered) after the part is ejected and cooled down to room temperature. The value is relative to the model coordinate.

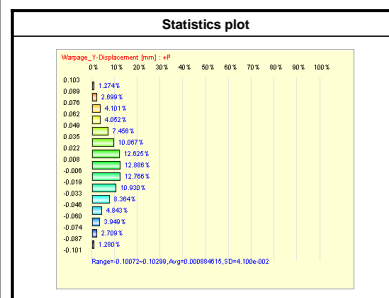


True 3D CAE for Injection Molding

Moldex3D Warpage-Y-Displacement

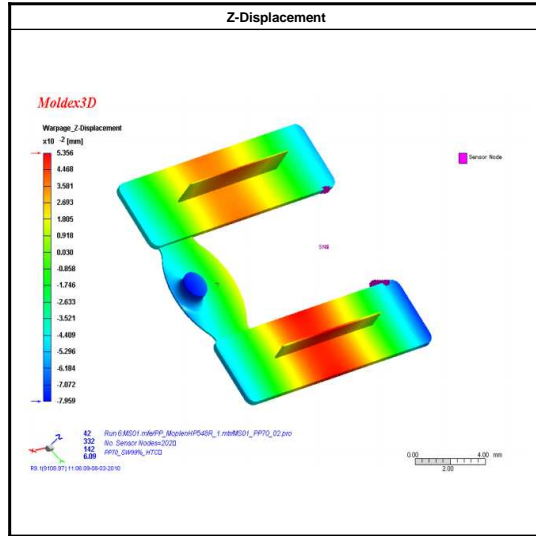


Shows the Y-component of the total displacement (All effects are considered) after the part is ejected and cooled down to room temperature. The value is relative to the model coordinate.

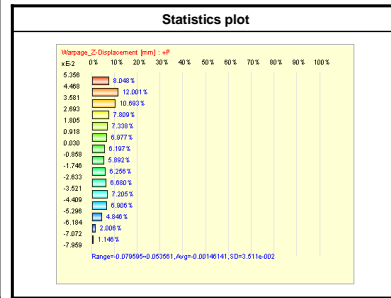


True 3D CAE for Injection Molding

Moldex3D Warpage-Z-Displacement

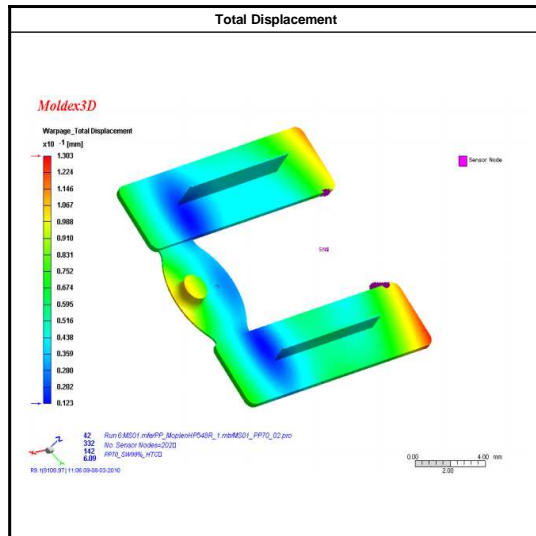


Shows the Z-component of the total displacement (All effects are considered) after the part is ejected and cooled down to room temperature. The value is relative to the model coordinate.

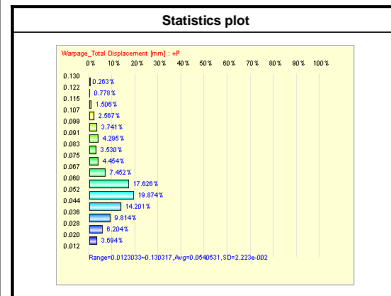


True 3D CAE for Injection Molding

Moldex3D Warpage-Total Displacement

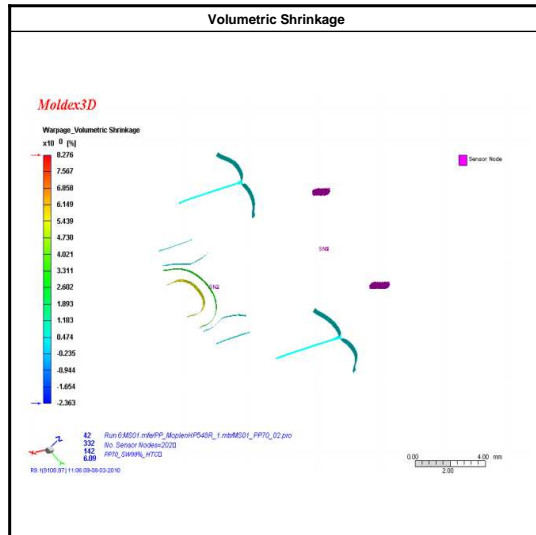


Shows the length of the total displacement vector (All effects are considered) after the part is ejected and cooled down to room temperature. The value is relative to the model coordinate.

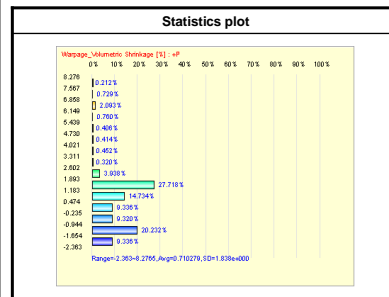


True 3D CAE for Injection Molding

Moldex3D Warpage-Volumetric Shrinkage

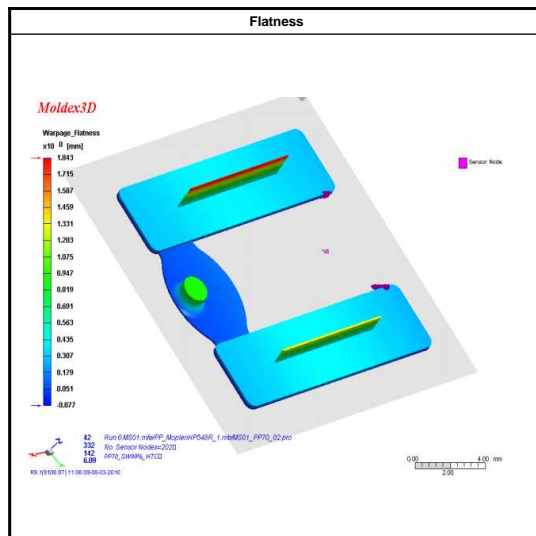


This data show the volumetric shrinkage percentage of molded part due to pVT change as the part is cooled down from high temperature, high pressure condition after packing stage to room temperature, ambient temperature conditions. Positive value represents volume shrinkage while negative value is an indicator of volume expansion. Non-uniform volumetric shrinkage will lead to warpage and distortion of demolded parts.

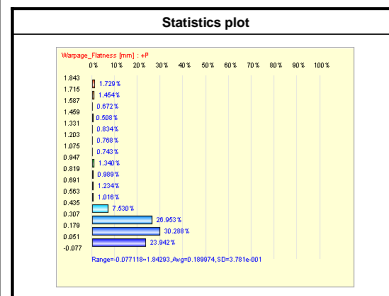


True 3D CAE for Injection Molding

Moldex3D Warpage-Flatness

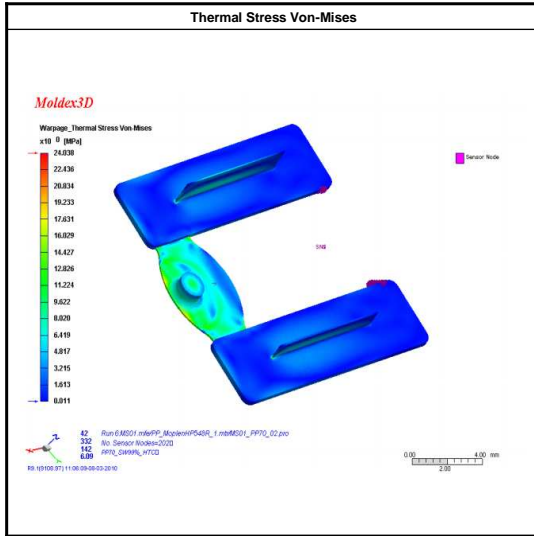


Flatness is the distance between the nodes to the user specified reference plane.

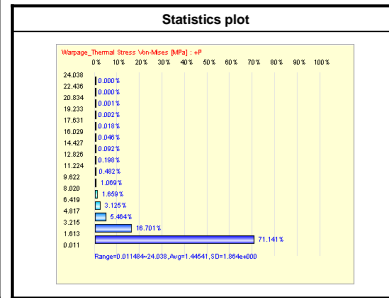


True 3D CAE for Injection Molding

Moldex3D Warpage-Thermal Stress Von-Mises



Von-Mises thermal residual stress of the ejected part.



True 3D CAE for Injection Molding

Annex A3

Thermo-rheological behaviour of polymer melts in microinjection moulding, J. C. Vasco, J. M. Maia and A. S. Pouzada, *Journal of Micromechanics and Microengineering*, ISSN 0960-1317, 19, 105012, pages 1-8, 2009

Thermo-rheological behaviour of polymer melts in microinjection moulding

This article has been downloaded from IOPscience. Please scroll down to see the full text article.

2009 J. Micromech. Microeng. 19 105012

(<http://iopscience.iop.org/0960-1317/19/10/105012>)

[The Table of Contents](#) and [more related content](#) is available

Download details:

IP Address: 193.137.239.24

The article was downloaded on 18/09/2009 at 14:42

Please note that [terms and conditions apply](#).

Thermo-rheological behaviour of polymer melts in microinjection moulding

J C Vasco¹, J M Maia^{2,3} and A S Pouzada²

¹ Department of Mechanical Engineering, Polytechnic Institute of Leiria, Leiria, Portugal

² Institute for Polymers and Composites, University of Minho, Guimarães, Portugal

³ Department of Macromolecular Science and Engineering, Case Western Reserve University, Cleveland, OH, USA

E-mail: asp@dep.uminho.pt

Received 7 May 2009, in final form 3 August 2009

Published 17 September 2009

Online at stacks.iop.org/JMM/19/105012

Abstract

Microinjection has proven to be one of the most efficient replication methods for microcomponents and microsystems in various domains of microengineering. The use of available commercial microinjection equipment to evaluate the polymeric flow in microchannels would surely contribute to enhancing knowledge on polymeric flow at the microscale under industrial conditions. This approach is appropriate since rheological phenomena such as wall slip, surface tension, melt pressure drop and polymer flow length can be studied. These aspects are not fully dealt with in current commercial simulation software packages. In this study a micromould was designed to assess and characterize the flow in microchannels under realistic industrial conditions.

1. Introduction

Microinjection moulding is one of the most flexible, reliable and effective replication methods for microcomponents and microsystems for high-demand client industries such as medical applications, personal well-being, automobile and aerospace industry, and military and defence applications (Martin *et al* 2003). Along with microhot embossing, this process has played a major role in bringing to the market several microsystems at reasonable end-user prices such as microelectro/mechanical components, microoptic systems and microfluidic devices (Giboz *et al* 2007, Zhao *et al* 2003). The massification of microtechnologies depends directly on the effectiveness of their production (Piotter *et al* 1997). The market for microcomponents obtained by microinjection is growing, showing high business potential and is surely becoming one of the key technologies for micromanufacturing (Sha *et al* 2005). The need for quickly and accurately getting the moulding zone of moulds for microinjection moulding originated the development of the Variotherm system (Piotter *et al* 2002). The original system was the object of various developments as recently reviewed by Giboz and co-workers (Giboz *et al* 2007). These systems are for the accurate replication of high-aspect-ratio microstructures, and precise process control as is the case of optical components

(Piotter *et al* 2002, Giboz *et al* 2007). Despite its success in the replication of microdetails, as in CDs or DVDs, the polymer filling behaviour of mould cavities still requires further study since the simulation tools currently available cannot fully predict flow effects at the microscale. Aspects such as wall slip, surface tension and heat transfer phenomena, require further study to avoid or minimize re-engineering costs or even to prevent wrong options in the microcomponent or microsystem design (Kim *et al* 2002, Piotter *et al* 2002, Su *et al* 2004).

2. Flow models

The viscosity of liquids and polymer solutions flowing in microchannels has been observed to increase up to 80% near the wall of the channel. During the polymer flow such an effect is believed to be due to its high intermolecular interaction and the disentanglements between bulk and wall chains (Eringen and Okada 1995, Awati *et al* 2000). Effects such as microscale viscosity, wall slip and surface tension need to be studied for a full comprehension of the rheological behaviour of the flow in microchannels (Yao and Kim 2002).

2.1. Capillary and slit flow models

The polymer flow in microchannels is quite similar to that in capillary viscosity measurements (Chien *et al* 2005, Hatzikiriakos and Dealy 1992, Rosenbaum and Hatzikiriakos 1997, Sha *et al* 2005). These measurements are based on the relationships between the pressure drop along the capillary channel and the imposed flow rate (Carreau *et al* 1997). For capillary rheometry, the following assumptions are made:

- the Reynolds number (Re) is smaller than 2000; thus, laminar flow is occurring;
- steady state, $\frac{\partial}{\partial t} = 0$;
- there is a fully developed unidirectional flow: $V_r = V_\theta = 0$ and $V_z = V_z(r)$ and
- there is no slip at the capillary walls: $V_z(r = R) = 0$ and $\frac{dV_z}{dr} = \frac{dV_z}{dr}(\sigma_{rz})$.

Considering the microchannel geometry to be used, the mathematical models used to describe the polymer flow are the same as for capillary rheometry (equation (1)) and slit flow:

$$\dot{\gamma}_{w(\text{app})} = \frac{4Q}{\pi \cdot R^3}. \quad (1)$$

After the Rabinowitsch procedure for the shear rate at the wall, the following equation for the non-Newtonian fluid shear rate results in equation (2) (Chen *et al* 2008):

$$\dot{\gamma}_{w(\text{real})} = \frac{4Q}{\pi \cdot R^3} \left(\frac{3}{4} + \frac{1}{4}n \right), \quad (2)$$

where Q is the volumetric flow rate, R is the radius of the capillary channel and n is the slope obtained by the bi-logarithmic correlation between $\log \dot{\gamma}_{w(\text{app})}$ and $\log \tau_w$.

Furthermore, the Bagley correction is applied to the apparent shear stress τ_w , given by equation (3), in order to eliminate the viscous and elastic effects on the capillary entrance:

$$\tau_{w(\text{app})} = \frac{\Delta P}{2L} R. \quad (3)$$

The shear stress at the wall is now given by equation (4) (Chen *et al* 2008):

$$\tau_{w(\text{real})} = \frac{\Delta P}{2 \left(\frac{L}{R} + e \right)} = \frac{\Delta P - P_0}{2L} R, \quad (4)$$

where ΔP is the pressure drop along the capillary, L and R are the length and radius of the capillary, e is the Bagley correction factor and P_0 is the pressure drop for a capillary with zero length for a given rate of shear.

The slit flow model also derives from the equations used for the capillary viscometer in a similar way to the previous flow models. A microchannel must be designed to meet the requirements of a slit flow, enabling pressure monitoring at both ends to generate specific experimental data (figure 1).

The apparent shear rate of a slit is given by

$$\dot{\gamma}_{w(\text{app})} = \frac{6Q}{w \cdot h^2}. \quad (5)$$

After applying the Walter correction for non-Newtonian fluids (Chen *et al* 2008), it becomes

$$\dot{\gamma}_{w(\text{real})} = \frac{6Q}{w \cdot h^2} \left(\frac{2}{3} + \frac{1}{3}n \right), \quad (6)$$

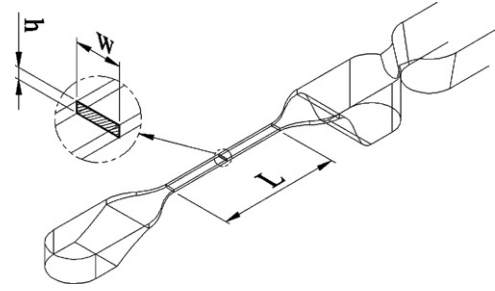


Figure 1. Overall dimensions of a slit channel.

where Q is the volumetric flow rate, w and h are width and height of the rectangular cross-sectioned channel, respectively, and n is the slope obtained by the bi-logarithmic correlation between $\log \dot{\gamma}_{w(\text{app})}$ and $\log \tau_w$.

In the particular case of the slit, the edge effect on the shear stress must be corrected when the width by thickness ratio is below 10. The real shear stress equation for Newtonian fluids (equation (7)) then becomes equation (8) (Chen *et al* 2008):

$$\tau_{w(\text{real})} = \frac{h}{2} \left(\frac{-\Delta P_{\text{real}}}{L} \right) \quad (7)$$

$$\tau_{w(\text{real})} = \frac{w \cdot h}{2(w + h)} \left(\frac{-\Delta P_{\text{real}}}{L} \right). \quad (8)$$

After the corrections on the capillary and the slit flow models, the real viscosity can be calculated for each type of flow by dividing the real shear stress by the real shear rate, resulting in equation (9) (Carreau *et al* 1997, Chen *et al* 2008):

$$\eta_{(\text{real})} = \frac{\tau_{\text{real}}}{\dot{\gamma}_{\text{real}}}. \quad (9)$$

2.2. Wall slip effect

The concept of wall slip was first addressed by Mooney (1931), who found that certain flow curves depended on the radius of the capillary once the shear stress exceeded a critical value (Lee and Mackley 2000). The effect takes place when the shear stress at the microchannel wall exceeds a critical value, typically, above 0.1 MPa (Hatzikiriakos and Dealy 1992, Yao and Kim 2002, Mitsoulis *et al* 2005). As the magnitude of the shear stresses varies, polymer melts flow in a way that is a superposition of slipping at the wall and shearing within the melt (Gleißle and Windhab 1985). When wall slip occurs at a critical wall shear stress value the flow curves (wall shear stress versus apparent shear rate) diverge from each other and become dependant on channel dimensions. Usually the boundary conditions at the wall are known and their influence on the flow behaviour close to the wall is relevant. Assuming a constant heat flux at the wall ($\delta T / \delta r = \text{constant}$ and $Bi(T_0 - T_w)$), a simplified power-law slip model (equation (10)) was introduced for the slip velocity without considering any pressure or temperature dependence (Rosenbaum and Hatzikiriakos 1997):

$$u_s = \frac{a}{1 + (\tau_c / \tau_w)^{10}} \tau_w^m, \quad (10)$$

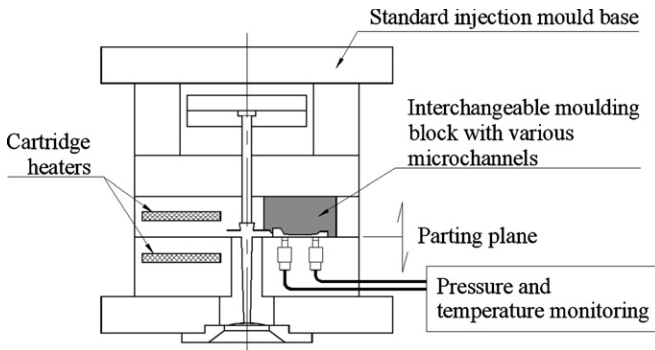


Figure 2. Concept of a tool for rheometric studies in microchannels.

where τ_w is the wall shear stress, τ_c is the critical shear stress for slip, a is the scalar coefficient and m is the mass flow rate constancy equation given by

$$m = 2\pi \int_0^R \rho \cdot v_z \cdot r \, dr. \quad (11)$$

3. Experimental methods

3.1. Concept

Currently available capillary rheometers are difficult to operate with channels with dimensions at the microregion. Alternative experimental setups guaranteeing the flow through the microchannel must generate pressure high enough and support the high stresses developed during the flow (Chien et al 2005). A concept meeting these requirements consists of using a small injection mould structure (100 × 130 mm) with a set of interchangeable moulding blocks with calibrated microchannels, in an injection moulding machine. The operation of such a device requires accurate temperature control during the heating and cooling phases of the moulding cycle, as well as pressure control at the extremities of the microchannel. The concept is sketched in figure 2.

It must be stressed that equipment based on this concept is not exactly a microrheometer, but it is a setup capable of replicating the flow conditions in real micromoulding situations. More precisely it is a viscometer that can be used on standard injection moulding equipment to analyse the flow using processing parameters characteristic of microinjection moulding.

The use of miniature pressure sensors and a suitable data acquisition system makes it possible to gather the information required for rheological characterization of the flow in the microchannel as suggested in figure 3.

The pressure drop, Δp , measured from the pressure sensor data is required for calculating the shear stress using equation (8). The average melt flow rate is obtained from the data acquisition system that enables the flow time between the locations of the pressure sensors, Δt , to be determined. The shear rate can then be calculated using equation (6).

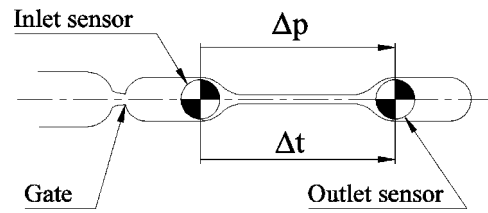


Figure 3. Variables for the rheological assessment of the flow in microchannels. Δp —pressure drop; Δt —time interval.

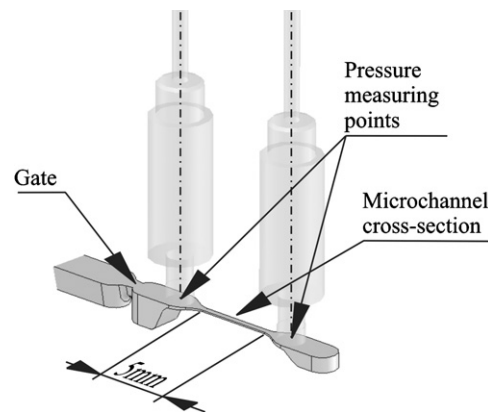


Figure 4. Layout of the microchannel and pressure sensors.

3.2. Methodology

The use of commercial microinjection moulding equipment led to the full design and development of a research mould that could be used in injection tests with various microchannels. The mould was designed to support two interchangeable moulding blocks, allowing the replacement of the microcavities. Furthermore, the tool can be used to test new types of moulding blocks, e.g. manufactured using additive technologies. Two moulding blocks with two different microchannel cross-sections were tested: a slit with a rectangular section, 400 μm wide by 100 μm deep, and a square section of 200 × 200 μm dimensions. The length of both microchannels is identical, 5 mm. The general layout of the cavities is shown in figure 4.

Concerning the location of the pressure sensors, there is a source of error that must be addressed. The physical dimensions of the commercial sensors used are from a different scale to that of the microchannel dimensions. So, the microchannels are wider at both ends to allow the assembly of the sensors for a proper pressure reading. However, such section variation causes pressure distortion and therefore an entry correction procedure for pressure drop was performed using zero-length microchannels for each cross-section tested. Therefore, two additional moulding blocks with a zero-length microchannel were manufactured to correct the measurements for entry effects (figure 5).

When the moulding blocks with microchannels are implemented, the mould can be used as a high-pressure viscometer enabling high injection pressures in the microchannels, which are difficult to achieve in conventional viscometers (Chen et al 2008, Chien et al 2005, Song et al

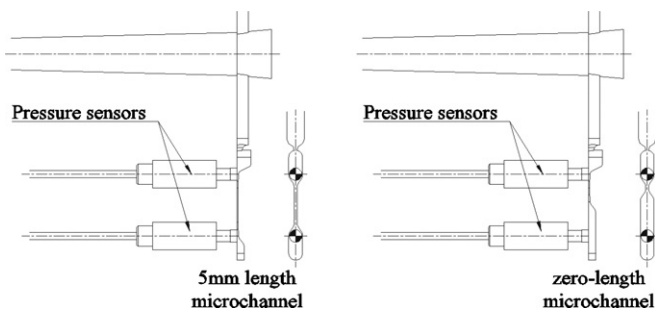


Figure 5. 2D views of the $400 \times 100 \mu\text{m}$ microchannel showing the 5 mm length (on the left) and the zero-length versions (on the right).

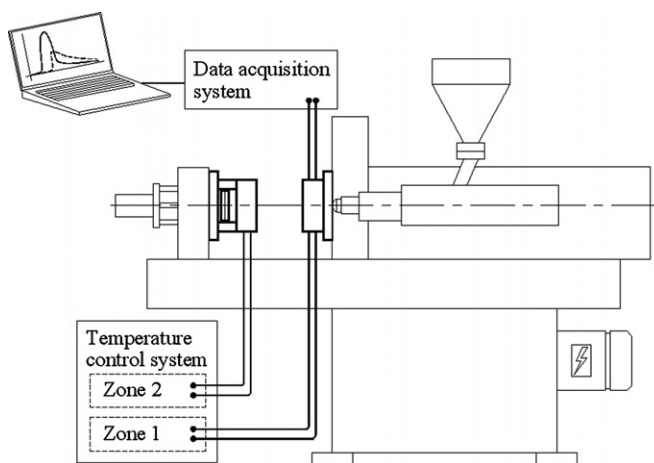


Figure 6. Layout of the injection micromoulding cell, showing the two temperature control zones and the pressure data acquisition system with sensors located on the fixed platen of the mould.

2007, Yao and Kim 2002). Since the goal is to promote the flow in microchannels, an external control unit for the heating system will provide the temperatures suitable for polymer injection at this scale, enabling quantitative flow evaluation at the same time and under the same processing conditions.

3.3. Microinjection equipment

Since the 1980s microinjection equipment has evolved to meet the requirements for microparts such as minimal shot weight and precise control of the processing conditions (pressure, injection speed, melt and mould temperatures) to achieve the high repeatability required in the applications (Piotter *et al* 2002). In this work, a Boy 12 A injection moulding machine (Dr Boy, Neustadt-Fernthal, Germany) that combines technical characteristics for microinjection and affordability (Piotter *et al* 1997, Song *et al* 2007) was used.

The microinjection cell consists of the Boy 12 A injection moulding machine with $\varnothing 14$ mm injection screw, a mould temperature regulator and an external control unit for the cartridge heaters used in the temperature control system of the mould (figure 6). Concerning the injection unit ability for microinjection, the Boy 12 A machine is able to meter with high precision an injection volume as small as 0.1 cm^3 at a high flow rate, up to $15.6 \text{ cm}^3 \text{ s}^{-1}$. The maximum injection pressure is 240 MPa.

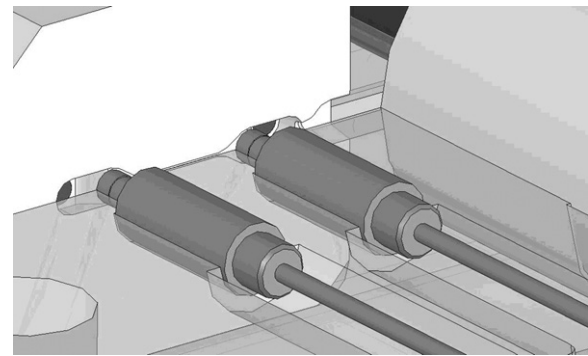


Figure 7. Assembly of the pressure sensors at the microchannel inlet and outlet.

3.4. Instrumentation

The rheological characterization of the polymer flow in the microchannel is achieved by monitoring melt pressure at the microchannel inlet and outlet using two miniature piezoelectric pressure sensors Priamus 6006B (Priamus System Technologies, Schaffhausen, Switzerland) (figure 7). The pressure drop between the two locations and the flow velocity are used to relate the shear viscosity to the shear rate (Chen *et al* 2008, Chien *et al* 2005). The assembly of the pressure sensors is depicted in figure 7.

The data acquisition system consisted of two physical units, the input module, Multi DAQ 8101 A, and the amplifier module, Mobile DAQ 8001B, both from Priamus. The user interface was based on the Priamus Moulding Monitor software.

3.5. Materials

The injection tests were carried out with polyoxymethylene (POM), Hostaform C27021 grade from Ticona (Kelsterbach, Germany). This semi-crystalline polymer is a very easy flow injection moulding type with a MFR of $24 \text{ cm}^3/10 \text{ min}$ ($190 \text{ }^\circ\text{C}$, 2.16 kg) that is commonly used in microinjection moulding (Heckele and Schomburg 2004).

3.6. Microinjection moulding

The initial approach for the injection tests was close to conventional rheometry. The melt speed was increased gradually to establish the data required for shear rate and viscosity calculation.

Several injection speeds were imposed to reach different values of shear rate on each microchannel. For each injection speed a time interval, Δt , defined as the time lag between the melt touching each pressure transducer, was measured, enabling the calculation of the average melt speed within the microchannel. Pressure data from the inlet and outlet sensors, for typical injection moulding conditions ($T_{\text{inj}} = 205 \text{ }^\circ\text{C}$; $T_{\text{mould}} = 145 \text{ }^\circ\text{C}$; $t_{\text{inj}} = 0.35 \text{ s}$), are shown in figure 8.

Differently from the microinjection process, no packing pressure was used since the goal was only to obtain a fully established flow within the microchannel without pressure

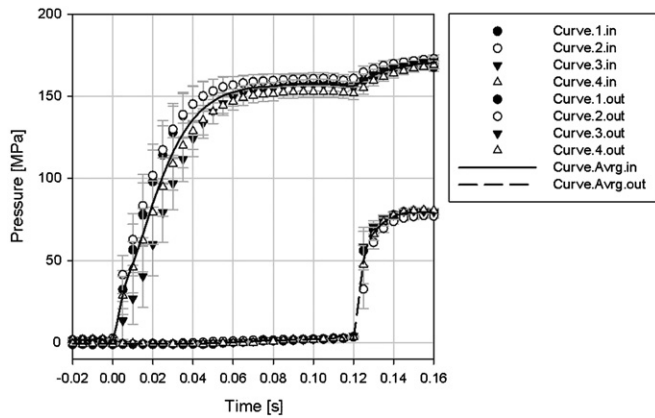


Figure 8. Typical pressure profiles during the flow in the microchannel. Suffix *in* corresponds to the signal at the channel inlet and suffix *out* at the channel outlet. The lines correspond to the average of the experimental points.

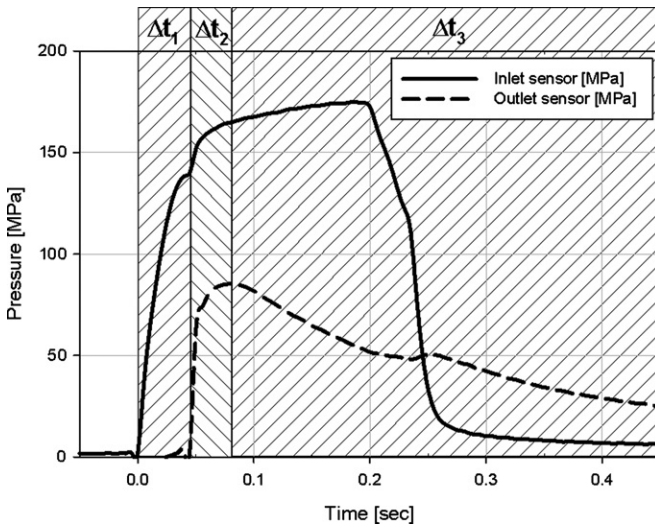


Figure 9. Sample pressure curves for the $200 \times 200 \mu\text{m}$ microchannel moulding.

disturbances. The other process parameters, namely the mould and the melt temperature had to be raised gradually until complete mouldings were obtained. The 14 mm screw injection speed was varied within the capability of the equipment from 20 to 200 mm s^{-1} . The required mould temperature was 145 °C and the melt temperature was set at 235 °C. For each microchannel the data for analysis were those corresponding to full-shot mouldings, when pressure data were obtained by both pressure sensors. A typical set of data is shown in figure 9.

Three different time frames, identified as Δt_1 , Δt_2 and Δt_3 , can be identified in this sample. The first time frame, Δt_1 , starts when the melt reaches the inlet pressure sensor at the entrance of the microchannel (solid line on the graph). The end of this interval corresponds to the instant when the melt reaches the outlet sensor at the exit of the microchannel (dashed line on the graph). After Δt_1 the flow fully develops in the microchannel, as pressure signals are recorded on both sensors, and the measurements for the viscosity evaluation can be initiated. During the second time frame, Δt_2 , which

ends when the outlet sensor reaches its peak, the melt fills completely the impression. After this point, the melt flow stops and the microchannel freezes off, leading to the pressure drop monitored by the two sensors. This phase occurs during the last time frame, Δt_3 , where the peak on the inlet pressure sensor value corresponds to the solidification of the gate. After this point, pressure rapidly decreases as a result of the variation of the specific volume of the melt.

4. Results and discussion

4.1. Conventional rheometry

Preliminary characterization of the polymer was made using a twin-bore Rosand RH10 capillary rheometer from Malvern Instruments (Malvern, UK). The determination of traditional flow curves was carried out at the temperatures of 180 °C, 200 °C, 220 °C and 240 °C. The flow activation energy was calculated since at these temperatures, POM is a thermo-rheologically simple material and the time-temperature superposition (TTS) principle is expected to apply. For semicrystalline polymer melts and for amorphous polymer melts as well this applies when the flow temperatures are more than 100 °C above the glass transition temperature. The shift factor for each temperature, a_T , can be expressed by an Arrhenius relation (Wagner et al 1996) as

$$a_T = \exp\left(\frac{E}{R} \cdot \left(\frac{1}{T} - \frac{1}{T_0}\right)\right), \quad (12)$$

where E is the flow activation energy, R is the gas constant and T and T_0 are absolute temperatures.

As the TTS principle holds for this melt, the flow activation energy, E , is approximately 44 800 $\text{J K}^{-1} \text{mol}$. The flow curves obtained from capillary rheometry are shown in figure 10(a) and the master curve is depicted in figure 10(b).

4.2. Microchannel flow

In the injection moulding tests the mould temperature was kept at 145 °C to enable the complete filling of the impressions. This was particularly critical with the thinnest $400 \times 100 \mu\text{m}$ slit microchannels. The data were obtained from fully filled mouldings, i.e. short shots were discarded.

During the tests, the two pressure profiles were recorded, from the sensors at the inlet and the outlet of the microchannel. This information, as exemplified in figure 9, allows obtaining the following information: (a) the pressure drop between inlet sensor and microchannel inlet, Δp_1 ; (b) the pressure drop in the microchannel itself, Δp_2 and (c) the pressure drop between the microchannel outlet and the outlet sensor, Δp_3 . To determine Δp_2 , the value for Δp_1 must be removed from the total pressure drop value obtained assuming that Δp_3 is much smaller than $\Sigma \Delta p_i$. The zero-length microchannel (L0) is meant to determine its initial pressure drop, which will be equivalent to Δp_1 so the values for the 5 mm microchannel (L5) could be corrected (figure 11).

In the injection tests, the melt flow rate was varied. For each condition, the time difference, Δt , was calculated between the signals of the inlet and outlet pressure sensors that

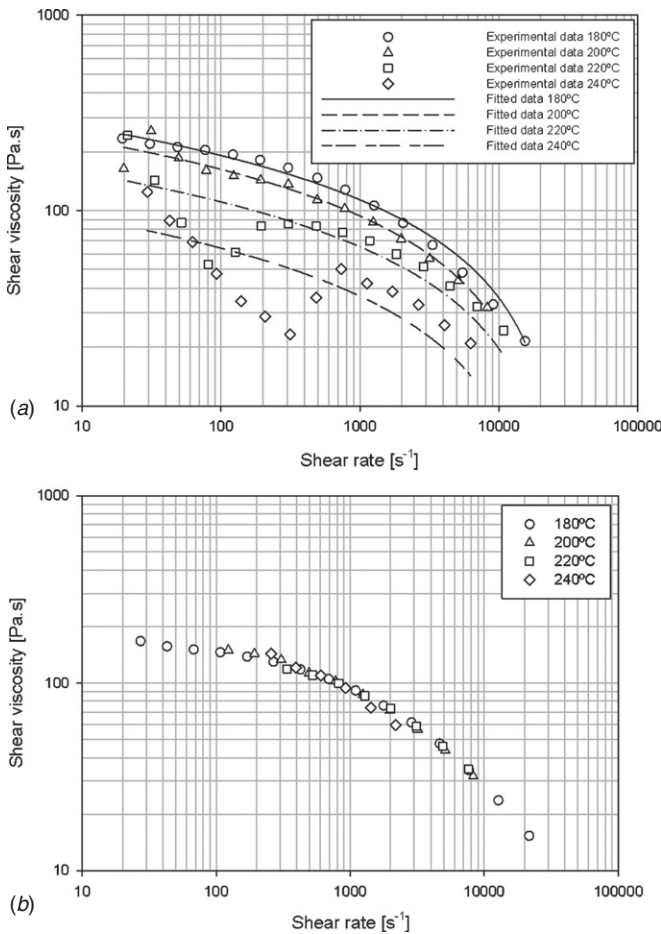


Figure 10. (a) Flow curves from conventional capillary rheometry for Hostaform C 27021. (b) Master curve for the same data, observing the time-temperature superposition principle.

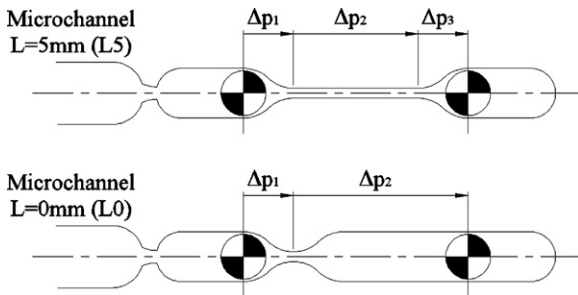


Figure 11. Determination of the pressure drop within the microchannel.

provided the flow rate value required for shear rate calculation from equation (6). The pressure drop was also obtained, allowing the calculation of shear stress through equation (8). With these two values for each melt speed, shear viscosity could be determined by the ratio between shear stress and shear rate (equation (9)) and is plotted in figure 12.

4.3. Plug flow transition

From the plot in figure 12, it is noticeable that there is an important change in the flow behaviour of each microchannel as the shear rate increases. Both curves show a transition from

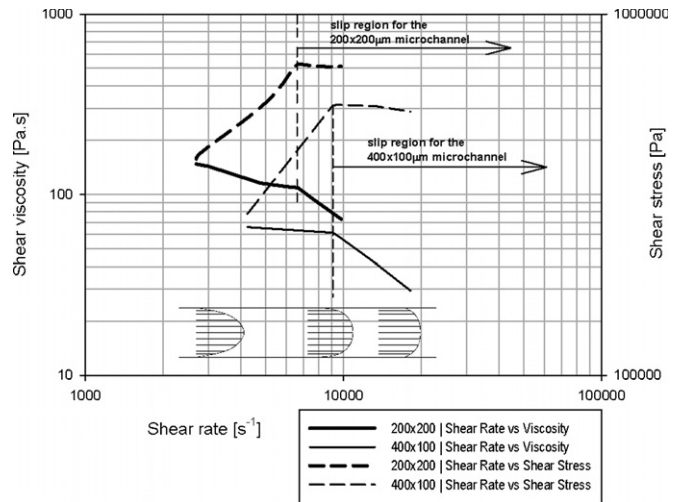


Figure 12. Flow curves from rheometry calculations based on the 200 × 200 μm and 400 × 100 μm microchannel pressure data.

a normal flow to a new type of flow where the index of non-Newtonian behaviour, n , is close to 1, indicating the onset of wall slip. The horizontal segment of both curves at constant shear stress clearly states that a change in behaviour from shear to plug flow due to the wall slip effect has occurred. The non-horizontal component of the curves corresponds to shear flow, immediately before the critical shear rate is achieved for both microchannels. It is also possible to observe in this figure that the critical shear rate for this particular material and the 200 × 200 μm microchannel is around 5000 s⁻¹. The critical shear rate for the 400 × 100 μm microchannel, for which successful shots were difficult to obtain at lower melt speeds, is estimated to be approximately 6000 s⁻¹. The different shear rate values at which the plug flow transition occurred for both microchannels can be explained by their hydraulic diameter and the aspect ratio of both cross-sections. The 200 × 200 μm square section, with an aspect ratio of 1:1, corresponds to an equivalent round section 200 μm in diameter. On the other hand, the 400 × 100 μm section with an aspect ratio of 4:1 has a hydraulic diameter of just 160 μm and therefore, a less favourable geometry for flow. This difference on the hydraulic diameter leads to a 20% decrease on the effective flow cross-section on the 400 × 100 μm microchannel, causing it to reach its critical shear rate at lower values. After these critical values of shear rate, a plug flow is fully developed in both microchannels.

4.4. Interpreting plug flow transition

Despite the processing temperature used for flow in the microchannels being 235 °C, the corresponding flow curve is located above the 180 °C flow curve, as shown in figure 13. This means that the real temperature on the microchannel is much lower than the imposed processing temperature.

Such fact is certainly due to the high surface area to volume ratio, which makes conventional heat transfer equations insufficient to describe what happens at this scale. Analysing the flow curve for the 200 × 200 μm microchannel, two segments can be observed. From A to B, shear flow

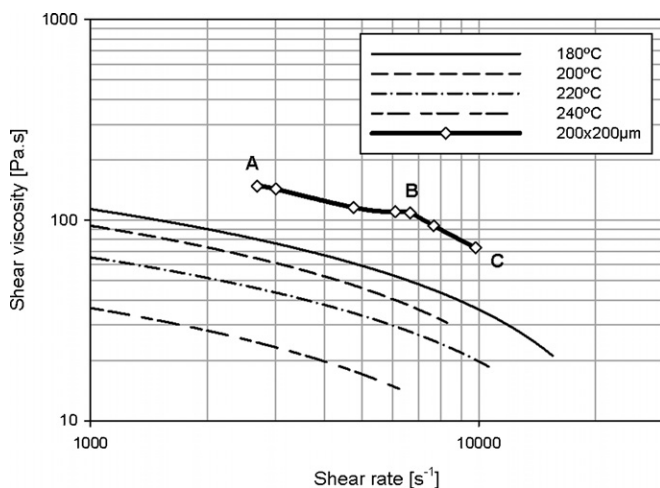


Figure 13. Plot data from conventional capillary rheometry and rheometry calculations based on the $200 \times 200 \mu\text{m}$ microchannel pressure data.

is found although the end of this segment represents the transition to the next segment, B to C, in which plug flow is fully developed. The cooling of the molten material in the microchannel means that the temperature of the flowing melt is expected to be well below the initial 235°C . The amplitude of the decrease, however, cannot be predicted from TTS, which is known to be valid for this material (see above). In fact, an application of TTS to the microchannel flow data in order to superimpose it with the other data yields an apparent flow temperature of less than 80°C , which is impossible because not only it is more than 60°C lower than the mould wall temperature, but is also lower than the no-flow temperature of POM.

This fact clearly indicates that the heat transfer analysis that is normally done in injection moulding is not directly transferable to the microscale due to the high surface area to volume ratio. Given their sub-millimetric dimensions, the microchannels exhibit a high heat diffusion rate which causes filling to occur almost isothermally (Yao and Kim 2002). In this particular case, there is effectively little or no bulk in the moulding, so our results indicate that heat transfer equations that are typically valid at the macroscale should be disregarded here.

The evaluation of the local wall slip velocity was made using equation (10). The mass flow-rate consistency value was calculated through equation (11), using the hydraulic radius of both microchannels. The melt front profile was estimated as a gradual shifting from shear flow to plug flow as shear stress increases. The data obtained for the $400 \times 100 \mu\text{m}$ microchannel might not be conclusive since there are not enough data under shear flow conditions to establish a reliable trend to this value. However, the few calculated local wall slip velocity values for this microchannel seem to corroborate the conclusions already obtained on the shear stress versus shear rate plot (figure 14).

Nevertheless, both curves in figure 14 show the same trend: when shear stress is less than the critical shear stress, the local wall slip velocity is nearly zero. As predicted, the

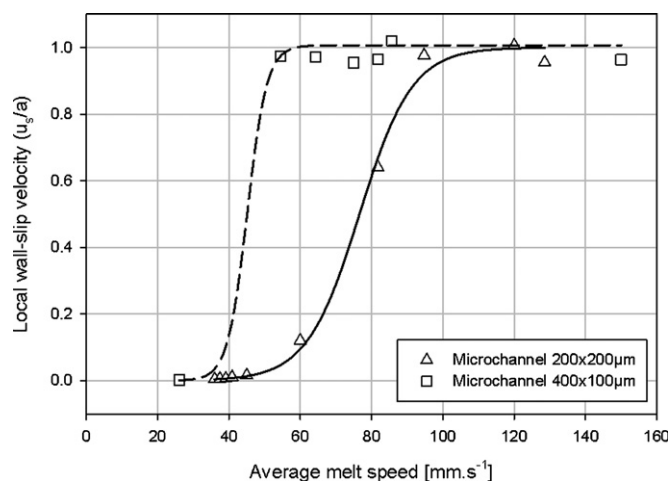


Figure 14. Plot of the average melt speed versus local wall-slip velocity.

local wall slip velocity becomes close to 1 if shear stress keeps increasing (Rosenbaum and Hatzikiriakos 1997).

An immediate conclusion of this study is that the flow inside the mould is non-isothermal, which means that the data eventually obtained are not to be regarded as quantitatively accurate rheometrical data. As already stated before, the equipment setup in this study is not a microrheometer, but rather a viscometer that replicates the flow conditions in real flow situations, i.e. it is a process analyser and simulator.

5. Conclusions

In this work a tool for the quantitative evaluation of the rheological behaviour of polymer melts under typical microinjection moulding conditions was developed. The use of a microinjection moulding tool for rheometry purposes provided the establishment of flow curves for POM at pressures higher than the ones obtained on traditional rheometry, enabling critical shear rate determination for each microchannel used.

Unlike conventional capillary rheometry devices, this setup used microinjection process parameters, namely the injection speed to obtain different shear rates, enabling the plotting of flow curves. Therefore, the results could be easily applied onto the microinjection process itself or on microinjection simulation.

An important microscale effect such as wall slip was detected and the critical values of shear rate were determined for both microchannels studied. Furthermore, the local wall slip velocity was calculated and compared to the average melt velocity imposed on the process, to determine its relevance to the flow behaviour. It was noticed that the shifting between the shear flow and plug flow is much more abrupt on the $400 \times 100 \mu\text{m}$ microchannel, due to the less favourable cross-section.

The results proved the validity of the experimental concept and also suggested that the heat transfer phenomena in very thin microinjection mouldings, with a very large surface area/volume ratio, play an important role that will require further study.

Acknowledgment

This research work was supported by the Portuguese Foundation for the Science and Technology under the grant SFRH/BD/36982/2007.

References

- Awati K M, Park Y, Weisser E and Mackay M E 2000 Wall slip and shear stresses of polymer melts at high shear rates without pressure and viscous heating effects *J. Non-Newton. Fluid Mech.* **89** 117–31
- Carreau P J, De Kee D and Chhabra R 1997 *Capillary Rheometry, Rheology of Polymeric Systems—Principles and Applications* (München: Hanser)
- Chen C-S, Chen S-C, Liaw W-L and Chien R-D 2008 Rheological behavior of POM polymer melt flowing through micro-channels *Eur. Polym. J.* **44** 1891–8
- Chien R-D, Jong W-R and Chen S-C 2005 Study on rheological behavior of polymer melt flowing through micro-channels considering the wall-slip effect *J. Micromech. Microeng.* **15** 1389–96
- Eringen A C and Okada K 1995 A lubrication theory for fluids with microstructure *Int. J. Eng. Sci.* **33** 2297–308
- Giboz J, Copponnex T and Mele P 2007 Microinjection molding of thermoplastic polymers: a review *J. Micromech. Microeng.* **17** R96–109
- Gleißle W and Windhab E 1985 The ‘twin capillary’ a simple device to separate shear- and slip-flow of fluids *Exp. Fluids* **3** 177–80
- Hatzikiriakos S G and Dealy J M 1992 Wall slip of molten high density polyethylenes: II. Capillary rheometer studies *J. Rheol.* **36** 703–41
- Heckele M and Schomburg W K 2004 Review on micro molding of thermoplastic polymers *J. Micromech. Microeng.* **14** R1–14
- Kim D S, Lee K C, Kwon T H and Lee S S 2002 Micro-channel filling flow considering surface tension effect *J. Micromech. Microeng.* **12** 236–46
- Lee K and Mackley M R 2000 The significance of slip in matching polyethylene processing data with numerical simulation *J. Non-Newton. Fluid Mech.* **94** 159–77
- Martin M T, Whiteside B, Coates P D, Allan P S, Greenway G and Hornsby P 2003 Micromoulding: consideration of processing effects on medical materials *ANTEC 2003—61st Annual Technical Conference & Exhibition*
- Mitsoulis E, Kazatchkov I and Hatzikiriakos S 2005 The effect of slip in the flow of a branched PP melt: experiments and simulations *Rheol. Acta.* **44** 418–26
- Mooney M 1931 Explicit formulas for slip and fluidity *J. Rheol.* **2** 210–23
- Piotter V, Hanemann T, Ruprecht R and Haußelt J 1997 Injection molding and related techniques for fabrication of microstructures *Microsyst. Technol.* **129**–33
- Piotter V, Mueller K, Plewa K, Ruprecht R and Hausselt J 2002 Performance and simulation of thermoplastic micro injection molding *Microsyst. Technol.* **8** 387–90
- Rosenbaum E and Hatzikiriakos S 1997 Wall slip in the capillary flow of molten polymers subject to viscous heating *AICHE J.* **43** 598–608
- Sha B, Dimov S S, Pham D T and Griffiths C A 2005 Study of factors affecting aspect ratios achievable in micro-injection moulding *Int. Conf. 4M2005*. (Oxford: Elsevier)
- Song M C, Liu Z, Wang M J, Yu T M and Zhao D Y 2007 Research on effects of injection process parameters on the moulding process for ultra-thin wall plastic parts *J. Mater. Process. Technol.* **187** 668–71
- Su Y C, Shah J and Lin L W 2004 Implementation and analysis of polymeric microstructure replication by micro injection molding *J. Micromech. Microeng.* **14** 415–22
- Wagner M H, Schulze V and Göttfert A 1996 Rheotens – Mastercurves and drawability of polymer melts *Polym. Eng. Sci.* **36** 925–35
- Yao D and Kim B 2002 Simulation of the filling process in micro-channels for polymeric materials *J. Micromech. Microeng.* **12** 604–10
- Zhao J, Mayes R H, Chen G E, Xie H and Chan P S 2003 Effects of process parameters on the micro molding process *Polym. Eng. Sci.* **43** 1542–54

Annex A4

Microinjection Moulding – Wall-Slip Evaluation of POM Flow in Microchannels, J. C. Vasco, J. M. Maia and A. S. Pouzada, *Proceedings of PPS-26, The 26th Annual Meeting of the Polymer Processing Society*, 6th July 2010, Banff, Canada

MICROINJECTION MOULDING – WALL-SLIP EVALUATION OF POM FLOW IN MICROCHANNELS

J. C. Vasco^{1,2}, J. M. Maia^{2,3} and A. S. Pouzada^{2*}

¹ Department of Mechanical Engineering, Polytechnic Institute of Leiria, Leiria, Portugal – jvasco@estg.ipleiria.pt

² IPC - Institute for Polymers and Composites, University of Minho, Guimarães, Portugal – asp@dep.uminho.pt

³ Department of Macromolecular Science and Engineering, Case Western Reserve University, Cleveland, USA – jmaia@dep.uminho.pt

Abstract - Microinjection is recognized as one of the most efficient replication methods for microcomponents and microsystems in several domains of application. Features such as ultrathin walls or microchannels may be present in the geometry of the plastic parts causing microscale flow phenomena to occur. These phenomena can not be predicted accurately by simulation software packages so far. A micromould with commercial microinjection equipment was used to evaluate the polymer flow in microchannels and the results are seen as useful contributes to enhance the knowledge of the melt flow at the microscale. These findings may have interest in industrial applications. In this paper, rheological phenomena such as wall-slip, melt pressure drop and polymer flow length were studied and compared with standard commercial injection moulding simulator data.

Introduction

Microinjection is one of the most efficient replication methods for microcomponents and microsystems in domains of microengineering, such as optical grating elements, micro pumps, micro fluidic devices and micro gears (Griffiths *et al.*, 2006). The market for microcomponents obtained by microinjection is growing, showing high business potential and is surely becoming one of the key technologies for micromanufacturing (Sha *et al.*, 2005). The need for quickly and accurately getting the moulding zone of moulds for microinjection moulding originated the development of the Variotherm concept. These systems are important for the accurate replication of high aspect-ratio microstructures, and precise process control as is the case optical components (Piotter *et al.*, 2002; Giboz *et al.*, 2007). Despite the success on the replication of microdetails, as in CDs or DVDs, the polymer filling behaviour of mould cavities still requires further study since the simulation tools currently available cannot fully predict flow effects at the microscale. Aspects such as wall slip, surface tension and heat transfer phenomena, require further study to avoid or minimize re-engineering costs or even to prevent wrong options on microcomponents or microsystems design (Kim *et al.*, 2002; Piotter *et al.*, 2002; Su *et al.*, 2004).

This paper is based on the knowledge gathered on previously performed microrheometry studies. Such knowledge is here applied to a test part that replicates situations that may occur in an industrial product.

Experimental

Microrheometry tool

Conventional capillary rheometers are difficult to operate, especially with channels at the microscale. Alternative setups guaranteeing the flow through the microchannel must generate pressure high enough and support the high stresses developed during flow (Chien *et al.*, 2005). A concept tool for microrheometry evaluations at the microscale consisting of a set of interchangeable moulding blocks with calibrated microchannels, assembled on an injection mould structure was used. Its operation requires accurate temperature control during the moulding cycle, as well as pressure control at the extremities of the microchannel (Vasco *et al.*, 2009). The use of miniature pressure sensors and a data acquisition system makes it possible to gather the information required for rheological characterization of the flow in the microchannel. The tool is sketched in Figure 1.

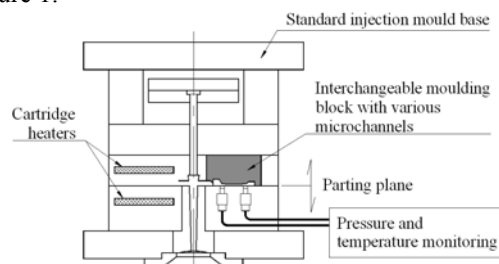


Figure 1 – Microrheometry/microinjection tool

For this study, two microchannel cross sections were tested: a slit with rectangular section, 400 μm wide by 100 μm deep, and a square section of 200 \times 200 μm . The length of both microchannels is identical, 5 mm. The pressure sensor location is depicted in Figure 2.

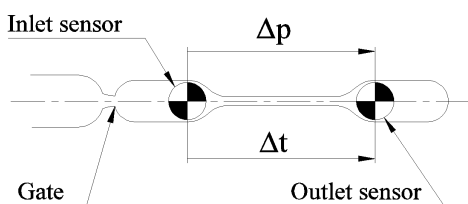


Figure 2 – Variables for microrheometry: Δp – pressure drop; Δt – time interval

The physical dimensions of the sensors used are from a different scale of the microchannel dimensions. This makes necessary the sensors being located outside the microchannel which is a source of error. Therefore, additional zero length microchannels moulding blocks were manufactured to correct for entry effects.

The injection moulding machine was a Boy 12A (Dr Boy, Germany) that combines technical characteristics for microinjection and affordability (Piotter *et al.*, 1997; Song *et al.*, 2007). It is adequate for microinjection, for being able to meter with high precision an injection volume as small as 0,1 cm^3 at flow rates up to 15,6 $\text{cm}^3\cdot\text{s}^{-1}$. The maximum injection pressure is 240 MPa. The microinjection cell consists of the Boy 12A injection moulding machine with $\varnothing 14$ mm injection screw, a mould temperature regulator and an external control unit for the cartridge heaters used in the temperature control system of the mould (Figure 3).

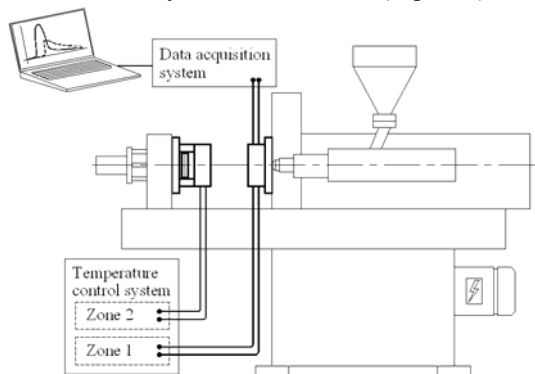


Figure 3 – Layout of the microinjection cell.

Data for microrheometry

Conventional capillary rheometry relies on the variation of the piston speed to impose different shear rates, establishing the characteristic flow curves. In this case, such variation can only be made cycle-by-cycle and not, within the injection cycle, which requires several injection cycles with different melt velocities. Each point of the flow curve must be obtained directly from a single standardized injection cycle. Unlike the microinjection process, no packing pressure was used since the goal was only to obtain a fully established flow in

the microchannel. The other process parameters, namely the mould and the melt temperatures had to be raised gradually until complete mouldings were obtained. The 14 mm-screw injection speed was varied within the capability of the equipment from 20 to 200 $\text{mm}\cdot\text{s}^{-1}$. The required mould temperature was of 145°C and the melt temperature was set at 235°C. For each microchannel the data for analysis were those corresponding to full-shot mouldings, when pressure data were gathered by both pressure sensors.

In which concerns microrheometry evaluation, the pressure drop, Δp , calculated from the pressure sensor data is required for working out the shear stress. The pressure drop between the two locations and the average melt flow velocity are used to relate the shear viscosity to the shear rate (Chien *et al.*, 2005; Chen *et al.*, 2008). The flow time between the two pressure sensors, Δt , is directly obtained from the data acquisition system, enabling the immediate calculation of an average flow rate.

Results and Discussion

The wall-slip phenomenon

The concept of wall slip was first addressed in 1931 by Mooney, who found that certain flow curves depended on the radius of the capillary once the shear stress exceeded a critical value (Lee and Mackley, 2000). The effect takes place when the shear stress at the microchannel wall exceeds a critical value, typically, above 0,1 MPa (Hatzikiriakos and Dealy, 1992; Yao and Kim, 2002; Mitsoulis *et al.*, 2005). As the magnitude of the shear stresses varies, polymer melts flow in a way that is a superposition of slipping at the wall and shearing within the melt (Gleissle and Windhab, 1985). The data gathered initially from the experimental setup enabled important conclusions concerning flow behaviour within both microchannels. The wall-slip effect described above was clearly observed in this study, since a clear shift on the flow regime occurs when critical values of shear rate are achieved (Figure 4).

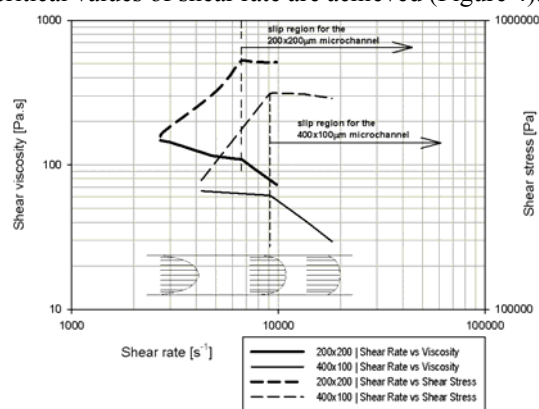


Figure 4 – Flow curves from rheometry calculations based on the 200 \times 200 μm and 400 \times 100 μm microchannels pressure data.

Both curves show a transition from a normal flow to a new type of flow where the index of non-Newtonian behaviour, n , is close to 1, indicating the onset of wall-slip. The horizontal component of both curves at constant shear stress clearly states that a change in behaviour from shear to plug flow due to the wall-slip effect as occurred. The non-horizontal component of the curves corresponds to shear flow, immediately before the critical shear rate is achieved on both microchannels. It is also possible to observe in this figure that the critical shear rate for this particular material and the $200 \times 200 \mu\text{m}$ microchannel is around 5000 s^{-1} . The critical shear rate for the $400 \times 100 \mu\text{m}$ microchannel, for which successful shots were difficult to obtain at lower melt speeds, is estimated to be approximately 6000 s^{-1} .

Comparing these flow curves with conventional rheometry ones, another important difference arises. Despite of the processing temperature used for flow in the microchannels being 235°C , the corresponding flow curve is located above the 180°C flow curve, as shown in Figure 5. This means that the actual temperature on the microchannel is much lower than the imposed processing temperature.

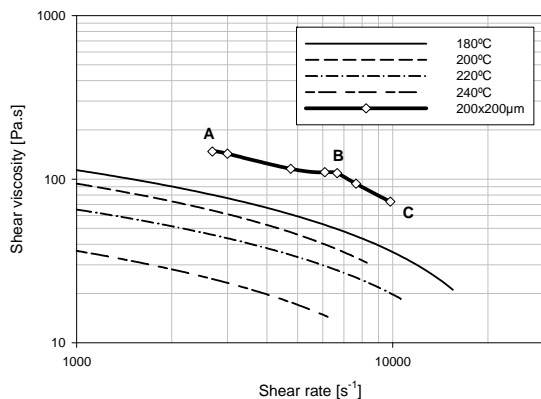


Figure 5 – Experimental data from conventional capillary rheometry and calculations based on $200 \times 200 \mu\text{m}$ microchannel pressure data.

Such fact is certainly due to the high surface area to volume ratio, which makes conventional heat transfer equations insufficient to describe what happens at this scale. Analyzing the flow curve for the $200 \times 200 \mu\text{m}$ microchannel, two segments can be observed. From A to B, shear flow is found although the end of this segment represents the transition to the next segment, B to C, in which plug flow is fully developed. The cooling of the molten material in the microchannel means that the temperature of the flowing melt is expected to be well below the initial 235°C . However, the amplitude of the decrease can not be predicted from the TTS principle. In fact, an application of TTS to the microchannel flow data to superimpose it with the other data yields an apparent flow temperature of less than 80°C . This is impossible, not only because it is more than 60°C lower than the mould wall temperature, but is

also lower than the no-flow temperature of POM which is quoted as 160°C , according to manufacturer data.

The evaluation of the local wall-slip velocity was made using a simplified power-law slip model introduced for the slip velocity without considering any pressure or temperature dependence (Rosenbaum and Hatzikiriakos, 1997). The melt front profile was estimated as a gradual shifting from shear flow to plug flow as shear stress increases. The data obtained for the $400 \times 100 \mu\text{m}$ microchannel may be inconclusive since there is not enough data in shear flow conditions to establish a reliable trend. However, the few calculated local wall-slip velocity values for this microchannel seem to corroborate the conclusions already obtained from the shear stress vs. shear rate plot (Figure 6).

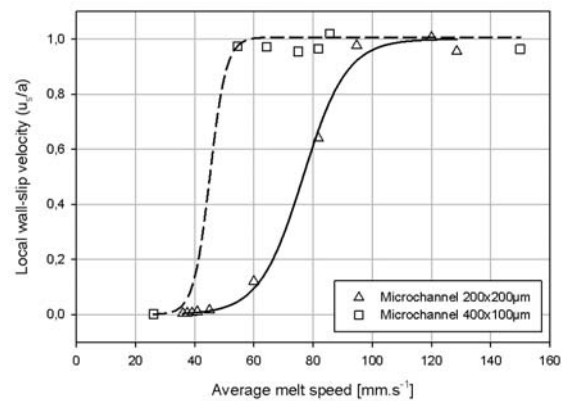


Figure 6 – Average melt speed vs. local wall-slip velocity

Nevertheless, both curves in Figure 6 show the same trend: when shear stress is less than the critical shear stress, the local wall-slip velocity is nearly zero. As predicted, the local wall-slip velocity becomes close to 1 if the shear stress keeps increasing (Rosenbaum and Hatzikiriakos, 1997).

Industrial applications

An immediate conclusion of this study is that the flow inside the mould is non-isothermal, this meaning that the data to be obtained eventually are not to be regarded as quantitatively accurate rheometrical data. At this stage it is important to let clear that the equipment setup used in this study is not a microrheometer, but rather a viscometer that replicates the flow conditions in real flow situations, *i.e.*, it is a process analyser and simulator.

This setup, besides its use on the microrheometry studies, also enables a knowledge enhancement on the flow behaviour in microinjection tests of sample test parts. Thin walls and microdetails are typical features in microsystem components such as gyroscopes, accelerometers, microswitches or transducers.

a) Case study

A sample test part was designed for this case study, depicting institutional logos. In the moulding there is

thickness variation, with thin walls down to 100 μm and microdetails with low aspect-ratio (Figure 7).

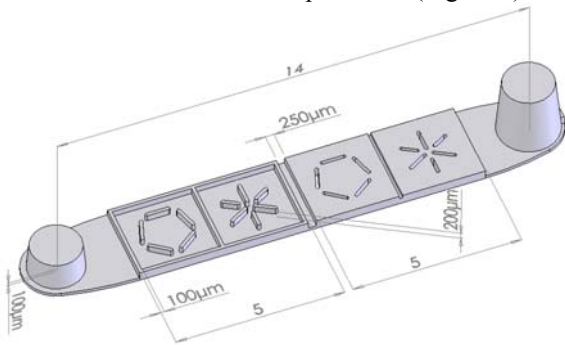


Figure 7 – Sample test part for microinjection tests (dimensions in mm)

This test part presents several challenges since the gate is located on the right tip of the part. The melt must flow through all the obstacles in the first section and then, fill the microfeatures in the second section. The first section contains low-relief logos with local thickness of 300 μm . The second section contains the 200 μm high-relief microfeatures. Throughout the part, except for the protrusions located at the extremities and the first section, the overall thickness is 100 μm . Such geometry enables the evaluation of polymer flow length on a thin wall depending on processing conditions.

The melt pressure drop is monitored by the same acquisition system used previously on the microchannels, enabling the determination of a possible wall-slip flow despite the fact that thickness decreases from the first section to the second section of the part.

b) Processing conditions

The same POM grade, Hostaform[®] C27021 used on the microrheometry study was also used here. Considering that the injection unit has a plasticizing screw with L/D ratio of 18, recommended processing temperatures for this grade are, respectively, 190 to 230°C for melt temperature, and 60 to 120°C for mould temperature. Pressure of 120 MPa is recommended, both for filling and packing. Preliminary injection tests were performed to establish processing conditions for full-shots of the sample test part. The set of values that achieved that purpose are detailed on Table 1.

Table 1 – Processing conditions

	Pressure	Time	Temperature
Injection	60 MPa	0,2	Melt 215°C
Packing	20 MPa	2	Mold 100°C

c) Experimental data

From the pressure sensors installed on the cavity, it is possible to obtain i) the pressure at the sensors, enabling the calculation of pressure drop between them, and ii) the time span for the melt touching each sensor, enabling the determination of an average melt speed, since the thickness varies along the part. The evaluation of an average polymer flow length can be estab-

lished by measurements carried out on the moulded parts. Figure 8 illustrates the average data measured by the pressure sensors.

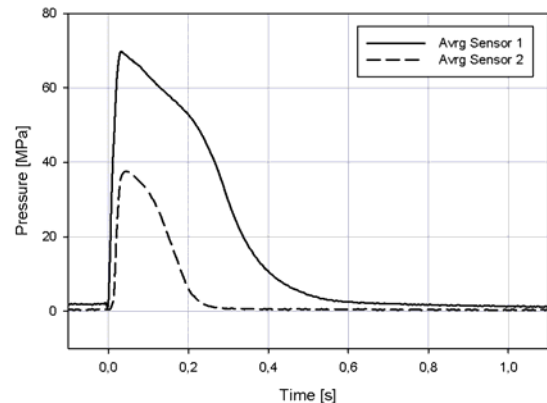


Figure 8 – Curves obtained from the average values obtained by the pressure sensors

A preliminary conclusion arises from the analysis on the previous figure: the melt speed is very high since the time delay between the signals of both pressure sensors is very short. Zooming at the beginning of both curves, it is possible to see that the time delay is around 15 ms, as shown in Figure 9.

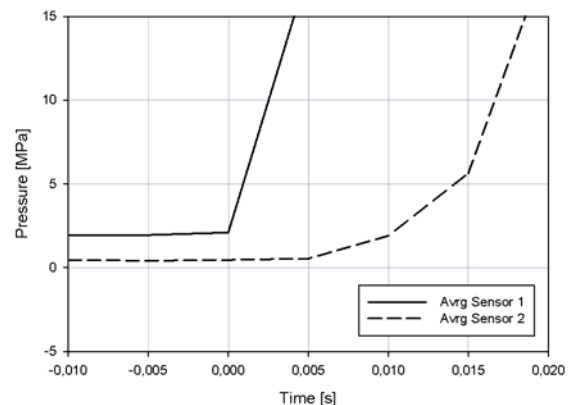


Figure 9 – Detail of the beginning of pressure curves

Considering the distance between the pressure sensors, for such short time span, the resulting average melt speed is roughly 600 $\text{mm}\cdot\text{s}^{-1}$. The melt speeds corresponding to the flow transition shown on Figure 6 refer to a much smaller cross-section and therefore, less favourable to flow. Further analysis of flow parameters are required to determine if wall-slip is occurring in this cavity.

d) Data analysis

Preliminary analysis of the pressure drop obtained from the various microinjection tests enabled the establishment of a trend on flow curves. Following a data gathering procedure similar to the one used previously on the microchannels, small variations on the melt speed were imposed, allowing the plotting of shear rate vs. viscosity on Figure 10.

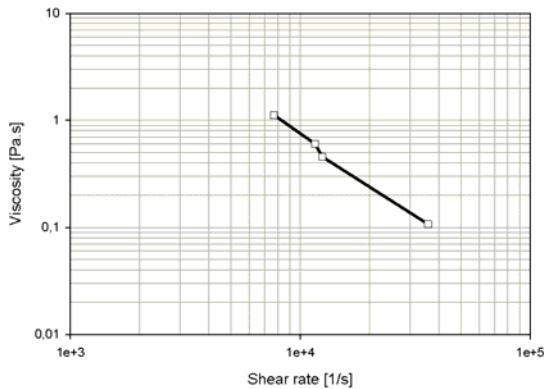


Figure 10 – Flow curve obtained at 215°C on the test part cavity

The curve plotted in Figure 10 shows a particular trend since the calculated index of non-Newtonian flow is always negative, allowing the suspicion that wall-slip is occurring.

Numerical simulations

Filling simulations were performed with the software Moldex 3D R9.1 (CoreTech, Taiwan). This software release incorporates the latest refinements concerning heat transfer, which is the most important factor, determining the process behaviour at the microscale. Filling simulations were performed with the same processing parameters used on microinjection. Furthermore two sensor nodes were located at the same place of the pressure sensors located in the cavity. A hybrid solid mesh was used, optimizing the number of elements and calculation time. At least, four elements are present on the part thickness improving simulation reliability. On the bottom face of the simulation model is located the sensor node as shown on Figure 11.

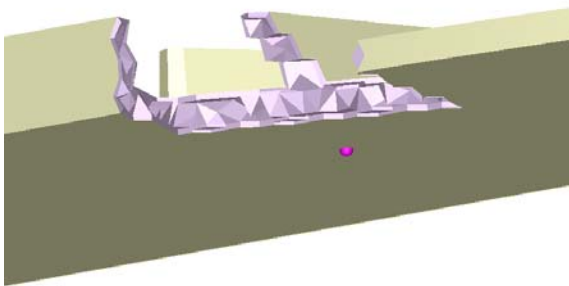


Figure 11 – Mesh section showing the solid hybrid elements across the part thickness

The filling simulations resulted on full-shots, as in the microinjection tests. The same processing parameters were used and the heat transfer coefficient was adjusted for this kind of numerical simulation. The filling results are shown in Figures 12 and 13. The sprue was removed.

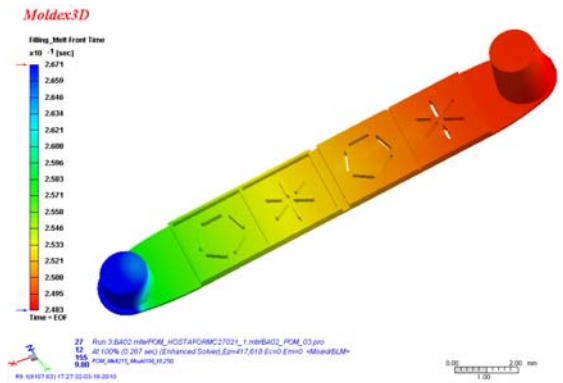


Figure 12 – Melt front time from numerical simulation

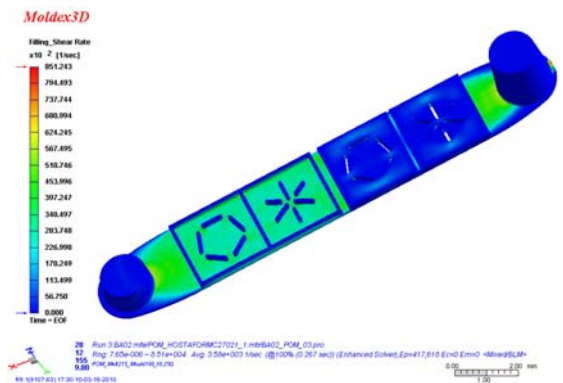


Figure 13 – Shear rate results from numerical simulation

From Figure 12 it is possible to conclude that the filling of the part took slightly less than 0,2 s, which is coherent with the values used on microinjection. The shear rate plot on Figure 13 shows the areas of the part with higher shear rates, coherent with flow in thin walls. The highest shear rate, as expected, occurred at the gate of the part. However, significant shear rates (*ca.* 60.000 s⁻¹) are also obtained at the second section where thickness is almost constant.

The sensor nodes located on the simulation model enable the comparison of the simulation pressure values on the cavity with the average pressure values obtained on microinjection. Figure 14 shows the overlapping of numerical data on experimental data. The pressure values are different concerning their magnitude, but the melt speed determined from numerical simulation is similar, since the time spans where pressure peaks occur are coincident in the time scale.

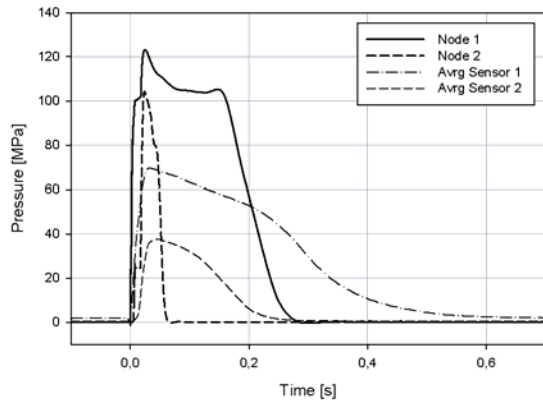


Figure 14 – Overlapping of numerical and experimental values of pressure

Conclusions

The data gathered in this study provided useful information for wall-slip evaluation. From the preliminary conclusions, it is possible to foresee the existence of a mixed-flow, a combination of classic shear flow and plug-flow that occurs when the wall-slip is perfectly established.

The measurement of the pressure drop on a test part shows that wall-slip can also be present on microinjection moulded parts.

The use of numerical simulation at this scale is currently much more reliable. However, the difference between the pressure data is still substantial. This fact may enable the conclusion that when wall-slip occurs and the material detaches from wall cavity, the cavity pressure decreases.

Acknowledgements

The authors would like to thank to Core-Tech Systems (Taiwan) and Simulflow (Portugal) for their technical support on the numerical simulations. This research work was supported by the Portuguese Foundation for the Science and Technology under the grant SFRH/BD/36982/2007 and by the Calouste-Gulbenkian Foundation.

References

Chen, C.-S., Chen, S.-C., Liaw, W.-L., *et al.*, "Rheological behavior of POM polymer melt flowing through micro-channels", *European Polymer Journal*, **44**, 1891-1898 (2008)

Chien, R.-D., Jong, W.-R., Chen, S.-C., "Study on rheological behavior of polymer melt flowing through micro-channels considering the wall-slip effect", *Journal of Micromechanics and Microengineering*, **15**, 1389-1396 (2005)

Giboz, J., Copponex, T., Mélé, P., "Microinjection molding of thermoplastic polymers: a review", *Journal*

of Micromechanics and Microengineering, **17**, R96-R109 (2007)

Gleissle, W., Windhab, E., "The "Twin capillary" a simple device to separate shear- and slip-flow of fluids", *Experiments in Fluids*, **3**, 177-180 (1985)

Griffiths, C. A., Dimov, S. S., Pham, D. T. Micro injection moulding: the effects of tool surface finish on melt flow behaviour. Multi-Material Micro manufacture. W. Menz, S. S. Dimov and B. Fillon. Oxford, Elsevier Ltd. 373-376 (2006)

Hatzikiriakos, S. G., Dealy, J. M., "Wall slip of molten high density polyethylenes II. Capillary rheometer studies", *Journal of Rheology*, **36**, 703-741 (1992)

Kim, D. S., Lee, K.-C., Kwon, T. H., *et al.*, "Micro-channel filling flow considering surface tension effect", *Journal of Micromechanics and Microengineering*, **12**, 236-246 (2002)

Lee, K., Mackley, M. R., "The significance of slip in matching polyethylene processing data with numerical simulation", *Journal of Non-Newtonian Fluid Mechanics*, **94**, 159-177 (2000)

Mitsoulis, E., Kazatchkov, I., Hatzikiriakos, S., "The effect of slip in the flow of a branched PP melt: experiments and simulations", *Rheological Acta*, **44**, 418-426 (2005)

Piotter, V., Hanemann, T., Ruprecht, R., *et al.*, "Injection molding and related techniques for fabrication of microstructures", *Microsystem Technologies*, 129-133 (1997)

Piotter, V., Mueller, K., Plewa, K., *et al.*, "Performance and simulation of thermoplastic micro injection molding", *Microsystem Technologies*, **8**, 387-390 (2002)

Rosenbaum, E., Hatzikiriakos, S., "Wall slip in the capillary flow of molten polymers subject to viscous heating", *AIChE Journal*, **43**, 598-608 (1997)

Sha, B., Dimov, S. S., Pham, D. T., *et al.*, "Study of Factors Affecting Aspect Ratios Achievable in Microinjection Moulding", *International Conference 4M2005*, 107-110 (2005)

Song, M. C., Liu, Z., Wang, M. J., *et al.*, "Research on effects of injection process parameters on the moulding process for ultra-thin wall plastic parts", *Journal of Materials Processing Technology*, **187**, 668-671 (2007)

Su, Y.-C., Shah, J., Lin, L., "Implementation and analysis of polymeric microstructure replication by micro injection molding", *Journal of Micromechanics and Microengineering*, **14**, 415-422 (2004)

Vasco, J. C., Maia, J. M., Pouzada, A. S., "Thermorheological behaviour of polymer melts in microinjection moulding", *Journal of Micromechanics and Microengineering*, **19**, 1-8 (2009)

Yao, D., Kim, B., "Simulation of the filling process in micro-channels for polymeric materials", *Journal of Micromechanics and Microengineering*, **12**, 604-610 (2002)

Annex A5

A study on the mouldability of POM microdetails in moulding blocks using micromanufacturing technologies”, J. C. Vasco, A. Selada, T. Neves and A. S. Pouzada, *Proceedings of PMI 2010, Polymer and Moulds Innovation*, 17th September 2010, Ghent, Belgium

A study on the mouldability of POM microdetails in moulding blocks using micromanufacturing technologies

J. C. Vasco^{1,2}, A. Selada^{1,2}, T. Neves³ & A. S. Pouzada¹

¹ Institute for Polymers and Composites/I3N, University of Minho, Guimarães, Portugal

² Polytechnic Institute of Leiria, Leiria, Portugal;

³ Simulflow, Lda.-Moldex 3D, Leiria, Portugal

Abstract

The integration of micro fabrication and micro-moulding techniques contributed to the massification of microsystems in several domains of activity at feasible costs. In this study the mouldability of microdetails generated by microEDM, micromilling and laser milling in microinjection moulding blocks is assessed. For that purpose, a polyacetal for precision microparts is used to evaluate how microfeatures are replicated in microinjection moulding. The mouldings were produced in a instrumented micromould with two interchangeable moulding blocks, enabling the test of various mould inserts. The processing conditions were simulated with the Moldex3D commercial software. Despite the commercial success of microinjection moulding, the process involves microscale phenomena that make the polymer flow different from the conventional flow at the macro scale. The microinjection tests and the simulation allowed the gathering of knowledge to incorporate on mathematical models and simulation software, enabling the filling simulations at this scale being more accurate. Further to the assessment of the microdetails mouldability, the surface replication and finishing of the mouldings were analysed by optical and SEM microscopy.

Introduction

There has been a significant increase in the application of miniature components and availability of microtechnologies in recent years. The main driver of this trend was mainly the electronics industry requiring smaller and smaller components and effective manufacturing processes. Until recently, the production of this miniature parts was focused on technologies traditionally used in the world of electronics and semiconductor industry, like etching, lithography and other fabrication techniques. Using these technologies extremely small feature sizes could be produced. Optical lithography, for example, produces features as small as 0.2 μm and X-ray lithography can be used to produce even smaller features [1].

There is an increasing trend towards product miniaturization with the rapid development of mi-

croengineering technologies. The development of new microdevices is highly dependent on manufacturing systems that can reliably and economically produce microparts in large quantities. In this context, microinjection moulding of polymer materials is one of the key technologies for serial micromanufacture [2].

Microinjection moulding of thermoplastics is one of the most promising fabrication techniques for non-electronic microdevices. The production costs of moulded microparts are hardly affected by the complexity of the design. Once the mould is made, thousands of parts can be moulded with little additional costs. In most cases the cost of the raw material is negligibly low, because only small material quantities are required for microcomponents. Therefore, parts fabricated by micromoulding, even from high-tech materials, are suitable for applications requiring low-cost and disposable components [3]. Thus the market is continuously demanding technologies for manufacturing large numbers of products at a reasonable price. These two requirements are met by the use of replication technologies, mainly microinjection moulding and micro hot-embossing. There is an agreement on two aspects of the microtechnologies [4]:

- o Mass production of microparts must be based on replication technologies.
- o Quality and performance of a replicated micropart depend mainly on the quality and performance of the corresponding microtool.

In context of the mould industry, the term micromanufacturing refers to the generation of high precision three-dimensional (3D) components with dimensions ranging from tens of micrometers to some millimetres. Nevertheless, some of the micromachining processes lack the capability to produce complex 3D parts with high aspect ratios.

Some of the best suited processes to create these parts, are for example laser beam machining, mechanical micromachining, electrochemical machining, electro-beam machining, focused ion beam machining and micro electro discharge machining.

Micromanufacturing Processes

The micromanufacturing technologies are a high added value key-element, to a large number of industrial sectors. Besides the creation of 3D microparts with a high aspect ratio, the achievable

accuracy and the possibility to produce microdetails are a challenge in micromachining. Frequently many factors interact and the arrangement of these factors determines the capabilities of a technique. The more common techniques used by the micromouldmaking industry include laser beam machining, micromilling and microEDM, which have advantages and disadvantages that lead to their combined use in the manufacturing of the microtools.

Micromilling

Milling plays a key role in the production of microstructured cavity inserts. In comparison to other manufacturing techniques, such as electroerosion, laser processing or semiconductor technologies, milling has advantages for low volume production:

- Able to work with hardened tool steels;
- Flexible manufacture of complex geometries;
- Use of existing CAD/CAM infrastructure;
- Comparatively small capital investment.

Micromilling still a rather young process in the micromachining domain is one of the techniques currently associated to microinjection moulding and hot embossing which imply the machining of thin features [5]. In general, micromilling has requirements exceeding those of conventional machining:

- Very high spindle speeds to achieve adequate cutting speeds for the smallest milling cutters.
- Unbalance (short cutting force)
- Very small tools and parts that are difficult to fix.
- Part size and features limited by the smallest diameter of the tools available (currently 40 μm).
- Higher positioning resolution is required.

Laser Beam Machining (LBM)

In laser beam machining (LBM), the source of energy is a laser, which focuses high density light energy on the surface of the workpiece. The maximum depth where absorption occurs is the penetration depth and leads to the conduction of the heat to the material [6]. This mechanism is used in several technologies: laser drilling, laser cutting, engraving and, more recently, 3D-laser machining.

The advantages of laser beam technologies over other processing technologies are:

- Easy conversion to automatic operation
- No processing forces
- No tool wear
- High processing speed combined with excellent reproducibility
- Capable to process very hard, brittle and soft materials
- Easy integration with other complementary manufacturing technologies

However, LBM exhibits some disadvantages, such as the formation of a heat affected zone (HAZ), poor surface roughness, and low aspect ratio.

MicroEDM (μEDM)

Electrical discharge machining is often used for machining complex work piece geometries in tools for injection moulding. Low surface roughness and filigree structures in microtools are obtained with very small discharge energies this making it necessary additional process parameters that make μEDM different from conventional EDM. In μEDM the energy of the discharge must be minimized and the frequency of the discharges increased [7]. μEDM is very appropriate with conductive materials which cannot be machined by micromilling, e.g. hard alloyed, chemically highly resistant 1.4539 steel for chemical microreactors. Furthermore, as micro milling is limited to rather small aspect ratio of the geometries in the work pieces, μEDM became a domain of deep concave geometries.

μEDM is advantageous due to:

- Machinability being independent of raw material hardness
- Versatile forms can be machined
- No mechanical forces involved (available to erode ribs with high aspect ratio)

The disadvantages result from only conductive or semi conductive materials being machined, limited surface roughness possible, existence of a heat affected layer and the wear of the electrode.

Experimental

Test parts

Two test parts were designed to evaluate a) the manufacturing issues for a microinjection moulding cavity such as the technology adopted and the obtained surface finishing; and b) the polymer behaviour on filling features such as thin walls and high aspect-ratio ribs. From the manufacturing point of view, the cavities for the ribs represent a challenge even considering the small aspect ratio of the features. The surface finishing of the side walls should enable a smooth ejection process, requiring the selection of appropriate strategies for manufacturing.

The first test part, featuring two ribs, was manufactured using micromilling and μEDM , and is represented in Figure 1. The second test part (*Figure 2*) combines the use of LBM for the manufacture of the rib with a cylindrical protrusion with a through hole manufactured by micromilling.

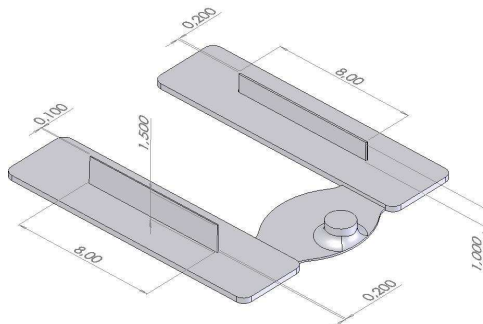


Figure 1 – Geometry of the first test part

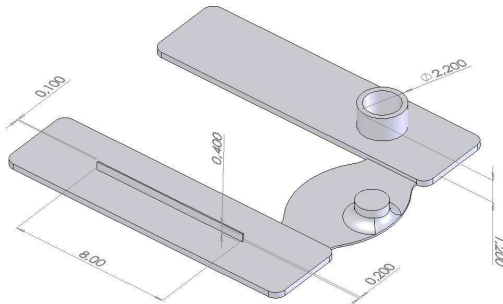


Figure 2 – Geometry of the second test part

Materials

The moulding blocks were manufactured with stainless steel DIN X42Cr13 after quenching and tempering to a hardness of 490 ± 9 (HV0.01). This 13% chromium stainless steel is used in moulds for plastics where high hardness upon heat treatment and good polishing are required. The moulding blocks are depicted on Figure 3.

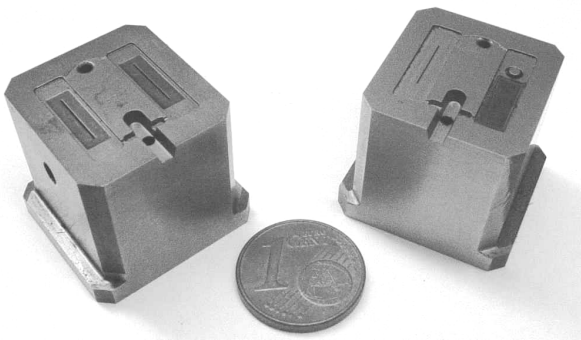


Figure 3 – Moulding blocks

The injection tests were carried with polyoxymethylene (POM), Hostaform C27021 from Ticona-Europe (Kelsterbach, Germany). This grade is very easy flow injection moulding with MFR of $24 \text{ cm}^3/10 \text{ min}$ (190°C , 2.16 kg) and is commonly used in microinjection moulding [3].

Manufacturing equipment

The micromilling operations were made with a FIDIA HS644 High Speed Micro Machining Center (Torino, Italy) with a spindle speed of 36.000 min^{-1} . The parameters used for manufacturing are listed in Table 1.

Table 1 – Micromilling parameters

Parameter	Units	Values
Cutting Speed (V_c)	$\text{m} \cdot \text{min}^{-1}$	68
Spindle Speed (n)	min^{-1}	36.000
Feed per tooth (f_z)	μm	4
Width of cut (a_e)	μm	4

For the laser beam machining process, a Deckel-Maho DML 40 SI equipment (Bielefeld, Germany) with 100 W Nd:YAG-type pulsed laser with wavelength of 1064 nm was used. The operating parameters used for manufacturing are listed in Table 2.

Table 2 – Laser beam machining parameters

Parameter	Units	Values
Pulse frequency	kHz	30
Cutting depth	μm	2
Hatching	μm	10

μEDM was performed with an AgieCharmilles Hyperspark (Geneve, Switzerland). The operating parameters are described in Table 3.

Table 3 – μEDM parameters

Parameter	Units	Values
Current Intensity	A	0,8
Voltage	V	120
Pulse time	μs	7,5 - 32
Pause time	μs	2,4

Microinjection moulding cell

The microinjection cell consists of a Boy 12A injection moulding machine, a mould temperature regulator and an external control unit for the cartridge heaters used in the temperature control system of the mould (Figure 4).

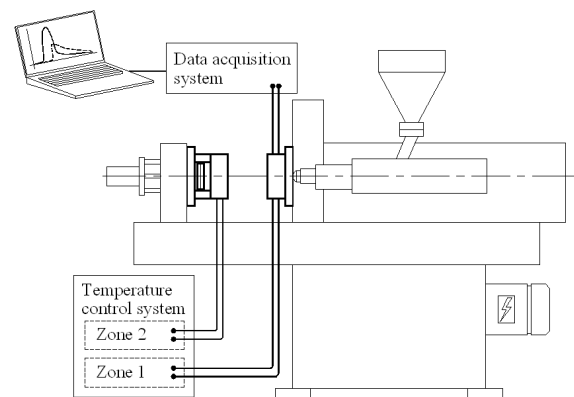


Figure 4 – Layout of the microinjection cell

The injection moulding machine Boy 12A (Dr Boy GmbH, Germany) with $\text{Ø}14 \text{ mm}$ injection screw combines technical characteristics for microinjection and affordability [8, 9]. It is adequate for microinjection, for being able to precisely meter with

injection volume as small as $0,1 \text{ cm}^3$ at flow rates up to $15,6 \text{ cm}^3 \cdot \text{s}^{-1}$. The maximum injection pressure is 240 MPa.

The processing conditions summarized in Table 4.

Table 4 – Processing conditions

Parameter	Units	Values
Melt temperature	°C	200
Mould temperature	°C	95
Injection speed	$\text{mm} \cdot \text{s}^{-1}$	100
Injection pressure	MPa	100
Holding pressure	MPa	80
Holding time	s	2

Filling simulation

Numerical simulations were performed with the software Moldex3D R9.1 (CoreTech, Taiwan). This software release incorporates the latest refinements concerning heat transfer, which is one of the most important factors determining the process behaviour at the microscale. Filling simulations were performed with the same processing parameters used in microinjection. A hybrid solid mesh was used, optimizing the number of elements and calculation time. At least, four elements are present on the part thickness improving simulation reliability, required to model polymer flow on thin walls, such as the ribs created on the test parts. Figure 5 shows an internal detail of the hybrid mesh.

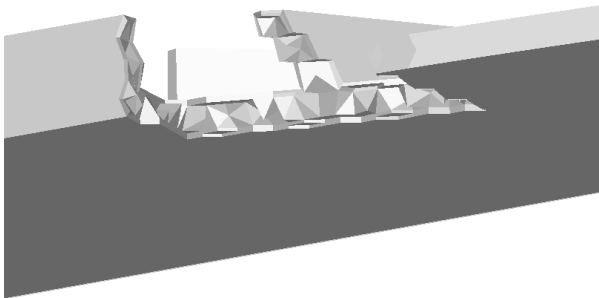


Figure 5 – Mesh detail on the simulation model

Results and discussion

Three evaluations were performed, concerning a) cavities characterization, before and after being used for the microinjection process, b) replication and shrinkage analysis of the plastic parts; and c) comparison of experimental results with numerical simulations concerning shrinkage and warpage behaviour of the plastic microparts.

Cavity characterization

The characterization of the textured surfaces was done by tactile roughness profilometry using a Perthometer M1 roughness tester (Mahr, Germany) with resolution of 10 nm. The measurements followed the ISO 4287 standard. The parameter used to evaluate the surface roughness

was the arithmetic mean roughness (Ra) as relative heights in microtopographies are more representative, especially when measuring flat surfaces. The topography evaluation of the surfaces was done by Scanning Electron Microscopy using JEOL JSM-5310 equipment (JEOL Ltd, Japan).

The roughness evaluation performed on the moulding blocks before and after the microinjection procedure showed that wear due to polymer flow had a significant effect on the surface. This may be considered as an unexpected result, considering that tool steel has been used for this application. The results of both roughness evaluations are listed on Table 5.

Table 5 – Roughness Ra data

Surface machining	Before	After
Micromilling	0,221 μm	0,022 μm
LBM	0,588 μm	0,485 μm
μEDM	0,075 μm	0,023 μm

This effect is particularly noticeable on the micromilling and LBM surfaces where a significant decrease on surface roughness occurs. The slight improvement on the LBM surface is no surprise since the process causes the re-solidification of debris over the processed area. Such debris may have been partially dragged by polymer flow, an effect that could be enhanced by the increase of shear rate up to critical values, causing a shift on the flow regime to a plug-flow [10]. There is no enough evidence to support the existence of high melt speeds on the cavity. However, the dragging of moulding block particles enables that suspicion. The moulding surfaces, prior to the microinjection procedure are shown on the Figures 6 to 8, respectively, for micromilling, LBM and μEDM .

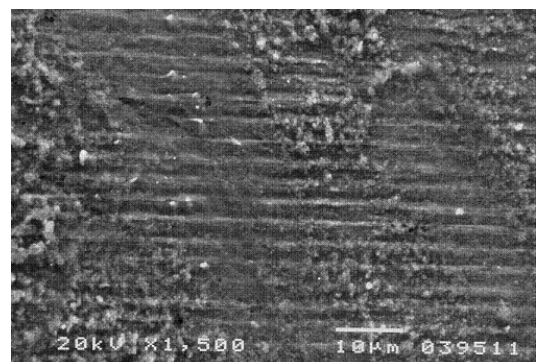


Figure 6 – SEM micrograph of the micromilled surface

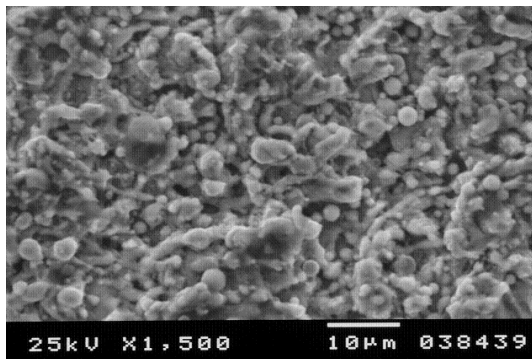


Figure 7 – SEM micrograph of the LBMed surface

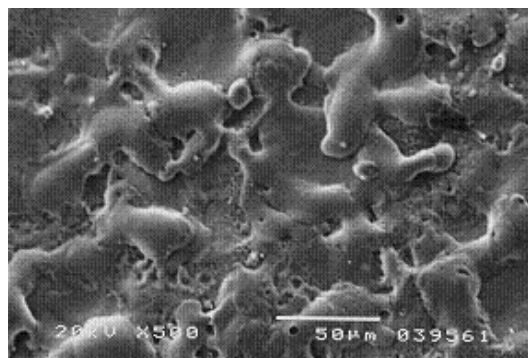


Figure 8 – SEM micrograph of the µEDMed surface

Part analysis

The plastic parts produced were analysed to determine the quality of replication on to cavity surface. Therefore, measurements were carried out to determine shrinkage at this level of dimensions and visual inspection was performed to detect any surface defect or anomalies. The shrinkage data of the two test parts are listed in Table 6.

Table 6 – Shrinkage analysis

Shrinkage		Base	Rib/Boss
First test part	Along X axis	3,15%	2,41%
	Along Y axis	3,04%	20,14%
	Along Z axis	2,06%	2,83%
Second test part	Along X axis	2,91%	3,35%
	Along Y axis	3,14%	19,57%
	Along Z axis	1,65%	5,42%

Although the X, Y and Z axes data on the base of the parts are quite similar, the shrinkage values in the Y-direction is highly affected by the measurements on the base of the rib, an area that shows the highest values of shrinkage. This effect is expected considering that the material at the base of the rib is the last to solidify. Despite the fact that there is virtually no core on thin walls, a significant shrinkage value still occurs at that location.

Concerning defects on the plastic parts, a frequent anomaly is the warpage of the part. Two additional causes contribute to that problem: the location of the ejector pins on the extremities of the part and the friction associated to the depth of the ribs. As expected, the higher is the aspect-ratio, the higher

is the probability of occurring problems on the ejection phase.

Filling simulation versus experimental

The comparison between numerical simulation and actual micromoulding considered the shrinkage referred to in the previous topic and the warpage of the mouldings. Furthermore, considering the accuracy of the simulations, it is important to access the effectiveness of the simulation by using the same processing parameters as used on the microinjection procedure. For that purpose, a simulation model of the first test part was used to perform such comparison. Concerning the filling, the part was predicted to correctly fully fill as shown in Figure 9.

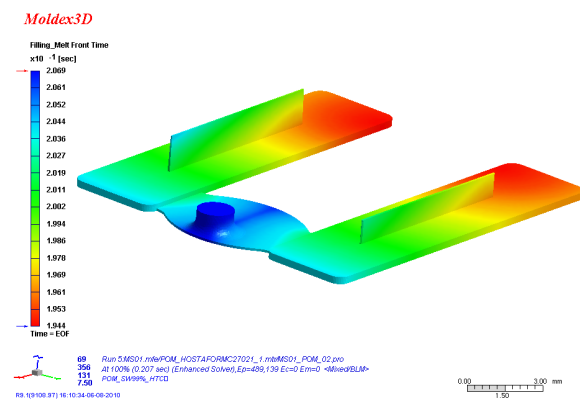


Figure 9 – Filling melt front time

Regarding shrinkage, the Moldex3D values were realistic. Shrinkage slightly below 3% was observed for this test part as referred to in the previous topic. The simulation predicted a maximum volumetric shrinkage value close to 9%, as illustrated on Figure 10. Considering that the linear shrinkage is approximately one third of the volumetric shrinkage, it is possible to conclude that the numerical simulation was quite accurate.

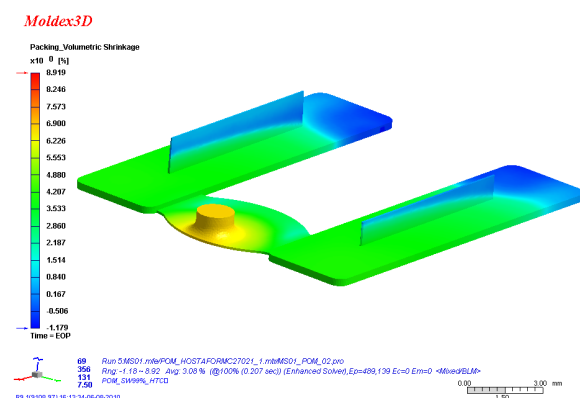


Figure 10 – Volumetric shrinkage upon packing

However, the moulded parts exhibited high shrinkage values at the base of the ribs while Moldex 3D® predicts values ranging from 3,5% to 4,8% in that area.

In which concerns to the warpage of the plastics parts, the numerical simulation also proved to be

reliable, the warpage prediction was coherent with the experiments and to what is normally expected for this type of geometry. The results of the warpage simulation carried out for the first test part are shown in Figure 11.

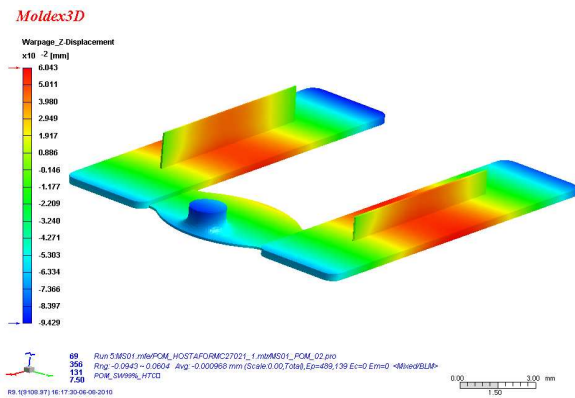


Figure 11 – Warpage on the Z direction

The moulded parts exhibited a higher displacement at the middle in the Z direction than the correspondent simulation result. Moldex 3D® predicts a maximum deflection of 155 μm while the parts show deflection values close to 500 μm at the middle. Due to the additional causes described before it is not possible to compare directly the warpage magnitude between the numerical solution and the experiment.

Conclusions

For martensitic stainless steels, as X42Cr13, the surface roughness deteriorates with increasing laser intensity. The adjustment of other laser parameters carried out a significant improvement in surface finishing quality. The lowest roughness for the X42Cr13 steel is reached with hatching and overlapping of 10 μm using a 30 μm spot diameter. Although it cannot yet be fully proved, it is possible that plug-flow is the cause for the decrease of surface roughness on machined surfaces.

Despite the fact that numerical simulation tools are still not fully adjusted to the rheological description of the flow at the microscale, Moldex3D predicted with reasonable accuracy the filling process, the shrinkage and the warpage of micromouldings.

Acknowledgements

The authors acknowledge Centimfe for metrology and roughness evaluations. This research work was supported by the Portuguese Foundation for the Science and Technology under the grant SFRH/BD/36982/2007 to J. C. Vasco.

Bibliography

- [1] Malek, C.K. and V. Saile, *Applications of LIGA technology to precision manufacturing of high-aspect-ratio micro-components and -systems: a review*. *Microelectronics Journal*, 2004. **35**: p. 131-143.
- [2] Sha, B., et al., *Study of Factors Affecting Aspect Ratios Achievable in Micro-injection Moulding in 4M2005 Conf. on Multi-material Micro Manufacture*. 2005, Elsevier: Karlsruhe. p. 107-110.
- [3] Hecke, M. and W.K. Schomburg, *Review on micro molding of thermoplastic polymers*. *Journal of Micromechanics and Microengineering*, 2004. **14**(3): p. R1-R14.
- [4] Uriarte, L., et al., *Comparison between microfabrication technologies for metal tooling*. *Proceedings of the Institution of Mechanical Engineers, Part C: Journal of Mechanical Engineering Science*, 2006. **220**(11): p. 1665-1676.
- [5] Popov, K., et al., *Micromilling: material microstructure effects*. *Proceedings of the Institution of Mechanical Engineers, Part B: Journal of Engineering Manufacture*, 2006. **220**(11): p. 1807-1813.
- [6] Jackson, M., *Micro and Nanomanufacturing*, ed. Springer. 2006.
- [7] Descoudres, A., *Characterization of electrical discharge machining plasmas*. 2006, École Polytechnique Fédérale de Lausanne: Lausanne. p. 125.
- [8] Piottter, V., et al., *Injection molding and related techniques for fabrication of microstructures*. *Microsystem Technologies*, 1997. **3**(3): p. 129-133.
- [9] Song, M.C., et al., *Research on effects of injection process parameters on the molding process for ultra-thin wall plastic parts*. *Journal of Materials Processing Technology*, 2007. **187**: p. 668-671.
- [10] Vasco, J.C., J.M. Maia, and A.S. Pouzada, *Thermorheological behaviour of polymer melts in microinjection moulding*. *Journal of Micromechanics and Microengineering*, 2009. **19**(10).